The stellar populations of early-type galaxies in groups and clusters

Richard Gwyn Bower

THE STELLAR POPULATIONS OF EARLY-TYPE GALAXIES IN GROUPS AND CLUSTERS

by

Richard Gwyn Bower

March 1990

An account of work done at the Department of Physics, submitted to the University of Durham in accordance with the regulations for admission to the degree of Doctor of Philosophy.

ABSTRACT

This thesis investigates the relationship between the environment of an early-type galaxy and its stellar populations. Most importantly, we wish to determine whether the star formation histories of early-type galaxies depend on the density of the group or cluster to which they belong. This issue is of considerable consequence, as it provides a means to distinguish whether the early-type morphology of these systems is determined at their formation, or whether it is assumed at a later time due to the action of their changing surroundings.

We have applied two methods to compare the stellar populations of these galaxies. Firstly, we have analysed the strengths of surface gravity sensitive spectral lines in order to compare the relative contributions of dwarf and giant stars to the blue light. Several samples of E and S0 galaxies, drawn from a wide variety of environments, have been measured with this technique. Secondly, we have made a precise comparison of the broad-band colours of early-type galaxies in the Coma and Virgo clusters. These clusters have very different average densities, and distinctly disparate mixtures of galaxy morphological types. The findings of these studies appear to be contradictory, however. Although the surface gravity analysis indicates that early-type galaxies in lower density regions contain more substantial populations of relatively young stars, the broad-band colours of galaxies in the Virgo and Coma clusters are indistinguishable.

A third section of the thesis develops the Press-Schechter theory for the evolution of gravitational structure in an expanding universe. Our work allows us to compare the past histories of the environments of galaxies as a function of the mass of the group or cluster to which they presently belong.

In the final chapter, we discuss how the results from these three areas of research relate to each other, and suggest two ways in which the apparent paradox of our observational work may be resolved. Considering the implications of our theoretical work leads us to review the fundamental differences between the 'nature' and 'nurture' scenarios for the origin of galaxy morphology.

PREFACE

The work presented in this thesis was carried out under between 1987 and 1990 while the author was a research student under the supervision of Prof. R. S. Ellis, in the Physics department at the University of Durham.

Some of the work was carried out in collaboration with the following research staff: Dr. J. A. Rose (of the University of North Carolina), Dr. R. M. Sharples (of the Anglo-Australian Observatory) and Prof. R. S. Ellis (Chapter 3); Dr. J. R. Lucey and Prof. R. S. Ellis (Chapter 4); Dr. C. S. Frenk (Chapter 5). The major part of the research presented is, however, the author's own work. This work has not been submitted for any degree, diploma or other qualification at any other university.

Certain results have appeared in the following papers:

Bower, R. G., Ellis, R. S., Rose, J. A. & Sharples, R. M., 1990. *Astron. J.*, **99**, 530.

Rose, J. A., Sharples, R. M., Ellis, R. S. & Bower, R. G., 1988. in *The Epoch of Galaxy Formation*, ed. Frenk, C. S., et al. (Dordrecht: Kluwer).

To my parents

Upon this Primrose Hill,

Where, if heav'n would distill

A shoure of raine, each severall drop might goe

To his owne primrose, and grow Manna so;

And where their forme, and their infinitie

Make a terrestriall Galaxie,

As the small starres doe in the skie:

I walke to finde a true Love; and I see

That 'tis not a mere woman, that is shee,

But must, or more, or lesse than woman bee.

John Donne (1572–1631)

from *The Primrose*

LIST OF CONTENTS

CHAPTER 1: INTRODUCTION 1

1.1 Galaxies, Groups and Clusters 1

1.2 The Question of 'Nature' versus 'Nurture' 3

1.3 The Aims of this Thesis 7

CHAPTER 2: OVERVIEW OF POPULATION SYNTHESIS AND THE MEASUREMENT OF STELLAR POPULATIONS 11

CHAPTER 3: THE SURFACE GRAVITIES OF EARLY-TYPE GALAXIES AS A FUNCTION OF THEIR ENVIRONMENT 17

3.1 Introduction 17

3.2 The Data 19

3.2.1 Observations and data reduction 19

3.2.2 Sample selection 20

3.2.3 Co-addition of spectra and measurement of line indices 24

3.3 Results 28

3.3.1 The mean surface-gravities of galaxies in high- and low-density environments 28

3.3.2 Assement of random errors 34

3.3.3 Statistical significance 35

3.4 Systematic Errors 38

3.4.1 Instrumental transformations 38

3.4.2 Zero-level error 39

3.4.3 Method of sample selection 39

3.4.4 Aperture effects 43

3.5 Summary and Conclusions 44

CHAPTER 4: COMPARISON OF THE COLOURS OF EARLY-TYPE GALAXIES IN VIRGO AND COMA 47

4.1 Introduction 47

4.2 Infrared Photometry 50

4.2.1 Instrumental set-up 50

4.2.2 Observational technique 50

4.2.3 Selection of galaxies 52

4.2.5 Photometric conditions 53

4.2.5 Reduction of infrared photometry 53

4.3 Optical CCD Photometry 59

4.3.1 Instrumental set-up 59

4.3.2 Observational technique 61

4.3.3 Selection criteria 62

4.3.4 Photometric conditions 63

4.3.5 Reduction of CCD photometry 64

4.4 UVJK Colours for Galaxies in Virgo and Coma 91

4.4.1 Correcting for intra-cluster light 91

4.4.2 Comparison with the photometry of PFA 93

4.4.3 Tables of U, V, J and K Magnitudes 98

4.5 Galaxy Colours Corrected for Redshift and Reddenning 108

4.5.1 K-corrections 108

4.6.2 Galactic reddenning 113

4.6 Tables of U-V and V-K Colours 120

4.7 The Colours of Galaxies in Virgo and Coma 124
4.7.1 Analysis of an improved data set 124
4.7.2 Discussion of the outlying points and scatter in the C–M relation . . . 131
4.8 Comparison with APF 133
4.9 Summary and Conclusions 134

CHAPTER 5: THE EVOLUTION OF GROUPS OF GALAXIES IN THE PRESS-SCHECHTER FORMALISM 136
5.1 Introduction 136
5.1.1 Motivation 136
5.1.2 The basic principles of the PS theory 137
5.2 The Evolution of Groups — Mathematical Results 140
5.2.1 Conditional probabilities in random Gaussian fields 140
5.2.2 Computation of the cross-correlation between scales 142
5.2.3 The conditional probability distribution of density fluctuations 146
5.2.4 The conditional multiplicity function 147
5.2.5 The joint multiplicity function 154
5.2.6 Recovering the universal Press-Schechter distribution 156
5.2.7 Comparison with N-body simulations 160
5.3 Application to the Evolution of Groups of Galaxies 166
5.4 Application to Galaxy Evolution and the Stellar Populations of Early-Type Galaxies 174
5.4.1 The evolution of the infall rate 178
5.4.2 The dependence of the infall rate on cluster mass 180
5.4.3 The half-mass epoch 180
5.4.4 The present-day environment of 'old' galaxies 183
5.5 Summary and Discussion 185

CHAPTER 6: CONCLUSIONS AND FURTHER WORK 192

6.1 Conclusions 192

6.2 Directions for Future Work 198

6.2.1 Line index analysis 198

6.2.2 The colours of early-type galaxies 198

6.2.3 Cosmological models of galaxy evolution 199

ACKNOWLEDGMENTS 201

BIBLIOGRAPHY 202

1 INTRODUCTION

1.1 Galaxies, Groups and Clusters

Since the 1920's, galaxies have been recognised as isolated systems of stars, comparable in size to the Milky-Way but at very great distances from us (Hubble, 1925). The great variety in appearance and star formation properties of these extra-galactic 'nebulae' was quickly recognised and classified (Hubble 1925, 1936). A good pictorial review of the morphological types is to be found in the ***Hubble Atlas of Galaxies*** (Sandage, 1961). The reader will readily appreciate the great contrasts in the degree of activity exhibited by the galaxies in the Atlas, from the gas-rich Sc types that seem almost to 'boil', to the S0 and E types that are little more than dull smudges on the photographic plates. For the purposes of this thesis, it is sufficient to distinguish 3 types of galaxies: the *spiral* types, that are actively forming stars in a thin gaseous disk; the *S0* types, that possess a thin stellar disk, but are no longer forming new stars; and the *elliptical* galaxies, that appear as amorphous ellipsoids, and from which young stars are absent. The passively evolving E and S0 galaxies are collectively referred to as *early-type* galaxies. In addition to these classes of giant galaxies, there is a wide variety of *dwarf* galaxies; however, we will not attempt to discuss the origin of the morphology of these fainter systems in this thesis.

Even before the extra-galactic nature of these nebulae had become established, it became apparent that galaxies did not occupy space uniformly, but tend to be clustered together to form distinct structures ranging from pairs of galaxies to clusters containing several thousand

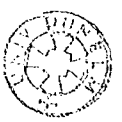

individual nebulae (eg., Wolf, 1865). It is convenient to imagine that this continuous hierarchy may be divided up into into three tiers: *isolated* galaxies; *groups* containing ~ 10 galaxies; and *clusters* containing between 100 and 1000 galaxies. The surroundings of a galaxy (its *environment*) are largely determined by the level of the hierarchy into which it has been bound. Collectively, we refer to galaxies that are isolated or bound into small groups as *the field*. Clusters are divided into *rich* and *poor* depending on the number of galaxies that they contain and their density contrast (Abell, 1958). Further subdivisions depending on the cluster's compactness and degree of regularity (Rood & Sastry, 1971), or its dominance by a single central galaxy (Bautz & Morgan, 1970) are also possible, but the details of *cluster* morphology do not concern us here.

With the observation of galaxy clustering, came the realisation that the morphology of a galaxy was closely linked with its environment (Hubble & Humason, 1931). Galaxies that occur in cluster environments are predominantly of early-type, the very densest environments (ie., the centres of rich clusters) being dominated by elliptical galaxies. The relation between environment and galaxy morphology is not a simple one, however, as many early-type galaxies occur in relative isolation. We consider the theoretical understanding of this problem in Section 1.2.

Modern telescopes and instrumentation have made it possible to map the distribution of galaxies on scales of several hundred Mpc (eg., Davis et al., 1982). The hierarchy of structure continues to these scales: the clusters form associations referred to as *super-clusters*; large holes (*voids*) appear in the galaxy distribution giving the universe a sponge-like structure on the largest scales (Gott et al., 1989). Advances in computer technology have made it possible to follow the evolution of density perturbations in a 'gas' of collisionless, self-gravitating particles with *N-body* algorithms (eg., Efstathiou et al., 1985). If the gas is placed in an expanding co-ordinate system, it is possible to simulate the formation of gravitational structure from small density perturbations present in the universe at early times. Davis et al. (1985) have shown that the density perturbation spectrum that is expected to arise in a universe

dominated by *Cold Dark Matter* (eg., non-relativistic axions) may be evolved to give a (reasonably) good match to the range of structures that are observed. Throughout this thesis, we will assume that the texture of the universe grows in this hierarchical manner (though we will not necessarily assume that the CDM perturbation spectrum is correct); we will not consider universes in which the structure is formed by the fragmentation of large scale perturbations (eg., Doroshkevich et al., 1974) or those in which extremely energetic explosions form the voids in the galaxy distribution (eg., Ostriker & Cowie, 1981). In Chapter 5, where we need to make more specific assumptions about the evolution of the density perturbations, we will assume that the initial power spectrum is well represented by a power law (of unspecified index) over the scales of interest, and that the universe has closure density (ie., $\Omega = 1$).

1.2 The Question of 'Nature' versus 'Nurture'

What has dictated that there should be such variety in the morphology of galaxies? Current thought on the subject is best summarised by contrasting theories in which galaxies are *formed* differently by 'nature' with those in which they are ***distinguished*** by 'nurture'.

(1) **The 'nature' hypothesis.** While maps of the X-ray emission from clusters (eg., Sarazin, 1988) show that the mass is (in most cases) smoothly distributed, the luminous parts of the galaxies remain identifiable as distinct units. At some epoch, therefore, the star forming gas must have dissipated sufficient energy in gas-dynamical processes to *freeze out* of the growth of the mass structure. Rees & Ostriker (1977) were able to show that our understanding of the radiative cooling of the primordial gas is sufficient to account (in the order of magnitude) for the observed range of the sizes of galaxies. If the efficiency of star formation (ie., the rate at which stars are formed from a unit mass of gas) is not a universal constant, but depends on the details of the collapse of the proto-galactic gas cloud, then galaxy morphology may be established at this early epoch. For example, if stars form rapidly in the collapsing gas cloud, a spheroidal system will result (resembling an elliptical galaxy); if the stars form more slowly, a large fraction

of the primordial gas dissipates energy until it lies in a thin disc that is supported from further collapse by its angular momentum. Specific models for these effects have been advanced by (eg.) Larson (1975), Gott & Thuan (1976) and more recently Carlberg (1984). The earlier models produced elliptical galaxies that were flattened by rotation, an effect that is not observed in giant galaxies (Illingworth, 1977). However, this problem can be circumvented if turbulent viscosity is introduced to transport angular momentum away from the central parts of the collapsing proto-galactic gas cloud. Unfortunately, while these models show that elliptical and spiral-like galaxies can be produced by tuning the same physical processes, the results depend on the details of the gas-cloud physics (ie., the star formation efficiency and the turbulent viscosity). At best, these processes are poorly understood.

(2) **The nurture hypothesis.** In the most extreme version of this scenario, the initial formation phase always produces a galaxy of similar appearance, possibly resembling one of todays spiral systems. Various physical processes have been proposed to make morphological distinctions at a later epoch. For example, it has been suggested that gas may be removed from the disk by the exhaustion of the gas supply by starformation (Larson, Tinsley & Caldwell, 1980), by supernovae driven winds (Matthews & Baker, 1971), by weak galaxy collisions (Spitzer & Baade, 1951), or by the stripping of the gas by ram pressure (Gunn & Gott, 1972) or evaporation (Cowie & Songaila, 1977) in the presence of a hot and sufficiently dense intra-cluster medium. These process may form galaxies resembling S0's. Catastrophic mergers are held responsible for the formation of elliptical systems (Toomre & Toomre, 1972). The violent relaxation (Lynden-Bell, 1969) that takes place during a galaxy merger is efficient at redistributing the angular momentum of the stellar disks to the outer parts of the halo; the resulting objects therefore rotate slowly.

The second of the scenarios presented above is appealing as galaxies *are* observed to interact with their environment in ways which demonstrably alter their morphology. Examples are: (a) Peculiar galaxies — shown often to be the result of recent galaxy mergers (Toomre &

Toomre, 1977); (b) Ring galaxies, (elliptical galaxies that are surrounded by faint stellar rings, cf., Hernquist & Quin, 1988, and references therein) — the arcs in these systems are the relic of a less recent galaxy merger; (c) observations of the HI-gas deficiency (and smaller HI-gas discs) of spiral galaxies in X-ray clusters as compared with equivalent galaxies in the field (Giovanelli & Haynes, 1983, 1985).

Naively, we might interpret the Hubble sequence as an evolutionary sequence in which environmental processes cause galaxies to evolve from later-type spirals towards either E or S0 final states. A more detailed consideration of this scenario encounters severe difficulties, however. We discuss the problems with this origin of E and S0 galaxies separately below.

(1) S0 galaxies are more dominated by bulge light (in the sense that they have both larger bulge-to-disk ratios and *absolutely* brighter bulges) than their spiral counterparts of the same magnitude (Burstein, 1979, Dressler, 1980). Selection effects, and the fading of the disc after the truncation of star formation are unable to account for both of these effects and yet explain the close similarity of the spiral and S0 luminosity functions. The presence of S0 galaxies in low density regions where the intergalactic gas density is far too low to affect galaxy evolution is also a difficulty for the rudimentary theory.

(2) In the past, several lines of argument have been used to suggest that elliptical galaxies cannot be formed by the merger of two spiral systems. The central phase-space densities in elliptical galaxies are higher than those in spiral disks. As phase-space density cannot increase in a merger, this was taken to imply that the stellar system resulting from the coalescence of two spiral galaxies could not possibly obey the same relationship between luminosity and central velocity dispersion as bona-fide elliptical galaxies (Carlberg, 1986). However, both observational studies and computer simulations have shown that the central phase-space density of the merger remnant is considerably higher than that of the progenitors' stellar *disks* (Lake & Dressler, 1986, Barnes, 1988). The explanation is that violent relaxation does not completely scramble the initial distribution of the stars, the most bound stars in the initial galaxies being also the most bound in the merger

remnant. It is therefore relevant to compare the phase-space densities of ellipticals with the *bulges* of spiral galaxies. The inefficiency of violent relaxation in mixing the initial distribution of stars also explains why metallicity gradients can be preserved in the merger (White, 1980). Although, both of the above objections to the merger origin of elliptical galaxies have been repudiated, the globular cluster populations of these galaxies do present a serious difficulty for the theory. Measurements of the specific frequency of globular clusters show (Harris & Racine, 1979, and references therein) that elliptical galaxies have up to an order of magnitude more clusters per unit luminosity than is typical in later-type systems; this problem is particularly acute in the central Dominant galaxies of rich clusters (D. Carter, priv. comm.).

In view of the objections raised above, it is customary to conclude that the morphology of galaxies must derive from the conditions in effect at their formation. We have previously outlined some of the theoretical investigations into the formation processes that are capable of producing the observed variety of present-day structures; however, we view these theories with some scepticism as their conjectures are not open to be directly tested by observation. More fundamentally, we may advance two observations that these theories, in their simplest form, have difficulty in explaining. Firstly, the morphology of a galaxy is strongly correlated with its environment (Hubble & Humason, 1931, Oemler, 1974, Dressler, 1980). While this circumstance arises naturally in the 'nurture' scenario†, it is difficult to believe that the very weak excess mean overdensity (at the epoch of galaxy formation) of a region that is destined to become a rich cluster (at the present) is able to have a major effect on the formation physics of the proto-galaxies contained within it. Secondly, galaxies *are* observed to evolve. In particular, the galaxy populations of rich clusters at moderate redshifts ($z \sim 0.3 - 0.5$) have been shown (Butcher & Oemler, 1978) to contain a much higher fraction of blue galaxies than similar clusters today. In addition, spectroscopy of these galaxies (Dressler

† Dressler's conclusion (1980) that galaxy morphology is significantly better correlated with the density defined locally for each individual galaxy, than with the mean radial value, has been shown to be invalid by the resampling technique of Salvador-Sole et al. (1989).

& Gunn 1983, Couch & Sharples, 1987) shows that they are not ordinary spirals, but are galaxies undergoing, or seen shortly after, an intense burst of star formation. A most natural interpretation is that these are the progenitors of todays S0's. Population synthesis studies provide further evidence of recent star formation activity in early-type galaxies. A common conclusion of such investigations (eg., O'connell, 1980, Pickles, 1985) is that a relatively young stellar population (age ~ 5 Gyrs) must be present in these systems in order to account for the high flux of blue light. This issue will be addressed in greater detail in the following chapter.

1.3 The Aims of this Thesis

The present work is concerned to study the relationship between the evolution of a galaxy and its environment. In particular, we are interested to see if there is evidence to suggest that the morphology of elliptical and S0 galaxies may have arisen from the action of the environment on otherwise 'normal' galaxies. The thesis naturally divides into two parts corresponding to our observational studies that compare the stellar populations of early-type galaxies in high- and low-density environments, and to our theoretical work on the evolution of the environment.

(1) **Theory.** Many previous authors have considered the effect of a galaxy's surroundings on its evolution (eg., Gisler, 1979, Larson et al., 1980, Icke, 1985). These authors assume that the environment of the 'test' galaxy is static. While such models are useful and necessary for the study of the details of the evolutionary processes themselves, but they cannot be expected to bear direct comparison to the real universe. For example, the galaxies in a rich cluster have not all been resident in the dense environment for an equally long time: some of the galaxies will have recently infallen in small groups; others will have been completely isolated before suddenly becoming bound into the deep potential well; yet others may have been present in the growing proto-cluster since it was seeded by an unusually large group early in the history of the universe. It is our

aim to develop a mathematical formalism that allows us to investigate the mix of the histories of the galaxies that we see in a rich cluster like the one described above, and to see how this mix can be expected to vary with the size of the present-day cluster. The fundamental principles of such a formalism were developed by Press & Schechter (PS, 1974) to study the evolution of the hierarchical distribution of mass in the universe as a whole. Only recently has the importance of their work been realised, as N-body simulations (Efstathiou et al., EFWD, 1988) showed that the theory made surprisingly good numerical predictions despite an apparent flaw in the arguments used by PS in its derivation. EFWD extended the formalism to include the effect of the modulation of the mass hierarchy by a background density perturbation. This gives some insight into the *biasing* of the histories of high- and low-density environments, but, because cross-correlation terms between the scales of the mass hierarchy and the background density perturbation were ignored, the solution is neither self-consistent nor does it give good *numerical* results. By including these cross-correlation effects, we further extend the PS formalism to allow us to study the mass distribution of groups (at an arbitrary epoch) in a region that will collapse to form a group/cluster of given mass at the present epoch. This mass distribution function (*multiplicity function*) contains the information we need to compare the histories of different present-day groups and clusters, and we make a rudimentary attempt to apply the theory to compare the evolutionary histories of galaxies as a function of their present-day environment.

(2) **Observation.** The observational part of this thesis applies two separate techniques to compare the stellar populations of early-type galaxies in high- and low-density environments. The first approach, using the diagnostic spectral index method developed in Rose (1985), provides a particularly clear test of the mean stellar surface gravity of a composite stellar system, and thus of its *age* (where we identify the age of a composite stellar system as the last epoch at which a significant fraction of the stars were formed). However, extremely high quality spectra are required in order that the strengths of the spectral lines can be measured with sufficient accuracy. For this reason, Rose was

only able to apply his technique to the study of a few nearby galaxies. By adding together the spectra of many individual galaxies, it is possible to obtain a single high-quality spectrum, representative of a 'typical' galaxy, although each individual spectrum is of relatively low signal-to-noise ratio. This technique, combined with the availability of fibre-optic coupling between telescope and spectrograph (this allows ~ 40 galaxies to be observed in a single exposure), has allowed us to obtain high signal-to-noise ratio spectra of 'typical' galaxies in relatively distant (by comparison with the galaxies studied by Rose) rich cluster environments. In addition to spectra of galaxies in the rich clusters Abell 2670 and Shapley 8, we have been provided with longslit spectra of galaxies in the Coma cluster, and more nearby galaxies in the field and the outer parts of the Virgo cluster. This sample is complemented with the spectra of M32 and two field E's observed by Rose. The sample contains sufficient signal that we may compare the average *age* of the E/S0 galaxies in rich clusters with that of similar galaxies in lower density environments.

The second method of comparison is based on precise U, V and K-band measurements of the luminosities of galaxies in the Virgo and Coma clusters. While galaxy colours do not provide an absolute test for the *ages* of galaxies (as it is not possible to disentangle the separate effects of metallicity and age), a relative comparison of the colours of galaxies of the same luminosity might be able to demonstrate that their stellar populations are different. In particular, the presence of Asymptotic Giant Branch stars in a galaxy of intermediate age will make its V-K colour redder while the hotter main-sequence stars make its U-V colour bluer. This effect is readily distinguished from a residual difference in the extinction of the systems as this will affect both colours in the same sense. A study of this nature has previously been attempted by Aaronson et al. (1981, APF). While they *do* find a systematic difference in the colours of the early-type galaxies in the two clusters, their result has not been generally accepted because of doubts about the homogeneity of their optical photometery and uncertainties in the instrumental corrections that have been applied to their K-band photometery of the Coma cluster. Taking advantage of the availability of CCD detector systems, we have obtained

new U and V-band photometry for a large sample of early-type galaxies in both clusters. In addition, we have repeated and extended APF's sample of K-band photometery of galaxies in the Coma cluster. This new, extremely homogeneous data-base allows us both to compare the mean colours of the E/S0 galaxies in the two clusters, and to investigate the intrinsic variations in the stellar populations of early-type galaxies within the same cluster.

Below, we briefly summarise the chapter structure of this work. In Chapter 2, we provide a brief overview of the techniques that may be applied to investigate the stellar populations of early-type galaxies. This provides the reader with background to our application of two of these techniques in Chapters 3 & 4. Chapter 3 describes our analysis of the spectra of 'typical' galaxies drawn from high- and low-density environments using the diagnostic spectral index method due to Rose (1985). Chapter 4 presents our observations and analysis of U, V, K photometery of early-type galaxies in the Virgo and Coma clusters. In Chapter 5, we present our theoretical work. The Press-Schechter (1974) formalism describing the growth of gravitational structure is extended to allow us to compare the histories of present-day groups of varying mass. We make a rudimentary attempt to link this work with the comparison of the stellar populations and morphologies of galaxies in different environments. Chapter 6 draws together the results of the previous three chapters and attempts to present a unified picture comparing the evolution of galaxies found in groups and in clusters at the present-day.

2 OVERVIEW OF POPULATION SYNTHESIS AND THE MEASUREMENT OF STELLAR POPULATIONS

The stellar populations of nearby stellar systems (such as star clusters or, more recently, dwarf spheroidal galaxies in the local group) may be studied from the distribution of the colours and magnitudes of individual stars in the Hertzsprung-Russell (H–R) diagram (eg., Schlesinger, 1969, and references therein). An estimate of the age of the system and its metal abundance (*metallicity*) is obtained by comparing the observed distribution with the theoretical prediction for a single-age, single-metallicity population of model stars. (The locus defined by the model stars is referred to as an *isochrone*.) A system that is a composite of several stellar populations, will show a spread in the observed properties of the stars that cannot be matched by a unique isochrone. This technique is extremely powerful, but it can only be applied to systems in which the individual stars can be clearly resolved. It cannot, therefore, be used to study the starformation histories of the external giant galaxies with which we are concerned in this thesis. Below, we describe several different methods of *population synthesis*; their common aim is to determine the stellar mix of a system from its integrated light alone.

Initial attempts (eg., Wood, 1966, McClure & van den Bergh, 1968, Faber, 1972) to deconvolve the distribution of the individual stars from their composite light were based on a *library* of stellar properties (eg., the broad-band UBVRIJHK colours of stars in the solar neighbourhood). Stars were selected from the library in the combination that best minimised the difference between the properties of the observed and synthetic systems. However, in the absence of further constraints, a large range of solutions are indistinguishable within the observational uncertainties. Progress must then be made by noting that many of these

solutions may be rejected on physical grounds. For example, it seems implausible that giant stars should be present in the solution without introducing some number of dwarf stars of the same age. This principle has been formalised in the system of *Evolutionary Population Synthesis* (EPS) that we describe below.

The fundamental assumption of EPS is that stars are at all times born with the same Initial Mass Function (IMF), (ie., the physical processes that determine the mass spectrum with which stars are formed do not change as the system evolves). For each epoch our knowledge of stellar evolution (see references in Tinsley, 1972) is used to follow the distribution of a single-age (single-metallicity) population of stars in the theoretical H–R diagram (ie., Effective Temperature vs. Luminosity). These *isochrones* are used to select appropriate stars from the library, additional theoretical input being required to relate the calculated effective temperatures and bolometric luminosities to the positions of real stars in the observational H–R diagram. The properties of the stars are then combined with the weighting defined by the Initial Mass Function. This gives a series of synthetic single-age (single-metallicity) stellar populations, which may be compared directly with observations of globular clusters, or combined to synthesise a more complicated system, such as an early-type galaxy. While this outline describes the basic technique of EPS, we have glossed over a number of difficulties that arise in its application. We identify the two main problems.

(1) Theoretical evolutionary tracks have not been successfully computed for stars after the onset of helium core burning (ie., the Horizontal Giant Branch). While the subsequent evolution is extremely rapid, so that only a small fraction of the stellar population is in more advanced stages of evolution, the luminosity of such stars is very great. They may therefore make a significant contribution to the properties of the composite system, and should not be omitted from the synthesis. In addition, these stars are rare in the solar neighbourhood and nearby open clusters. It is therefore difficult to include an appropriate variety of such stars in the library.

(2) In the system for which synthesis is to be attempted, stars with a wide range of metallicities may be present. In particular, stars that are considerably more metal rich than those in the solar neighbourhood are likely to be formed in the cores of elliptical galaxies. It is not yet possible to form a stellar library that covers this complete range of metal abundance. Thus even if appropriate isochrones were to be calculated, it would still not be possible to include these high-metallicity components in the synthesis.

In the original EPS system, due to Tinsley (1972), problem (1) was made more severe by the absence of evolutionary tracks for stars beyond even the Sub-Giant Branch. This deficiency was, in part, circumvented by using an empirical luminosity function to define the distribution of stars on the Red Giant Branch. It was assumed that this distribution did not evolve with the age of the stellar population. However, stars in more exotic evolutionary states (eg., the Horizontal and Asymptotic Giant Branches) were omitted completely from the synthesis. In addition, while Tinsley's model took into account the ejection of metals into interstellar medium by the more massive stars, and thus the chemical evolution of the model galaxy, no attempt was made to allow for the effect of this increasing metal abundance on either the evolutionary tracks of the stars, or the line blanketing corrections to their luminosities and colours. Instead, the synthesis was performed using solar metal abundance isochrones and a library of solar metallicity stars.

A more sophisticated treatment of these problems has been devised by Arimoto and Yoshii (1986). Advances in the theory of stellar evolution have allowed evolutionary tracks to be calculated as far as the tip of the Red Giant Branch (ie., until Helium core burning commences). An evolving Red Giant Branch may therefore be included in the model. For high mass stars, the Horizontal Branch and Asymptotic Giant Branch phases can be included using semi-empirical evolutionary tracks (in the same manner as Tinsley done for the Red Giant Branch). In addition, since the model is limited to the calculation of broad-band colours a sophisticated treatment of problem (2) is possible — the stellar library is extended to include low metallicity stars through observations of Magellanic Cloud star clusters, and to super metal-rich stars through the use of theoretical line blanketing corrections. The

dependence of the evolutionary tracks on stellar metallicity is included, and an additional level of sophistication is used to follow the chemical evolution of the gas. Once the IMF and the time variation of the starformation rate has been specified, this model calculates the colour evolution of the synthetic galaxy. However, despite the complexity of this approach, two problems become apparent. Firstly, although a very wide range of stellar evolutionary phases are incorporated, the model still fails to accurately reproduce either the extreme blueness of the U-V band colours, or the redness of the V-K colours (if an IMF similar to that measured in the solar neighbourhood is used). It is likely that this is due to the absence from the model of low mass stars on the Horizontal and Asymptotic Giant Branches. Secondly, if different models are compared, it readily becomes apparent that, on the basis of broad-band colours alone, it is impossible to distinguish systems that are genuinely old (age $>$ 10 Gyrs) from intermediate-age systems (age $\sim$ 5 Gyrs) of higher metallicity; ie., the tendency of the younger galaxy to be bluer is cancelled by the reddenning effect of its higher metallicity. If we wish to avoid this ambiguity, then the information contained in the depths of the absorption lines must be incorporated into the synthesis.

One such technique, in which the synthetic spectrum is required to match both the spectral energy distribution and the strengths of selected spectral lines, has been advanced by O'Connell (1976). Many other authors have produced similar schemes (eg., Tinsley, 1972, Faber, 1972 and references therein), but these works are plagued by the absence of accurate line strength measurements for stars covering a wide range of metallicities and ages. However, O'Connell (1980) realised that this limitation was not a problem in the synthesis of a *dwarf* elliptical galaxy (eg., M32). His synthesis code used only weak evolutionary constraints to draw stars from a library containing a full range of solar metallicity dwarfs and giants, super metal-rich K-giants and composite spectra of two metal poor globular clusters. The minimisation preferred a solution containing only solar metallicity stars, implying that the metallicity of M32 was well matched to that of the library. The main-sequence turn-off (ie., the most massive stars still in the main-sequence phase of their evolution) was placed between spectral types F6 and F9. Such a blue turn-off, combined with the solar metallicity

of the system, implies that the galaxy contains a substantial population of stars that are only ~ 6 Gyr old.

In its application to larger galaxies, O'Connell's technique suffers from the lack of metal rich main-sequence stars in the stellar library and, more generally, from the absence of stars in advanced states of evolution. For example, Gunn et al. (1981) have argued that the absence of Horizontal Branch stars may artificially cause bluer dwarfs to be selected, leading to a spurious young age for the system. A method has, however, recently been introduced by Bica & Alloin (1986, 1987) that is largely successful at side-stepping these problems. Firstly, their method uses a library that consists exclusively of spectra of star *clusters*, and not of individual stars. In this way, all need to refer to theoretical isochrones and the IMF is avoided. In addition, *all* phases of stellar evolution are automatically included. Suitable clusters have been observed in our galaxy and the Magellanic clouds in order to provide a wide coverage of both metallicity and age. However, the most metal rich globular clusters in our galaxy only reach $[Z/Z_{\odot}] = 0.1$ dex. The second development is therefore to include *artificial* high metallicity clusters into the library by extrapolating the strengths of a small number of spectral lines that are well behaved with both the age and the metal abundance of the observed clusters. The information used in the synthesis is confined to these spectral features plus the spectral energy distribution. Using this technique, Bica (1988) was able to show that the properties of early-type galaxies were very varied, both in terms of their metal content, and in the age of their youngest stellar components. In particular, they were able to confirm O'Connell's (1980) suggestion that many giant elliptical galaxies contained a significant population of intermediate-age stars.

An alternative to these full synthesis techniques has been established by Rose (1985). Rather than attempting to reconstruct the full details of an observed spectrum, a few carefully chosen spectral lines are used to diagnose particular properties of the constituent stars. We will be concerned with the indices formed from the absorption lines at 4063Å (FeI), 4077Å (SrII) and 4101Å (Hδ). These lines may be combined in such a way as to indicate the relative contributions of dwarf and giant stars to the integrated light (cf., Section 3.1). In turn,

this measurement is diagnostic of the presence of a significant population of intermediate-age stars, since these main-sequence dwarfs will then dominate the blue light of the galaxy. This method is more robust than conventional synthesis techniques as the inferred surface gravity is insensitive to both metallicity and to the presence of stars in poorly understood phases of stellar evolution. Rose applied his technique to study the stellar populations of M32 and a sample of nearby E and S0 galaxies. In agreement with the studies we have discussed previously, the light at 4000Å was found to be dominated by dwarf stars — implying the presence of a substantial intermediate-age stellar component.

In Chapters 3 and 4 of this thesis, we will be concerned with comparing the stellar populations of E and S0 galaxies in high- and low-density environments. Specifically, in Chapter 3, we will apply Rose's spectral index technique to compare the spectra of nearby early-type galaxies in the field and the outer parts of the Virgo cluster with composite spectra (ie., high signal-to-noise spectra formed coadding many spectra of spectra of lower quality) of E/S0 galaxies in rich clusters. This method provides direct evidence for a difference in the contributions of intermediate-age stars to the galaxian light in these contrasting environments. In Chapter 4, we will present high precision UVK colours for galaxies in the Virgo and Coma clusters. As we have outlined above, it is difficult to make an absolute interpretation of broad-band colours because of the confusion between metallicity and age, and because of the important contribution made to the U and K bands by stars in poorly understood phase of their evolution. However, a relative comparison of the galaxies in these very different environments is not precluded. Indeed, the remarkable uniformity of the colours of these galaxies is seemingly at odds with the differences in their stellar populations implied by the spectral index analysis. This point is discussed in detail in Chapter 6.

3 THE SURFACE GRAVITIES OF EARLY-TYPE GALAXIES AS A FUNCTION OF THEIR ENVIRONMENT

3.1 Introduction

In Chapter 2, we outlined the historical background to the 'diagnostic spectral index' technique for the determination of the mean stellar surface gravity of a composite stellar population. In this chapter, we apply this technique to compare the stellar populations of early-type galaxies in rich clusters with those of similar galaxies in low-density regions. Our aim is to infer the similarity, or difference, of the star formation histories of the galaxies in these very different present-day environments.

Before proceeding to an involved discussion of the sources of our data, their calibration onto a common system, and the results that we derive thereby, we briefly describe the method by which the strengths of the FeI, SrII and Hδ absorbtion lines are to be compared. A more detailed discussion may be found in Rose (1985). Conventionally, the strength of spectral lines is assessed by their *equivalent width*, ie., the ratio of the flux removed by the line from the continuum to the continuum flux per unit wavelength. This measure is largely insensitive to changes in the slope of the continuum, and is also insensitive to line broadening if the line is unblended. However, the equivalent width is not an appropriate measure for weak lines in the blue part of the spectrum since the density of spectral lines is so great that no true continuum can be resolved. As a result, the *pseudo-continuum* level can be significantly altered by changes in chemical composition and temperature of the composite stellar system, and is also strongly dependent on the instrumental resolution employed and the Doppler broadening of the spectral lines. Instead, we use an alternative method which involves comparing the ratios of the residual central intensities of neighbouring lines. An

index that is sensitive to stellar surface gravity may be formed from the ratios SrII/FeI and Hδ/FeI (these lines are identified in Figure 3.2). Because the continuum level is not itself involved in the determination of the index, extraneous effects of metallicity and temperature are avoided, and the sensitivity to Doppler or instrumental line broadening is greatly reduced. As with the equivalent widths, the SrII–FeI–Hδ indices are, because of their small wavelength coverage, largely unaffected by uncertainties in reddening and the relative flux calibration of the spectra.

The disadvantage of this system is that an absolute measurement of the surface gravity cannot be provided; rather, the ratios that are measured for the composite system must be compared with dwarf and giant stars that have been observed with the same instrumental system, and that have been smoothed to match the Doppler broadening of the composite. Empirically, it is found that dwarf and giant stars form two distinct sequences in the SrII/FeI vs. Hδ/FeI plane, regardless of their metallicity (this is illustrated in Figure 3.3). The position of a star along one of the sequences is determined by its effective temperature. The separation of the sequences arises from the different stellar surface gravities (ie., compactness) of the stars in these different evolutionary states. The relative separation of a composite system from the dwarf and giant stellar sequences gives an indication of its mean surface gravity, ie., of the relative contributions of dwarf and giant stars to the total light at 4000Å. In principle, the position of a system in the direction parallel to the stellar sequences can be used to gain insight into the metallicity of the system, but the interpretation of this information is fraught with theoretical and observational difficulties, and is not attempted here.

While this technique provides a particularly clean test for the presence of intermediate-age stellar populations, it has the disadvantage that the spectral lines used to form the index are extremely weak. In order to measure them to an accuracy that is significantly better than the discrimination between dwarf and giant stars (a 7% difference in the SrII/FeI index), spectra with signal-to-noise ratios in excess of 100 : 1 are required. For nearby galaxies, it is practical to obtain spectral of this quality with extended exposure times. However, the exposure time required for a galaxies in the nearest rich clusters is prohibitive. Therefore, rather than

attempting to obtain high quality spectra of individual galaxies in these environments, we combine lower quality spectra of many galaxies to obtain a single high quality spectrum of a 'typical' galaxy in the cluster. The availability of fibre-optic multiobject spectroscopic instrumentation at the Anglo-Australian Observatory that allows spectra of up to 50 galaxies to be collected in a single exposure makes this coaddition technique particularly attractive.

3.2 The Data

3.2.1 Observations and data reduction

Many previous workers have already obtained spectra at resolutions appropriate for the determination of cluster and galaxian velocity dispersions. As these spectra are also suitable for use in this project, it is not necessary for us to make fresh observations. Drs. Sharples, Rose and Teague provided us with one-dimensional spectra that had been wavelength calibrated, and had been corrected for the flux received from the night sky. Our data-set consists of: (1) intermediate dispersion longslit spectra taken on the 2.5m Isaac Newton Telescope of early-type galaxies in the Coma cluster, and NGC 2778, 3605, 4168, 4564, 4660 in the field and the outer parts of the Virgo cluster (we refer to this as the 'Virgo' sample); (2) multiobject spectroscopy at the 3.9m Anglo-Australian Telescope of the rich clusters Abell 2670 and Shapley 8; and (3) the spectra of the galaxies M32, NGC 3377 and NGC 5576 that had previously been analysed in Rose (1985). The latter spectra were obtained with the University of Hawaii 2.2m telescope on Mauna Kea, further details of the instrumentation used can be found in Rose (1985). The three rich clusters, Coma, A2670 and Shapley 8 are of similar richness and represent environments substantially more dense than Virgo (ie., the rich clusters have typical central velocity dispersions of ~ 1000 km s^{-1} whereas the field and 'Virgo' samples are drawn from regions where the local velocity dispersion is 100–600 km s^{-1}). In addition, stellar spectra, observed with the same detector system as M32, NGC 3377 and NGC 5576, were made available to calibrate the surface gravity measurements. The sources of

the different data-sets are summarised in Table 3.1; their spectral resolutions and reciprocal dispersions are given in Table 3.2.

A sample of spectra drawn from a rich-cluster will include a few objects that are field galaxies associated with the cluster only in projection. To exclude such galaxies, we rejected any galaxy with a redshift that was different from the cluster mean by more than three times the cluster velocity dispersion. The velocity dispersions were taken from Teague (1988), Sharples et al. (1987) and Kent & Gunn (1982).

In order to determine Rose's diagnostic line indices to an accuracy sufficient to discriminate between systems dominated by dwarf or giant stars, spectra with a signal in excess of 10000 photon detections per 2Å pixel are required. Only the new 'Virgo' data allows this to be done on a galaxy-by-galaxy basis. To study the rich clusters, we must coadd the spectra of between 10 and 130 individual cluster members to obtain a single representative spectrum. Although the signal in each individual spectrum varies greatly amongst the data-sets, the more distant clusters Abell 2670 and Shapley 8 contain many more objects so that the final composite spectra are of comparable quality. In addition, the resolution and dispersion varies from one set of observations to another. We therefore broadened all the spectra to a common resolution of 4.3Å FWHM to match the least resolved data.

3.2.2 Sample selection

Two issues remain before we can create and analyse the composite spectrum. Firstly, we must determine as accurately as possible which galaxies are of early-type. Most of the cluster redshift surveys from which our spectra are taken were purely magnitude-limited samples with no selection by type or colour. For 'Virgo' and Coma there is little difficulty since galaxies can be reliably selected as E or S0 from morphological data available in the literature (de Vaucouleurs et al. (1976), Dressler (1980)). However, both Abell 2670 and Shapley 8 are more distant. In the case of Abell 2670, we have experimented with selection based on morphology (Thompson, private communication, see Sharples et al., 1987), photographic B – R colours,

Table 3.1 — Sources of Spectra

Target	Telescope and Instrumentation	Source	No. Spectra
A2670	AAT/FOCAP+IPCS	Sharples, Ellis and Gray (1987)	269
Shapley 8	AAT/Flex+IPCS	Teague (1988)	94
Coma	INT/longslit+IDS+IPCS	Sharples (1989)	15
Virgo/Field	INT/longslit+IDS+IPCS	Sharples (1989)	6
Virgo/Field	Univ. Hawaii 2.2m/longslit+Cassegrain Spectrograph+ "Carnegie" image intensifier+IIIaJ photographic plate	Rose (1985)	6

Table 3.2 — Details of Observations

	Redshift	Aperture (arcsec)	Dispersion Å/mm	Pixel Size Å/pixel	Resolution Å (FWHM)
A2670	0.076	2.6	66	2.0	4.3
Shapley 8	0.047	2.6	66	2.0	4.3
Coma	0.023	2.0	264	0.5	1.7
Virgo/Field	—	2.0	264	0.5	1.7
Virgo/Field	—	3.7	50	0.6	2.5
Stars	—	1.7	50	0.6	2.5

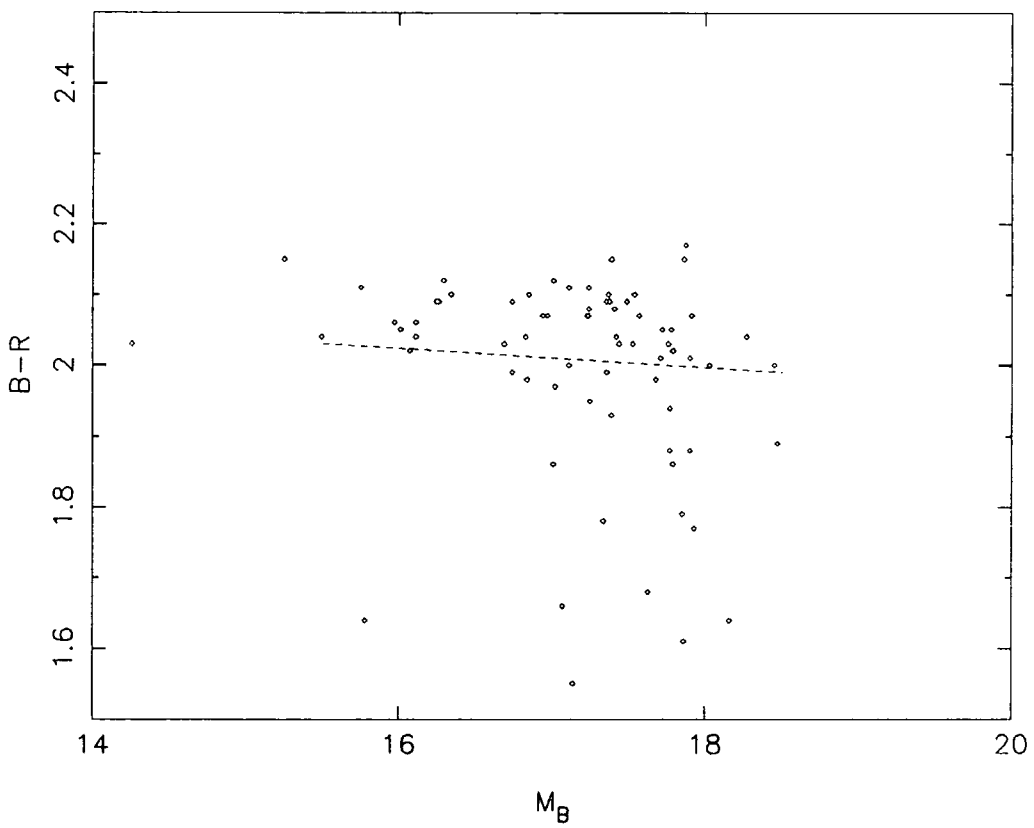

Figure 3.1. The colour–magnitude relation used to select galaxies in the cluster Shapley 8. Galaxies in the region below the dashed line were rejected from the 'early-type' sample. Photographic colours and magnitudes are from Metcalfe (1983).

and the amplitude of the 4000Å break, (D_{4000}, as defined by Dressler & Schectman, 1988). As is described in Section 3.4.3, the mean surface gravity of the cluster composite spectrum depends very little on the selection criteria applied. Our preferred sample in A2670 combines the galaxies classified as early-types by Thompson with untyped galaxies having $D_{4000} > 1.8$. Galaxies in the cluster Shapley 8 were selected using photographic B − R colours (Metcalfe, 1983) to distinguish galaxies lying close to the colour–magnitude relation (cf. Figure 3.1). In addition, we experimented with rejecting individual spectra that registered less than 150 counts per channel, but this was found to have negligible effect on the indices that we derived.

The second issue concerns the dependance of Rose's line indices on the internal stellar velocity dispersion of the galaxies. Broadening experiments show that, because of the increased blending of the lines, the indices become much less sensitive to surface gravity when the galaxy velocity dispersion is greater than about 250 $\mathrm{km\,s^{-1}}$. Velocity dispersions of galaxies in Coma and 'Virgo' are obtained from the studies of Dressler (1984) and Davies et al. (1983) and those few galaxies with dispersions greater than this limit were removed from the sample. For A2670, dispersions could only be obtained for the brighter galaxies and in Shapley 8 no direct measurements are possible. To identify those galaxies with $\sigma_v > 250$ $\mathrm{km\,s^{-1}}$ we use the correlation between luminosity and σ_v (Faber and Jackson, 1976) normalising with respect to Coma on the basis of a pure Hubble flow. Since it is the dispersion of the *composite* spectra that must be matched in order to ensure that the sensitivity of the indices is uniform, the excision of the few galaxies with excessive velocity dispersions is not critical. Ignoring this selection criterion affects the indices by less than 0.3%.

3.2.3 Coaddition of spectra and measurement of line indices

We have now defined the sample of galaxies that will be included in the cluster-composite spectrum. This section describes the procedure used to combine the spectra of the individual

galaxies and to place the resulting composite on a homogeneous system. We also outline the method used to derive mean surface gravities from each of the final spectra.

The procedure used to obtain the composite is as follows: firstly, the spectrum of each galaxy is de-redshifted to the observer's rest-frame; these spectra are then coadded and, if necessary, the composite is smoothed to a resolution of 4.3Å FWHM, and resampled at 2Å/pixel. Finally, since Rose's line index measurements are not based on any absolute scale, the composite spectra must be transformed to allow for the differences in spectral response between Rose's photographic detector system and the Image Photon Counting System (IPCS) used for the remainder of the observations. The transform is determined by matching the spectral energy distribution of the composite to Rose's photographic spectrum of the elliptical NGC 3377 over the wavelength range 3900–4300Å. As is shown in Section 3.4.1, the surface gravities measured from the spectra are not sensitive to the photographic spectrum used to define the transformation. Examples of the composite spectra used in this study are shown in Figure 3.2.

The velocities used to de-redshift the spectra are generally accurate to better than 80 $\mathrm{km\,s^{-1}}$ and this process therefore contributes negligible additional broadening. The internal velocity dispersion of the galaxies does make a significant contribution to the effective resolution of the spectral lines. In practice, however, the effective velocity dispersion of the composite spectrum varies little from cluster to cluster. To ensure all reference stars and individual galaxies (eg., M32) had the same broadening characteristics as the cluster composites, we smoothed these spectra to provide a total Doppler broadening of 180 $\mathrm{km\,s^{-1}}$. We note, however, that only very gross discrepancies in the broadening can affect the indices by more than 1%.

The minima of the FeI, SrII and Hδ spectral lines were identified by searching the 3 pixels around the tabulated central wavelength of the feature. The ratios SrII/FeI and Hδ/FeI are formed from the count rates in these pixels. Table 3.3 summarises the results derived by applying the techniques described in this section. For each spectrum, we present our

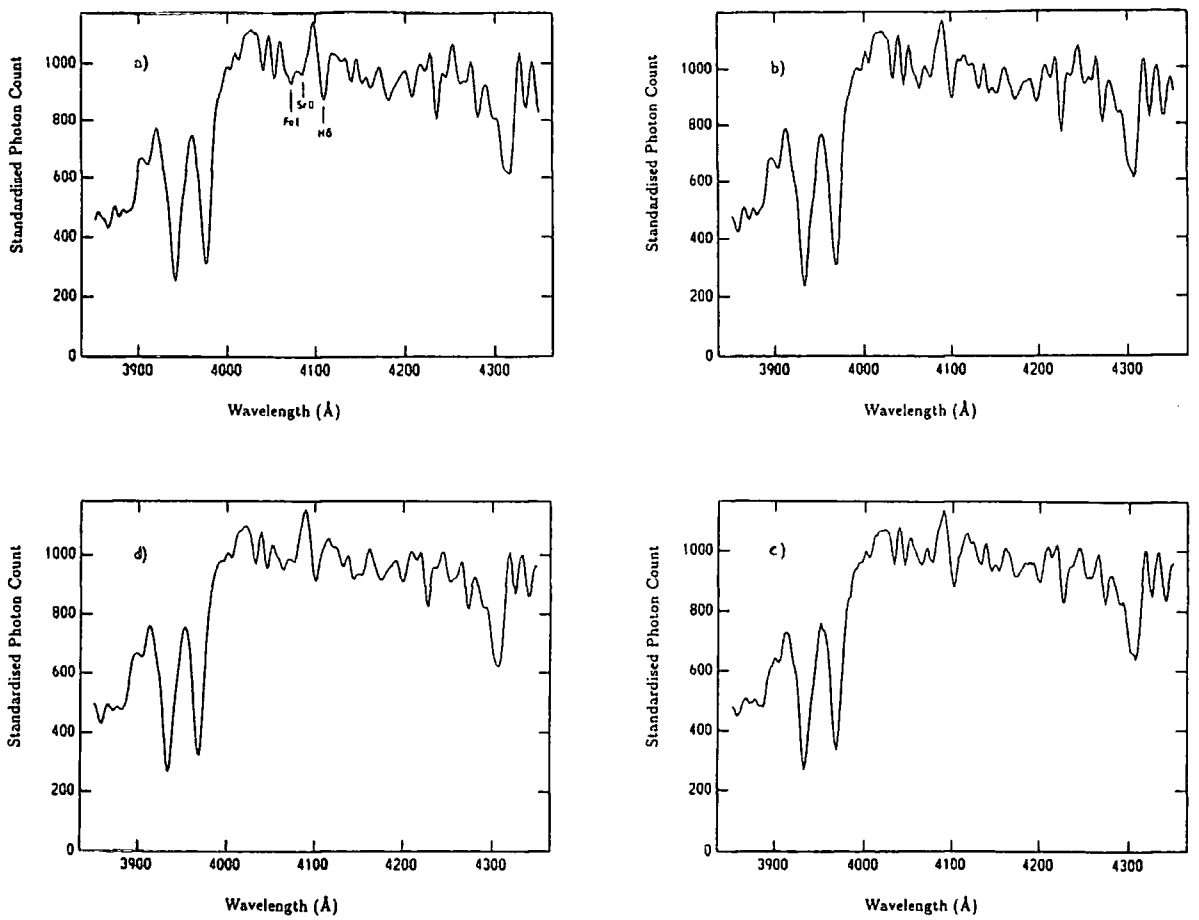

Figure 3.2. Examples of reduced and standardised spectra from which surface-gravities were measured: (a) NGC 3377, a field elliptical from Rose (1985); (b) the Virgo composite spectrum; (c) the A2670 composite spectrum; (d) the Coma composite spectrum. Details of the criteria used to select galaxies for inclusion into these spectra are given in the text. We have marked the FeI, SrII and Hδ absorption lines that are used to determine the mean stellar surface gravity of these composite systems.

Table 3.3 — Results

	Velocity Limits $km\,s^{-1}$	Selection Criteria	$N_{spectra}$	Hδ/FeI	SrII/FeI	Photon Noise[1]
A2670	19500–26000	E/S0 Morphology, or D_{4000} if untyped	128	0.921 ± 0.011	1.005 ± 0.012	0.013
Shapley 8	11000–19500	Departure from Colour-Magnitude relation	38	0.963 ± 0.013	1.029 ± 0.012	0.012
Coma	—	E/S0 Morphology	14	0.957 ± 0.015[2]	1.028 ± 0.011[2]	0.008
Virgo/Field	—	E/S0 Morphology	5	0.965 ± 0.016[2]	1.046 ± 0.008[2]	0.005
N3377			1	0.942 ± 0.007[3]	1.036 ± 0.007[3]	—
N5576			1	0.935 ± 0.007[3]	1.033 ± 0.007[3]	—
M32			4	0.902 ± 0.004[2]	1.016 ± 0.005[2]	—

Notes:

1. Errors presented with each of the indices are determined from Bootstrap Resampling of the selected galaxies (cf., Section 3.2), or estimated from the spread in measurements of individual galaxies. In the 'photon noise' column, we present errors determined from the photon count in each composite spectrum.
2. Error estimate from variance of indices for individual galaxies.
3. Crude estimate of error from comparison with M32 observations.

preferred selection criterion, the number of spectra used to make up the composite and the values measured for the Hδ/FeI and SrII/FeI indices. The various error estimates that are given will be discussed in detail in Section 3.3.2.

3.3 Results

3.3.1 The mean surface-gravities of galaxies in high- and low-density environments

As we have previously described, the luminosity-weighted mean surface gravity of a composite stellar population can be determined by comparing the strength of the gravity-sensitive SrII/FeI spectral index with the temperature-sensitive Hδ/FeI index. Figure 3.3 shows the discrimination possible for normal dwarf and giant stars. It is important to note that all F–K dwarf stars, regardless of metal abundance, lie along a single line in the diagram, and that all giants with [Fe/H] > -1.5 lie along a line that is well separated from the dwarfs. The distance of a point, corresponding to the indices determined for a composite stellar population, from the dwarf and giant sequences in Figure 3.3 indicates the relative contributions of dwarf and giant stars to the light of the 'galaxy' at 4000 Å. The direction *parallel* to the dwarf/giant sequences depends on the mean effective stellar temperature and metal abundance, and to a lesser extent on reddening and the transformation between the various instrumental systems. The crucial measurement for a composite spectrum is therefore its separation from the two sequences rather than its exact x,y location in the diagram.

Figure 3.3 presents the basic result of this chapter. The position of the new field/Virgo composite spectrum is seen to lie close to the dwarf relation in the Hδ/FeI – SrII/FeI plane, having a giant star contribution to its mean surface gravity of only 17%. This agrees well with the surface gravities determined for NGC 3377, NGC 5576 and M32, and confirms Rose's original result. The small contributions to the light of these galaxies at 4000Å from giant stars implies that stars were formed in these systems well after the initial epoch of galaxy formation.

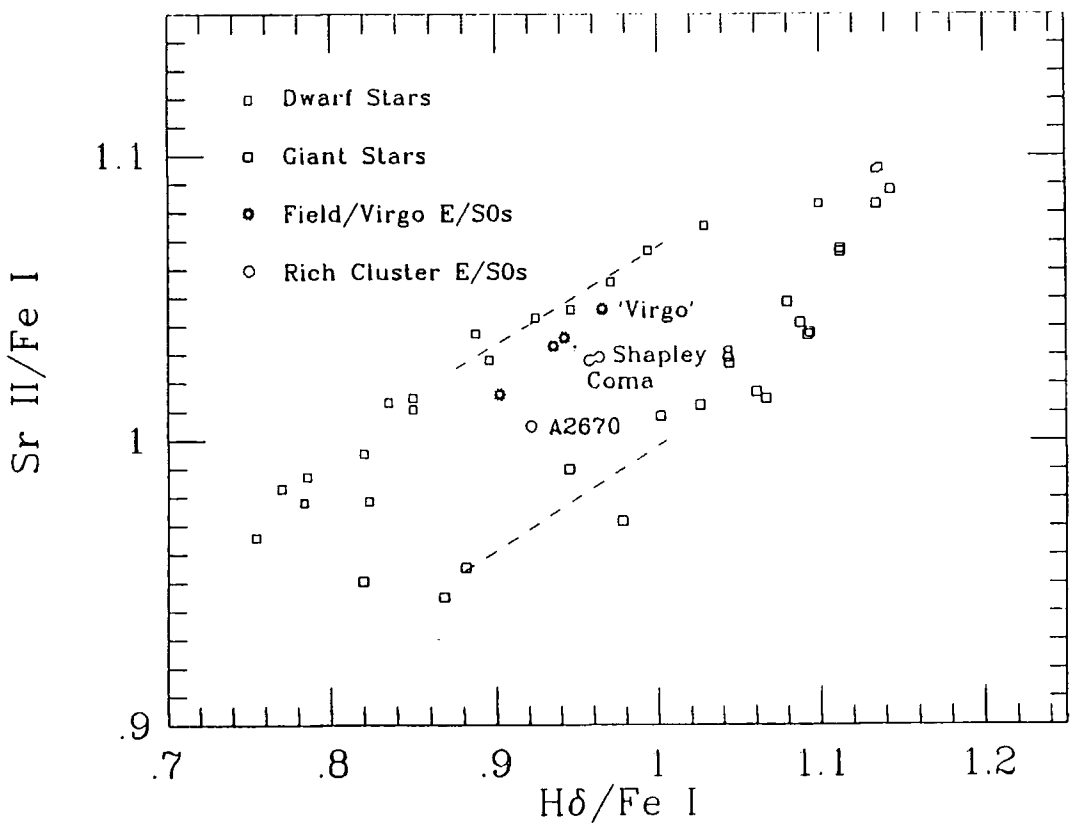

Figure 3.3. The Hδ/FeI – SrII/FeI plane, showing the dwarf- and giant-star sequences. Dashed lines show the relations adopted in order to define a quantitative measurement of the surface gravity. The field/Virgo galaxies (starred symbols) are seen to lie closer to the dwarf star locus than equivalent rich-cluster galaxies (solid dots).

However, the three rich-cluster composite spectra are all displaced further from the dwarf star relation. giant stars contribute more than 35% of the light in these systems, suggesting that star formation was truncated at a substantially earlier epoch than in equivalent low-density environment galaxies. Extreme changes in the initial mass function are required if this result is to be otherwise interpreted (cf., Rose and Tripicco, 1986). We emphasise our result therefore: *early-type galaxies in high-density environments are* (on average) *older than similar galaxies in low-density clusters and groups.*

For clarity, no error-bars have been displayed in Figure 3.3. Figure 3.4 shows an expanded view of the central part of the SrII/FeI – Hδ/FeI plane. Two sets of error-bars are presented to distinguish uncertainties determined from Poisson statistics, and those determined from Bootstrap Resampling (cf., Section 3.3.2) of the composite spectra (ie., we distinguish errors arising from the finite signal-to-noise ratio of the spectra from the total error that includes a contribution from the intrinsic scatter in the galaxy population).

We delay a consideration of the statistical significance of the distribution of points presented above until Section 3.3.3, and continue discussion of the basic result. We define the 'mean surface gravity' of a point in the SrII/FeI – Hδ/FeI diagram by its deviation from the dwarf star sequence:

$$\text{Surface Gravity} = \frac{\Delta(\text{SrII/FeI})}{\Delta(\text{SrII/FeI})_{\text{giant}}}$$

In addition, it is useful to quantify the different environments from which each of our samples have been drawn. We parameterise environment by the *virial temperature* of the group or cluster (ie., the square of its velocity dispersion) as this is much better defined than the typical mass, or mean density of the system. The choice of the environment parameter is not, however, important. We have estimated the virial temperature appropriate to each of our samples as follows: for the rich clusters, we use the square of the core velocity dispersion; for the 'Virgo' sample we use a value somewhat lower than the maximum dispersion reached in the core (ie., 500 km s^{-1} as opposed to 700 km s^{-1}, Huchra et al., 1983) to allow for the fact that field galaxies and galaxies in the periphery of the cluster are included in the

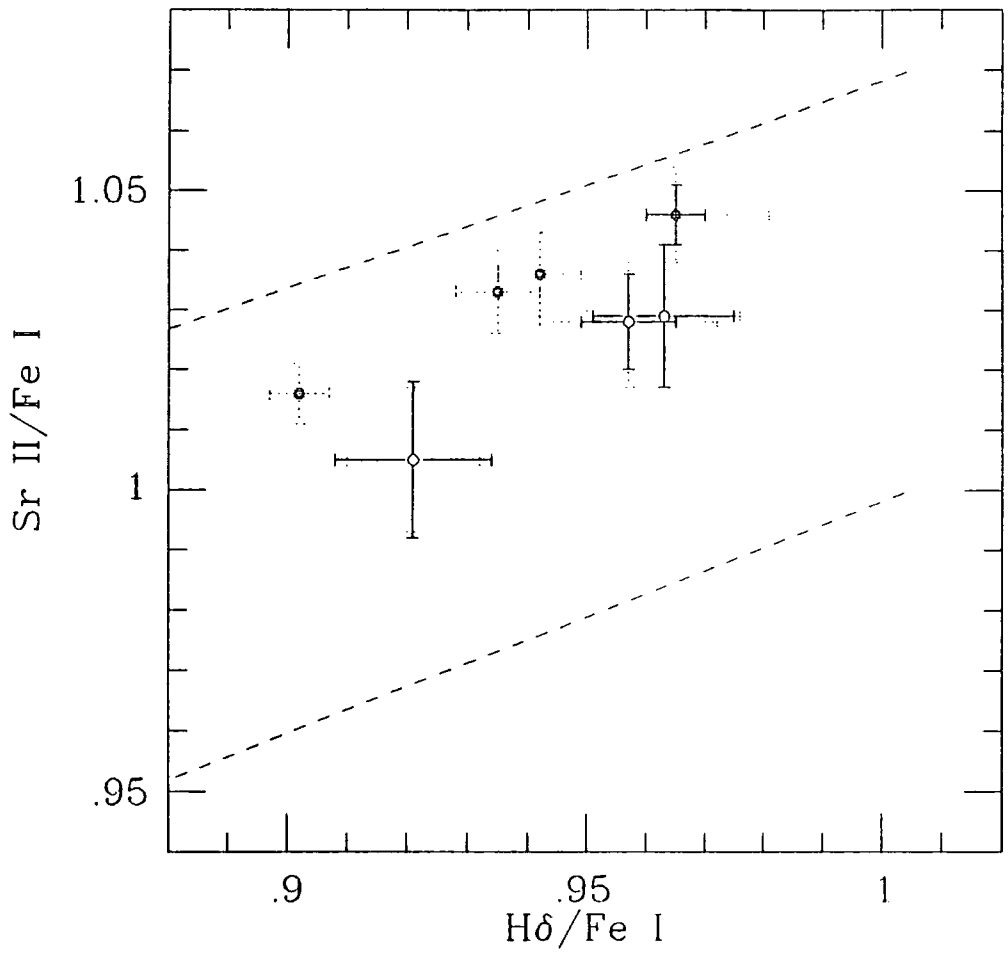

Figure 3.4. An expanded view of the central portion of the Hδ/FeI – SrII/FeI plane. The symbols and dashed lines are as described in Figure 3. Two estimates of uncertainty are distinguished: (1) — solid lines — errors determined from the total flux in each line trough, and (2) — dotted lines — errors estimated from the spread in measurements for individual galaxies, or from the Bootstrap Resampling of the data-set (cf., Section 3.3.2). For the reasons outlined in the text, these are lower and upper limits, respectively, to the true uncertainty in each of the measurements.

Table 3.4 — Surface Gravities, Environments and Effective Apertures

Spectrum	Mean Surface Gravity	'Virial Temperature' of Environment	Luminosity-Weighted Mean Aperture of Observation (units of r_e)
M32	0.24 ±0.07,	0.080	0.150–0.780
NGC 5576	0.18 ±0.10,	0.090	0.194
NGC 3377	0.17 ±0.10,	0.063	0.246
'Virgo'	0.14 ±0.11, 0.07	0.250	0.104
Shapley 8	0.37 ±0.16, 0.16	0.947	0.260
Coma	0.36 ±0.15, 0.11	1.210	0.222
A2670	0.49 ±0.16, 0.16	1.061	0.406

Notes:

1. Mean Surface Gravity is defined as

$$\frac{\Delta(\mathrm{SrII/FeI})}{\Delta(\mathrm{SrII/FeI})_{\mathrm{giant}}}$$

ie., the deviation of the SrII/FeI index value of spectrum from the index value of a dwarf star of the same Hδ/FeI index, expressed as a fraction of the separation between the dwarf- and giant-star loci. Over the range of interest, $\Delta(\mathrm{SrII/FeI})_{\mathrm{giant}} = -0.072$. The errors displayed are from Bootstrap and Poisson estimates respectively.

2. The 'virial temperature' of the environment is estimated as

$$\left(\frac{\text{central velocity dispersion}}{1000\,km\,s^{-1}}\right)^2$$

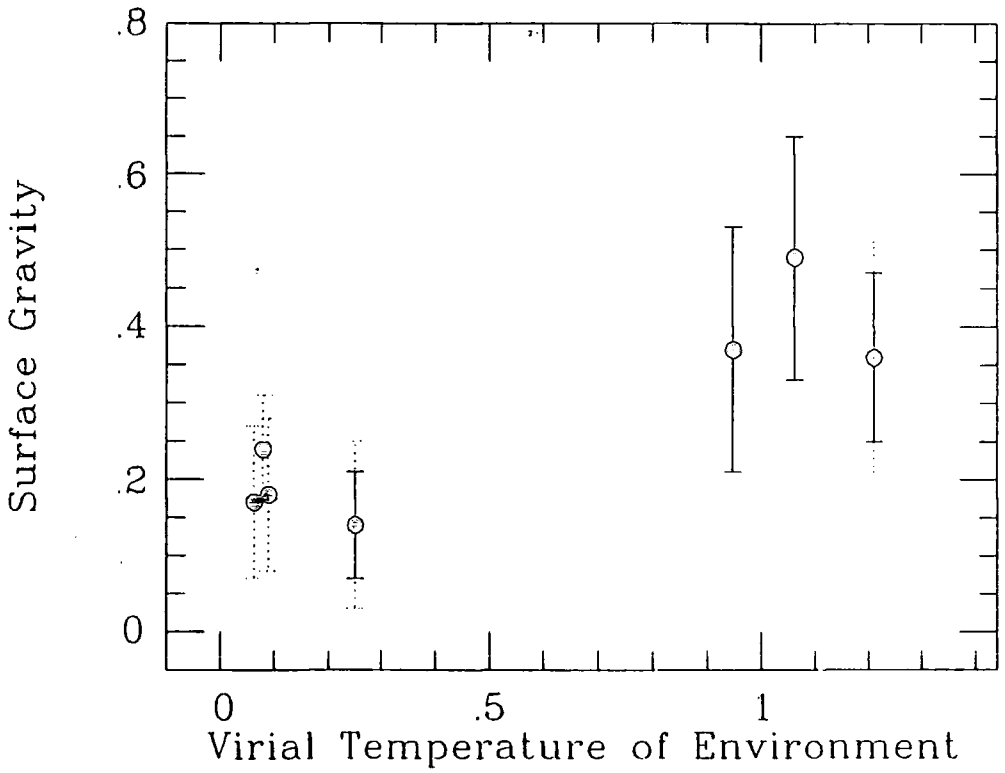

Figure 3.5. The evidence for a correlation between mean surface gravity and the 'virial temperature' of the environment. The dotted and solid lines used to distinguish error bars are described in Figure 4. The effective virial temperature has been estimated as

$$\left(\frac{\text{central velocity dispersion}}{1000\,\text{km s}^{-1}}\right)^2.$$

sample; in the field we assume values close to 270 kms^{-1} since this is typical (Rood and Dickel, 1976) of the groups in which these early-type galaxies may have originated.

In Table 3.4, we present the surface gravities measured from each of our spectra together with our estimate of the environment parameter and the luminosity-weighted mean aperture of the observations (see Section 3.4.4). Figure 3.5 presents the evidence for a correlation between environment and the mean surface gravity of the early-type galaxies in a more accessible manner. The Abscissa of the figure shows our estimate of the virial temperature of the galaxies surroundings; against this we have plotted the measured mean stellar surface gravity. It can be seen that the surface gravity falls (ie., the deviation of the SrII/FeI increases) as the environment becomes more dense. This implies that the galaxies in the denser surroundings contain smaller populations of intermediate-age stars.

3.3.2 Assement of random errors

There are three sources of random error that affect the results given above: (1) photon noise due to the limited number of counts in the absorption line trough, (2) imperfect alignment of the individual spectra as a result of errors in measuring their redshift, and (3) intrinsic differences among the galaxies themselves.

Photon noise can be determined from Poisson statistics applied to the total counts in the trough of the absorption line. Allowance must be made for the rebinning and smoothing needed to place all the spectra on a consistent system, and for the photon noise of the sky flux that has been subtracted off.

An error estimate which includes contributions from all three of the sources listed above can be made using the Bootstrap Resampling technique described by Barrow et al (1984). The method involves random sampling from the catalogue of galaxies used to form the composite spectrum so as to simulate the effect of drawing a completely new sample of galaxies from the cluster (with the same selection criteria). Each galaxy may contribute to the final spectrum once, many times or not at all. Selection is terminated when the total

photon-count in the 'new' composite is equal to that in the original. The scatter in the spectral indices derived from these resampled composite spectra gives a robust estimate of the uncertainty in the indices that were measured from the original composite spectrum. Note that we use the symmetric 66-percentile points of the distribution to define the 1σ errors as the rms scatter is unduly influenced by outlying points.

For the 'Virgo' sample, there are too few individual spectra for the Bootstrap Resampling test to be meaningful. Instead, we estimate the total error in the spectral indices from the scatter in the indices measured for the individual spectra. This procedure has also been applied to the Coma cluster; the errors derived are consistent with those determined by the Bootstrap technique.

Table 3.3 summarises the total and Poisson error estimates for each of the clusters. For the clusters A2670 and Shapley 8, it can be seen that the two estimates are comparable. For the 'Virgo' and Coma samples, the empirical error estimate is found to be greater than that determined by applying Poisson statistics. This suggests that there is some intrinsic dispersion in the properties of the cluster population. However, we emphasise that a part of this scatter is due to the well known metallicity–luminosity (ie., colour–magnitude) relation — the variation in the effective temperature of individual galaxies which this causes will result in a *correlated* spread in the Hδ/FeI and SrII/FeI indices even if all galaxies possess the same mean stellar surface gravity. We therefore chose to present both sets of error bars. The empirical errors (ie., Bootstrap or rms scatter estimates) and Poisson errors being upper and lower limits, respectively, to the true uncertainty in the average surface gravity of the galaxies in each of the clusters studied.

3.3.3 Statistical significance

In Table 3.5, we estimate the level of confidence with which we can reject the null hypothesis that the distribution of surface-gravities of galaxies in high- and low-density environments is the same. Note that in the tests described below, we have allowed only for

Table 3.5 — Estimates of Statistical Significance

	Poisson Errors		Bootstrap Errors	
Method	mean offset	confidence	mean offset	confidence
unweighted difference of means	0.224 ±.056	99.997%		
weighted difference of means	0.211 ±.088	99.2%	0.209 ±.101	98.2%
mean of differences	0.207 ±.073	99.7%	0.212 ±.082	99.5%

errors in the SrII/FeI index because the errors in the second index (ie., Hδ/FeI) are correlated so as to make the error ellipse elongated nearly parallel to the dwarf and giant loci; the uncertainties in determining the exact shape of this ellipse would not justify a more detailed analysis.

In the absence of observational errors, we may assess the significance of our results by comparing the means, and standard deviations of the means, of the two samples. This test allows the null hypothesis to be rejected with 99.997% confidence. However, a better estimate should take into account the observational errors estimated for each point (either from Poisson statistics, or by Bootstrap resampling) by applying a weighting factor of $1/\sigma_i^2$. The null hypothesis can then be rejected (applying a one-tailed test) with 99.2% confidence if the errors estimated from Poisson statistics are applied.

However, we prefer to assess the significance of our result without making the assumption that all rich-clusters of galaxies (or equivalently, all low-density groups) have a unique mean surface gravity (or equivalently, a unique age). This is best achieved by examining the distribution of the differences in surface gravity between pairs of points drawn from the high- and low-density ensembles. An observational uncertainty for each difference is estimated by adding errors in quadrature. Weighting each difference by its inverse variance, this gives a mean difference between the samples of $0.207 \pm .073$, (for Poisson errors) indicating that the two samples are different at a confidence level of 99.7% (equivalent to a 3σ deviation in a two-tailed test). If errors derived from the Bootstrap technique are used, the corresponding significance level is 99.5%. Note that in estimating the error in the mean, allowance has been made for the fact that there are only 5 degrees of freedom in the 12 differences.

We conclude that there is a less than 1% chance that the surface gravities of the high- and low-density environment samples are the same, the exact level of significance being dependant on the way in which the observational errors are taken into account. We do not attempt to resolve this problem, preferring to note that all of these tests indicate that our results are unlikely to arise unless there is a genuine difference in surface gravity between the

two samples. In the following section, we investigate possible systematic effects that might give rise to an offset between the two data-sets, even if there were no real variation in the properties of early-type galaxies with their environment.

3.4 Systematic Errors

The archival nature of our data makes any direct intercomparison between the data sources impossible, and we must therefore estimate possible systematic effects by varying the manner in which we place all the spectra on a consistent system. Below, we set out the effects that could lead to a systematic difference between the rich-cluster and low-density environment data-sets, and estimate of the maximum error in dwarf/giant ratio that they could introduce. It will be seen that the only effect that may be able to compromise the results of the previous section is the mismatch between the effective apertures of the fibre and longslit observations.

3.4.1 Instrumental transformations

In order to relate our rich-cluster data (taken with the IPCS) to Rose's original photographic system, we have taken the differing spectral response curves of the instrumentation into account by matching the spectral energy distribution of the composite for each cluster (the transform will vary with the redshift and reddening of the cluster observed) to a standard galaxy (NGC 3377) observed by Rose. This process is less critical than at first appears because any error in the slope of the transform tends to move the indices along a path of constant dwarf/giant ratio; only a substantial error in the curvature of the relation (over a wavelength range of 40Å) would grossly affect our conclusions.

We have investigated the effect of using alternative galaxy spectra to define the transformation. The spectra cover a range of $0.^m2$ in B-V; this is greater than the range of the cluster-composite colours. Although the Hδ/FeI index is affected by 2.4%, the change is

correlated with that in the SrII/FeI index so that the surface gravity is only affected by at most 1%.

3.4.2 Zero-level error

The measured surface gravity could also be affected by an error in the zero-level of the spectrum. The Shapley 8 observations are most at risk here by virtue of a poor sky-subtraction (blueward of 3900Å (in the cluster reference frame) a few of the spectra are seen to register negative counts). By examining individual spectra, we estimate that the zero-level of the composite spectrum could be in error by at most 2%. Because the difference between the line-depths is very small (3%), the largest total change in the indices is only 0.06%. In the unlikely event that there is an error in the zero-level of the *composite* of as much as 10%, the error in the indices is still less than 0.3%. Larger zero-level errors would be obvious from their effect on the depths of the Ca H & K lines.

3.4.3 Method of sample selection

For galaxies in the field and the Virgo and Coma clusters, reliable morphological classification is available. These samples are therefore well defined and consistent. Because of the greater distance of the clusters Shapley 8 and A2670, direct morphological information is not available for all the galaxies in these spectroscopic samples. We must therefore determine the galaxies' morphology indirectly, either from their adherence to the colour-magnitude relation for the cluster, or from the amplitude of the 4000Å break, D_{4000}, (defined by Bruzual, 1985). Figure 3.6 presents the correlation between morphological type and D_{4000} for galaxies in A2670 that have been classified by Thompson (priv. comm., see Sharples et al., 1987). It can be seen that 90% of elliptical galaxies have $D_{4000} > 1.8$. The accuracy with which S0 and spiral galaxies can be discriminated using D_{4000} is substantially lower, but this may be due, in part, to Thompson's missclassification of some S0s as Sa types, and vice-versa.

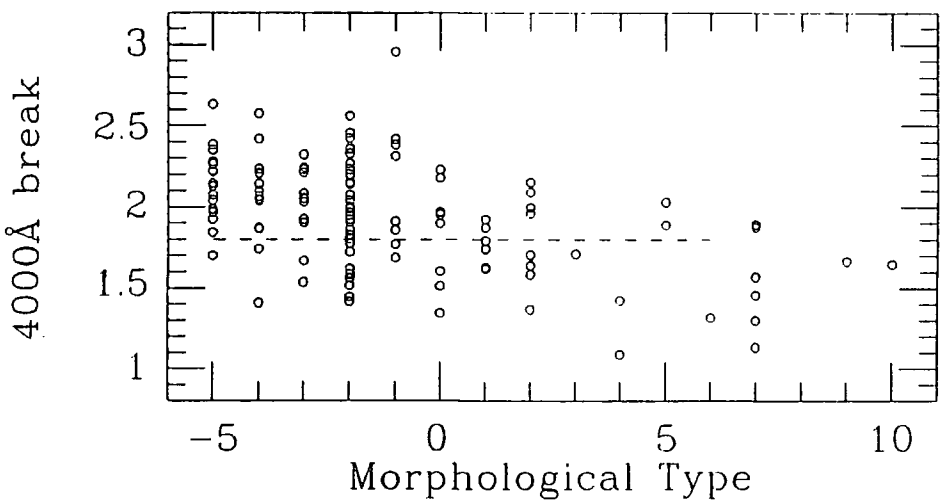

Figure 3.6. The correlation between Thompson's (priv. comm.) morphological classification (according to the system of de Vaucouleurs et al., 1976) and the amplitude of the 4000Å break for galaxies in the cluster A2670. Galaxies selected for inclusion in the composite have $D_{4000} > 1.8$.

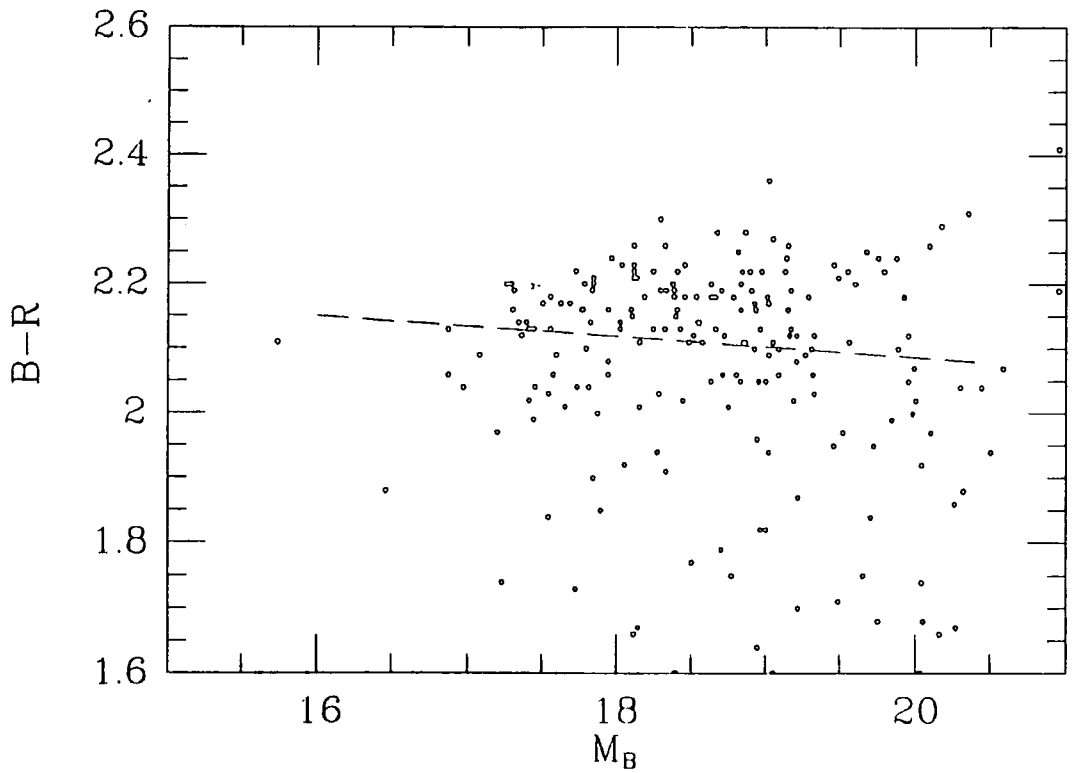

Figure 3.7. The colour-magnitude diagram for galaxies in the cluster A2670 (Sharples et al., 1987). Galaxies falling below the dashed line are rejected from the 'early-type' sample.

Table 3.6 — Consistency of Selection Criteria

Selection Criteria	$N_{spectra}$	Hδ/FeI	SrII/FeI	Surface Gravity
Galaxies typed as E/S0 plus untyped with $D_{4000} > 1.8$	128	0.921 ± 0.011	1.005 ± 0.012	0.49 ± 0.16
Galaxies typed as E/S0	80	0.915	0.992	0.61
All galaxies with $D_{4000} > 1.8$	129	0.934	1.011	0.46
Deviation from C–M relation	106	0.920	1.004	0.48

In order to determine the sensitivity of the surface gravity measured from the composite spectrum to the galaxy selection criteria, we have selected galaxies from the A2670 cluster using the following independent criteria: (1) selection of E/S0 galaxies based on Thompson's classification, (2) selection of galaxies measured to have $D_{4000} > 1.8$, (3) rejection of galaxies $0.^m07$ bluer in B-R than the mean colour-magnitude relation for the cluster (cf., Figure 3.7). The spectral indices and surface gravities measured from each of these composites are presented in Table 3.6. While the indices can differ by $\sim$ 15%, the change is almost parallel to a line of constant integrated surface gravity. The change in the giant-light contribution to the surface gravity is therefore much less than the uncertainty introduced by the photon noise. This result is not too surprising since 70% of galaxies typed as E/S0 satisfy both the colour and D_{4000} selection criteria. We conclude that galaxy samples selected by any of the techniques described all give fair representations of the mean stellar surface gravity of the early-type galaxies in each of the clusters studied.

3.4.4 Aperture effects

It is well established that the colours of early-type galaxies vary with radius (eg., Tifft, 1969). Conventionally, this is interpreted as a metallicity effect, but, for the reasons outlined in Chapter 2, an (additional) gradient in the mean age of the stellar population cannot be ruled out. A systematic difference may therefore arise if the effective apertures used to observe the high- and low-density environment galaxies are different.

A direct comparison of metric aperture sizes is not possible because the observations have made use of both single-slit and fibre-optic techniques. To allow a comparison, therefore, we have determined luminosity-weighted mean aperture diameters for each of our data-sets by assuming the galaxy surface brightness profiles are well fit by the de Vaucouleurs $r^{1/4}$ law (de Vaucouleurs, 1948). Values for r_e are taken from the literature or estimated from the

redshift of the cluster. The effective radii of the surface gravity measurements (expressed as a function of r_e) are given in Table 3.4.

It can be seen that the observations of the two distant clusters, Shapley 8 and A2670, sample the mean surface gravity at larger radii than is the case for the galaxies in the low-density environment samples. Figure 3.8 presents the evidence for a correlation between surface gravity and effective aperture. While the relationship is not so well defined as that found between surface gravity and the environment (cf., Figure 3.5), we cannot present strong statistical arguments to suggest that the latter is more fundamental. The scale of these gradients would be such that the 'age' of the stellar population must change by ~ 5 Gyrs (Rose and Tripicco, 1986) between the nucleus and a radius of ~ 1.3 Kpc ($H_0 = 50\,\mathrm{km\,s^{-1}\,Mpc^{-1}}$). In the absence of an additional metallicity gradient, this 'age gradient' would make early-type galaxies bluer towards their centres, contrary to observation. In addition, we note that Rose (1985) was unable to find any evidence for a surface gravity gradient in the *dwarf* galaxy M32. By itself, this does not rule out the presence of such gradients in giant elliptical galaxies. Finally, Couture & Hardy (1990) find that line index gradients at redder wavelengths ($\sim$ 5000Å) are compatible pure metallicity gradients. However, since Giant stars dominate the galactic light at these wavelengths, this also is not a strong constraint.

3.5 Summary and Conclusions

In this chapter, we have applied the spectral index technique developed by Rose (1985) to compare the mean stellar surface gravities of early-type galaxies in rich clusters with those of similar galaxies in lower density environments (namely, the field and the outer parts of the Virgo cluster). We have presented evidence to suggest that the galaxies located in high-density environments have lower mean stellar surface gravity. This implies that giant stars (ie., stars that have evolved away from the main sequence) make a greater contribution to the blue light of these galaxies. Before we proceed to present our detailed interpretation of this result, it is important to note that the existence of *any* difference between early-type galaxies

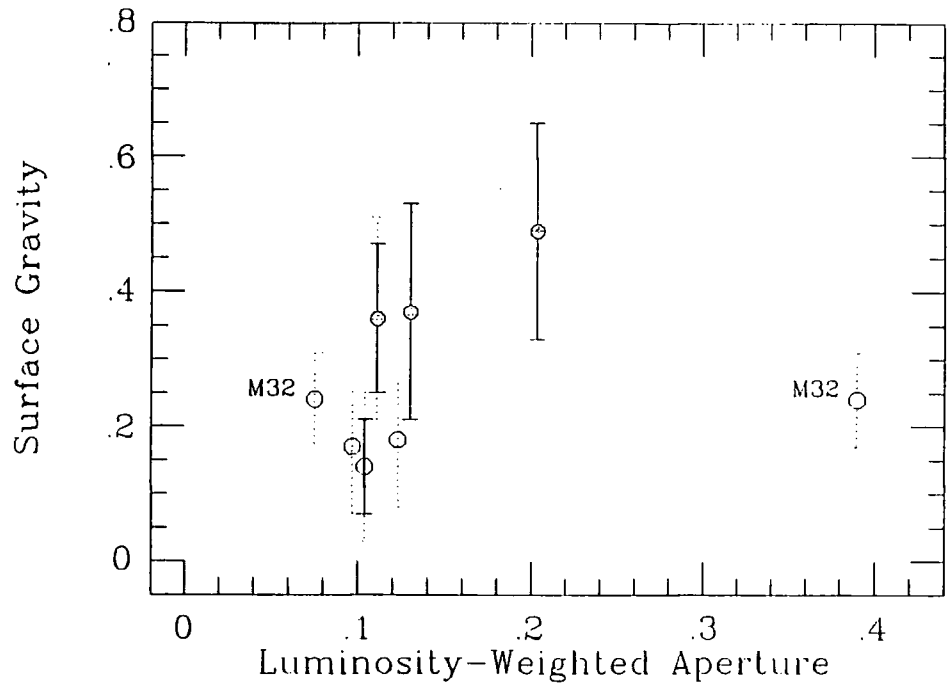

Figure 3.8. The evidence for 'age gradients' in early-type galaxies: the variation of surface gravity with the luminosity-weighted mean aperture (measure in terms of the half-light radius r_e). Open and filled circles, respectively, represent galaxies drawn from low- and high-density environments respectively. The two measurements for the dwarf galaxy M32 clearly rule-out any correlation in this galaxy, but it is not clear that the same relation should apply to the other (giant) galaxies that are shown.

in high- and low-density environments implies that the environment has played an important role in either the formation or evolution of these galaxies. However, the greater contribution of giant stars to the light of the galaxy is readily interpreted as implying that the turn-off of the stellar main-sequence is less luminous in these systems. In turn, this implies that (on average) *starformation terminated at a more recent epoch in field and poor-cluster galaxies than in galaxies that are today found in high-density environments.* A possible alternative explanation can be provided if the stellar Initial Mass Function (the mass distribution with which stars are born) varies strongly with the environment of the host galaxy. However, Rose & Tripicco (1986) showed that, since only stars in a small mass range near the main-sequence turn-off make a significant contribution to the total light at 4000Å, the change required in the IMF index is uncomfortably large (ie., changing the slope between the 'reasonable' extremes of 0.0 and 2.35, has an insignificant effect on the relative contributions of dwarf and giant stars). Therefore, in the absence of any theoretical motivation for this hypothesis, our first interpretation of the result (ie., as a variation in the *age* of the stellar population) is to be preferred.

Because of the small absolute size of the effect that we measure, and because of the heterogeneous nature of our data-set, we have been careful to examine possible sources of systematic error. The construction of the indices makes them insensitive to error in the zero-level of the spectrum and to uncertainties in the transformation between the IPCS and photographic detector systems. However, our data for galaxies in the rich clusters samples the light from a larger physical aperture than is the case for the more nearby field galaxies. Therefore, if there were a strong radial variation in the age of the stellar population within an individual galaxy, this could provide an alternative explanation of our basic result. In the absence any evidence to support this hypothesis, however, the large gradients required seem unlikely. We therefore retain our confidence in the result that there is a genuine difference between early-type galaxies found in high- and low-density environments; but clearly, the issue can only be considered settled if further evidence can be provided from an independent source.

4 COMPARISON OF THE COLOURS OF EARLY-TYPE GALAXIES IN VIRGO AND COMA

4.1 Introduction

In chapter 3, we used the depths of selected absorption lines in a very narrow region of the spectrum near 4000Å to compare the stellar populations of early-type galaxies in different environments. This approach has the advantage that the confusion between age and metallicity is avoided, but this gain is made at the expense of the high signal-to-noise ratio required in the spectra in order that the line depths can be measured with sufficient accuracy. Such high quality data can only be realistically obtained for distant galaxies by coadding the individual spectra to obtain a single composite spectrum of a 'typical' galaxy in the environment under investigation. In this chapter, we address the same problem by comparing the broad-band colours of early-type galaxies over a wide wavelength range spanning from the near-ultraviolet to the near-infrared. This method suffers from the disadvantage that it is sensitive to the presence of stars in poorly understood phases of stellar evolution (ie., stars on the Horizontal and Asymptotic Giant Branches of the H-R diagram). The interpretation of any difference that may be found is therefore complicated. However, the method benefits from the ability to make the comparison on a galaxy-by-galaxy basis; and thus to give insight into the variation in the properties of galaxies in a single environment.

For this project, we have chosen to study early-type galaxies in the Virgo and Coma clusters. The two clusters represent very different environments. The central part of the Coma system is very dense, rich in elliptical galaxies and has a high velocity dispersion. The Virgo cluster is a much weaker association; a large fraction of the galaxies have spiral morphology, and the velocity dispersion is roughly half that in the Coma cluster. A comparison of the

colours of E and S0 galaxies in these clusters has previously been made Aaronson et al. (1981, APF) by combining their own K-band photometry (Frogel et al., 1978, FPAM, and Persson et al., 1979, PFA) with optical and near-ultraviolet photometry published by Sandage (1972, S72) and Sandage & Visvanathan (1978, SV). They found evidence for a systematic difference of $0.^m10$ in V-K colour, the offset being in the sense that the early-type galaxies in the Virgo cluster were redder than similar galaxies of the same absolute magnitude in the Coma cluster. They found no evidence for any difference in U-V colour. APF suggest that this effect might be explained if the Virgo galaxies contained a population of intermediate-age Asymptotic Giant Branch (AGB) stars absent from the E/S0 galaxies in the Coma cluster. This hypothesis fits in well with evidence, presented in the previous chapter, that suggests that early-type galaxies in lower density environments continued to form stars until a more recent epoch than their counterparts in rich clusters.

The result presented by APF has, however, been criticised.

(1) Several corrections must be made to the IR magnitudes before they can be compared with optical measurements. These are each subject to uncertainty. Firstly, the IR photometer does not measure the flux from the target galaxy through a 'top-hat' aperture. A correction for this effect must therefore be determined by convolving the measured beam profile with the surface-brightness profiles of model galaxies. Secondly, PFA found that an additional correction was required since their observations had been made with a chopping distance between the galaxy and the blank sky channel of only 2–3 galaxy diameters. The sky flux measured by the photometer is then contaminated by light from the outer parts of the galaxy. In addition, we suggest that the galaxies in the very central parts of the cluster must be corrected for the intra-cluster light that contaminates the sky-channel of the photometer.

(2) The optical photometry adopted by APF may not be as homogeneous as has previously

been claimed. For example, Michard (1982) finds that the u-V colours† of galaxies in the Virgo cluster are systematically redder (by $0.^m05$) than the rest of the SV sample. Clearly great care is required to ensure that the photometric zero-points of the two clusters are precisely the same. The transformations that have been established between the photometric systems of S72 and SV may not, therefore, be sufficiently accurate for this application.

An independent study of the colours of early-type galaxies in the two clusters is therefore of considerable importance. We have three aims: (1) to significantly enlarge upon the sample of galaxies available to APF; (2) to check for systematic differences between the photometric systems in the two clusters; and (3) to increase the accuracy of the optical photometry (this is possible by virtue of improvements in photometric detector technology).

A brief outline of the strategy of this project is as follows. Firstly, we have obtained independent K-band photometry of E/S0 galaxies in the Coma cluster, the mode of operation of the photometer being carefully chosen so as to minimise the problems incurred by PFA. The measurements are used both to enlarge on PFA's sample and to test the precision of their photometry. Secondly, this data has been complimented with new homogeneous optical CCD photometry of samples of early-type galaxies in *both* clusters. By these means, we obtain accurate and homogeneous raw colours in the two clusters. Corrections for the differing extinctions and redshifts of the clusters have been estimated independently of APF, but are found to be the same. We choose not to transform these colours, that are obtained within approximately matching physical (ie., Kpc) aperture sizes, to colours within an aperture relative to the diameter of the galaxy (this departs from the procedure adopted by APF). The colours of the galaxies are now plotted as a function of their isophotal magnitude (V_{26}). The distance modulus between the clusters is determined from the colour–magnitude (C–M) correlation in each of the colour bands, and compared with the value derived from the

† We use the symbol u to distinguish the narrow-band definition of this filter used by SV from the standard broad-band definition of U (Johnson & Morgan, 1953).

Faber-Jackson (1976) (L–σ) relation (Dressler, 1984, D84). We also compare the distance-independent U-V vs. V-K colour–colour (C–C) relations in the two clusters.

4.2 Infrared Photometry

4.2.1 Instrumental set-up

The observing runs that provided data for use in this project are summarised in Table 4.1. The infrared photometry of early-type galaxies in the Coma cluster was obtained during 5 dark nights (7–12 March, 1986) at the U. K. Infrared Telescope (UKIRT) on Mauna Kea, Hawaii. The observer was Dr. M. Mountain of the Royal Observatory, Edinburgh. The photometry was performed through a relatively large aperture of 19.6″ nominal diameter. As a result, the measurements are insensitive to atmospheric seeing and to the accuracy with which the galaxy was centred. Since this increases the relative intensity of the sky flux, a reduction in the sensitivity of the photometer does, however, result. Consequently integration times of typically 6 mins. were required to reach the desired 1% accuracy. The chopping throw of the telescope was set to the large value of 150″ in order that there would be no contamination of the sky channel of the photometer by flux from the outer parts of the galaxy (cf., Frogel et al., 1978, FPAM). Consecutive exposures of each galaxy were made in the J, K and, if sky conditions appeared stable, H photometric bands. Standard UKIRT filters — described in the UKIRT Observer's Manual (U. K. Infrared Telescope Support Unit, 1988) — were used throughout the run.

4.2.2 Observational technique

Precision photometry in the infrared is made difficult by two factors — the rapid variation in the sky brightness, and the slower drift of the atmospheric transmission. Sky brightness variation is accounted for by the chopping and nodding of the telescope. The variation

Table 4.1 — Summary of Observing Time

Dates	Telescope	Observer(s)	Photometric Bands	Number of useful nights
7–12 March, 1986	UKIRT	Mountain	J, H, K	$3\frac{1}{2}$
21–25 March, 1987	INT	Lucey	U, B, V	1
18–21 March, 1988	INT	Bower & Ellis	U, V	2
9-12 April, 1989	INT	Bower & Lucey	U, V	3

in the calibration of the photometry must be traced by frequently re-observing three 'reference' stars in the field of the Coma cluster. These stars were in turn calibrated onto the standard California Institute of Technology (CIT) photometric system (described by FPAM) by observing standard stars selected from Elias et al. (1982). In order to check the consistency of the magnitudes derived from this procedure, a substantial number of measurements were repeated on different nights.

Accurate positions of the galaxies were obtained from a PDS scan of a Schmidt plate of the cluster (kindly supplied by Dr. Metcalfe, cf., Metcalfe, 1983). For each galaxy, we determined an offset from one of several astrometric reference stars in the cluster field. The telescope was then pointed by centering this star in the field of view of the guide television camera. Since the camera could be accurately offset from the field of view of the photometer, the galaxy should then be accurately centered in the photometer beam. In practice, the accuracy of this positioning was then checked by maximising the signal received by the photometer. On alternate nights, the telescope was chopped in E–W and N–S orientations. The appropriate direction for each galaxy was chosen so that the two positions of the sky channel of the photometer were not contaminated by brighter stars or another galaxy. A few galaxies were observed with both chop orientations in order to check for consistency.

In order that we would be able to compare the 'beamed' infrared magnitudes with optical magnitudes measured inside 'top-hat' apertures, the telescope beam profile had to be determined by scanning a star across the aperture of the photometer. This procedure was carried out on each night, in all photometric bands and in both E–W and N–S orientations.

4.2.3 Selection of galaxies

In selecting galaxies for observation, priority was given to elliptical galaxies with stellar velocity dispersions and Mg_2 indices published in D84. In order that an accurate transformation to the photometric system of PFA could be established, a substantial number of

the galaxies included in these authors' publication were re-observed. Additional early-type galaxies were selected at random from Dressler's (1980) list of galaxies with morphological types. Subsequent to these observations, Dressler (1987) published a list of velocity dispersion parameters for a number S0 galaxies in the cluster; it is unfortunate that greater overlap with this sample could not have been achieved.

4.2.4 Photometric conditions

Apart from the first and last nights of the run, sky conditions were good and the magnitudes determined for the reference stars varied smoothly throughout the night. Cloud prevented observation during the first half of the first night, but after 10.00 UT, conditions became sufficiently stable for accurate J and K photometry to be performed. The fifth night started well, but after the first few observations had been made, conditions deteriorated. It is not possible to trace the variation in the extinction with sufficient confidence during the later part of this night, so we have excluded the data obtained from further analysis. The beam profile of the telescope was also noticeably degraded on the last night. During the 5 nights, the seeing was typically 1″–2″.

4.2.5 Reduction of infrared photometry

Preliminary data reduction at the telescope supplies the observer with a first estimate of the magnitudes of the objects observed by applying standard values for the zero-point and extinction to the raw signal received from the photometer. The next step in the reduction is to calibrate the magnitudes of the reference stars onto the standard CIT system. This has been achieved by comparing the preliminary magnitudes of 'standard' stars with observations of the reference stars made shortly before and after the particular exposure. Since the standard stars have well-determined CIT magnitudes, accurately calibrated magnitudes may be inferred for the reference stars. Applying this procedure to all the standard star observations made in good conditions gives the absolute calibration of the reference stars to

better than $0.^m007$ (1σ confidence). Consequently, this is also the precision to which the galaxy photometry is zero-pointed.

The small amplitude variations in the extinction that occur throughout the night may now be allowed for by using the observations of the reference stars to provide a frequent recalibration of the extinction towards Coma cluster. In practice, it is sufficient to determine the recalibration every half-hour or so. (The frequency was increased if the photometric conditions were suspect.) The gradient of the variation is typically less than $0.^m02$ in 3 hours. Photometry obtained during the periods in the first and last nights when the recalibration became erratic was rejected from further analysis.

In order to relate photometry performed with the UKIRT beam to measurements measured through a top-hat aperture, the beam profiles measured each night were convolved with (V-band) aperture photometry of Coma galaxies of varying magnitudes. A mean correction, that converted the 'beamed' measurement into a magnitude measured through a 17″ top-hat aperture, could then be defined for each galaxy. This correction is typically $0.^m02$ with an uncertainty (arising from the different surface brightness profiles of the galaxies) of much less than $0.^m01$. Uncertainties introduced by the gradient in the V-K colour are entirely negligible. The top-hat aperture size of 17″ dia. was selected to match the FWHM (full width at half maximum) of the beam profile.

Because of the high galactic latitude of the Coma cluster, and the relatively small size of the photometer aperture, few of the magnitudes measured were affected by contaminating galactic stars. The two galaxies for which contamination is a significant problem (D121 and D159) have been deleted from our sample as accurate subtraction of the secondary component is not possible.

In Table 4.2, we present the J and K-band photometry that was obtained in good conditions. The magnitudes quoted have been corrected for the beam profile of the telescope, but not for the diffuse intra-cluster light that, in a few cases, contaminates the sky channel of the photometer (this is discussed and a correction applied in Section 4.4.1). The internal

Table 4.2

Raw J- and K-Band Photometry in the Coma Cluster

Galaxy I.D.	Date	Chop Dir.	J	K
D10	11/3/87	NS	13.52	12.62
D31	7/3/87	NS	11.54	10.58
	7/3/87	NS	11.57	
	9/3/87	NS	11.52	10.55
D49	8/3/87	EW	11.56	10.57
D67	10/3/87	EW	13.25	12.32
D69	7/3/87	NS	12.32	11.36
	9/3/87	NS	12.32	11.35
D70	8/3/87	EW	12.95	12.01
	10/3/87	EW	12.93	11.98
D78	8/3/87	EW	12.09	11.15
	9/3/87	NS	12.13	11.16
D79	10/3/87	EW	12.12	11.17
	11/3/87	NS	12.12	11.15
D81	10/3/87	EW	13.43	12.53
D84	10/3/87	EW	13.09	12.13
D87	7/3/87	NS	13.95	13.04
	8/3/87	EW	13.94	13.00
	9/3/87	NS	13.94	13.01
D91	10/3/87	EW	12.26	11.31
D95	10/3/87	EW	12.53	11.55
D96	10/3/87	EW	12.82	11.83
D97	10/3/87	EW	11.99	11.03
D107	7/3/87	NS	13.60	12.68
	9/3/87	NS	13.60	12.68
D110	10/3/87	NS	13.51	12.58
D118	8/3/87	EW	12.48	11.54
D121	8/3/87	EW	11.84:	10.84:
	10/3/87	EW	11.83:	10.81:
D124	8/3/87	EW	12.53	11.58
D125	7/3/87	NS	13.51	12.59
	8/3/87	EW	13.46	12.53
	9/3/87	NS	13.50	12.60
D126	8/3/87	EW	14.05	13.21
D127	9/3/87	NS	13.80	12.86
D128	8/3/87	EW	13.58	12.65
	11/3/87	NS	13.58	12.60
D129	8/3/87	EW	11.56	10.56
	10/3/87	EW	11.59	10.58
D130	7/3/87	NS	12.42	11.44
	9/3/87	NS	12.45	11.48
D133	7/3/87	NS	12.46	11.50
	9/3/87	NS	12.43	11.46

Table 4.2 (cont.)

Galaxy I.D.	Date	Chop Dir.	J	K
D136	7/3/87	NS	13.41	12.48
	7/3/87	NS	13.41	12.48
	8/3/87	EW	13.43	12.48
D143	7/3/87	NS	12.08	11.12
D144	8/3/87	EW	12.38	11.41
D148	8/3/87	EW	10.84	9.85
	10/3/87	EW	10.84	9.85
D150	8/3/87	EW	13.17	12.22
	10/3/87	EW	13.14	12.23
D151	7/3/87	NS	12.47	11.55
D152	9/3/87	NS	12.85	11.88
D153	8/3/87	EW	13.24	12.29
	9/3/87	NS	13.26	12.30
D154	9/3/87	NS	14.05	13.21
D159	7/3/87	NS	star superposed	
D164	10/3/87	EW	11.67	10.74
D165	11/3/87	NS	13.40	12.46
D168	8/3/87	EW	12.13	11.13
	9/3/87	NS	12.11	11.13
D170	9/3/87	NS	13.07	12.05
D172	7/3/87	NS	12.94	11.94
	9/3/87	NS	12.90	11.89
D174	7/3/87	NS	12.71	11.72
	8/3/87	EW	12.71	11.71
D175	8/3/87	EW	12.45	11.47
	9/3/87	NS	12.47	11.50
D184	10/3/87	EW	14.21	13.33
D193	8/3/87	EW	13.33	12.42
	9/3/87	NS	13.38	12.44
D194	7/3/87	NS	11.82	10.83
	9/3/87	NS	11.79	10.80
D207	7/3/87	NS	13.03	12.10
	9/3/87	NS	13.08	12.11
D217	8/3/87	EW	12.07	11.12
D225	10/3/87	NS	14.28	13.38
D240	7/3/87	NS	11.51	10.55
	8/3/87	NS	11.52	10.56
D242	10/3/87	EW	13.27	12.31
D245	10/3/87	EW	13.09	12.14
RB74	10/3/87	EW	14.09	13.28

Notes:

1. Where possible, galaxies have been identified following Dressler's (1980) list of morphological types. RB74 is identified in Rood & Baum, 1967.
2. All measurements have been corrected to a 17″ top-hat aperture. No correction has been applied for the intra-cluster light.
3. The measurements of galaxy D121 are contaminated by light from D120.

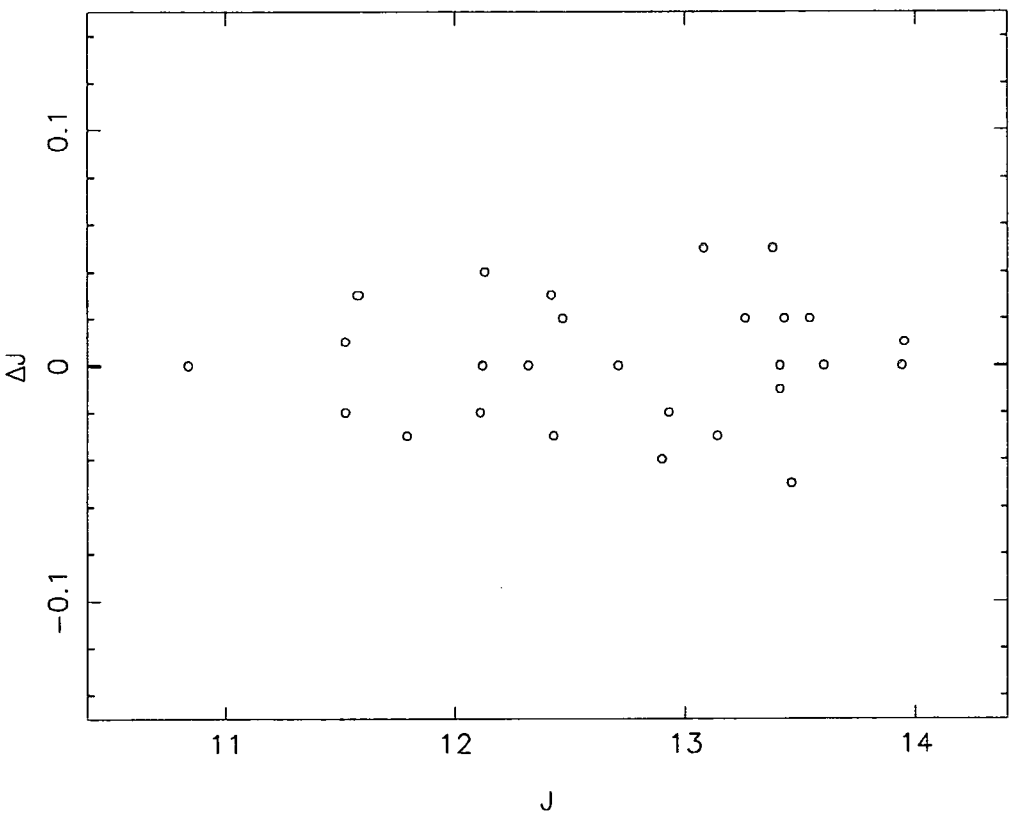

Figure 4.1. A comparison of repeated J-band photometric measurements of galaxies in the Coma cluster. The rms (root mean square) scatter of the points is $0.^m023$.

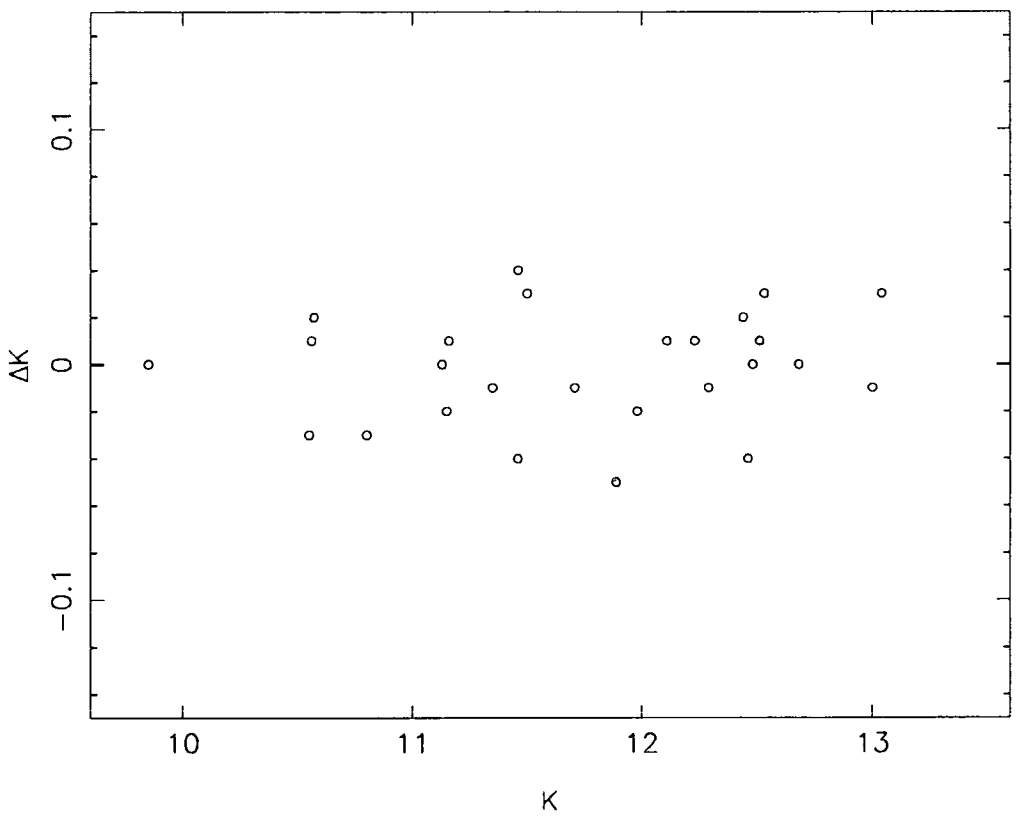

Figure 4.2. A comparison of repeated K-band measurements of galaxies in the Coma cluster. The rms scatter is $0.^m026$.

scatter in our repeated measurements (no distinction has been drawn between observations with NS and EW chopping directions) is $0.^m023$ (J-band, n=29) and $0.^m026$ (K-band, n=28). Note that two of the galaxies in this comparison will be found to require different 'chopping corrections' (to allow for intra-cluster light) in the two observations. These corrections are, however, so small that the internal scatter of the whole sample is not significantly altered when they are applied. A graphical representation of the comparison is presented in Figures 4.1 and 4.2.

4.3 Optical CCD Photometry

4.3.1 Instrumental set-up

U- and V-band observations of the Virgo and Coma clusters were made on three successive years (21–25 March 1987, 18–21 March 1988 and 9–12 April 1989) at the 2.5m Isaac Newton Telescope, La Palma (INT). A summary is given in Table 4.1. Of the total of 10 nights allocated by PATT (Panel for the Allocation of Telescope Time), 6 were of sufficient photometric quality to yield data of use in this project. The detector used was the RCA CCD (mounted at Prime Focus), this detector being chosen for its superior blue response over the *uncoated* GEC CCD that was the only available alternative during the 1987 observations. For subsequent runs, the same set-up was used in order to maintain a homogeneous photometric system. We used the set of 'La Palma' glass filters provided by observatory (details are given in the CCD User Manual — Wall, et al., 1989), the same set being used for all observations. These filters closely match those of the standard Johnson system (Johnson & Morgan, 1953). However, the effective U-band filter defined by the combined responses of the glass filter and the RCA CCD detector does not match the Johnson definition well because of the sharp fall-off in the blue response of the CCD. This effect is illustrated in Figure 4.3. The tracking of the telescope proved sufficiently accurate that autoguiding was only required during the long U-band exposures of the Coma cluster.

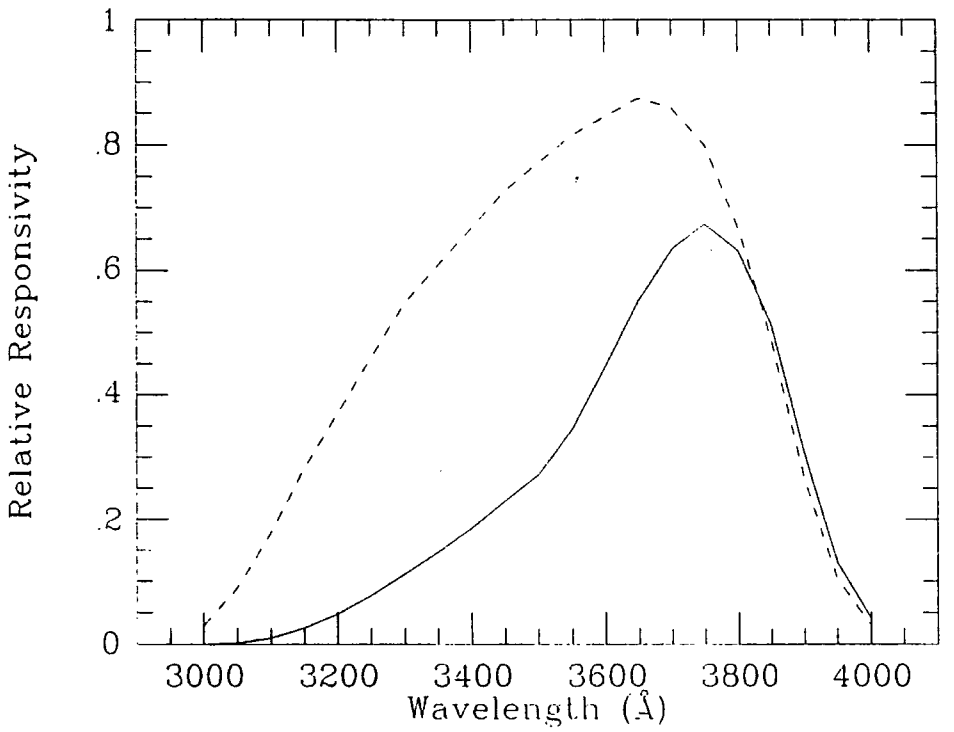

Figure 4.3. A comparison of the spectral responses of the 'La Palma' glass U-band filter (dashed line), and of the same filter convolved with the response of the RCA CCD detector (solid line). The reponsivity is given in arbitrary units.

4.3.2 Observational technique

The aim of this project requires that we are able to photometer galaxies in the Virgo and Coma clusters to a precision of better than 0.02 mag. This constraint requires that great care is taken to establish the calibration of each night, and to detect any change in the stability of photometric conditions. Below, we outline the observational procedure that was adopted.

Before sunset and after sunrise on each night, a series of bias frames (zero second exposures) were taken to ensure that there had been no change in the dc-bias of the CCD pre-amplifier; we also experimented with dark exposures, but found that the dark count was in all cases negligible. During twilight, flat-field frames were obtained for each of the filters. These were found to give a much better match to the variation seen on night-sky exposures than flat-field frames made by exposing on the telescope dome when illuminated with a tungsten lamp.

During the night, as well as immediately after dusk and before twilight, standard stars, selected from Landolt's lists (1982, 1983), were observed over a range of airmasses from 1.0 to 1.7. The telescope was driven slightly out of focus during these observations to avoid saturating the CCD. Care was taken to ensure the colours of the stars matched the range of galaxian colours, and that observations of stars at one particular airmass were not biased to one extreme of colour. In addition to our observations of standard stars, we frequently made repeated measurements of selected 'standard' galaxies in the Virgo and Coma clusters. These observations were intermingled with measurements of previously unobserved galaxies so as to monitor the consistency of photometric conditions. This precaution is especially important in the U-band as the standard stars used to transform the raw CCD magnitudes to the Johnson system have different spectral energy distributions to the galaxies.

In addition to the careful calibration described above, we attempted to frequently cycle between the two clusters and the two colour bands to ensure the homogeneity of the measurements obtained. Reduction of the data from the earlier runs showed that this was

not, however, an important requirement, and, under the pressure of equipment failure, this philosophy was not rigidly applied during the later observations.

The close proximity of the Virgo cluster ensures that good signal could be obtained for a typical galaxy in 50 sec. (V-band) and 400 sec. (U-band). The U-band exposure was extended for observations of fainter galaxies. Longer exposure times were required for the Coma cluster (150 sec. in V, 1200 sec. in U). For fainter galaxies, it would have been preferable to lengthen the U-band exposure, but the cosmic ray flux would have become unacceptable. The presence of a 7^{th} magnitude star near the centre of the Coma cluster caused some frames in this region to be contaminated by diffraction spikes and scattered light. In some cases it was possible to remove this effect by making a small shift in the position of the telescope.

4.3.3 Selection criteria

In order to optimise our observing strategy, early-type galaxies were selected for optical observation on the basis of the following criteria. In Virgo, preference was given to galaxies with published K-band photometry by PFA, and U and V observations by Michard (1982). In Coma, galaxies were required to have been observed in the K-band at UKIRT, but preference was also given to frames on which two or more galaxies could be photometered in a single exposure. Additionally, galaxies in both clusters were preferred if they were of elliptical morphology and had internal velocity dispersion and magnesium index measurements available in the literature. The aim of this selection process was to obtain a large sample of elliptical (and S0) galaxies, well spread over the range of accessible magnitudes, with a complete set of colour, 'metallicity' and dynamical parameters. To ensure the reliability of our data, we attempted, within the constraints of the photometric conditions and the available observing time, to obtain at least two observations of each galaxy.

Finally, we were concerned to determine the contamination of the sky channel of the infrared photometer by intra-cluster light during the K-band observations of the galaxies in

the core of the Coma cluster. As it was questionable whether a single CCD frame was sufficiently large to enclose the full extent of the halo, we obtained a series of overlapping V-band images of the cluster centre in order to allow us to map the intra-cluster light in this region.

4.3.4 Photometric conditions

We divide our brief outline of the photometric conditions by the years during which the observations were made.

1987. Out of 4 nights, only the second was clear and suitable for accurate photometry.

1988. Night 1 was initially clear, but clouded over before any useful data had been obtained. Night 2 appeared clear, and the zero-point stable, but some obscuration of the Coma cluster occurred as it passed through the zenith. We have used the frequently repeated measurements of standard galaxies to reject any part of this night for which the conditions are not certain to have been completely photometric. Night 3 was initially cloudy, but cleared to give good, stable photometric conditions.

1989. Night 1 was clear, but the cloud level did not fall far below the observatory. Some obscuration was detected towards the middle of the night, and data from around this time has been rejected from further analysis. Night 2 was clear, with stable extinction. Although Night 3 was clear, the extinction falls during the night. Our observations of standard galaxies allow us to chart the variation and to include the effect in the calibration.

Rejecting the measurements obtained during the uncertain conditions that we have noted above, we obtain typical residuals of 0.008 and 0.015 for the V- and U-band measurements of the standard stars. (The calibration procedure is described in the Section 4.3.5.) However, repeated measurements of our standard galaxies show that there is often a residual offset of $\pm 0.^{m}01$. Where this was judged to be statistically significant, we have incorporated an

adjustment into the calibration of each night. The measurements of our standard galaxies then have an rms scatter of $0.^m007$ ($n = 45$) in the V-band, and $0.^m012$ in the U-band.

During all three of the runs, the atmospheric seeing was very variable. At best, the FWHM of the seeing disk was 1.5″, but at times this increased to greater than 3″. We therefore include a seeing correction in our reduction of the photometry. During poor conditions, observations were confined to the Virgo cluster as the large aperture (ie., 60″ dia.) photometry that we require for this project (in this cluster) will be insensitive to seeing effects.

4.3.5 Reduction of CCD photometry

The reduction of the CCD images was carried out using the software developed by Dr. J. Lucey on the Starlink computer network. As the standard techniques are described in detail elsewhere (eg., the RGO CCD User's Guide, Wall et al., 1989), we confine ourselves to a brief outline of the procedure adopted.

After checking that there was no significant variation amongst the individual bias-frames, a master was made for each run by median filtering the bias frames at the beginning and end of each night. Similarly, a master flat-field was created for both filters on each night of each run. With one marginal exception, it proved unnecessary, in practice, to distinguish between the different nights of the same run. Each CCD image was then bias-subtracted to allow for the dc-bias current of the amplifier, and flat-fielded to allow for the variation in the detection efficiency. The imperfections that remain after this process are a dud part-column in the NW corner of the CCD, and some vignetting of one edge of the chip by the under-sized U-band filter.

The magnitudes of the stars and galaxies were determined by applying the relation

$$\text{magnitude} = \text{zero-point} - \text{extinction} * \text{airmass} - \text{colour-term} * \text{colour} - 2.5 \log \left(\frac{\text{total flux in aperture} - \text{sky flux}}{\text{exposure time}} \right)$$

where the extinction and colour terms have been determined (for each night) by minimising the residuals of the measurements of standard stars. The measured extinctions and colour-terms were typically 0.14 and 0.05*(B-V) in the V-band, and 0.45 and −0.04*(U-B) (for stars redder than 0.3) in the U-band. In the U-band, it was found impossible to fit a consistent colour term to the bluer stars, although the offset for individual stars was repeatable. As we have mentioned previously, this effect is not surprising given the non-standard nature of our effective U-band. As a result, however, there may be a small residual offset between our CCD U-band *galaxy* photometry and that measured through the standard filter. As we will not adopt any measurements from other sources, this effect is of no consequence for the present project. Over the colour range covered by the galaxies that we observed, the colour-term may be regarded as constant in both bands. Finally, we tested for a colour dependence of the extinction, but none was detected in either band (ie., the effect is less than $0.^m01$).

For galaxy exposures, the sky flux was determined from manually selected regions devoid of contaminating stars. The dispersion in these sky measurements was used to estimate the corresponding random uncertainty in the galaxy magnitude. For larger galaxies in the Virgo cluster, and galaxies on the frames that contain the two dominant galaxies of the Coma cluster, it is difficult to be certain that a true background sky flux can be measured. Fortunately, the galaxies in the Virgo cluster (for which this is a problem) are sufficiently bright that the uncertainty in the adopted sky flux has negligible effect on their magnitudes out to $90''$. This is not, however, the case for the fainter galaxies embedded in the haloes of the central D galaxies (Dressler numbers D129 and D148) in the Coma cluster. Fortunately, the mosaic of V-band images that we have obtained of the cluster core shows that a reasonable sky flux (limited by the accuracy of the flat-fielding) can be obtained from the long-axis edges of the frame. Nevertheless, it can be seen in the tables that the errors in the magnitudes measured for these galaxies on different frames tend to vary systematically with magnitude, showing that we have not always obtained a consistent sky flux. We have not attempted to correct for this small effect as it reflects a true additional uncertainty in our data.

The long U-band exposures of Coma galaxies are severely contaminated by the interaction of cosmic rays with the CCD. It is therefore necessary to 'clean' the frames using an automatic algorithm to detect and interpolate over individual pixels that are unusually high in comparison with their neighbours. Care must be taken to ensure that no stars or galaxy cores are removed in this automatic process. Residual cosmic ray events that were within photometric apertures were manually identified and removed by interpolation.

The routines to measure the magnitudes of the galaxies were first run on the frames without any attempt being made to remove contaminating stars and companion galaxies. The frames were then inspected and any contaminating objects found within the outer photometric aperture were removed by interpolation. It was found that the resulting magnitudes were altered appreciably in only a few cases.

Finally, a correction was applied to account for the light lost from inside an aperture due to atmospheric seeing. The factor by which the magnitude needed to be increased was determined (to first order) by convolving model $r^{1/4}$-law galaxies with a Gaussian point spread function (PSF). The FWHM of the seeing PSF was measured from stars in the same frame or, if this was not possible, by interpolation between adjacent frames. The correction is only very weakly dependant on the size of the model galaxy. In the Coma cluster we adopted $r_e = 5''$ for all galaxies, in the Virgo cluster $r_e = 30''$. For most measurements, the correction was less than $0.^m02$. There is, however, some evidence (cf., Figure 4.4) that our corrections in the Virgo cluster under-estimate the effect when the seeing becomes poor (ie., worse than $2.5''$ FWHM), this suggests that the Gaussian profile is then a poor approximation to the true seeing PSF. We therefore make the conservative choice to caution any measurements which have been corrected by more than $0.^m05$, or for which the seeing FWHM is greater than $3.5''$. Otherwise, the size of the correction is so small that its uncertainty is negligible in comparison with the other sources of random error.

Tables 4.3–4.6 present the individual measurements of the U- and V-band magnitudes of galaxies in the Virgo and Coma clusters. We have chosen to present a range of standard

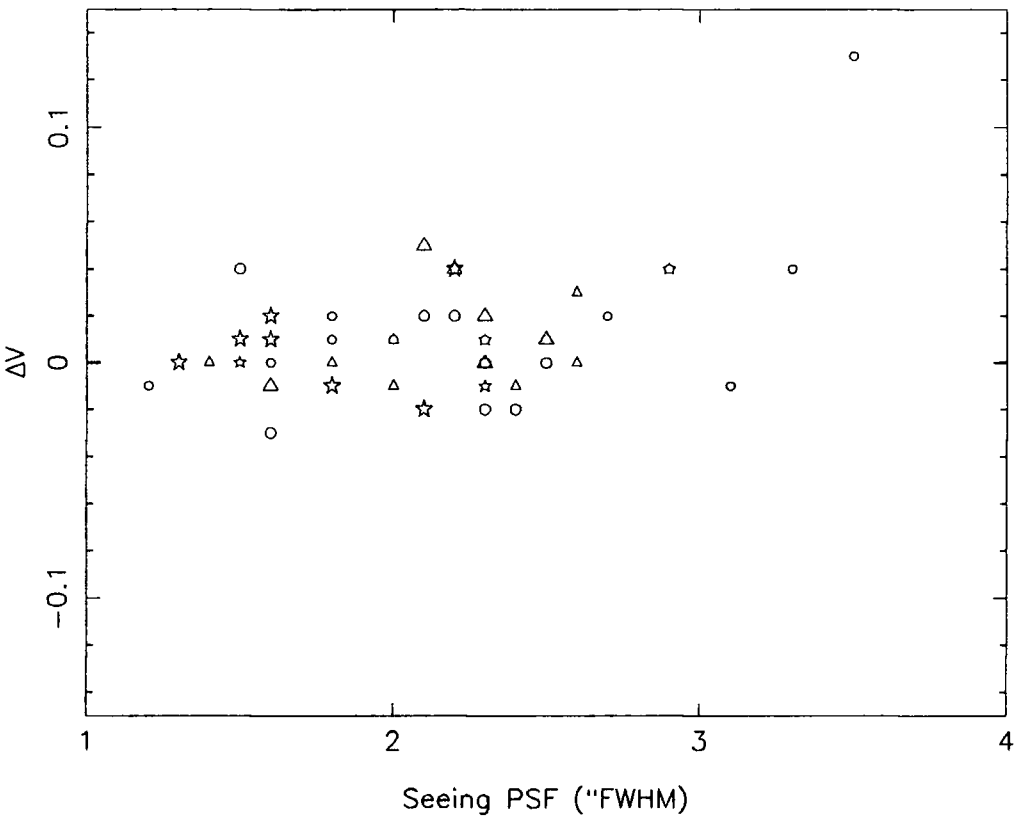

Figure 4.4. The evidence for a residual seeing correction. ΔV is the difference of the V-band magnitude (at 10″) measured in the seeing plotted on the ordinate, from the average magnitude measured in good seeing (ie., better than 2″). The seeing corrections described in the text have already been applied, so no correlation should be evident. Selected galaxies in the Coma cluster are shown as filled symbols (circle: D126, triangle: D129, star:D217); galaxies in the Virgo cluster are represented as open symbols (circle: N4552, triangle: N4486, star: N4660). There is some evidence that our seeing correction becomes inadequate (*in this small aperture*) beyond 2.5″.

Table 4.3 — Raw V-band Photometry in the Virgo Cluster

Galaxy	Frame	Seeing	Date	Aperture Dia. (″)										
				10.0	13.0	16.0	20.0	25.0	32.0	40.0	50.0	60.0	63.0	79.0
N4124	389P	2.4″	12/04/89	14.37	14.00	13.73	13.45	13.18	12.92	12.69	12.46	12.28	12.23	12.04
N4339	142P	2.0″	10/04/89	13.61	13.35	13.13	12.91	12.72	12.54	12.38	12.23	12.11	12.07	11.93
N4339	404P	1.4″	12/04/89	13.59	13.32	13.13	12.92	12.73	12.54	12.38	12.23	12.11	12.07	11.93
N4365	128P	2.4″	10/04/89	12.65	12.31	12.09	11.85	11.62	11.40	11.20	11.01	10.88	10.84	10.68
N4371	135P	2.0″	10/04/89	13.21	12.89	12.65	12.40	12.18	11.97	11.79	11.62	11.49	11.46	11.30
N4371	401P	1.4″	12/04/89	13.20	12.88	12.65	12.41	12.19	11.98	11.80	11.63	11.50	11.47	11.32
N4374	134P	1.9″	23/03/87	12.16	11.85	11.60	11.35	11.15	10.93	10.74	10.56	10.42	10.39	10.23
N4377	133P	2.5″	10/04/89	13.13	12.93	12.79	12.65	12.51	12.35	12.22	12.09	12.00	11.99	11.92
N4377	409P	2.1″	12/04/89	13.11	12.92	12.79	12.64	12.52	12.36	12.21	12.08	11.99	11.97	11.90
N4382	134P	1.8″	10/04/89	12.14	11.86	11.65	11.43	11.24	11.02	10.83	10.64	10.49		
N4382	136P	4.0″	10/04/89	12.34:	12.00:	11.76:	11.51:	11.28:	11.05:	10.85:	10.67:	10.51:	10.47:	10.28:
N4382	178P	2.8″	10/04/89	12.19	11.90	11.67	11.45	11.24	11.02	10.84	10.65	10.50	10.45	10.27
N4387	107P	1.8″	23/03/87	13.73	13.45	13.24	13.06	12.89	12.72	12.60	12.49	12.42	12.41	12.34
N4387	146P	2.2″	10/04/89	13.78	13.47	13.26	13.06	12.89	12.72	12.60	12.50	12.43	12.41	12.36
N4406	132P	2.1″	10/04/89	12.51	12.20	11.96	11.71	11.48	11.24	11.03	10.83	10.66	10.62	10.43
N4435	138P	3.5″	10/04/89	12.78:	12.47	12.26	12.04	11.86	11.68	11.52	11.39	11.28	11.25	11.14
N4435	411P	2.0″	12/04/89	12.70	12.42	12.21	12.02	11.85	11.69	11.54	11.41	11.31	11.28	11.18
N4442	140P	2.2″	10/04/89	12.47	12.17	11.96	11.75	11.56	11.38	11.22	11.08	10.99	10.96	10.87
N4442	413P	1.4″	12/04/89	12.45	12.16	11.96	11.76	11.57	11.38	11.23	11.09	10.99	10.97	10.88
N4458	179P	2.5″	20/04/88	13.95	13.72	13.53	13.33	13.16	12.97	12.80	12.65	12.54	12.51	12.38
N4458	126P	3.5″:	10/04/89	14.13:	13.82:	13.61:	13.38:	13.19:	12.99:	12.82:	12.68:	12.58:	12.55:	12.45:
N4458	145P	2.0″	10/04/89	13.94	13.71	13.52	13.32	13.14	12.96	12.80	12.66	12.55	12.53	12.42
N4464	124P	2.8″	10/04/89	13.62	13.41	13.26	13.11	12.99	12.88	12.81	12.75	12.71	12.70	12.67
N4464	392P	2.0″	12/04/89	13.57	13.38	13.24	13.10	12.98	12.89	12.81	12.75	12.71	12.70	12.67
N4468	414P	1.4″	12/04/89	14.93	14.66	14.45	14.23	13.02	13.81	13.63	13.48	13.38	13.35	13.25
N4472	119P	2.3″	23/03/87	12.11	11.75	11.47	11.18	10.94	10.67	10.44	10.22	10.06	10.02	9.83
N4473	104P	1.7″	23/03/87	12.30	12.03	11.84	11.64	11.48	11.31	11.17	11.05	10.94	10.92	10.80

Table 4.3 (cont.) — Raw V-band Photometry in the Virgo Cluster

Galaxy	Frame	Seeing	Date	Aperture Dia. (″)										
				10.0	13.0	16.0	20.0	25.0	32.0	40.0	50.0	60.0	63.0	79.0
N4476	139P	2.1″	10/04/89	13.90	13.63	13.43	13.26	13.10	12.95	12.82	12.71	12.63	12.61	12.52
N4476	416P	2.1″	12/04/89	13.92	13.65	13.45	13.27	13.11	12.96	12.84	12.73	12.65	12.63	12.55
N4478	148P	1.8″	20/04/88	13.15	12.85	12.61	12.38	12.18	11.99	11.84	11.73	11.65	11.64	11.56
N4486	101P	1.8″	23/03/87	12.68	12.26	11.90	11.56	11.27	10.95	10.69	10.47	10.29	10.25	10.06
N4486	116P	2.0″	23/03/87	12.69	12.26	11.91	11.56	11.27	10.95	10.69	10.46	10.29	10.25	10.05
N4486	128P	2.4″	23/03/87	12.67	12.25	11.90	11.55	11.26	10.95	10.69	10.46	10.28	10.24	10.05
N4486	122P	2.6″	10/04/89	12.71	12.27	11.93	11.58	11.26	10.94	10.70	10.46	10.29	10.24	10.05
N4486	144P	2.6″	10/04/89	12.68	12.27	11.94	11.58	11.26	10.94	10.69	10.46	10.28	10.24	10.04
N4486	297P	1.4″	11/04/89	12.68	12.23	11.90	11.57	11.26	10.94	10.69	10.45	10.28	10.24	10.04
N4486	309P	2.0″	11/04/89	12.67	12.23	11.90	11.56	11.26	10.94	10.68	10.45	10.28	10.23	10.04
N4486	316P	2.0″	11/04/89	12.69	12.24	11.91	11.56	11.26	10.94	10.69	10.46	10.28	10.24	10.05
N4550	127P	2.5″	10/04/89	13.46	13.14	12.91	12.68	12.47	12.27	12.14	12.02	11.94	11.92	11.84
N4550	394P	1.6″	12/04/89	13.46	13.14	12.89	12.68	12.48	12.29	12.15	12.03	11.96	11.94	11.87
N4551	395P	2.1″	12/04/89	13.79	13.49	13.26	13.05	12.85	12.66	12.51	12.38	12.29	12.27	12.19
N4552	131P	1.2″	23/03/87	12.19	11.93	11.71	11.50	11.33	11.15	10.99	10.85	10.73	10.70	10.57
N4552	146P	1.8″	20/04/88	12.22	11.95	11.73	11.52	11.35	11.17	11.01	10.86	10.75	10.72	10.58
N4552	157P	1.8″	20/04/88	12.21	11.95	11.72	11.52	11.35	11.16	11.00	10.86	10.74	10.71	10.58
N4552	170P	2.5″	20/04/88	12.21	11.94	11.72	10.51	10.30	11.14	11.00	10.85	10.74	10.70	10.57
N4552	178P	2.5″	20/04/88	12.21	11.94	11.73	11.52	11.34	11.15	11.01	10.86	10.75	10.72	10.58
N4552	184P	3.1″	20/04/88	12.19:	11.92	11.71	11.50	11.33	11.14	11.00	10.85	10.73	10.70	10.57
N4552	121P	3.5″	10/04/89	12.34:	12.02	11.79	11.57	11.36	11.16	11.00	10.86	10.75	10.72	10.59
N4552	131P	2.9″	10/04/89	12.25	11.95	11.73	11.52	11.34	11.15	11.00	10.86	10.74	10.71	10.58
N4552	143P	2.1″	10/04/89	12.22	11.94	11.72	11.51	11.34	11.15	11.00	10.85	10.73	10.70	10.57
N4552	180P	2.3″	10/04/89	12.21	11.92	11.71	11.51	11.32	11.15	11.00	10.85	10.74	10.71	10.58
N4552	375P	2.0″	12/04/89	12.21	11.94	11.72	11.51	11.34	11.16	11.00	10.86	10.74	10.71	10.58
N4552	387P	3.3″	12/04/89	12.25:	11.95	11.74	11.52	11.34	11.15	10.99	10.86	10.74	10.71	10.58
N4552	407P	1.6″	12/04/89	12.20	11.92	11.72	11.52	11.34	11.16	11.01	10.86	10.75	10.72	10.59
N4552	432P	2.7″	12/04/89	12.22	11.94	11.73	11.52	11.33	11.15	11.01	10.86	10.75	10.72	10.59

Table 4.3 (cont.) — Raw V-band Photometry in the Virgo Cluster

Galaxy	Frame	Seeing	Date	Aperture Dia. (″)										
				10.0	13.0	16.0	20.0	25.0	32.0	40.0	50.0	60.0	63.0	79.0
N4564	130P	3.0″:	10/04/89	12.98:	12.69	12.49	12.30	12.12	11.94	11.80	11.67	11.57	11.55	11.44
N4564	396P	2.4″	12/04/89	12.85	12.61	12.44	12.26	12.10	11.94	11.80	11.67	11.57	11.54	11.44
N4621	129P	4.8″	10/04/89	12.66:	12.29:	12.03:	11.76:	11.53:	11.29:	11.10:	10.93:	10.79:	10.76:	10.61:
N4621	397P	2.0″	12/04/89	12.31	12.06	11.85	11.65	11.45	11.26	11.08	10.91	10.78	10.75	10.60
N4636	141P	2.2″	10/04/89	12.98	12.59	12.31	12.03	11.78	11.53	11.31	11.10	10.93	10.89	10.70
N4636	179P	4.0″	10/04/89	13.08:	12.67:	12.38:	12.08:	11.81:	11.54:	11.31:	11.10:	10.94:	10.89:	10.70:
N4660	123P	2.9″	10/04/89	12.61	12.39	12.22	12.06	11.91	11.76	11.66	11.57	11.50	11.48	11.42
N4660	177P	2.3″	10/04/89	12.58	12.36	12.20	12.04	11.90	11.77	11.66	11.56	11.50	11.48	11.41
N4660	399P	1.5″	12/04/89	12.57	12.35	12.21	12.05	11.91	11.77	11.66	11.57	11.51	11.49	11.42
N4660	426P	2.3″	12/04/89	12.56	12.35	12.20	12.05	11.90	11.78	11.67	11.58	11.51	11.50	11.43
N4697	424P	2.9″	12/04/89	12.41	12.08	11.83	11.59	11.35	11.10	10.90	10.70	10.55	10.50	10.32

Notes:

1. Galaxies are identified by NGC number (Dreyer, 1888).
2. Measurements have been corrected for seeing effects. Bright stars have been removed by interpolation.

Table 4.4 — Raw U-band Photometry in the Virgo Cluster

Galaxy	Frame	Seeing	Date	Aperture Dia. (″)										
				10.0	13.0	16.0	20.0	25.0	32.0	40.0	50.0	60.0	63.0	79.0
N4124	390P	2.8″	12/04/89	15.53	15.15	14.88	14.60	14.31	14.03	13.78	13.53	13.34	13.29	13.07
N4339	406P	1.8″	12/04/89	15.07	14.79	14.58	14.36	14.17	13.97	13.80	13.64	13.48	13.45	13.29
N4365	197P	2.7″:	10/04/89	14.28	13.95	13.70	13.45	13.22	12.97	12.77	12.57	12.42	12.38	12.22
N4365	391P	2.5″:	12/04/89	14.27	13.92	13.69	13.44	13.20	12.95	12.75	12.55	12.40	12.36	12.19
N4371	205P	3.0″:	10/04/89	14.74:	14.41	14.17	13.92	13.71	13.48	13.31	13.14	13.02	12.98	12.83
N4371	402P	1.9″	12/04/89	14.76	14.42	14.17	13.92	13.71	13.48	13.29	13.12	12.99	12.95	12.80
N4374	136P	2.0″	23/03/87	13.87	13.53	13.25	12.99	12.77	12.53	12.33	12.14	11.99	11.95	11.77
N4374	283P	1.8″	21/04/88	13.86	13.51	13.25	12.98	12.76	12.52	12.31	12.13	11.98	11.94	11.77
N4377	206P	3.3″	10/04/89	14.57:	14.37	14.21	14.06	13.91	13.73	13.57	13.42	13.32	13.30	13.21
N4377	410P	2.1″	12/04/89	14.57	14.36	14.21	14.05	13.89	13.73	13.57	13.43	13.34	13.31	
N4382	207P	3.5″	10/04/89	13.48:	13.18	12.98	12.77	12.57	12.37	12.18	12.01	11.87	11.83	11.65
N4382	412P	2.0″	12/04/89	13.47	13.19	12.98	12.77	12.57	12.37	12.19	12.02	11.87	11.83	11.65
N4387	109P	2.3″	23/03/87	15.27	14.97	14.74	14.52	14.34	14.16	14.02	13.88	13.81	13.79	13.70
N4387	203P	2.4″	10/04/89	15.25	14.93	14.72	14.50	14.32	14.14	14.01	13.90	13.83		
N4387	274P	2.1″	11/04/89	15.25	14.94	14.71	14.50	14.32	14.15	14.01	13.90	13.82:		
N4406	209P	3.0″:	10/04/89	14.10	13.79	13.55	13.28	13.05	12.79	12.57	12.35	12.19	12.14	11.91
N4406	272P	1.6″:	11/04/89	14.15	13.82	13.57	13.32	13.08	12.83	12.60	12.39	12.22	12.18	11.97
N4435	292P	1.9″:	11/04/89	14.19	13.91	13.71	13.51	13.33	13.14	12.97	12.82	12.70:		
N4442	293P	1.9″	11/04/89	14.08	13.78	13.55	13.33	13.13	12.92	12.75	12.59	12.48	12.45	12.34
N4458	198P	2.6″	10/04/89	15.31	15.06	14.87	14.66	14.48	14.28	14.13	13.98	13.88	13.86	
N4464	199P	2.0″	10/04/89	15.01	14.81	14.66	14.51	14.39	14.26	14.17	14.09	14.03	14.01	
N4464	393P	2.2″	12/04/89	15.02	14.81	14.65	14.50	14.38	14.26	14.16	14.09	14.01	14.00	13.96
N4468	294P	1.9″:	11/04/89	16.28	15.97	15.72	15.46	15.26	15.01	14.78	14.60:			
N4468	415P	3.0″:	12/04/89	16.22:	15.93	15.69	15.44	15.23	15.00	14.81	14.65	14.53:		
N4472	121P	2.3″	23/03/87	13.82	13.45	13.15	12.85	12.60	12.32	12.08	11.85	11.68	11.64	11.44
N4473	106P	3.1″	23/03/87	13.89:	13.62	13.40	13.19	13.03	12.84	12.69	12.55	12.44	12.41	12.28
N4476	417P	3.0″:	12/04/89	15.03:	14.76	14.57	14.38	14.21	14.03	13.91	13.77	13.67	13.65	

Table 4.4 (cont.) — Raw U-band Photometry in the Virgo Cluster

Galaxy	Frame	Seeing	Date	Aperture Dia. (″)										
				10.0	13.0	16.0	20.0	25.0	32.0	40.0	50.0	60.0	63.0	79.0
N4486	103P	2.0″	23/03/87	14.26	13.87	13.54	13.20	12.90	12.56	12.30	12.07	11.89	11.85	11.65
N4486	118P	2.2″	23/03/87	14.25	13.86	13.53	13.19	12.89	12.55	12.28	12.05	11.87	11.83	11.62
N4486	130P	2.5″	23/03/87	14.23	13.85	13.52	13.18	12.88	12.53	12.27	12.04	11.87	11.82	11.61
N4486	200P	1.9″	10/04/89	14.22	13.83	13.52	13.18	12.85	12.52	12.26	12.03	11.85	11.81	11.61
N4486	208P	3.1″	10/04/89	14.20:	13.81	13.51	13.17	12.84	12.51	12.26	12.03	11.85	11.81	11.61
N4486	273P	1.7″	11/04/89	14.25	13.84	13.53	13.19	12.86	12.53	12.27	12.04	11.87	11.82	11.62
N4486	296P	1.8″	11/04/89	14.24	13.84	13.52	13.19	12.87	12.53	12.27	12.04	11.87	11.82	11.62
N4486	308P	2.3″	11/04/89	14.26	13.86	13.54	13.20	12.88	12.55	12.28	12.05	11.87	11.82	11.61
N4486	315P	3.0″	11/04/89	14.19	13.81	13.50	13.17	12.84	12.51	12.26	12.02	11.85	11.80	11.60
N4550	290P	1.8″:	11/04/89	14.88	14.56	14.29	14.05	13.84	13.62	13.45	13.32	13.24	13.21	13.12
N4551	291P	1.9″	11/04/89	15.29	14.99	14.76	14.53	14.33	14.14	13.98	13.85:			
N4552	133P	2.0″	23/03/87	13.90	13.62	13.39	13.17	12.98	12.79	12.61	12.45	12.32	12.29	12.13
N4552	147P	2.4″	20/04/88	13.89	13.60	13.38	13.17	12.97	12.79	12.62	12.47	12.34	12.31	12.18
N4552	156P	2.3″	20/04/88	13.87	13.58	13.37	13.16	12.95	12.77	12.60	12.44	12.32	12.28	12.14
N4552	282P	1.8″	21/04/88	13.88	13.60	13.37	13.16	12.97	12.77	12.61	12.45	12.33	12.29	12.15
N4552	196P	2.7″	10/04/89	13.88	13.60	13.39	13.17	12.96	12.76	12.60	12.44	12.32	12.28	12.13
N4552	204P	2.5″	10/04/89	13.87	13.57	13.37	13.16	12.95	12.76	12.60	12.44	12.31	12.28	12.13
N4552	271P	1.6″	11/04/89	13.89	13.59	13.38	13.17	12.97	12.77	12.61	12.45	12.32	12.29	12.14
N4552	289P	1.8″	11/04/89	13.88	13.60	13.38	13.18	12.98	12.79	12.62	12.46	12.34	12.30	12.16
N4552	374P	2.5″	12/04/89	13.92	13.61	13.39	13.17	12.96	12.77	12.61	12.45	12.32	12.29	12.14
N4552	388P	2.5″	12/04/89	13.88	13.59	13.38	13.16	12.96	12.77	12.60	12.44	12.32	12.28	12.14
N4552	408P	2.0″	12/04/89	13.88	13.58	13.37	13.16	12.97	12.77	12.60	12.45	12.32	12.29	12.15
N4552	431P	3.3″	12/04/89	13.92:	13.63	13.40	13.18	12.98	12.77	12.60	12.45	12.32	12.29	12.14
N4621	201P	2.2″	10/04/89	14.01	13.72	13.50	13.27	13.06	12.84	12.65	12.46	12.31	12.28	12.12
N4636	295P	1.8″	11/04/89	14.59	14.20	13.93	13.64	13.37	13.10	12.87	12.65	12.47	12.43	
N4636	398P	2.0″	12/04/89	14.56	14.18	13.90	13.62	13.35	13.08	12.85	12.63	12.44	12.39	12.19
N4660	202P	2.3″:	10/04/89	14.16	13.91	13.73	13.55	13.39	13.23	13.09	12.97	12.89	12.87	
N4660	400P	2.0″:	12/04/89	14.14	13.91	13.72	13.54	13.39	13.23	13.10	12.98	12.90	12.88	12.78
N4697	425P	3.3″	12/04/89	14.01:	13.66	13.39	13.10	12.85	12.58	12.35	12.14	11.97	11.93	11.73

Table 4.5 — Raw V-band Photometry in the Coma Cluster

Galaxy	Frame	Seeing	Date	Aperture Dia.								
				6.0″	8.0″	10.0″	13.0″	16.0″	17.0″	20.0″	25.0″	32.0″
D10	330P	1.6”	11/04/89	17.27	17.03	16.87	16.68	16.58	16.54	16.46	16.37	16.31
D31	329P	1.8”:	11/04/89	15.03	14.71	14.47	14.19	14.01	13.96	13.82	13.63	13.44
D49	328P	1.7”:	11/04/89	14.76	14.52	14.33	14.13	14.00	13.96	13.86	13.72	13.58
D64	212P	1.5”	20/04/88	16.92	16.69	16.52	16.35	16.21	16.18	16.08	15.95	15.82
D67	161P	2.5”	10/04/89	16.18:	15.96	15.82	15.68	15.60	15.57	15.52	15.48	15.44
D68	302P	1.4”	11/04/89	16.00	15.77	15.59	15.41	15.30	15.27	15.18	15.06	14.95
D69	302P	1.4”	11/04/89	15.40	15.17	15.02	14.86	14.76	14.73	14.65	14.56	14.47
D70	302P	1.4”	11/04/89	15.75	15.59	15.46	15.32	15.24	15.21	15.15	15.06	14.98
D71	185P	2.7”	20/04/88	17.04:	16.74:	16.59	16.40	16.26	16.23	16.12	16.02	15.88
D71	302P	1.4”	11/04/89	16.99	16.76	16.58	16.42	16.30	16.27	16.19	16.11	16.02
D72	185P	2.7”	20/04/88	15.75:	15.49:	15.37	15.23	15.13	15.11	15.04	14.99	14.92
D78	327P	1.7”	11/04/89	15.13	14.91	14.74	14.57	14.46	14.42	14.33	14.21	14.10
D79	153P	1.6”	20/04/88	15.25	14.98	14.84	14.66	14.53	14.50	14.41	14.32	14.23
D79	326P	1.8”	11/04/89	15.17	14.95	14.80	14.62	14.49	14.47	14.39	14.30	14.22
D81	326P	1.8”	11/04/89	16.23	16.03	15.90	15.73	15.61	15.59	15.51	15.40	15.28
D84	212P	1.5”	20/04/88	16.09	15.84	15.70	15.56	15.44	15.40	15.32	15.22	15.13
D85	212P	1.5”	20/04/88	17.17	16.98	16.85	16.74	16.69	16.68	16.65	16.63	16.62
D87	152P	1.6”	20/04/88	16.63	16.40	16.30	16.17	16.10	16.08	16.03	15.97	15.92
D87	325P	2.3”	11/04/89	16.55:	16.39	16.27	16.15	16.07	16.05	16.01	15.97	15.93
D87	438P	2.8”	12/04/89	16.61:	16.43:	16.30	16.17	16.09	16.07	16.02	15.99	15.95
D91	185P	2.7”	20/04/88	15.25:	15.00:	14.88	14.73	14.63	14.60	14.53	14.45	14.37
D95	177P	3.0”	20/04/88	15.33:	15.16:	15.05	14.93	14.83	14.81	14.74	14.66	14.60
D96	211P	1.5”	20/04/88	15.70	15.55	15.41	15.28	15.19	15.16	15.08	14.98	14.87
D96	324P	1.9”:	11/04/89	15.68:	15.53	15.41	15.28	15.18	15.15	15.09	15.00	14.92
D103	137P	1.8”	23/03/87	15.20	15.05	14.93	14.81	14.72	14.71	14.64	14.56	14.46
D103	213P	1.5”	20/04/88	15.24	15.07	14.95	14.84	14.75	14.72	14.66	14.56	14.45
D103	323P	1.9”	11/04/89	15.28	15.10	14.96	14.83	14.74	14.72	14.66	14.58	14.48
D104	125P	2.3”	23/03/87	15.63:	15.45	15.33	15.20	15.10	15.08	15.03	14.96	14.89
D104	213P	1.5”	20/04/88	15.65	15.45	15.32	15.18	15.09	15.07	15.00	14.91	14.82
D104	221P	1.6”	20/04/88	15.64	15.46	15.34	15.21	15.13	15.11	15.05	14.99	14.94
D104	322P	2.3”	11/04/89	15.69:	15.48	15.35	15.20	15.10	15.08	15.03	14.95	14.89

Table 4.5 (cont.) — Raw V-band Photometry in the Coma Cluster

Galaxy	Frame	Seeing	Date	Aperture Dia.								
				6.0″	8.0″	10.0″	13.0″	16.0″	17.0″	20.0″	25.0″	32.0″
D105	213P	1.5″	20/04/88	15.26	15.01	14.79	14.60	14.47	14.43	14.33	14.21	13.99
D105	323P	1.9″	11/04/89	15.28	15.03	14.80	14.60	14.47	14.43	14.35	14.24	14.12
D106	213P	1.5″	20/04/88	16.11	15.93	15.82	15.70	15.63	15.61	15.55	15.48	15.37
D106	323P	1.9″	11/04/89	16.14	15.98	15.83	15.72	15.65	15.64	15.61	15.56	15.50
D107	137P	1.8″	23/03/87	16.47	16.22	16.04	15.85	15.73	15.71	15.63	15.54	15.46
D107	213P	1.5″	20/04/88	16.50	16.24	16.05	15.86	15.74	15.71	15.62	15.52	15.42
D107	323P	1.9″	11/04/89	16.48	16.25	16.05	15.89	15.77	15.73	15.67	15.59	15.54
D110	205P	1.6″	20/04/88	15.79	15.54	15.41	15.24	15.11	15.07	14.98	14.89	14.78
D110A	205P	1.6″	20/04/88	16.48	16.22	16.08	15.92	15.80	15.77	15.68	15.59	15.48
D116	162P	2.7″	10/04/89	16.30:	16.03:	15.86	15.65	15.51	15.47	15.36	15.25	15.13
D116	435P	2.2″	12/04/89	16.19:	15.98	15.80	15.61	15.48	15.45	15.37	15.26	15.16
D117	304P	1.3″	11/04/89	16.47	16.24	16.07	15.91	15.81	15.78	15.71	15.65	15.59
D118	304P	1.3″	11/04/89	15.59	15.34	15.17	14.98	14.85	14.81	14.72	14.61	14.52
D119	435P	2.2″	12/04/89	16.18:	16.00	15.87	15.73	15.63	15.60	15.55	15.50	15.48
D122	110P	1.9″	23/03/87	16.05	15.88	15.70	15.55	15.43	15.40	15.32	15.22	15.13
D122	217P	1.4″	20/04/88	16.04	15.86	15.69	15.53	15.41	15.37	15.28	15.16	15.02
D122	307P	1.9″	11/04/89	16.01	15.84	15.71	15.55	15.43	15.39	15.32	15.22	15.11
D122	332P	2.1″	11/04/89	16.07:	15.87	15.73	15.58	15.46	15.43	15.36	15.26	15.16
D123	221P	1.6″	20/04/88	16.74	16.45	16.25	16.02	15.85	15.81	15.71	15.60	15.49
D123	322P	2.3″	11/04/89	16.78:	16.51	16.27	16.03	15.86	15.82	15.73	15.62	15.53
D124	125P	2.3″	23/03/87	15.49:	15.29	15.13	14.98	14.86	14.83	14.77	14.69	14.64
D124	221P	1.6″	20/04/88	15.54	15.31	15.15	14.97	14.87	14.84	14.77	14.69	14.63
D124	322P	2.3″	11/04/89	15.60:	15.35	15.16	14.98	14.87	14.83	14.77	14.69	14.62
D125	125P	2.3″	23/03/87	16.01:	15.86	15.80	15.73	15.68	15.66	15.64	15.61	15.57
D125	221P	1.6″	20/04/88	15.99	15.87	15.79	15.71	15.66	15.65	15.61	15.56	15.49
D125	322P	2.3″	11/04/89	16.03:	15.90	15.81	15.72	15.66	15.64	15.61	15.56	15.49
D126	113P	2.4″	23/03/87	16.58:	16.35	16.19	16.02	15.90	15.87	15.80	15.70	15.58
D126	222P	1.5″	20/04/88	16.83	16.50	16.25	16.06	15.93	15.90	15.82	15.69	15.55
D126	159P	2.1″	10/04/89	16.70:	16.41	16.23	16.04	15.92	15.89	15.82	15.72	15.62
D126	165P	2.2″	10/04/89	16.71:	16.41	16.23	16.05	15.92	15.89	15.83	15.73	15.62
D126	301P	1.6″	11/04/89	16.58	16.34	16.18	16.02	15.93	15.90	15.83	15.74	15.64

Table 4.5 (cont.) — Raw V-band Photometry in the Coma Cluster

Galaxy	Frame	Seeing	Date	Aperture Dia.								
				6.0″	8.0″	10.0″	13.0″	16.0″	17.0″	20.0″	25.0″	32.0″
D126	321P	2.3″	11/04/89	16.60:	16.38	16.19	16.02	15.91	15.88	15.81	15.72	15.61
D126	331P	2.3″	11/04/89	16.63:	16.37	16.21	16.03	15.92	15.89	15.82	15.73	15.62
D126	440P	2.5″	12/04/89	16.63:	16.37	16.21	16.03	15.92	15.88	15.81	15.72	15.61
D127	113P	2.4″	23/03/87	16.74:	16.56	16.38	16.22	16.08	16.03	15.91	15.74	15.49
D127	222P	1.5″	20/04/88	16.78	16.55	16.40	16.23	16.08	16.03	15.91	15.72	15.47
D127	159P	2.1″	10/04/89	16.88:	16.62	16.45	16.26	16.11	16.07	15.96	15.78	15.56
D127	165P	2.2″	10/04/89	16.86:	16.61	16.45	16.25	16.10	16.06	15.95	15.78	15.54
D127	301P	1.6″	11/04/89	16.76	16.54	16.40	16.23	16.11	16.06	15.96	15.79	15.56
D127	321P	2.3″	11/04/89	16.80:	16.59	16.41	16.23	16.10	16.05	15.95	15.77	15.53
D127	331P	2.3″	11/04/89	16.79:	16.58	16.42	16.24	16.10	16.06	15.95	15.78	15.55
D127	440P	2.5″	12/04/89	16.78:	16.59	16.41	16.23	16.09	16.05	15.93	15.76	15.52
D128	113P	2.4″	23/03/87	16.42:	16.22	16.06	15.91	15.77	15.73	15.64	15.46	15.23
D128	159P	2.1″	10/04/89	16.55:	16.29	16.13	15.95	15.81	15.77	15.68	15.51	15.29
D128	165P	2.2″	10/04/89	16.52:	16.31	16.12	15.94	15.81	15.77	15.67	15.51	15.28
D128	301P	1.6″	11/04/89	16.42	16.22	16.10	15.93	15.82	15.78	15.68	15.52	15.30
D128	321P	2.3″	11/04/89	16.44:	16.26	16.11	15.94	15.81	15.77	15.67	15.51	15.28
D128	331P	2.3″	11/04/89	16.45:	16.26	16.11	15.94	15.81	15.77	15.68	15.51	15.29
D128	440P	2.5″	12/04/89	16.44:	16.25	16.10	15.93	15.81	15.77	15.66	15.50	15.28
D129	113P	2.4″	23/03/87	15.28:	14.90	14.55	14.24	13.99	13.94	13.77	13.56	13.34
D129	159P	2.1″	10/04/89	15.39:	14.93	14.62	14.27	14.03	13.95	13.79	13.57	13.35
D129	165P	2.2″	10/04/89	15.36:	14.93	14.61	14.27	14.02	13.95	13.79	13.57	13.35
D129	301P	1.6″	11/04/89	15.26	14.86	14.56	14.23	14.01	13.94	13.78	13.57	13.34
D129	321P	2.3″	11/04/89	15.31:	14.89	14.57	14.25	14.00	13.94	13.78	13.57	13.34
D129	331P	2.3″	11/04/89	15.31:	14.87	14.59	14.25	14.01	13.94	13.78	13.57	13.34
D129	440P	2.5″	12/04/89	15.33:	14.87	14.58	14.26	14.01	13.95	13.77	13.57	13.34
D130	113P	2.4″	23/03/87	15.34:	15.16	15.02	14.88	14.77	14.73	14.65	14.53	14.37
D130	221P	1.6″	20/04/88	15.38	15.17	15.02	14.87	14.78	14.74	14.65	14.52	14.35
D130	159P	2.1″	10/04/89	15.48:	15.24	15.05	14.89	14.77	14.74	14.66	14.53	14.37
D130	301P	1.6″	11/04/89	15.34	15.15	15.01	14.86	14.77	14.74	14.66	14.53	14.37
D130	321P	2.3″	11/04/89	15.37:	15.17	15.03	14.88	14.77	14.73	14.66	14.53	14.37
D130	331P	2.3″	11/04/89	15.39:	15.19	15.03	14.88	14.76	14.74	14.66	14.53	14.37
D130	440P	2.5″	12/04/89	15.36:	15.17	15.02	14.87	14.77	14.74	14.65	14.53	14.37

Table 4.5 (cont.) — Raw V-band Photometry in the Coma Cluster

Galaxy	Frame	Seeing	Date	Aperture Dia.								
				6.0″	8.0″	10.0″	13.0″	16.0″	17.0″	20.0″	25.0″	32.0″
D131	113P	2.4″	23/03/87	15.58:	15.39	15.19	15.00	14.85	14.81	14.69	14.55	14.40
D131	159P	2.1″	10/04/89	15.69:	15.44	15.23	15.02	14.86	14.81	14.70	14.55	14.40
D131	165P	2.2″	10/04/89	15.68:	15.44	15.23	15.02	14.86	14.81	14.70	14.54	14.39
D131	301P	1.6″	11/04/89	15.57	15.36	15.19	14.99	14.85	14.81	14.69	14.54	14.40
D131	321P	2.3″	11/04/89	15.58:	15.38	15.21	15.01	14.86	14.80	14.70	14.55	14.40
D131	331P	2.3″	11/04/89	15.60:	15.37	15.21	15.01	14.85	14.80	14.70	14.54	14.39
D131	440P	2.5″	12/04/89	15.59:	15.38	15.19	15.00	14.85	14.81	14.69	14.55	14.40
D132	113P	2.4″	23/03/87	16.58:	16.42	16.25	16.11	16.00	15.97	15.89	15.77	15.67
D132	159P	2.1″	10/04/89	16.69:	16.43	16.27	16.11	15.98	15.94	15.87	15.74	15.63
D132	165P	2.2″	10/04/89	16.65:	16.43	16.27	16.11	15.98	15.95	15.86	15.74	15.62
D132	301P	1.6″	11/04/89	16.54	16.35	16.23	16.08	15.98	15.95	15.87	15.77	15.67
D132	305P	1.4″	11/04/89	16.54	16.35	16.22	16.07	15.95	15.92	15.84	15.72	15.62
D132	321P	2.3″	11/04/89	16.56:	16.38	16.23	16.08	15.97	15.94	15.86	15.75	15.64
D132	331P	2.3″	11/04/89	16.56:	16.39	16.24	16.09	15.97	15.94	15.86	15.74	15.63
D132	440P	2.5″	12/04/89	16.56:	16.38	16.25	16.09	15.98	15.94	15.86	15.75	15.63
D133	305P	1.4″	11/04/89	15.36	15.16	15.02	14.89	14.81	14.79	14.73	14.66	14.59
D134	320P	1.8″	11/04/89	16.70	16.57	16.47	16.38	16.35	16.33	16.30	16.27	
D134	439P	2.8″	12/04/89	16.77:	16.62:	16.51	16.41	16.37	16.35	16.32	16.30	
D135	320P	1.8″	11/04/89	16.74	16.55	16.40	16.25	16.17	16.15	16.10	16.05	
D135	439P	2.8″	12/04/89	16.78:	16.58:	16.44	16.28	16.19	16.16	16.11	16.07	
D136	320P	1.8″	11/04/89	15.98	15.87	15.79	15.72	15.68	15.68	15.65	15.62	
D136	439P	2.8″	12/04/89	16.03:	15.91:	15.81	15.73	15.69	15.68	15.65	15.62	
D143	149P	1.6″	20/04/88	15.54	15.21	14.99	14.72	14.54	14.49	14.35	14.18	14.01
D143	436P	2.9″	12/04/89	15.51:	15.23:	14.97	14.71	14.52	14.47	14.33	14.17	14.00
D144	162P	2.7″	10/04/89	15.57:	15.30:	15.14	14.95	14.83	14.79	14.69	14.57	14.45
D144	435P	2.2″	12/04/89	15.46:	15.23	15.07	14.91	14.80	14.76	14.69	14.57	14.46
D145	149P	1.6″	20/04/88	16.12	15.86	15.70	15.50	15.38	15.33	15.24	15.12	15.02
D145	162P	2.7″	10/04/89	16.20:	15.94:	15.74	15.53	15.38	15.34	15.24	15.12	15.03
D145	435P	2.2″	12/04/89	16.11:	15.86	15.69	15.49	15.36	15.32	15.23		
D145	436P	2.9″	12/04/89	16.10:	15.84:	15.67	15.49	15.35	15.31	15.22		
D147	435P	2.2″	12/04/89	16.51:	16.26	16.08	15.88	15.73	15.69	15.59	15.46	15.34

Table 4.5 (cont.) — Raw V-band Photometry in the Coma Cluster

Galaxy	Frame	Seeing	Date	Aperture Dia.								
				6.0″	8.0″	10.0″	13.0″	16.0″	17.0″	20.0″	25.0″	32.0″
D148	110P	1.9″	23/03/87	14.54:	14.10	13.85	13.58	13.36	13.31	13.16	12.98	12.78
D148	217P	1.4″	20/04/88	14.50	14.15	13.86	13.57	13.38	13.33	13.18	12.99	12.78
D148	307P	1.9″	11/04/89	14.47:	14.11	13.85	13.57	13.38	13.31	13.18	12.98	12.79
D148	332P	2.1″	11/04/89	14.57:	14.12	13.88	13.61	13.39	13.33	13.19	13.01	12.81
D150	110P	1.9″	23/03/87	16.13:	15.87	15.71	15.55	15.44	15.41	15.35	15.30	15.26
D150	217P	1.4″	20/04/88	16.09	15.88	15.71	15.55	15.43	15.40	15.33	15.24	15.16
D150	319P	1.9″	11/04/89	16.10:	15.87	15.71	15.55	15.44	15.41	15.35	15.29	15.24
D151	110P	1.9″	23/03/87	15.59:	15.30	15.12	14.92	14.76	14.72	14.59	14.45	14.29
D151	217P	1.4″	20/04/88	15.55	15.31	15.13	14.90	14.75	14.70	14.58	14.42	14.25
D151	222P	1.5″	20/04/88	15.54	15.30	15.12	14.89	14.75	14.70	14.58	14.42	14.25
D151	319P	1.9″	11/04/89	15.53:	15.31	15.11	14.91	14.76	14.70	14.60	14.45	14.29
D152	113P	2.4″	23/03/87	16.01:	15.79	15.59	15.39	15.24	15.20	15.10	14.99	14.90
D152	222P	1.5″	20/04/88	16.05	15.76	15.59	15.39	15.24	15.19	15.09	14.97	14.86
D152	159P	2.1″	10/04/89	16.11:	15.85	15.62	15.41	15.25	15.21	15.12	15.01	14.93
D152	165P	2.2″	10/04/89	16.10:	15.84	15.63	15.41	15.26	15.22	15.12	15.01	14.93
D152	301P	1.6″	11/04/89	15.99	15.77	15.58	15.37	15.24	15.20	15.11	15.00	14.92
D152	318P	1.8″	11/04/89	16.01	15.77	15.60	15.38	15.24	15.20	15.11	15.00	14.91
D152	321P	2.3″	11/04/89	15.99:	15.78	15.59	15.40	15.25	15.20	15.11	15.00	14.92
D152	331P	2.3″	11/04/89	16.01:	15.78	15.60	15.39	15.24	15.20	15.11	15.00	14.92
D152	440P	2.5″	12/04/89	16.01:	15.78	15.59	15.38	15.24	15.20	15.10	15.00	14.91
D153	222P	1.5″	20/04/88	16.11	15.91	15.77	15.63	15.54	15.51	15.45	15.36	15.26
D153	159P	2.1″	10/04/89	16.22:	15.98	15.82	15.66	15.55	15.53	15.49	15.42	15.37
D153	318P	1.8″	11/04/89	16.11	15.92	15.77	15.63	15.53	15.52	15.46	15.39	15.33
D154	159P	2.1″	10/04/89	17.19:	16.86	16.64	16.39	16.20	16.13	16.01	15.85	15.68
D154	165P	2.2″	10/04/89	17.17:	16.85	16.63	16.38	16.19	16.13	16.01	15.84	15.68
D154	301P	1.6″	11/04/89	17.05	16.76	16.57	16.34	16.16	16.11	15.99	15.83	15.68
D154	318P	1.8″	11/04/89	17.08	16.80	16.58	16.34	16.16	16.11	15.97	15.80	15.63
D154	321P	2.3″	11/04/89	17.10:	16.83	16.59	16.35	16.17	16.12	15.99	15.82	15.65
D154	331P	2.3″	11/04/89	17.08:	16.81	16.60	16.36	16.18	16.12	15.99	15.82	15.65
D154	440P	2.5″	12/04/89	17.08:	16.82	16.59	16.35	16.17	16.12	15.99	15.83	15.66

Table 4.5 (cont.) — Raw V-band Photometry in the Coma Cluster

Galaxy	Frame	Seeing	Date	Aperture Dia.								
				6.0″	8.0″	10.0″	13.0″	16.0″	17.0″	20.0″	25.0″	32.0″
D155	113P	2.4″	23/03/87	15.67:	15.43	15.24	15.03	14.88	14.84	14.74	14.63	14.52
D155	159P	2.1″	10/04/89	15.74:	15.48	15.27	15.04	14.89	14.84	14.75	14.63	14.51
D155	165P	2.2″	10/04/89	15.74:	15.47	15.27	15.05	14.88	14.84	14.75	14.62	14.51
D155	301P	1.6″	11/04/89	15.65	15.41	15.22	15.01	14.88	14.83	14.73	14.62	14.51
D155	318P	1.8″	11/04/89	15.68	15.40	15.22	15.02	14.86	14.83	14.73	14.62	14.50
D155	321P	2.3″	11/04/89	15.67:	15.42	15.24	15.02	14.87	14.83	14.74	14.62	14.51
D155	331P	2.3″	11/04/89	15.68:	15.45	15.23	15.02	14.87	14.83	14.74	14.62	14.51
D155	440P	2.5″	12/04/89	15.68:	15.43	15.24	15.02	14.88	14.84	14.74	14.63	14.52
D156	159P	2.1″	10/04/89	16.82:	16.57	16.42	16.27	16.17	16.15	16.11	16.05	15.98
D156	165P	2.2″	10/04/89	16.80:	16.58	16.42	16.27	16.17	16.15	16.11	16.05	15.97
D156	301P	1.6″	11/04/89	16.70	16.48	16.36	16.23	16.16	16.14	16.09	16.03	
D156	321P	2.3″	11/04/89	16.71:	16.52	16.37	16.24	16.15	16.13	16.09	16.02	
D156	331P	2.3″	11/04/89	16.72:	16.52	16.37	16.24	16.15	16.12	16.08	16.01	
D157	113P	2.4″	23/03/87	16.29:	16.13	15.98	15.85	15.76	15.75	15.68	15.58	15.45
D157	159P	2.1″	10/04/89	16.37:	16.15	16.00	15.84	15.74	15.72	15.66	15.58	15.48
D157	165P	2.2″	10/04/89	16.34:	16.14	15.97	15.82	15.73	15.70	15.64	15.56	15.45
D157	301P	1.6″	11/04/89	16.25	16.07	15.95	15.82	15.75	15.72	15.66	15.59	15.50
D157	305P	1.4″	11/04/89	16.27	16.07	15.95	15.81	15.72	15.70	15.63	15.56	15.45
D157	321P	2.3″	11/04/89	16.28:	16.09	15.96	15.82	15.74	15.71	15.66	15.58	15.47
D157	331P	2.3″	11/04/89	16.28:	16.10	15.97	15.82	15.73	15.71	15.65	15.57	15.46
D157	440P	2.5″	12/04/89	16.27:	16.09	15.96	15.81	15.73	15.71	15.64	15.56	15.46
D160	305P	1.4″	11/04/89	15.76	15.54	15.34	15.16	15.05	15.01	14.92	14.80	14.71
D164	204P	1.4″	20/04/88	14.61	14.36	14.23	14.06	13.95	13.92	13.83	13.73	13.62
D164A	204P	1.4″	20/04/88	16.48	16.12	15.91	15.68	15.51	15.46	15.34	15.20	15.05
D167	149P	1.6″	20/04/88	15.23	14.97	14.82	14.64	14.52	14.48	14.39	14.27	14.16
D168	303P	1.4″:	11/04/89	15.20	14.96	14.80	14.64	14.54	14.51	14.45	14.37	14.29
D170	219P	1.4″	20/04/88	15.95	15.73	15.56	15.38	15.24	15.20	15.11	15.00	14.89
D170	164P	2.2″	10/04/89	15.98:	15.73	15.55	15.34	15.20	15.16	15.07	14.96	14.85
D170	317P	2.3″	11/04/89	15.91:	15.69	15.52	15.33	15.19	15.16	15.07	14.96	14.85

Table 4.5 (cont.) — Raw V-band Photometry in the Coma Cluster

Galaxy	Frame	Seeing	Date	Aperture Dia.								
				6.0″	8.0″	10.0″	13.0″	16.0″	17.0″	20.0″	25.0″	32.0″
D171	219P	1.4”	20/04/88	16.30	16.14	16.03	15.93	15.84	15.81	15.74	15.68	15.61
D171	164P	2.2”	10/04/89	16.32:	16.16	16.02	15.90	15.81	15.79	15.74	15.68	15.63
D171	317P	2.3”	11/04/89	16.24:	16.10	15.99	15.87	15.78	15.76	15.71	15.64	15.57
D172	219P	1.4”	20/04/88	15.78	15.59	15.46	15.34	15.25	15.23	15.18	15.13	15.09
D172	164P	2.2”	10/04/89	15.77:	15.60	15.44	15.31	15.22	15.19	15.15	15.10	15.07
D172	317P	2.3”	11/04/89	15.73:	15.54	15.42	15.30	15.21	15.18	15.15	15.10	15.07
D173	219P	1.4”	20/04/88	16.05	15.89	15.78	15.65	15.57	15.55	15.49	15.42	15.35
D173	164P	2.2”	10/04/89	16.07:	15.90	15.77	15.64	15.55	15.52	15.48	15.43	15.39
D173	317P	2.3”	11/04/89	15.99:	15.83	15.74	15.62	15.53	15.51	15.47	15.41	15.37
D174	219P	1.4”	20/04/88	15.58	15.41	15.28	15.18	15.13	15.11	15.08	15.05	15.03
D174	317P	2.3”	11/04/89	15.52:	15.36	15.24	15.14	15.07	15.06	15.04	15.02	15.01
D175	163P	2.0”	10/04/89	15.65:	15.38	15.19	15.00	14.86	14.84	14.75	14.64	14.57
D175	310P	1.7”	11/04/89	15.61	15.37	15.17	14.98	14.85	14.83	14.74	14.64	14.56
D175	319P	1.9”	11/04/89	15.57:	15.35	15.16	14.97	14.85	14.81	14.74	14.64	14.56
D184	201P	1.4”	20/04/88	17.49	17.10	16.89	16.66	16.49	16.45	16.33	16.21	16.07
D191	303P	1.4”:	11/04/89	16.39	16.17	16.03	15.90	15.83	15.81	15.77	15.72	15.67
D193	314P	2.0”	11/04/89	16.23:	16.02	15.88	15.74	15.65	15.64	15.58	15.51	15.45
D193	437P	2.6”	12/04/89	16.30:	16.08:	15.92	15.76	15.66	15.64	15.57	15.51	15.45
D194	150P	1.6”	20/04/88	15.02	14.77	14.60	14.41	14.28	14.24	14.15	14.02	13.90
D194	306P	1.7”	11/04/89	14.99	14.73	14.57	14.39	14.27	14.23	14.14	14.03	13.92
D194	434P	2.3”:	12/04/89	15.18:	14.89	14.65	14.43	14.29	14.25	14.16	14.03	13.91
D195	306P	1.7”	11/04/89	16.58	16.16	15.87	15.62	15.50	15.47	15.39	15.32	15.25
D195	434P	2.3”:	12/04/89	16.71:	16.28	16.00	15.70	15.53	15.49	15.41	15.31	15.23
D196	150P	1.6”	20/04/88	16.25	16.08	15.96	15.83	15.74	15.72	15.65	15.56	15.48
D196	306P	1.7”	11/04/89	16.19	16.04	15.94	15.82	15.75	15.73	15.68	15.63	15.60
D196	434P	2.3”:	12/04/89	16.40:	16.17	16.01	15.86	15.76	15.73	15.67	15.60	15.55
D206	154P	1.8”	20/04/88	15.08	14.72	14.53	14.32	14.18	14.14	14.03	13.91	13.79
D206	313P	1.9”	11/04/89	14.98:	14.66	14.45	14.25	14.10	14.06	13.97	13.86	
D207	154P	1.8”	20/04/88	16.10	15.82	15.68	15.52	15.41	15.40	15.33	15.25	15.17
D207	176P	2.8”	20/04/88	16.01:	15.76:	15.62	15.48	15.38	15.36	15.29	15.23	15.16
D207	313P	1.9”	11/04/89	15.97:	15.77	15.62	15.47	15.38	15.35	15.29	15.22	15.15

Table 4.5 (cont.) — Raw V-band Photometry in the Coma Cluster

Galaxy	Frame	Seeing	Date	Aperture Dia.								
				6.0″	8.0″	10.0″	13.0″	16.0″	17.0″	20.0″	25.0″	32.0″
D217	122P	2.1”	23/03/87	15.21:	15.00	14.79	14.60	14.46	14.42	14.32	14.19	14.06
D217	151P	1.6”	20/04/88	15.25	15.02	14.83	14.63	14.49	14.45	14.34	14.21	14.07
D217	202P	1.5”	20/04/88	15.27	14.97	14.82	14.64	14.48	14.44	14.33	14.20	14.06
D217	207P	1.6”	20/04/88	15.26	14.97	14.82	14.62	14.48	14.44	14.32	14.19	14.05
D217	214P	1.3”	20/04/88	15.22	14.99	14.81	14.62	14.48	14.44	14.33	14.19	14.05
D217	220P	1.3”	20/04/88	15.24	14.99	14.81	14.62	14.48	14.43	14.33	14.19	14.05
D217	166P	2.2”	10/04/89	15.30:	15.03	14.85	14.63	14.48	14.43	14.33	14.20	14.06
D217	312P	1.8”:	11/04/89	15.22	14.97	14.80	14.61	14.47	14.43	14.33	14.19	14.05
D240	160P	2.5”	10/04/89	14.84:	14.55	14.34	14.10	13.93	13.87	13.76	13.60	13.43
D240	311P	1.8”	11/04/89	14.82	14.52	14.32	14.09	13.93	13.88	13.76	13.60	13.42
D240A	160P	2.5”	10/04/89	15.23:	14.98	14.79	14.57	14.41	14.37	14.26	14.10	13.92
D240A	311P	1.8”	11/04/89	15.21	14.96	14.77	14.56	14.40	14.37	14.25	14.10	13.92
D245	203P	1.4”	20/04/88	16.04	15.77	15.62	15.45	15.34	15.31	15.23	15.15	15.06

Table 4.6 — Raw U-band Photometry in the Coma Cluster

Galaxy	Frame	Seeing	Date		Aperture Dia.							
					6.0″	8.0″	10.0″	13.0″	16.0″	17.0″	20.0″	25.0″
D68	268	1.9″	11/04/89	U	17.44:	17.18	17.01	16.84	16.73	16.69	16.58	16.47
D69	268	1.9″	11/04/89	U	16.95:	16.74	16.57	16.39	16.29	16.25	16.17	16.07
D70	268	1.9″	11/04/89	U	17.28:	17.07	16.92	16.75	16.65	16.62	16.54	16.44
D71	268	1.9″	11/04/89	U	18.31:	18.00	17.80	17.60	17.45:	17.42:		
D87	427	2.5″	12/04/89	U	17.92:	17.71	17.56	17.40	17.31	17.28	17.25	17.21
D103	285	1.7″	21/04/88	U	16.72	16.54	16.44	16.31	16.24	16.22	16.16	16.08
D104	127	2.2″	23/03/87	U	17.13:	16.94	16.80	16.68	16.59	16.56	16.52	16.44
D104	285	1.7″	21/04/88	U	17.10	16.90	16.78	16.65	16.57	16.54	16.48	16.40
D106	285	1.7″	21/04/88	U	17.51	17.31	17.20	17.08	17.04	17.02	16.99	16.97
D107	285	1.7″	21/04/88	U	17.82	17.51	17.32	17.11	17.00	16.97	16.89	16.85
D116	429	2.6″	12/04/89	U	17.52:	17.21:	17.07	16.88	16.75	16.72:		
D117	270	1.8″	11/04/89	U	17.90	17.63	17.46	17.30:	17.22:	17.20:	17.10:	
D118	270	1.8″	11/04/89	U	17.11	16.86	16.65	16.44	16.29	16.25	16.15	16.01
D119	429	2.6″	12/04/89	U	17.64:	17.42	17.27	17.10	16.98:	16.94:		
D120	286	1.7″	11/04/89	U	16.53	16.29	16.09	15.85	15.65	15.59	15.46	15.34
D122	274	1.9″	21/04/88	U	17.36:	17.15	16.99	16.83	16.70	16.68	16.59	16.50
D122	286	1.7″	11/04/89	U	17.36	17.15	16.98	16.81	16.69	16.65	16.58	16.47
D124	127	2.2″	23/03/87	U	16.98:	16.78	16.60	16.46	16.35	16.32	16.26	16.20
D125	127	2.2″	23/03/87	U	17.45:	17.31	17.20	17.10	17.04	17.03	17.01	16.95
D126	115	1.8″	23/03/87	U	17.95	17.69	17.48	17.28:	17.17:	17.13:		
D126	267	1.9″	11/04/89	U	18.01:	17.68	17.47	17.31:	17.18:	17.15:		
D126	288	1.8″	11/04/89	U	17.88	17.66	17.47	17.32:	17.23:	17.22:		
D126	441	3.0″	12/04/89	U	18.10:	17.84:	17.63	17.41:	17.28:	17.23:		
D127	115	1.8″	23/03/87	U	18.25	17.98	17.79	17.57:	17.42:	17.36:		
D127	267	1.9″	11/04/89	U	18.32:	18.06	17.83	17.62:	17.49:	17.45:		
D127	288	1.8″	11/04/89	U	18.22	18.02	17.84	17.67:	17.54:	17.48:		
D127	430	2.5″	12/04/89	U	18.28:	18.03	17.87	17.69:	17.58:	17.53:		
D127	441	3.0″	12/04/89	U	18.25:	18.04:	17.86	17.65:	17.49:	17.45:		
D128	115	1.8″	23/03/87	U	17.77	17.55	17.39	17.19	17.04:	16.99:		
D128	267	1.9″	11/04/89	U	17.76:	17.53	17.38	17.22:	17.10:	17.07:		
D128	288	1.8″	11/04/89	U	17.79	17.56	17.42	17.26	17.13:	17.08:		
D128	441	3.0″	12/04/89	U	17.92:	17.67:	17.50	17.31	17.21:	17.16:		

Table 4.6 (cont.) — Raw U-band Photometry in the Coma Cluster

Galaxy	Frame	Seeing	Date		Aperture Dia. 6.0″	8.0″	10.0″	13.0″	16.0″	17.0″	20.0″	25.0″
D129	115	1.8″	23/03/87	U	16.92	16.52	16.16	15.82	15.57	15.52	15.34	15.11
D129	267	1.9″	11/04/89	U	16.85:	16.45	16.14	15.81	15.57	15.51	15.34	15.12
D129	288	1.8″	11/04/89	U	16.84	16.44	16.14	15.80	15.56	15.51	15.34	15.11
D129	441	3.0″	12/04/89	U	16.92:	16.47:	16.17	15.85	15.60	15.52	15.33	15.13
D130	115	1.8″	23/03/87	U	16.87	16.66	16.51	16.34	16.22	16.18	16.09:	
D130	267	1.9″	11/04/89	U	16.84:	16.64	16.48	16.32	16.20	16.18	16.08:	
D130	288	1.8″	11/04/89	U	16.88	16.62	16.49	16.33	16.22	16.18	16.10:	
D130	441	3.0″	12/04/89	U	16.87:	16.68:	16.50	16.34	16.23	16.19	16.09:	
D131	115	1.8″	23/03/87	U	17.11	16.88	16.71	16.49	16.34	16.28	16.16	15.99:
D131	267	1.9″	11/04/89	U	17.09:	16.85	16.67	16.48	16.33	16.28	16.17	16.01:
D131	288	1.8″	11/04/89	U	17.08	16.84	16.68	16.48	16.33	16.28	16.16	16.00:
D131	441	3.0″	12/04/89	U	17.14:	16.89:	16.71	16.51	16.34	16.29	16.17	16.03:
D132	115	1.8″	23/03/87	U	18.01	17.78	17.61	17.41	17.27:	17.23:		
D132	267	1.9″	11/04/89	U	18.08:	17.82	17.64	17.46	17.33:	17.30:		
D132	284	1.6″	11/04/89	U	17.96	17.74	17.58	17.39	17.26:	17.22:		
D132	288	1.8″	11/04/89	U	18.00	17.81	17.64	17.44	17.33:	17.28:		
D132	430	2.5″	12/04/89	U	17.97:	17.75	17.58	17.39	17.26:	17.21:		
D132	441	3.0″	12/04/89	U	18.08:	17.83:	17.69	17.49	17.36:	17.31:		
D133	284	1.6″	11/04/89	U	16.86	16.60	16.47	16.32	16.22	16.20	16.12	16.05
D134	428	2.3″	12/04/89	U	18.13:	17.95	17.85	17.73:	17.65:	17.64:		
D135	428	2.3″	12/04/89	U	18.16:	17.88	17.72	17.57	17.46:	17.43:		
D136	428	2.3″	12/04/89	U	17.48:	17.29	17.20	17.10	17.02	17.00	16.96:	
D143	284	1.9″	21/04/88	U	17.13:	16.80	16.55	16.27	16.07	15.99	15.85	15.66
D144	429	2.6″	12/04/89	U	16.92:	16.70:	16.55	16.37	16.26	16.23	16.13	16.01
D145	284	1.9″	21/04/88	U	17.50:	17.27	17.09	16.91	16.78	16.74:		
D147	429	2.6″	12/04/89	U	17.89:	17.61:	17.42	17.22	17.07:	17.02:		
D148	274	1.9″	21/04/88	U	16.17:	15.79	15.51	15.22	15.01	14.94	14.79	14.58
D148	286	1.7″	11/04/89	U	16.14	15.78	15.50	15.23	15.02	14.95	14.79	14.58
D150	274	1.9″	21/04/88	U	17.53:	17.28	17.10	16.92	16.81	16.78	16.72	16.64:

Table 4.6 (cont.) — Raw U-band Photometry in the Coma Cluster

Galaxy	Frame	Seeing	Date		Aperture Dia. 6.0″	8.0″	10.0″	13.0″	16.0″	17.0″	20.0″	25.0″
D151	274	1.9"	21/04/88	U	16.98:	16.69	16.49	16.27	16.10	16.05	15.93	15.77
D151	286	1.7"	11/04/89	U	16.96	16.71	16.51	16.28	16.12	16.06	15.94	15.77
D152	115	1.8"	23/03/87	U	17.58	17.32	17.12	16.90	16.75	16.72	16.63:	
D152	267	1.9"	11/04/89	U	17.46:	17.23	17.03	16.83	16.67	16.64	16.53:	
D152	288	1.8"	11/04/89	U	17.50	17.22	17.05	16.86	16.72	16.68	16.58:	
D152	430	2.5"	12/04/89	U	17.47:	17.19	17.00	16.82	16.69	16.66	16.58:	
D152	441	3.0"	12/04/89	U	17.52:	17.31:	17.12	16.91	16.76	16.72	16.62:	
D153	430	2.5"	12/04/89	U	17.66:	17.42	17.25	17.08	16.97:	16.95:		
D154	267	1.9"	11/04/89	U	18.39:	18.13	17.91	17.70:	17.55:	17.50:		
D154	288	1.8"	11/04/89	U	18.43	18.15	17.93	17.67:	17.50:	17.45:		
D154	430	2.5"	12/04/89	U	18.42:	18.15	17.91	17.64:	17.45:	17.41:		
D154	441	3.0"	12/04/89	U	18.45:	18.15:	17.97	17.71:	17.52:	17.46:		
D155	115	1.8"	23/03/87	U	17.15	16.90	16.68	16.47	16.31	16.25	16.13	15.98:
D155	267	1.9"	11/04/89	U	17.09:	16.85	16.64	16.42	16.26	16.23	16.11	15.96:
D155	288	1.8"	11/04/89	U	17.11	16.84	16.65	16.41	16.26	16.22	16.10	15.97:
D155	430	2.5"	12/04/89	U	17.16:	16.88	16.67	16.44	16.28	16.24	16.14	16.01:
D155	441	3.0"	12/04/89	U	17.16:	16.87:	16.68	16.44	16.28	16.22	16.10	15.97:
D156	288	1.8"	11/04/89	U	18.11	17.91	17.79	17.65:	17.57:	17.56:		
D156	430	2.5"	12/04/89	U	18.15:	17.87	17.67	17.50:	17.37:	17.35:		
D156	441	3.0"	12/04/89	U	18.10:	17.82:	17.66	17.49:	17.38:	17.37:		
D157	115	1.8"	23/03/87	U	17.77	17.48	17.34	17.18	17.07:	17.05:		
D157	267	1.9"	11/04/89	U	17.75:	17.51	17.35	17.21	17.13:	17.11:		
D157	284	1.6"	11/04/89	U	17.66	17.45	17.32	17.17	17.11:	17.09:		
D157	288	1.8"	11/04/89	U	17.67	17.48	17.33	17.20	17.12:	17.11:		
D157	430	2.5"	12/04/89	U	17.60:	17.41	17.25	17.08	16.97:	16.96:		
D157	441	3.0"	12/04/89	U	17.67:	17.49:	17.34	17.17	17.08:	17.06:		
D158	284	1.6"	11/04/89	U	18.38	18.14	17.99	17.85:	17.74:	17.72:		
D160	284	1.6"	11/04/89	U	17.28	17.02	16.85	16.65	16.53	16.50	16.40	16.28
D167	284	1.9"	21/04/88	U	16.69:	16.44	16.28	16.09	15.95	15.91	15.83	15.70
D168	269	1.9":	11/04/89	U	16.75:	16.52	16.32	16.14	16.04	16.01	15.93	15.84
D170	287	2.0"	21/04/88	U	17.38:	17.12	16.94	16.75	16.61	16.58	16.48	16.39

Table 4.6 (cont.) — Raw U-band Photometry in the Coma Cluster

Galaxy	Frame	Seeing	Date		Aperture Dia.							
					6.0″	8.0″	10.0″	13.0″	16.0″	17.0″	20.0″	25.0″
D171	287	2.0″	21/04/88	U	17.71:	17.53	17.41	17.30:	17.23:	17.20:		
D172	287	2.0″	21/04/88	U	17.18:	16.98	16.84	16.69	16.60	16.58	16.52	16.48
D173	287	2.0″	21/04/88	U	17.50:	17.30	17.17	17.03	16.93	16.91	16.84	16.76
D174	287	2.0″	21/04/88	U	17.08:	16.88	16.73	16.61	16.54	16.53	16.50	16.46
D175	287	1.6″	11/04/89	U	17.13	16.87	16.68	16.48	16.35	16.32	16.23:	
D191	269	1.9″:	11/04/89	U	17.78:	17.56	17.39	17.26:	17.17:	17.15:		
D194	285	1.6″:	11/04/89	U	16.63	16.37	16.17	15.97	15.82	15.78	15.68	15.55
D195	285	1.6″:	11/04/89	U	17.02	16.54	16.24	15.99	15.87	15.83	15.76	15.68
D196	285	1.6″:	11/04/89	U	17.72	17.49	17.37	17.25:	17.16:	17.13:		
D206	155	2.1″	20/04/88	U	16.49:	16.18	15.98	15.75	15.59	15.55	15.45	15.31
D207	155	2.1″	20/04/88	U	17.49:	17.25	17.07	16.92	16.82	16.81	16.75:	
D217	124	2.0″	23/03/87	U	16.85:	16.53	16.36	16.16	16.00	15.97	15.85	15.72
D217	286	1.9″	21/04/88	U	16.74:	16.52	16.32	16.12	15.97	15.93	15.82	15.68

apertures spaced so that magnitudes at any other aperture to be accurately determined by interpolating with an $r^{1/4}$-law profile. The inner limit to the apertures is set by the requirement that the seeing correction be reasonably small. The outer aperture is limited in Coma by statistical fluctuations in the sky flux, and in the brighter Virgo galaxies by the difficulty in establishing the true background sky level (ie., without contamination from the galaxian halo). Additionally, we present measurements at 17″ in Coma, and 60″ in Virgo as these are of special interest for this project. The magnitudes have been corrected for seeing and contaminating stars. We indicate with a colon magnitudes which are uncertain either because the seeing correction applied was greater than $0.^m05$ (smaller apertures), or because the statistical fluctuations in the sky flux are capable of altering the magnitude by more than $0.^m03$.

Table 4.7 summarises the internal comparisons that we have made using repeated measurements. The apertures presented will be used to derive galaxian colours. Unless noted otherwise, we have included all measurements, including those marked as uncertain in this comparison. The astute reader will note that the accuracy of the Coma U-band photometry is limited by the statistical uncertainties in the background sky flux. A graphical presentation of the comparison is given in Figures 4.5–4.8.

Table 4.7

Summary of the Internal Comparison of Optical Photometry

Cluster	Photometric Band	Aperture Dia.	Number of Comparisons	RMS Scatter	Comments
Virgo	V	60″	23	0.012	
	U	~60″	20	0.019	first good ap.
Coma	V	17″	145	0.018	
		13″	145	0.021	
	U	13″	29	0.035	U < 17.2
		13″	46	0.044	all galaxies

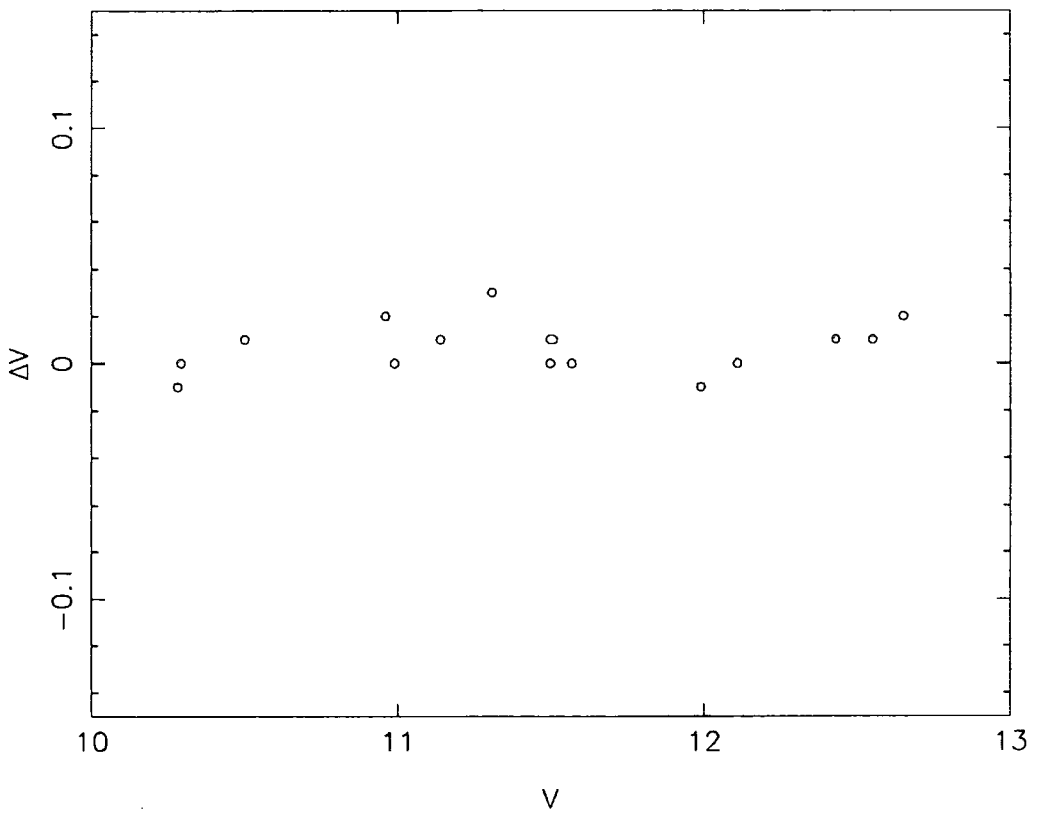

Figure 4.5. Internal comparison of V-band photometry of galaxies in the Virgo cluster. Measurements within a 60″ aperture are shown. The rms scatter of the points is $0.^m012$.

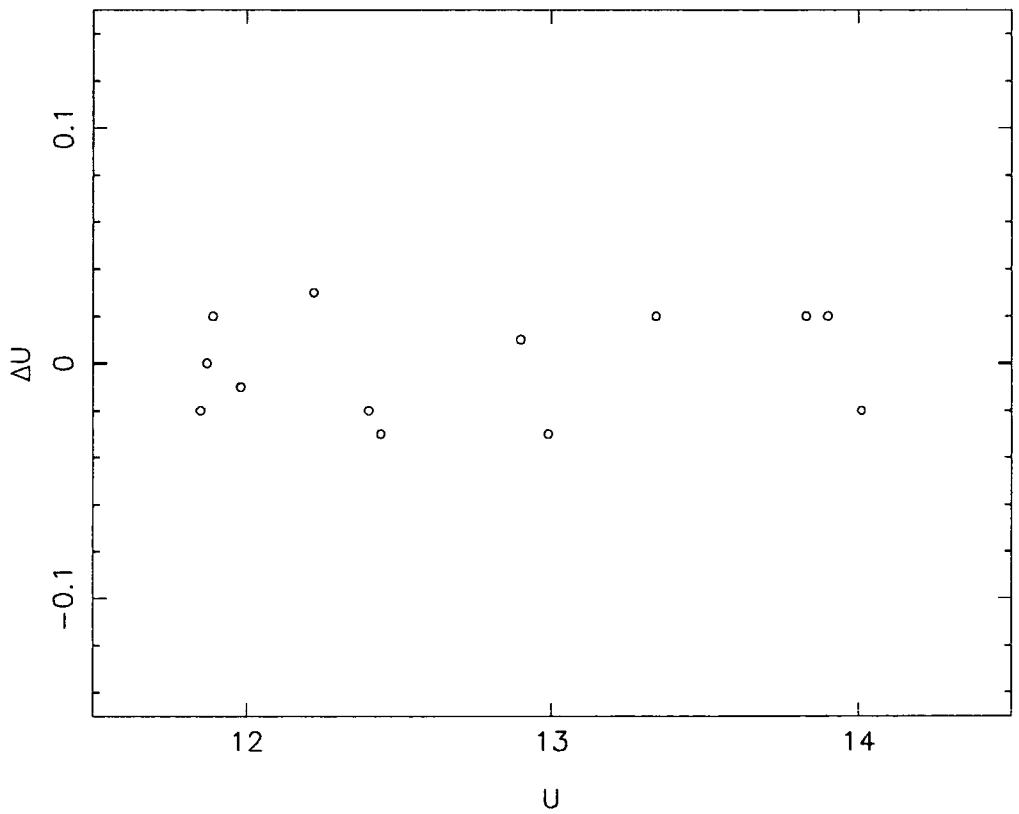

Figure 4.6. Internal comparison of galaxies in the Virgo cluster. Measurements within a 60″ aperture are compared unless the uncertainty introduced by the background sky subtraction is greater than $0.^m03$. In these cases, we compare the largest apertures for which this is not a source of additional uncertainty. The rms scatter of the points is $0.^m019$.

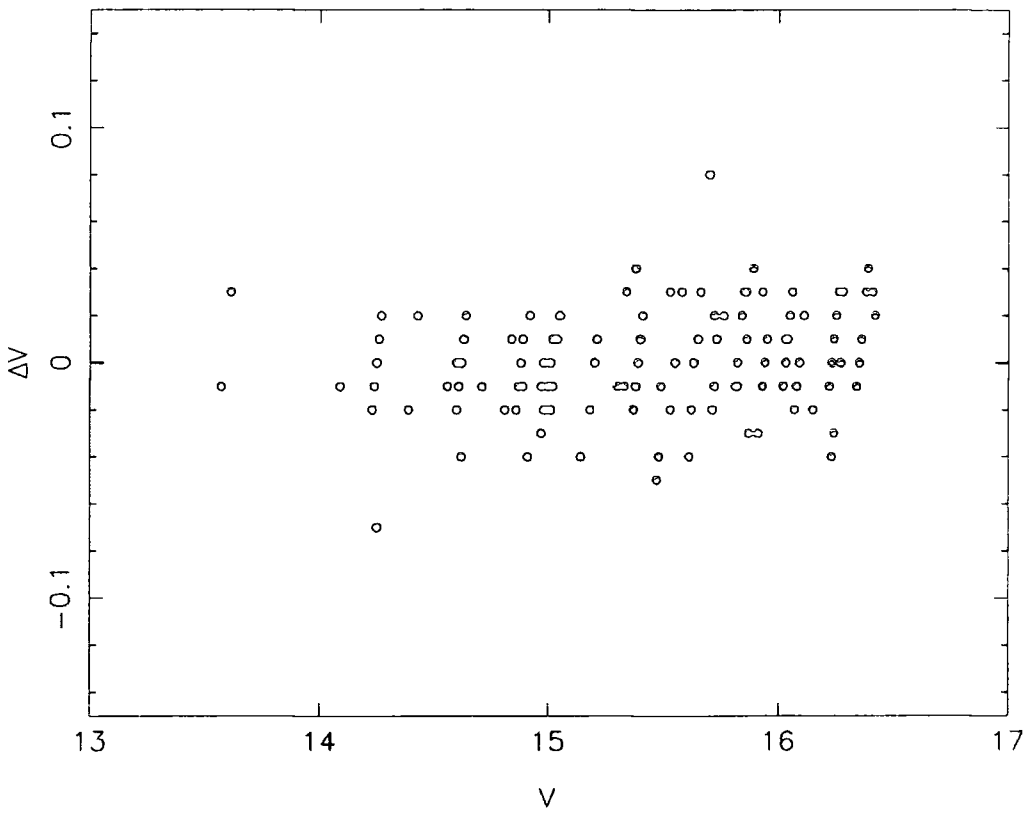

Figure 4.7. Internal comparison of V-band photometry of galaxies in the Coma cluster. Measurements within a 13″ aperture are compared. The rms scatter is $0.^{m}021$.

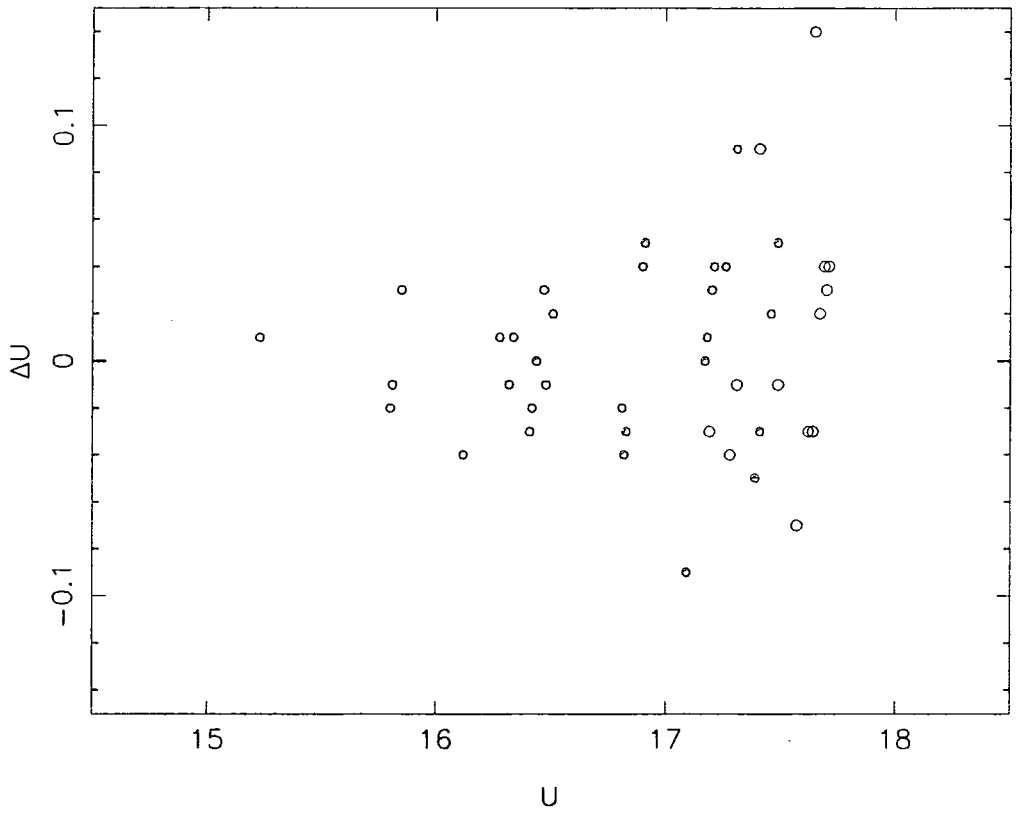

Figure 4.8. Internal comparison of U-band photometry of galaxies in the Coma cluster. Measurements within a 13″ aperture are presented. Open symbols denote measurements that have a associated uncertainty greater than $0.^m03$. For the brighter galaxies ($U < 1.2$), the rms scatter is $0.^m035$. The accuracy of this photometry is largely limited by the uncertainty in determining the sky background flux.

4.4 UVJK Colours for Galaxies in Virgo and Coma

4.4.1 Correcting for intra-cluster light

The two dominant galaxies in the Coma cluster have large extended haloes. In the previous tables, we have presented optical and infrared photometry for several galaxies that are embedded in this intra-cluster light. However, before we can compare these magnitudes, we must ensure that the contribution from the background light has been dealt with consistently in both cases. In our optical data, we were able to experiment with the determination of a local 'sky' flux from an annulus surrounding the galaxy. This allows background light from both the night sky and the haloes of the central galaxies to be subtracted off from the total flux measured in the galaxy aperture. We found, however, that the varying and sometimes steep slope of the halo makes it difficult to define a consistent background by this technique. We therefore prefer to include the contribution of the halo light in the magnitude of the galaxy, and to subtract off the sky flux alone. As described in Section 4.3.5, our mosaic of CCD images of the cluster core shows that the halo contribution at the outer edges of the CCD frame falls below the level of statistical variations and flat-fielding errors. Therefore, the sky background can be consistently defined from these regions. Because of the large chopping offset (150″) of the sky channels of the infrared photometer, the above definition of the galaxy's optical magnitude is in general consistent with the magnitude measured in the infrared. For a few galaxies, however, one of the sky channels lies in a region where the background is enhanced by the halo light. In these cases, we have used our mosaic of overlapping V-band CCD images to correct the UKIRT magnitude for this effect. Starting from the frame occupied by the galaxy to be measured, a normalization factor is added or subtracted to match-up the background flux in the common region on the adjacent frame. It is then possible to determine two V-band magnitudes for the galaxy — one subtracting the sky flux alone, the other removing the average background flux that would have been measured by the infrared photometer. Making the assumption that V-K colour differences between the halo and the galaxy are small, we apply this small correction to the infrared

Table 4.8

Corrections for Intra-Cluster Light

Galaxy	Chop Dir.	ΔV
D124	EW	0.00
D125	EW	0.00
	NS	−0.09
D126	EW	−0.32:
D127	NS	−0.04
D128	EW	−0.06
	NS	−0.04
D129	EW	−0.01
D130	NS	−0.02
D148	EW	0.00
D150	EW	0.00
D151	NS	0.00
D152	NS	−0.01
D153	EW	−0.02
	NS	−0.04
D154	NS	−0.16:

Note: the correction ΔV is to be added to the magnitude measured by UKIRT.

magnitude. The values derived are presented in table 4.8. We estimate that the uncertainty in a correction of $0.^m10$ arising from V-K colour differences and from uncertainty in the background flux is less than $0.^m02$. To be conservative, we caution any correction greater than $0.^m10$.

4.4.2 Comparison with the photometry of PFA

The purpose of this section is to examine the reliability of the photometry presented by PFA. We have two aims. Firstly by establishing the reliability of their Coma J- and K-band photometry, and by establishing the relationship between their photometric system and ours, we can determine whether to adopt the photometric measurements that they present for Virgo galaxies in these bands. Secondly, by comparing the optical magnitudes derived by these authors from Sandage (1972, S72) and Sandage & Visvanathan (1976, 1978, SV) for early-type galaxies in the Virgo and Coma clusters with our homogeneous V-band photometry, we will make a first step towards eliminating possible systematic effects that could give rise to a spurious colour difference between galaxies in the two clusters. We do not compare our RCA CCD U-band measurements and the SV u-band measurements adopted by PFA as the responses of the filters are so different that no information is to be gained. We present a summary of the results of this section in Table 4.13.

PFA present J- and K-band magnitudes for galaxies in the Coma cluster with an aperture diameter of 14.9″ (corrected for beam profile effects). In order to perform a comparison with our data (17″ aperture), we determine an aperture transformation from our V-band CCD data. Under the assumption that colour gradients are small, the difference in the J (or K) magnitudes at the two apertures is the same as that determined in V. The colour gradients measured by PFA and Peletier et al. (1990) suggest that the error in this procedure is much less than $0.^m01$. The comparison is presented in Tables 4.9 and 4.10, and shown graphically in Figures 4.9 and 4.10. We reject the 3 faint galaxies D170, D127 and D128 from the comparison as the errors are clearly not random. Comparing the 13 galaxies in common, we then find: in the K-band, $\sigma = 0.032$ with an offset of -0.005 ± 0.009; in the J-band, $\sigma = 0.048$

Table 4.9— Comparison with J-band Photometry of PFA

Galaxy	$J_{PFA}(14.9'')$	$J_{UKIRT}(17.0'')$	Ap. Corr.	$\Delta J_{UKIRT-PFA}$
D78	12.14	12.11	.08	.05
D97	12.12	11.99	–	
D118	12.54	12.48	.08	.02
D126	13.87	13.73:	.06	–
D127	14.03	13.76	.10	−.17
D128	–	13.53	.08	–
D129	11.76	11.57	.14	−.05
D144	12.51	12.38	.08	−.05
D148	11.03	10.84	.12	−.07
D150	13.27	13.16	.06	−.05
D151	12.65	12.47	.10	−.08
D152	12.95	12.84	.09	−.02
D153	13.31	13.22	.06	−.03
D154	14.20	13.90:	.11	–
D170	13.02	13.07	.09	.14
D172	12.89	12.92	.05	.08
D174	12.72	12.71	.03	.02
D175	12.52	12.46	.07	.01
D217	12.16	12.07	.08	−.01
RB74	14.19	14.09	–	

Table 4.10— Comparison with K-band Photometry of PFA

Galaxy	$K_{PFA}(14.9'')$	$K_{UKIRT}(17.0'')$	Ap. Corr.	$\Delta K_{UKIRT-PFA}$
D78	11.21	11.16	.08	.03
D97	11.15	11.03	–	
D118	11.60	11.54	.08	.02
D126	12.90	12.89:	.06	–
D127	13.20	12.82	.10	−.28
D128	12.89	12.57	.08	−.24
D129	10.75	10.56	.14	−.05
D144	11.48	11.41	.08	.01
D148	9.99	9.85	.12	−.02
D150	12.32	12.23	.06	−.03
D151	11.70	11.55	.10	−.05
D152	12.01	11.87	.09	−.05
D153	12.31	12.27	.06	.02
D154	13.30	13.01:	.11	–
D170	12.01	12.05	.09	.13
D172	11.94	11.91	.05	.02
D174	11.71	11.72	.03	.04
D175	11.56	11.49	.07	.00
D217	11.19	11.12	.08	.01
RB74	13.31	13.28	–	

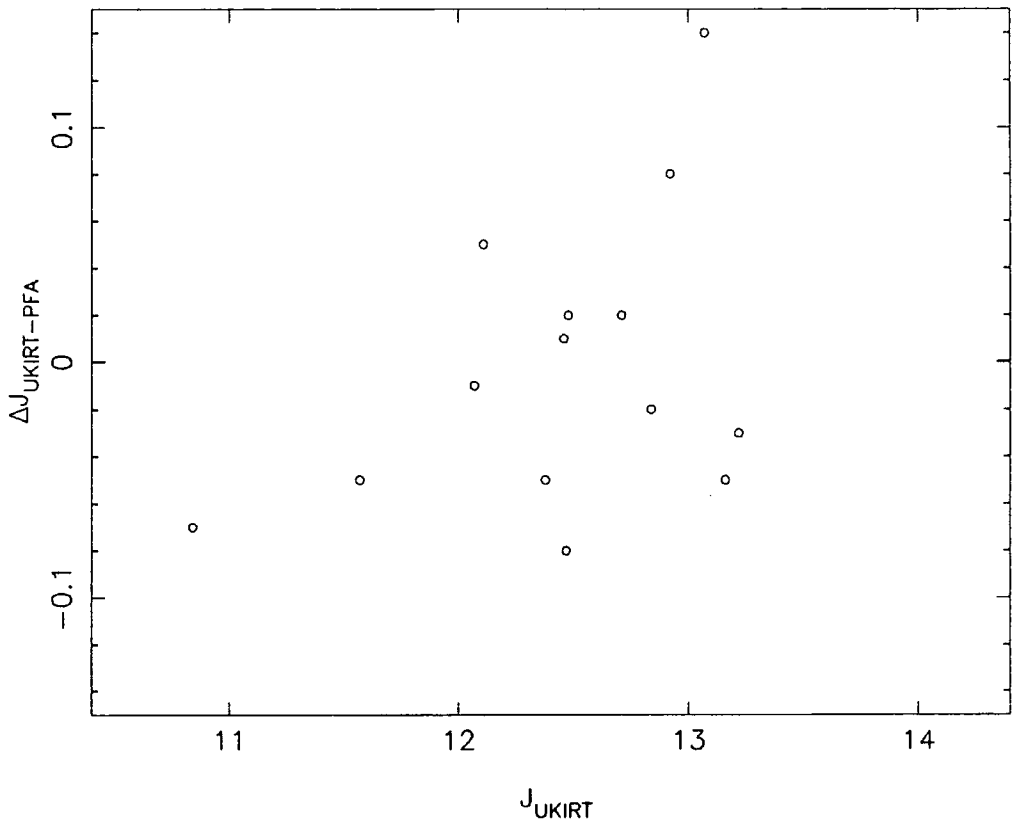

Figure 4.9. A comparison of our UKIRT J-band magnitudes with those presented by PFA. The apertures of the two photometric systems have been match by applying a correction determined from our V-band CCD photometry. Galaxy D127 is not shown because of the scale of this figure.

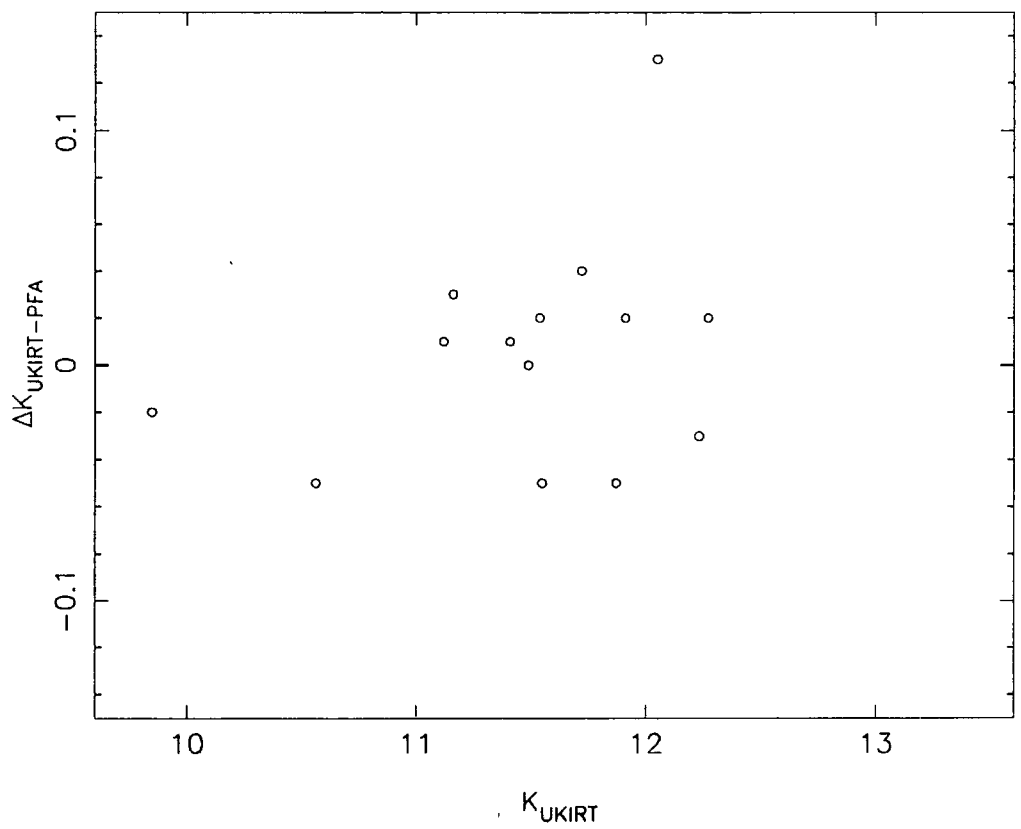

Figure 4.10. A comparison between our UKIRT K-band magnitudes and those presented by PFA. The scale of this figure does not allow galaxies D127 and D128 to be shown.

with offset -0.013 ± 0.013. The scatter in the K-band measurements is as expected if both data sets have errors $\sim 0.^m025$. The scatter between the J magnitudes is disappointing, but is consistent with the larger uncertainty quoted by PFA. In both bands there is no significant offset.

Further confidence in the homogeneity of the infrared photometry is given by the work of Peletier et al. (1990) as they have performed an independent check on the calibration of a few of the Virgo galaxies using the UKIRT telescope. The zero-points they derive for their aperture photometry from Elias et al. (1982) standard stars and from the measurements of PFA agree to 0.006 ± 0.009 (J-band, n=7) and 0.001 ± 0.012 (K-band, n=7). We therefore directly adopt PFA's J- and K-band photometry of galaxies in the Virgo cluster.

To complete our comparison with the aperture photometry presented in PFA, we compare our V-band measurements of samples of galaxies in the two clusters. The comparison is listed in Tables 4.11 and 4.12, and shown graphically in Figures 4.11 and 4.12. In the Virgo cluster, we find (rejecting the two discrepant galaxies N4478, which is contaminated by a bright star, and N4636, which has an unusually extended halo for its magnitude) $\sigma = 0.035$ with an offset of -0.011 ± 0.008 (n=20). For Coma, (n=18) $\sigma = 0.025$ with offset $+0.020 \pm 0.006$. While the scatter between the measurements is encouragingly small, it is clear that there is a significant offset (of $0.^m03$) between the zero-points of the photometry in the two clusters. We note that the offset is in such a sense as to make PFA's V-K colours of galaxies in the Virgo cluster appear redder than their counterparts in Coma.

4.4.3 Tables of U, V, J and K Magnitudes

Tables 4.14 and 4.15 present U and V magnitudes at 13″, and V, J, K magnitudes at 17″ for galaxies in the the Coma cluster. The values have been corrected for contaminating stars and companion galaxies, beam profile effects and intra-cluster light. We chose to determine U-band colours at a smaller aperture since the accuracy of these magnitudes is limited by the statistical fluctuations in the background. At 13″, most galaxies can be accurately

Table 4.11

Comparison with V-band Photometry of Virgo Adopted by PFA

Galaxy	Ap. Dia.	V_{PFA}	V_{CCD}	$\Delta V_{CCD-PFA}$
N4124	56″	12.37	12.35	−.02
N4179	53″	11.59	–	
N4270	29″	12.93	–	
N4365	29″	11.54	11.50	−.04
N4371	29″	12.13	12.07	−.06
N4374	56″	10.50	10.47	−.03
N4377	29″	12.43	12.43*	.00
N4382	29″	11.11	11.14	.03
N4387	29″	12.75	12.80	.05
N4406	56″	10.74	10.73	−.01
N4435	27″	11.86	11.80	−.06
N4442	29″	11.46	11.46	.00
N4458	29″	13.08	13.06	−.02
N4459	29″	11.70	–	
N4468	34″	13.81	13.77*	−.04
N4472	56″	10.10	10.13	.03
N4473	29″	11.42	11.39	−.03
N4476	34″	12.97	12.92	−.05
N4478	27″	12.24	12.11*	−.13
N4479	34″	13.50	–	
N4486	56″	10.38	10.35	−.03
N4550	29″	12.35	12.37	.02
N4552	56″	10.79	10.79	.00
N4578	29″	12.63	–	
N4621	29″	11.37	11.36	−.01
N4636	29″	11.88	11.64	−.24
N4660	29″	11.78	11.84	.06
N4754	29″	–		

Note: * indicates that a bright stars has been patched out within this aperture.

Table 4.12

Comparison with V-band Photometry of Coma Adopted by PFA

Galaxy	Ap. Dia.	V_{PFA}	V_{CCD}	$\Delta V_{CCD-PFA}$
D78	14.9″	14.51	14.50	−.01
D97	14.9″	14.55	–	
D118	14.9″	14.90	14.89	−.01
D126	14.9″	15.94	15.96	.02
D127	14.9″	16.13	16.16	.03
D128	14.9″	15.82	15.86	.04
D129	14.9″	14.04	14.10	.06
D144	14.9″	14.83	14.87	.04
D148	14.9″	13.42	13.46	.04
D150	14.9″	15.46	15.47	.01
D151	14.9″	14.81	14.81	.00
D152	14.9″	15.26	15.30	.04
D153	14.9″	15.56	15.58	.02
D154	14.9″	16.18	16.24	.06
D170	14.9″	15.27	15.26	−.01
D172	14.9″	15.25	15.25	.00
D174	14.9″	15.13	15.12	−.01
D175	14.9″	14.87	14.91	.04
D217	14.9″	14.53	14.53	.00

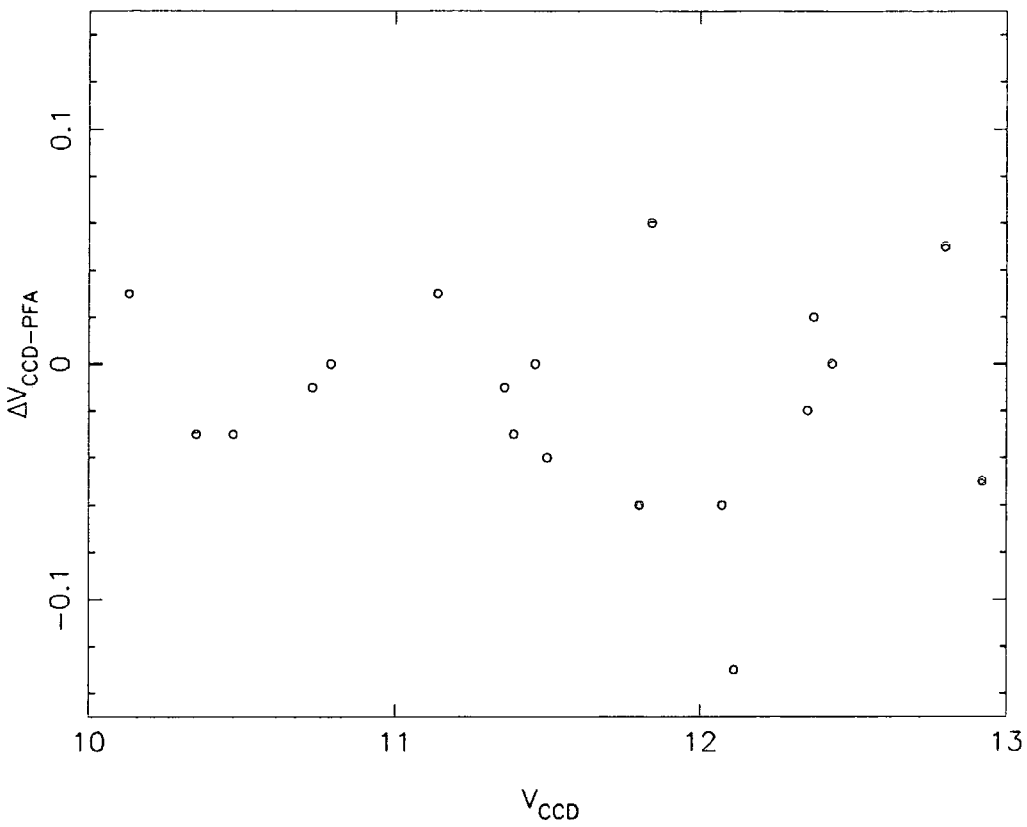

Figure 4.11. A comparison of our CCD V-band photometry of galaxies in the Virgo cluster with that adopted by PFA (from SV). The scale of the figure prevents the discrepant galaxy N4660 from being shown.

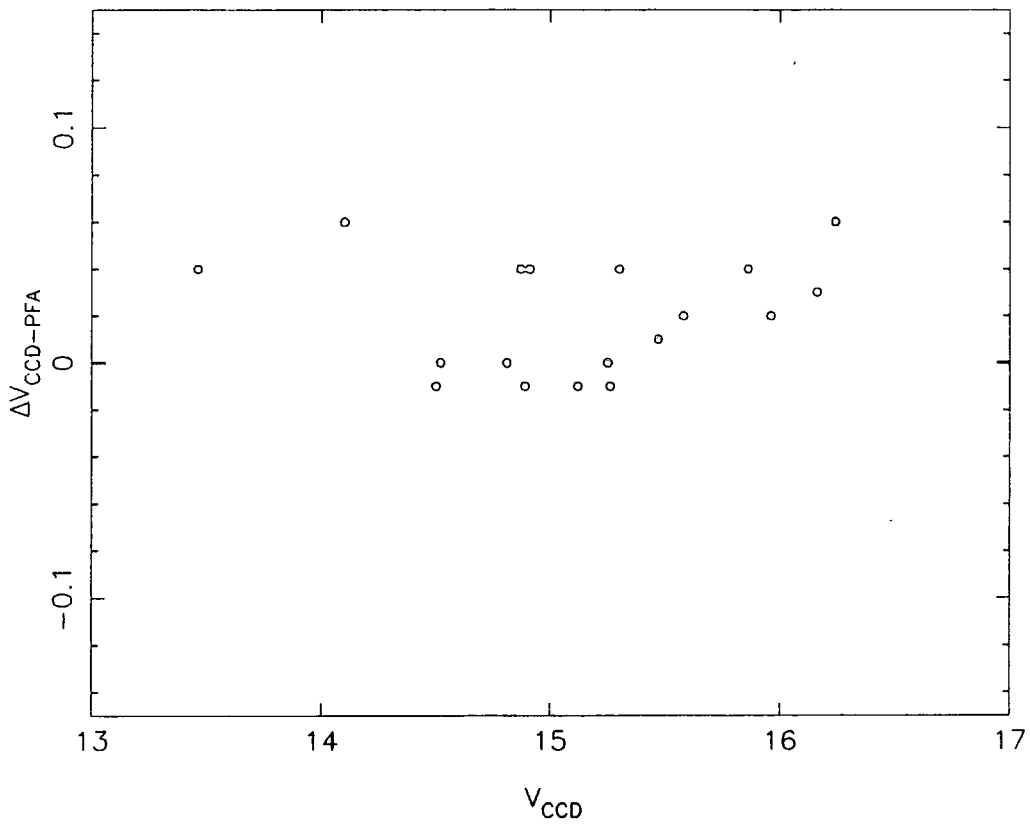

Figure 4.12. A graphical representation of the comparison between our V-band CCD photometry of galaxies in the Coma cluster and that adopted by PFA (from SV and S72).

Table 4.13

Summary of Comparison with Photometry Presented by APF

Cluster	Filter	Number of Points	RMS Scatter	Zero-point Offset	Comments
Virgo	V	20	.035	$-.011 \pm .008$	N4478, N4636 excluded
Coma	V	18	.025	$.025 \pm .006$	
	J	13	.048	$-.013 \pm .013$	D127, D170 excluded
	K	13	.032	$-.005 \pm .009$	D127, D128, D170 excluded

Table 4.14

Optical Photometry Adopted in the Coma Cluster

Galaxy	$U_{CCD}(13'')$	$V_{CCD}(13'')$
D68	16.84	15.41
D69	16.39	14.86
D70	16.75	15.32
D71	17.60:	16.41
D87	17.40:	16.16
D103	16.31	14.83
D104	16.67	15.20
D106	17.08	15.71
D107	17.11	15.86
D116	16.88	15.63
D117	17.30:	15.91
D118	16.44	14.98
D119	17.10	15.73
D120	15.85	–
D122	16.82	15.55
D124	16.46	14.98
D125	17.10	15.72
D126	17.32	16.03
D127	17.65	16.23
D128	17.23	15.94
D129	15.82	14.26
D130	16.33	14.88
D131	16.49	15.01
D132	17.43	16.09
D133	16.32	14.89
D134	17.73:	16.40
D135	17.57:	16.27
D136	17.10	15.73
D143	16.27	14.72
D144	16.37	14.93
D145	16.91	15.50
D147	17.22:	15.88
D148	15.23	13.58
D150	16.92	15.55
D151	16.28	14.91
D152	16.86	15.39
D153	17.08	15.64
D154	17.68	16.35
D155	16.44	15.02
D156	17.51	16.25
D157	17.18	15.82
D158	17.85:	–
D160	16.65	15.16

Table 4.14 (cont.)

Optical Photometry Adopted in the Coma Cluster

Galaxy	$U_{CCD}(13'')$	$V_{CCD}(13'')$
D167	16.09	14.64
D168	16.14	14.64
D170	16.75	15.35
D171	17.30:	15.90
D172	16.69	15.32
D173	17.03	15.64
D174	16.61	15.16
D175	16.48	14.98
D191	17.26	15.90
D194	15.97	14.41
D195	15.99	15.66:
D196	17.25:	15.84
D206	15.75	14.29:
D207	16.92	15.49
D217	16.14	14.62

Table 4.15

Near-Infrared Photometry Adopted in the Coma Cluster

Galaxy	$J_{UKIRT}(17'')$	$K_{UKIRT}(17'')$	$V_{CCD}(17'')$
D10	13.52	12.62	16.54
D31	11.54	10.57	13.96
D49	11.56	10.57	13.96
D67	13.25	12.32	15.58
D69	12.32	11.36	14.73
D70	12.94	12.00	15.21
D78	12.11	11.16	14.42
D79	12.12	11.16	14.49
D81	13.43	12.53	15.59
D84	13.09	12.13	15.40
D87	13.94	13.02	16.07
D91	12.26	11.31	14.61
D95	12.53	11.55	14.82
D96	12.82	11.83	15.16
D97	11.99	11.03	–
D107	13.60	12.68	15.72
D110	13.51	12.58	15.07
D118	12.48	11.54	14.81
D121	–	–	–
D124	12.53	11.58	14.84
D125	13.43	12.51	15.65
D126	–	–	–
D127	13.76	12.82	16.06
D128	13.53	12.57	15.78
D129	11.57	10.56	13.96
D130	12.42	11.44	14.75
D133	12.45	11.48	14.79
D136	13.41	12.48	15.69
D143	12.08	11.12	14.49
D144	12.38	11.41	14.79
D148	10.84	9.85	13.33
D150	13.16	12.23	15.41
D151	12.47	11.55	14.70
D152	12.84	11.87	15.21
D153	13.22	12.27	15.52
D154	–	–	–
D159	–	–	–
D164	11.67	10.74	13.92
D165	13.40	12.46	–
D168	12.12	11.13	14.51

Table 4.15 (cont.)

Near-Infrared Photometry Adopted in the Coma Cluster

Galaxy	$J_{UKIRT}(17'')$	$K_{UKIRT}(17'')$	$V_{CCD}(17'')$
D170	13.07	12.05	15.18
D172	12.92	11.91	15.21
D174	12.71	11.72	15.09
D175	12.46	11.49	14.83
D184	14.21	13.33	16.45
D193	13.35	12.43	15.65
D194	11.81	10.82	14.24
D207	13.05	12.11	15.39
D217	12.07	11.12	14.44
D225	14.28	13.38	–
D240	11.52	10.56	13.88
D242	13.27	12.31	–
D245	13.09	12.14	15.31
RB74	14.09	13.28	–

Note: Magnitudes are not quoted for galaxies contaminated by bright stars.

photometered. In the few cases where the statistical uncertainty is greater than $0.^m03$, we have cautioned the value quoted in the table unless the measurement has been repeated three or more times. We chose not to use an even smaller aperture as seeing effects would then have become important.

Tables 4.16 and 4.17 present similar data for the Virgo cluster. We present U-V colours at 60″ (following Michard 1982), or, if background uncertainties make the U-band measurements less reliable, at the nearest dependable aperture. J, K magnitudes were taken from PFA at apertures near 60″. We combine this photometry with our CCD measurements to get new V-K colours at these apertures. These values have also been fully corrected for instrumental effects.

4.5 Galaxy Colours Corrected for Redshift and Reddenning

4.5.1 K-corrections

The Virgo and Coma clusters have mean redshifts of 0.003 and 0.023 respectively. We must therefore apply K-corrections to our data to allow for the differing effective bandpasses and central wavelengths of the filters in the rest-frames of the two clusters. As these corrections amount (in some bands) to a substantial fraction of the intrinsic colour differences found by PFA, we carefully re-examine the values adopted by these authors. In addition, the blue cutoff of the spectral response of the RCA CCD makes our effective U-band substantially narrower than the standard Johnson definition of the band. The K-correction in this band may therefore differ from the term conventionally adopted. Finally, the revised study of the K-corrections allows us to estimate their uncertainty by varying the spectral response of the filter and the spectral energy distribution (SED) of the template galaxy.

Numerical values for each of the K-corrections were determined by convolving a variety of galaxy SEDs (at an appropriate redshift) with the combined spectral response of the relevant

Table 4.16

Optical Photometry Adopted in the Virgo Cluster

Galaxy	Ap. Dia.	U_{CCD}	V_{CCD}
N3640	60″	12.61	11.20
N3962	60″	12.96	11.48
N4124	60″	13.34	12.28
N4339	60″	13.48	12.11
N4365	60″	12.41	10.88
N4371	60″	13.01	11.50
N4374	60″	11.99	10.42
N4377	60″	13.33	12.00
N4382	60″	11.87	10.50
N4387	50″	13.90	12.50
N4406	60″	12.21	10.66
N4435	50″	12.82	11.40
N4442	60″	12.48	10.99
N4458	60″	13.88	12.55
N4464	60″	14.02	12.71
N4468	50″	14.65	13.48
N4472	60″	11.68	10.06
N4473	60″	12.44	10.94
N4476	60″	13.67	12.64
N4486	60″	11.87	10.29
N4550	60″	13.24	11.95
N4551	40″	13.98	12.51
N4552	60″	12.32	10.74
N4621	60″	12.31	10.78
N4636	60″	12.46	10.93
N4660	60″	12.90	11.51
N4697	60″	11.97	10.55

Table 4.17

Near-Infrared Photometry Adopted in the Virgo Cluster

Galaxy	Ap. Dia.	J_{PFA}	K_{PFA}	V_{CCD}
N4124	56″	10.17	9.35	12.35
N4179	53″	9.14	8.24	–
N4264	56″	10.81	9.98	–
N4270	56″	10.20	9.30	–
N4365	56″	8.52	7.59	10.93
N4371	56″	9.21	8.32	11.55
N4374	56″	8.06	7.14	10.47
N4377	56″	9.72	8.89	12.04
N4382	56″	8.29	7.44	10.56
N4387	66″	10.08	9.28	12.40
N4406	56″	8.32	7.45	10.73
N4435	53″	8.75	7.75	11.36
N4442	56″	8.65	7.76	11.03
N4458	56″	10.35	9.63	12.59
N4459	56″	8.79	7.84	–
N4468	66″	–	10.33	13.32
N4472	56″	7.67	6.76	10.13
N4473	56″	8.61	7.74	10.99
N4476	66″	10.45	9.63	12.60
N4478	53″	9.35	8.51	11.70
N4479	66″	10.68	9.88	–
N4486	56″	7.90	6.95	10.35
N4550	56″	9.71	8.85	11.98
N4552	56″	8.35	7.42	10.79
N4578	56″	9.86	9.01	–
N4621	56″	8.50	7.57	10.83
N4636	56″	8.67	7.74	11.00
N4660	56″	9.20	8.34	11.53
N4754	56″	8.92	8.06	–

Note: * indicates that a bright star has been patched out within this aperture.

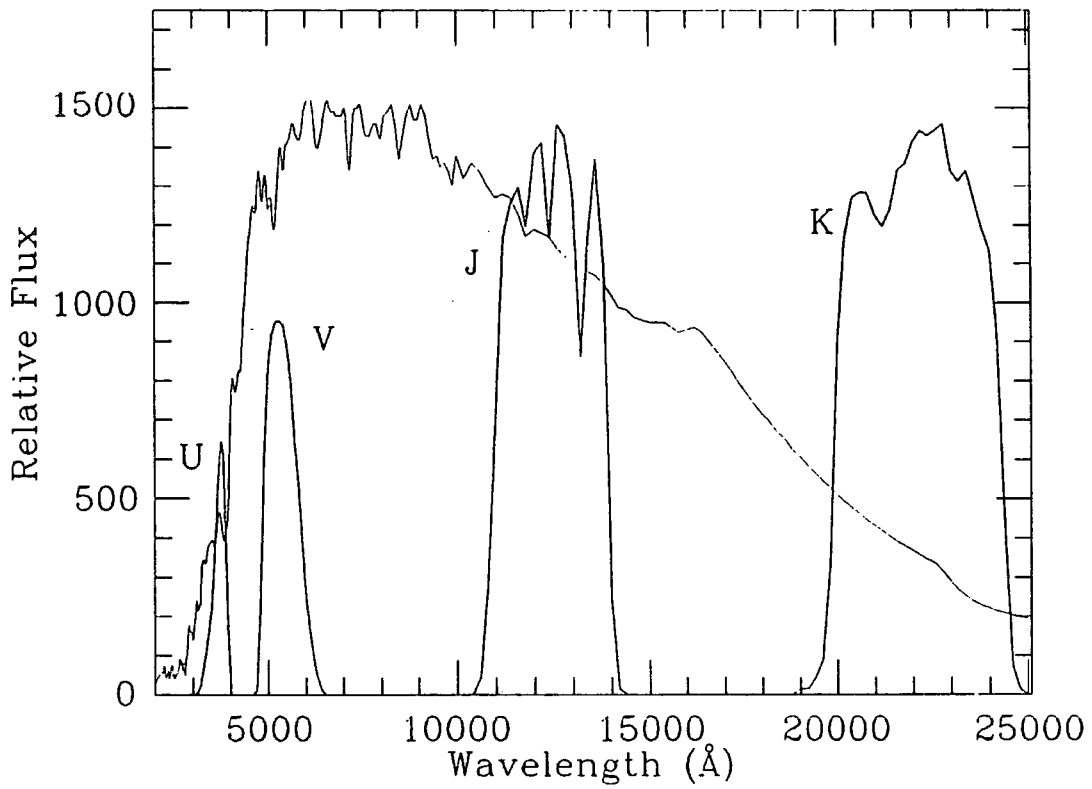

Figure 4.13. The inferred spectral energy distribution (SED) of a typical early-type galaxy from the near-ultraviolet to the near-infrared. The curve has been formed by appending the infrared SED of the K-giant star α Tau to the mean observed optical SED of several nearby elliptical galaxies. The heavier lines show the spectral response curves of the U, V, J and K filters used in this project.

filter and detector. A wide choice of template early-type galaxy SEDs were available to define the U- and V-band K-corrections (cf., Bruzual, 1984). These ranged from a composite SED made by combining several observations of elliptical galaxies to the uv-strong elliptical NGC 4649 and the budge of M31. Response curves for the filters and the RCA CCD were obtained from the RGO (cf., RGO CCD User's Guide, Wall et al., 1989). The correct working of the method was first checked using the standard U and V filter response curves. The K-corrections derived were in good agreement with those quoted by PFA. The filter response was then convolved with that of the CCD, and the procedure repeated. For the mean elliptical SED we found: in Virgo ($z = 0.003$) K(V) = 0.005, $K(U-V) = 0.002$; at Coma ($z = 0.023$) K(V) = 0.041, $K(U-V) = 0.003$. The K-correction we derive in the RCA CCD U-band is much smaller than the standard value ($K(U-V) = 0.026$ at $z = 0.023$). Figure 4.13 shows the elliptical galaxy SED and the effective response curves of each photometric band. Our effective U filter is peaked at the redward end of a plateau in the ultraviolet fall-off of the SED. The effect of redshifting the spectrum should therefore be similar in both the U- and V-bands — as we have found. Initially, we were concerned that this correction would be strongly dependant on galaxy colour, but experiment with the other energy distributions available to us, and with synthetic SEDs made by coadding spectra of young and old star clusters in variable ratios, showed that this is not the case — for all SEDs with colours resembling those of elliptical galaxies we find $K(U-V) < 0.^m01$. We have also experimented with the effects of atmospheric absorption on the effective 'filter' response curve, but find that this does not significantly alter the numerical values found. We therefore adopt $K(V) = 1.8z$ and $K(U-V) = 0.00$ in the rest of this work, the uncertainty being less than $0.^m01$ in both cases.

In the infrared, there is only one suitable spectral energy distribution available for the calculation of K-corrections for early-type galaxies — that of the K3 giant star α Tau, obtained in a balloon-borne observation by Woolf et al. (1964). As evolutionary population synthesis models suggest that such stars dominate the infrared light of older galaxies, we expect that the K-corrections determined from this SED will closely approximate the true

value. Using the UKIRT filter response curves (UKIRT Observer's Manual, UK Infrared Telescope Support Unit, 1988), we find (at $z = 0.023$): $K(K) = -0.080$, $K(J) = +0.003$. These figures are not significantly altered if the response curves of the standard Johnson filters are used instead. We note that while the K-band is in good agreement with the value of $3.3z$ published by FPAM, the correction in J is an order of magnitude smaller than the value of $0.7z$ that they quote. We do not understand the cause of this discrepancy.

4.5.2 Galactic reddenning

Because both the Coma and Virgo clusters have high galactic latitude ($b^{II} > 60\,\mathrm{deg}$), they can be expected to have very similar low reddenning. In the absorption-free polar cap model of Sandage (1973), the reddenning is exactly zero. PFA therefore applied no extinction corrections to their published colours. More recent reddenning estimates based on galaxy counts and HI gas column densities (Burstein & Heiles, 1984, BH) suggest that, while the mean absorption is similar for the two clusters, there is considerable scatter in the absorptions to individual Virgo galaxies because of the large angular size of the cluster. If correct, this could cause additional scatter and possible subtle systematic effects in the colour–magnitude (C–M) relation. We have therefore chosen to investigate this effect more thoroughly by comparing the deviation of a galaxy from the average C–M relation (Figures 4.14 and 4.15) with BH's estimate of the galactic extinction in its direction. The correlation is shown in Figures 4.16 and 4.17. If the BH reddenning are correct, we should expect to find a correlation of slope 1.0 (note that the absorbtion has only a very weak effect on the V_{26} axis of the C–M diagram). Such a correlation is absent from both the U-V and V-K colours. To reinforce this conclusion, in Figures 4.18 and 4.19 we plot the C–M relations after applying the BH reddenning corrections. It is evident that the colour–magnitude correlation is not as tight as that obtained previously. We conclude that the extinction estimates given by BH should not be applied on a galaxy-by-galaxy basis, and therefore apply the same extinction correction to all galaxies in both clusters (this is in agreement with the *mean* extinction

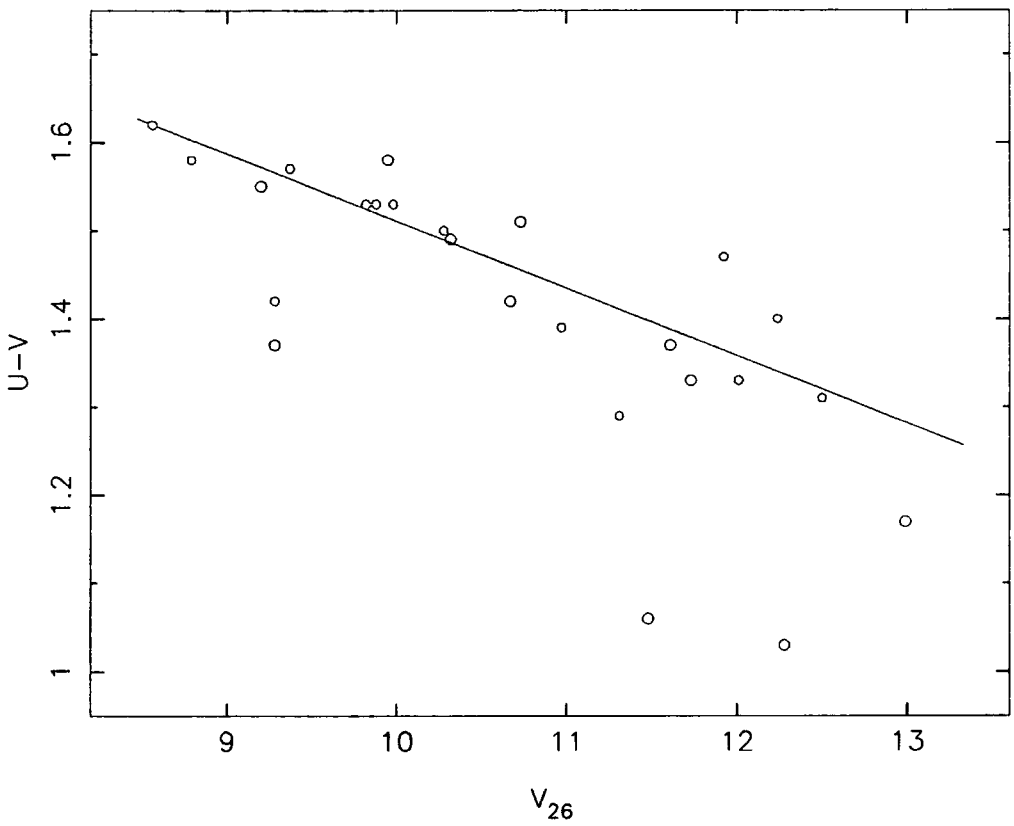

Figure 4.14. The U-V colour–magnitude relation for early-type galaxies in the Virgo cluster. Elliptical galaxies are identified as solid points, S0's as open points. The solid line shows the least-squares fit to the relation defined by the ridge-line points (U-V = 2.274 − 0.0763 V_{26}). Values for V_{26} are taken from SV. The U-V colours are formed from the CCD photometry presented in this work. No correction for galactic reddenning has been applied.

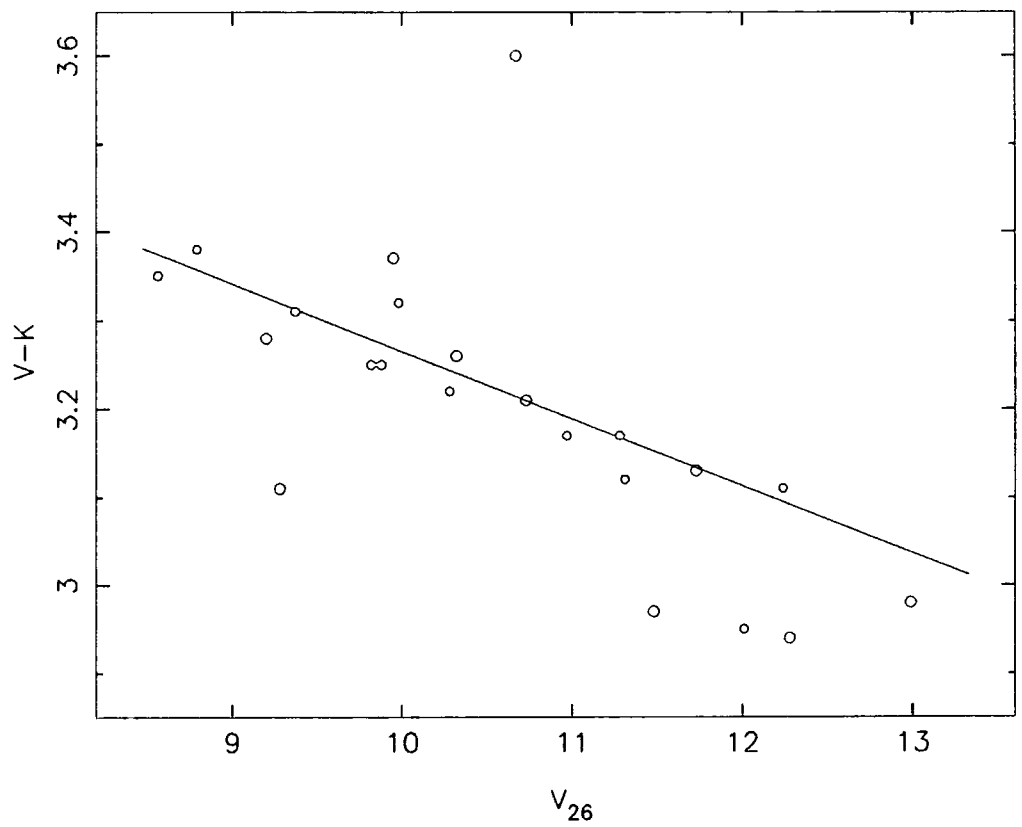

Figure 4.15. As for Figure 4.14, but showing the V-K colour–magnitude relation. The best-fit relation defined by the ridge-line points is $V\text{-}K = 4.025 - 0.0760\, V_{26}$.

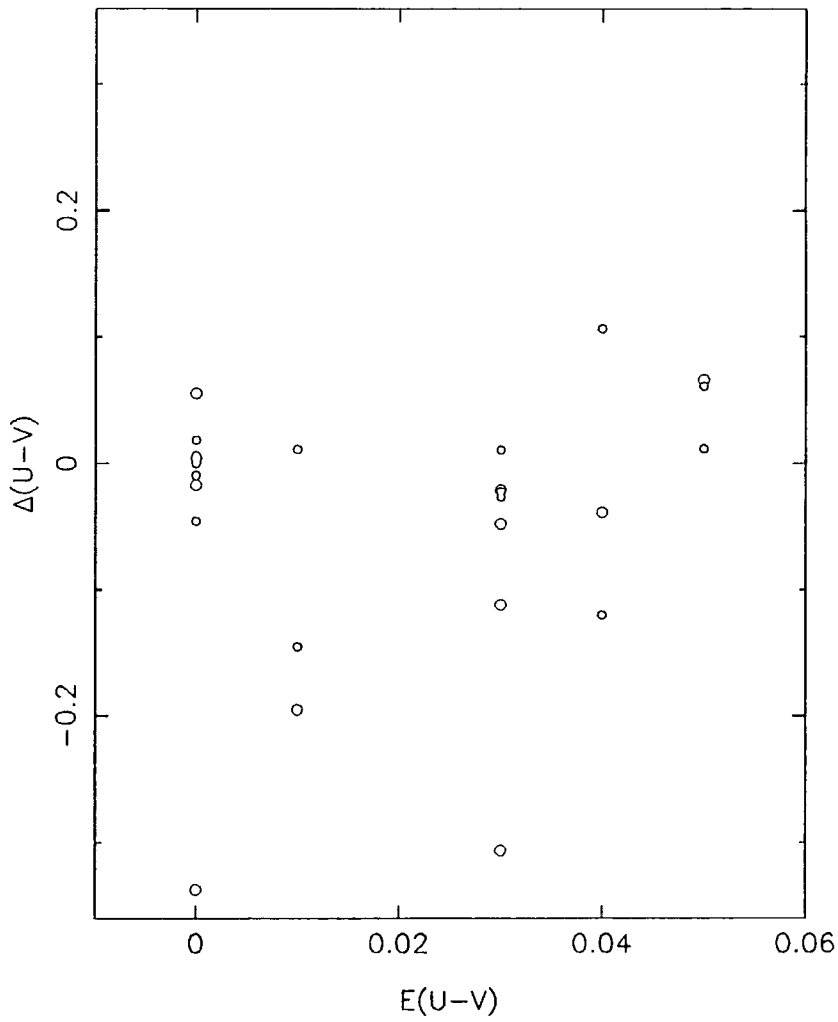

Figure 4.16. The departure of a galaxy from the average colour–magnitude relation defined in Figure 4.14 plotted as a function of the galactic U-V extinction estimated by BH. There is no evidence to suggest that the extinction estimate is correct. Filled and closed symbols distinguish E and S0 galaxies.

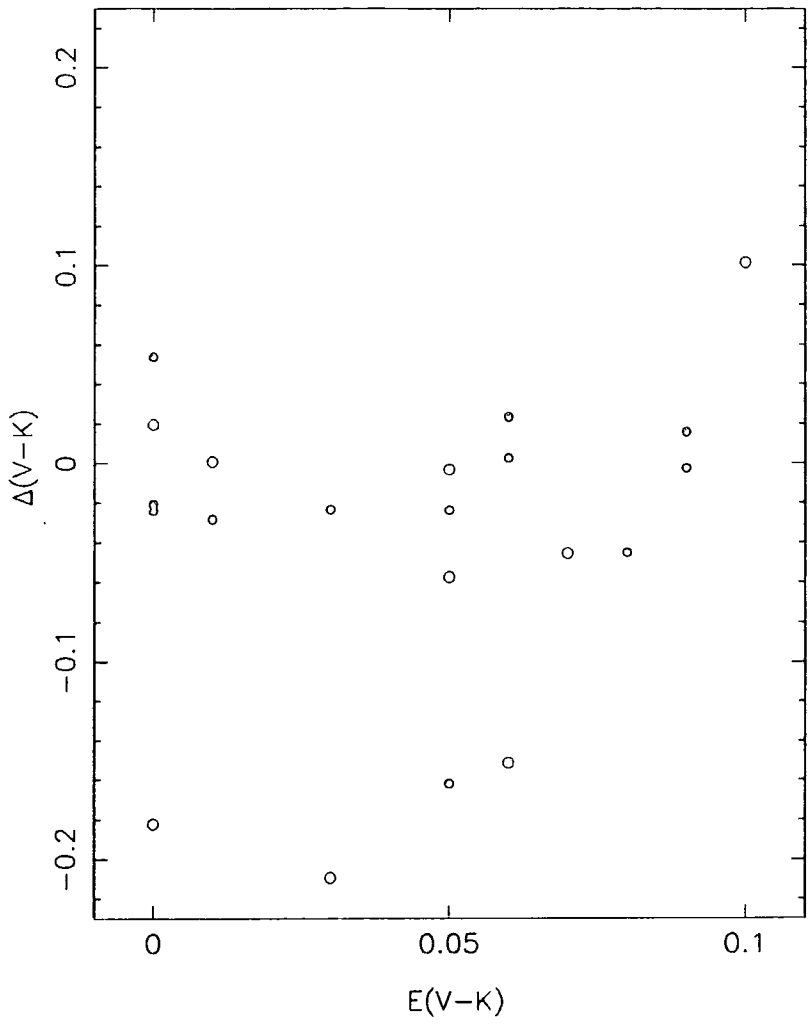

Figure 4.17. The departure of a galaxy from the V-K colour-magnitude relation as a function of the galactic V-K extinction estimate of BH. The scale of this figure does not allow the unusually red galaxy N4435 to be shown.

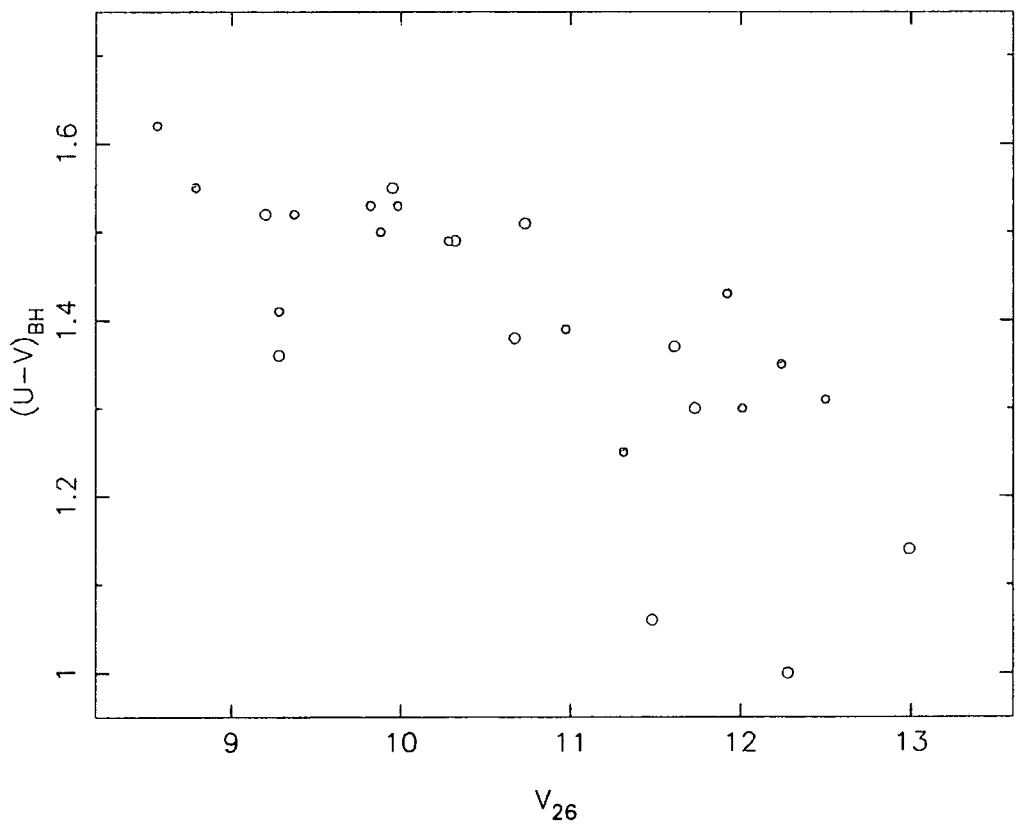

Figure 4.18. As for Figure 4.14, but using U-V colours corrected for galactic extinction according to the extinction estimates of BH. Comparison with the original figure shows that the scatter has been somewhat increased.

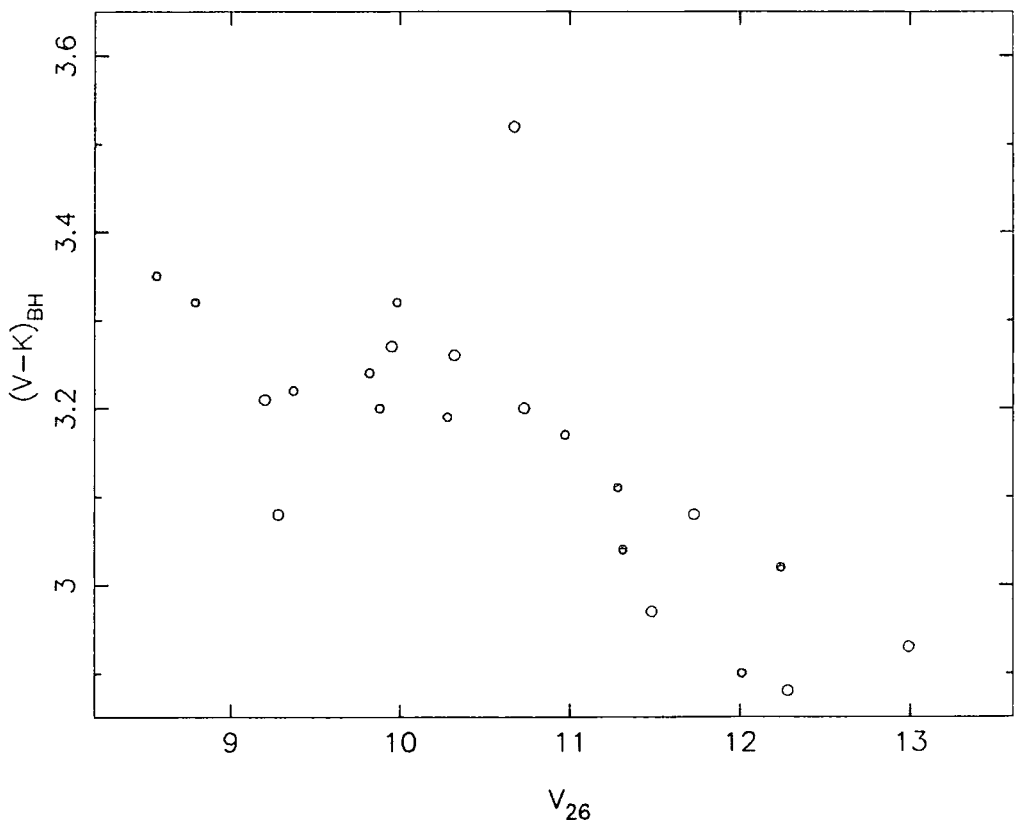

Figure 4.19. As for Figure 4.15, but using V-K colours corrected for galactic extinction according to the extinction estimates of BH. Comparison with the original figure shows that the scatter has been somewhat increased.

estimates of BH). For convenience we take this correction to be zero (corresponding to an absorbtion-free model of the polar cap).

4.6 Tables of U-V and V-K Colours

In tables 4.18 and 4.19, we present homogeneous U-V and V-K colours for galaxies in the Virgo and Coma clusters. The colours have been corrected for redshift using the K-corrections discussed in Section 4.5.1. In the Virgo cluster, the very small correction has been varied depending on the redshift of the individual galaxy (taken from Binggeli et al., 1985). As discussed in Section 4.5.2, no correction is required for galactic extinction in either of the clusters. Morphological types are taken from Binggeli et al., 1985, and de Vaucouleurs et al., 1976, (for the Virgo cluster), and from Dressler, 1980, (for the Coma cluster). Values for the isophotal magnitude are taken from SV and from Godwin and Peach, 1977, using the transformation described in Dressler, 1984 (further details are given in Section 4.7.1).

We have chosen not to present J-K colours in these tables for two reasons. Firstly, we cannot reproduce the large J-band K-correction proposed by FPAM. Secondly, the scatter between our J-band photometry of the Coma cluster and that of PFA is surprisingly large. For both these reasons, it is therefore difficult to ensure that the J-K colours of the two clusters are on a consistent absolute system. Since the slope of the J-K colour–magnitude relation is extremely shallow, this colour cannot be usefully applied to compare the clusters. We will therefore make no further use of the J-band photometry in the remainder of this chapter.

Table 4.18

Summary of Reduced Galaxy Parameters in the Virgo Cluster

Galaxy	Morph.	z	V_{26}	$(U-V)^{KE}$	$(V-K)^{KE}$	$\log\sigma$
N4124	$S0_3(6)$:	.0055	11.48	1.06	2.97	–
N4339	$S0_{1/2}(0)$	.0043	11.61	1.37	–	–
N4365	E3	.0039	9.98	1.53	3.32	2.412
N4371	$SB0_2(r)(3)$	.0031	10.73	1.51	3.21	2.104
N4374	E1	.0032	9.37	1.57	3.31	2.480
N4377	$S0_1(3)$	.0044	11.73	1.33	3.13	2.134
N4382	$S0_1(3)$pec	.0026	9.28	1.37	3.11	2.301
N4387	E5	.0017	12.24	1.40	3.11	2.059
N4406	$S0_1(3)/E5$	−.0010	9.20	1.55	3.28	2.355:
N4435	$SB0_1(6)$	.0029	10.67	1.42	3.60	2.233
N4442	$SB0_1(6)$	.0019	10.32	1.49	3.26	2.336
N4458	E1	.0013	12.01	1.33	2.95	1.949
N4464	E3	.0037	12.50:	1.31	–	2.079
N4468	S0/a	.0029	12.99	1.17	2.98	–
N4472	$E2/S0_1(2)$	.0032	8.56	1.62	3.35	2.474
N4473	E5	.0075	10.28	1.50	3.22	2.268
N4476	$S0_3(5)$	.0066	12.28	1.03	2.94	–
N4478	E2	.0049	11.28	–	3.17	2.170
N4486	E0	.0042	8.79	1.58	3.38	2.528
N4550	$E7/S0_1(7)$	.0012	11.31	1.29	3.12	–
N4551	E2	.0040	11.92	1.47	–	2.021
N4552	$S0_1(0)$	.0009	9.95	1.58	3.37	2.391
N4621	E4	.0014	9.88	1.53	3.25	2.338
N4636	$E1/S0_1(1)$	.0029	9.82	1.53	3.25	2.303
N4660	$E3/S0_1(3)$	.0034	10.97	1.39	3.17	2.262:
N4697	E6 :	.0049	9.28	1.42	–	2.276

Note: Colours shown are at a nominal aperture of 60″. The actual aperture diameters are given in tables 4.16 and 4.17. * indicates that the morphological type of this galaxy is not given in Binggeli et al., 1985.

Table 4.19

Summary of Reduced Galaxy Parameters in the Coma Cluster

Galaxy	Morph.	V_{26}	$(U-V)^{KE}$	$(V-K)^{KE}$	$\log \sigma$
D10	E	16.17	–	3.80	–
D31	E/S0	12.60*	–	3.27	2.449
D49	E	13.12*	–	3.27	2.394
D67	S0	13.12	–	3.14	2.169
D68	S0	14.73	1.43	–	2.111
D69	E	14.23	1.53	3.25	2.285
D70	E	14.86*	1.43	3.09	2.166
D78	E	13.77	–	3.14	–
D79	S0	13.91	–	3.21	–
D81	E	15.15	–	2.94	–
D84	S0	15.01	–	3.15	–
D87	E	15.88	–	2.93	1.863
D91	S0	14.22	–	3.18	–
D95	S0	–	–	3.15	–
D96	E	14.54	–	3.21	–
D103	S0/a	14.39	1.48	–	2.319
D104	S0	14.85*	1.47	–	2.260
D106	S0	–	1.37	–	2.201
D107	E	15.45	1.25	2.92	1.761
D110	S0/E	15.41	–	2.37	–
D116	SB0	15.06*	1.25	–	2.114
D118	E	14.36*	1.46	3.15	2.209
D119	S0	15.28	1.37	–	2.186
D122	S0	15.13	1.27	–	1.957
D124	E	14.53	1.48	3.14	2.243
D125	E	15.60	1.38	3.02	2.169
D126	S0	15.88	1.29	–	–
D127	S0	15.94*	1.42	3.12	–
D128	S0	15.61*	1.29	3.09	2.019
D129	D	12.27*	1.56	3.28	2.383
D130	E/S0	14.36*	1.45	3.19	2.311
D131	S0	14.25*	1.48	–	2.225
D132	S0	15.87*	1.34	–	2.104
D133	E	14.50*	1.43	3.19	2.339
D136	E	15.52*	1.37	3.09	2.251
D143	E	13.46	1.55	3.25	2.361
D144	S0/a	14.28*	1.44	3.26	2.210
D145	S0	14.82	1.41	–	2.124
D148	D	11.85*	1.65	3.36	2.584
D150	E	15.31	1.37	3.06	2.007

Table 4.19 (cont.)

Summary of Reduced Galaxy Parameters in the Coma Cluster

Galaxy	Morph.	V_{26}	$(U-V)^{KE}$	$(V-K)^{KE}$	$\log \sigma$
D151	E	13.98	1.37	3.03	2.180
D152	SB0	14.85	1.47	3.22	2.192
D153	E	15.28	1.44	3.13	2.099
D154	S0	15.80	1.33	–	–
D155	S0	13.98	1.42	–	2.175
D156	E/S0	15.83*	1.26	–	–
D157	S0	15.87*	1.36	–	2.100
D160	SB0	14.50	1.49	–	2.258
D164	S0	–	–	3.06	–
D167	S0/E	–	1.45	–	2.307
D168	E	14.11	1.50	3.26	2.320
D170	SB0	14.67	1.40	3.01	2.146
D172	E	14.87	1.37	3.18	2.191
D173	S0	15.09	1.39	–	2.138
D174	E	14.82	1.45	3.25	2.247
D175	S0	14.34	1.50	3.22	2.234
D184	S0	15.94	–	3.00	–
D191	S0	15.60	1.36	–	1.947
D193	E	15.37	–	3.10	2.059
D194	E	13.49	1.56	3.30	2.394
D207	E	15.00*	1.43	3.16	2.154
D217	E	13.67	1.52	3.20	2.274
D240	E	12.88*	–	3.20	2.383
D245	S0	–	–	3.05	–

Note: U-V colours at aperture dia. of 13″; V-K colours at 17″. * indicates that this galaxy was merged in the photometery of GP.

4.7 The Colours of Galaxies in Virgo and Coma

4.7.1 Analysis of an improved data set

Following APF, we investigate the homogeneity of galaxies in the Virgo and Coma clusters through the correlation between U-V and V-K colours and total V-band magnitudes. For the Virgo cluster, isophotal V_{26} magnitudes are taken directly from SV. In Coma, we use V_{25} magnitudes published by Godwin and Peach (GP, 1977). D84 has established a transformation to the V_{26} system of SV from the galaxies covered by both authors. We use this to place both clusters on a consistent system. As GP publish only x, y positions for their galaxies, galaxies with colour information had to be identified by fitting a plate solution based on the NGC galaxies named by GP. The reader should note that the larger errors in these total magnitudes introduce little additional scatter into the colour–magnitude relationship because of its shallow slope.

It is conventional to now transform the aperture colours that we have presented in the previous tables to colours within a fixed fraction of the optical diameter of the galaxy. Since the strengths of colour gradients in individual galaxies are highly variable, we do not make this transformation. We prefer to compare the intrinsic properties that we have measured. It should be noted, however, that the slopes of the colour–magnitude relations presented here will differ from those based on relative aperture sizes. There remains, however, a small mismatch between the *physical* aperture sizes (which were chosen to ensure the accuracy of our work) used in the two clusters. A 60″ aperture in the Virgo cluster should be matched by an aperture of 11″ in Coma (assuming an infall velocity to Virgo of 250 $\mathrm{km\,s^{-1}}$). In principle, we should apply mean colour gradient corrections to our measured colours of $0.^m01$ in U-V (measured at 13″) and $0.^m02$ in V-K (measured at 17″) in order to obtain colours within the correctly matched aperture. As these corrections are so small, and may vary between

galaxies, we prefer not to apply them to our data directly, but rather to make allowance for this effect when comparing the average colours of the two clusters.

Figures 4.14, 4.15, 4.20 and 4.21 present the C–M relations in U-V and V-K for the Virgo and Coma clusters. Although a few points scatter to bluer magnitudes, there is a well defined ridge-line that can be used to make an accurate estimate of the distance modulus. (This asymmetry in the distribution is to be expected if there is a scatter in the ages of the individual galaxies.) The figures show lines fitted by the least squares technique to the 'well-behaved' points. We can immediately estimate the distance modulus to be $\Delta m = 3.79$ in U-V, and 3.43 in V-K (including a correction to the distance moduli of +0.10, in U-V, and +0.20, in V-K to allow for the aperture mismatch).

This technique is, however, too subjective to give reliable results. The outlying points are best dealt with by using the distribution-free median difference technique developed in D84. The method works as follows. From the C–M relations in both of the clusters, we chose a universal slope for the relationship. A (median) line is then fitted to each of the clusters so as to bisect the distribution of points. The separation of these lines gives the distance modulus. Experiment shows that the distance modulus that we determine is largely insensitive to the slope chosen for the relation. We determine confidence limits (errors) to the difference using the Wilcoxson Distribution-Free Rank Sum Test (cf., Rey, 1980). The distance moduli found are given in table 4.20. We present the results with and without the obviously outlying points being excluded to show the effectiveness of the method. The changes that arise from adopting the slopes determined from the individual clusters are less than the statistical errors.

We compare our values with the distance modulus of 3.75 ± 0.18 found by D84 from the correlation between V_{26} and $\log\sigma$ (the stellar velocity dispersion). This value is consistent with the offset between the colour–magnitude relations. in both bands. The disagreement between the values derived from the two colours is not of statistical significance (ie., it is

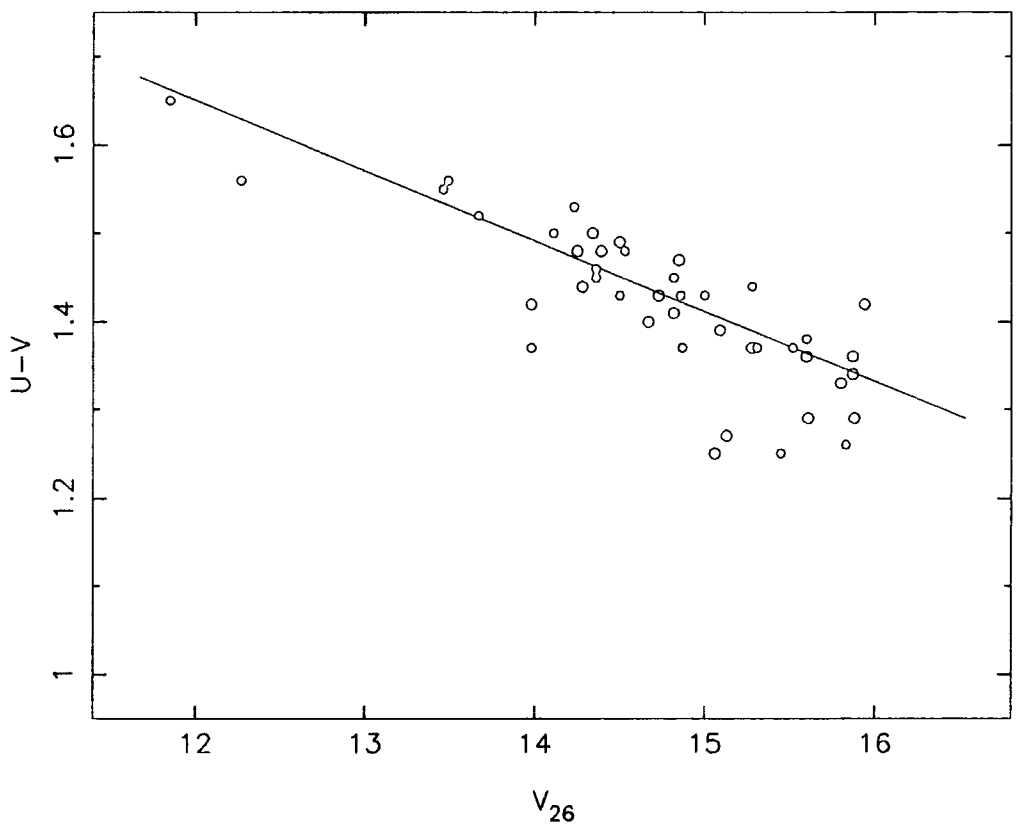

Figure 4.20. The U-V colour–magnitude relation in the Coma cluster. Solid and open symbols denote E and S0 galaxies respectively. The solid line shows the least-squared fit to the ridge-line points: $U\text{-}V = 2.607 - 0.0797\,V_{26}$. The colours have been measured within a 13″ aperture. This figure should be compared with Figure 4.14.

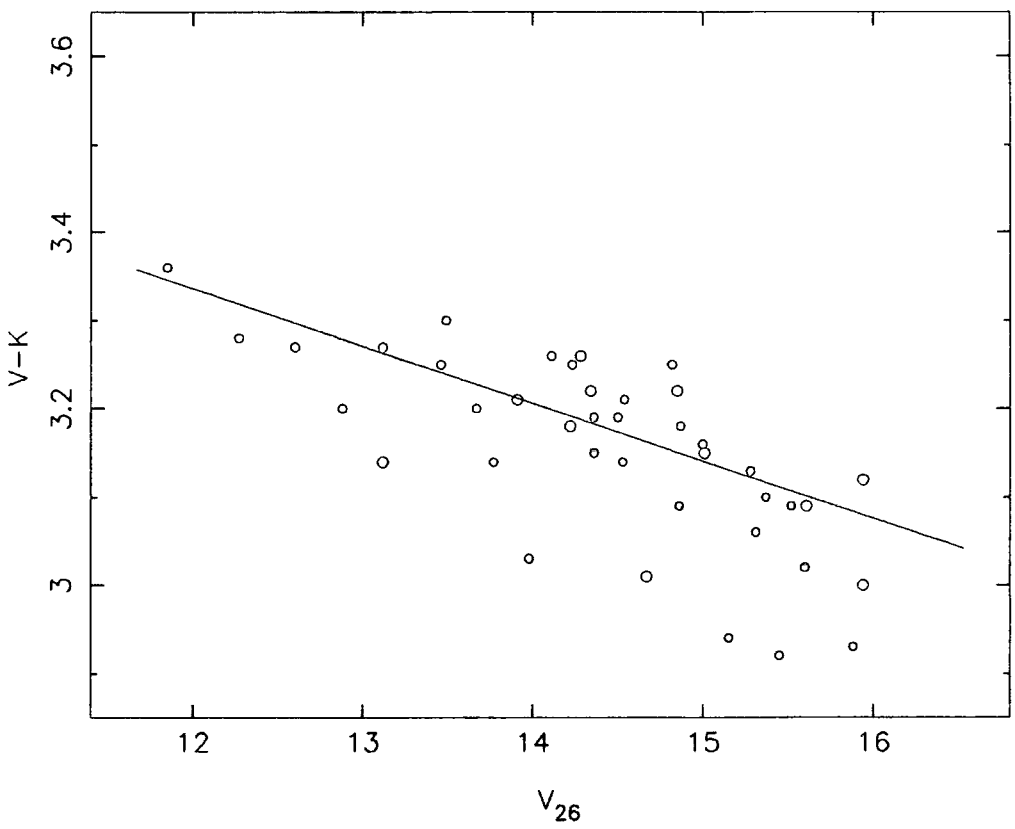

Figure 4.21. The V-K colour–magnitude diagram in the Coma cluster. Solid and open symbols denote E and S0 galaxies respectively. The solid line shows the least-squared fit to the ridge-line points: $V\text{-}K = 4.116 - 0.0650\,V_{26}$. The colours have been measured within a 17″ aperture. This figure should be compared with Figure 4.15.

Table 4.20

Estimates of the Virgo–Coma Distance Modulus

Colour	Slope	Distance Modulus	Comments
$U-V$	-0.078	4.10 ± 0.17	all points
$V-K$	-0.070	3.60 ± 0.23	all points
$U-V$	-0.078	4.03 ± 0.15	excluding outliers
$V-K$	-0.070	3.53 ± 0.20	excluding outliers

Notes: (1) We have defined the slope of the colour–magnitude relation as the change in colour per unit change in V_{26}. (2) Distance moduli include corrections of +0.10, in U-V, and +0.20, in V-K to allow for the aperture mismatch.

only a 1.6σ effect). There is therefore no cause to reject the hypothesis that the colours of early-type galaxies (of the same absolute magnitude) *are identical in both clusters.*

This conclusion can be verified by comparing the distance independent U-V and V-K colours directly. The colour–colour relations for the two clusters are shown in Figure 4.22. A small offset is apparent in the sense that Virgo galaxies are redder in V-K than their counter parts of similar U-V in Coma. The reader should note, however, that no correction for aperture missmatch has been made. In addition to the mean offset between the clusters, visual inspection of the figure suggests that there may be a small difference in the slope of the colour–colour relations. For several reasons, it is difficult to make a convincing case for the reality of this effect. Firstly, the visual impression comes largely from the three Virgo S0 galaxies having U-V colours bluer than $1.^m2$; no such blue galaxies were observed in the Coma cluster. If these galaxies are rejected, then the slope of the Virgo C–C relation is poorly determined. Secondly, it is difficult (and dangerous, since we perform the test *a posteriori*) to form a robust estimate of the slope in the relation and its uncertainty. Thirdly, even if the difference in slope were statistically significant, we would still have to be able to demonstrate that it was an effect intrinsic to the galaxies themselves, and not introduced by a colour term in the in the transformations between the photometric systems, or by a colour dependence of the K-corrections.

We apply the median difference technique to determine the average offset in V-K at a given U-V. We find (excluding the three very blue S0 galaxies):

$$\Delta(\text{V-K}) = 0.020 \pm 0.015$$

(including a correction of 0.01 to the V-K colour difference to allow for the aperture mismatch). We have used a common slope of 1.0, but slopes of 0.9 and 1.1 lie within the statistical error. The small offset is of no statistical significance, and is, in any case, small enough to have arisen from an error in the determination of the K-corrections, or from a residual reddenning difference between the two clusters. Indeed, considering the various sources of uncertainty, it would have been surprising if much better agreement had been

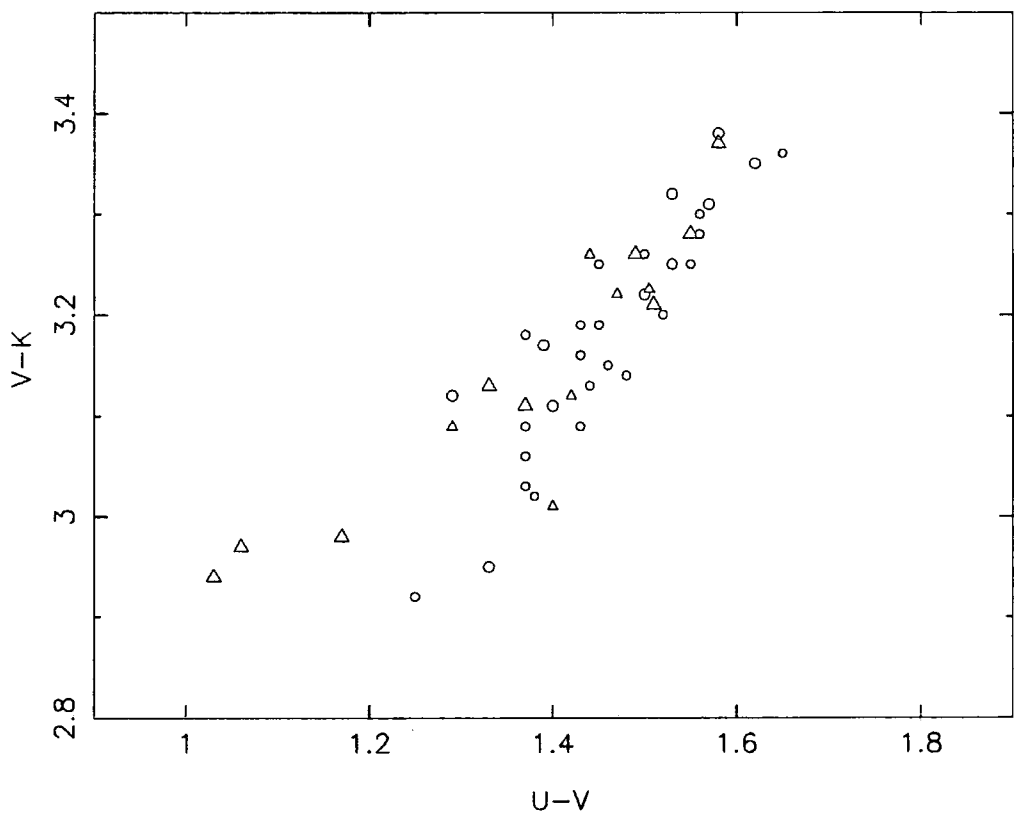

Figure 4.22. The U-V vs. V-K colour–colour relations in the Virgo and Coma clusters. Virgo galaxies are shown as open symbols, Coma galaxies as filled symbols. Circles and triangles distinguish E and S0 galaxies. The apparent differences in the zero-points and the slopes of the relations in the two clusters are discussed in the text of Section 4.7.1. The colours shown in this figure have *not* been corrected for aperture mismatch.

obtained. Therefore, our data provides *no support* for any intrinsic difference in the average colours of early-type galaxies in these very different environments.

4.7.2 Discussion of the outlying points and scatter in the C–M relation

It is evident that some galaxies (usually S0 types) are displaced significantly blueward of the relation obeyed by the majority of galaxies. These galaxies, where the data is available, tend to be discrepant in both colours suggesting that the effect is real and not due to an error in our photometry. In particular, we note that the three unusually blue Virgo galaxies NGC 4124, 4468 and 4476 are typed by Binggeli et al., (1985) as $S0_3$ (ie., dusty) or S0/a, and that although they are extremely blue in both U-V and V-K, they lie close to the extension of the relation defined by the other Virgo cluster galaxies in the colour–colour plot. This appears qualitatively consistent with the hypothesis that they contain relatively young stellar populations (Arimoto & Yoshii, 1987).

In relation to the question of the age spread between galaxies *in the same cluster*, we have investigated whether there is any evidence for an intrinsic scatter in the colour–magnitude and colour–colour relations discussed in the previous sections. Table 4.21 shows the observational error in each of the colours estimated from internal comparisons in each of the bands. Errors in the V_{26} magnitudes were estimated by D84; they translate into an equivalent scatter in galaxy colour that is reduced by a factor of $\sim 1/10$. Table 4.22 presents the scatter in each of the relations determined by least squares fitting to each of the individual C–M and C–C relations (ie., the slopes of the relations were allowed to differ between the clusters). As the scatter that is determined by this technique is unduly affect by the outlying points, we present values determined by fitting to the whole dataset, the dataset culled of 'obviously' outlying points, and the sample broken down by morphological type. There is evidence to suggest that the scatter in both the U-V and V-K C–M relations is somewhat larger than can be accounted for by observational error. This intrinsic scatter is present in both morphological types, but is more pronounced in the S0 types as the majority of outlying points have this morphology. In the Virgo U-V C–M and the Coma V-K C–M

Table 4.21

Estimated Errors from Internal Comparisons

Cluster	U-V	V-K	V_{26}
Virgo	0.022	0.034	0.13
Coma	0.040	0.038	0.13

Table 4.22

Scatter in Colour–Magnitude and Colour–Colour Relations

Cluster/ Variables	All		Culled		E		S0		obs. error
	rms	n	rms	n	rms	n	rms	n	
Virgo									
U-V vs. V_{26}	0.108	25	0.054	21	0.065	14	0.135	11	0.026
V-K vs. V_{26}	0.077	21	0.040	17	0.050	12	0.109	9	0.036
U-V vs. V-K	0.056	20	0.052	17	0.060	11	0.041	9	0.041
Coma									
U-V vs. V_{26}	0.054	44	0.037	39	0.052	22	0.058	22	0.042
V-K vs. V_{26}	0.075	40	0.054	35	0.075	29	0.078	11	0.040
U-V vs. V-K	0.054	27	0.054	27	0.046	21	–	–	0.055

relations, the intrinsic scatter remains in the main body of the points even when a substantial number of outliers are excluded from the sample. There is, however, no strong evidence for additional scatter in the colour–colour relation in either cluster; although there is a suggestion that the relation curves in the extreme blue. The small intrinsic scatter in the C–M relation may be driven by an additional dynamical parameter (ie., a further parameter describing the potential well of the galaxy, such as the surface brightness or degree of ellipticity), or it may arise because galaxies with identical mass distributions do not share a common starformation history. Models for the passive evolution of stellar populations (eg., Arimoto & Yoshii, 1987) suggest that both hypotheses are compatible with the absence of scatter in the C–C relation.

4.8 Comparison with APF

APF concluded from their study that the V-K colours of early-type galaxies in Virgo and Coma were different by $0.^m1$. In our study we find this difference to be only $0.^m02$, consistent with statistical uncertainty and the likely precision of our data. We have shown that $0.^m03$ of the discrepancy between our work and APF arises from the inhomogeneity of the raw V-band magnitudes derived from SV and S72. In addition, we note that although the vast majority of K-band magnitudes measured by PFA in the Coma cluster are in close agreement with our own measurements, there are large discrepancies with a few of the very faintest objects. This effect acts in the sense that PFA give these few objects V-K colours that appear to be far too blue. The transformation used by APF relate colours measured inside a constant aperture to colours inside an aperture of fixed relative diameter (ie., at constant $\log(A/D(0))$) is *unlikely* to introduce further systematic error as the correction is small and very similar for both clusters. We suggest that the remainder of the discrepancy may arise from: (1) differences in the actual galaxies included in the samples; and (2) the least squares fitting technique used by APF to derive the distance modulus. The least squares method is sensitive to the presence of skewness and outliers in the C–M relation — experimentation with our data set suggests the distance modulus may be wrongly estimated by as much as $0.^m02$

in extreme cases. We note, however, that although these effects may combine to account for the colour discrepancy, the distance modulus that APF measure (eg., $\Delta m_{(u-K)} = 3.1 \pm 0.2$) is still too small to be completely consistent with our data set. The solution to this problem remains unclear.

4.9 Summary and Conclusions

In order to test the homogeneity of the stellar populations of early-type galaxies in various environments, we have compared the broad-band UVK colours of E/S0 galaxies in the Coma and Virgo clusters. The galaxies in these clusters have very different environments — the velocity dispersions appropriate to the galaxies we have studied are 1100 $\mathrm{km\,s^{-1}}$, in Coma, and 600 $\mathrm{km\,s^{-1}}$, in Virgo (Kent & Gunn, 1982, and Binggeli et al., 1987); the early-type galaxy fraction in the Coma cluster (Dressler, 1980) is about 85%, compared to 40% in Virgo (Sandage et al., 1985). Our data set consists of new U and V-band CCD photometry of both clusters, new infrared K-band photometry of Coma and the K-band photometry of Virgo published by PFA. Great care has been taken to ensure that the measurements in both clusters have the same photometric calibration. A large number of repeated measurements were made in order that observational errors could be assessed. In all bands, a relative accuracy of 1% has been achieved.

In contradiction to the previous study by APF, we find no evidence to suggest that the colours of E/S0 galaxies in the two clusters are different. If galaxies, in both clusters, of the same absolute magnitude have equal metal abundances, then they must also share a common average age (to within ~ 1 Gyr). This constraint can only be relaxed if metallicity and age effects conspire so as to cancel out. While this is qualitatively possible — galaxies in which star formation continues until a more recent epoch are younger (making them bluer) but also reach a higher metalicity (making them redder) — but it seems unlikely that the collusion between these two effects should be so perfect. Further consideration is given to this issue, and to the contrasting conclusions of Chapter 3, in Chapter 6.

We explain the incorrect conclusion reached by APF in terms of (1) the inhomogeneity of their optical photometry, (2) measuring errors in their infrared photometry of the faintest Coma galaxies, (3) their smaller sample size, and (4) the sensitivity of the least squares fitting technique to outliers and the skewness of the scatter about the C–M relation.

In addition, we have investigated the scatter in the C–C and C–M relations in each of the separate clusters. The correlation between U-V and V-K colours appears to be perfect, even if galaxies not fitting the C–M relations are included. This is consistent with current models for the passive evolution of galaxy colours even if there is a spread in age. Even when outlying points are removed, a small intrinsic scatter of $\sim 0.^m04$ is present in both C–M relations. If real, this may be due to (1) the dependance of metallicity on a further parameter defining the shape of the mass distribution, eg. surface brightness, (2) variations in galaxy age, or (3) variations in the reddening towards individual galaxies, either in our galaxy, or in the intra-cluster medium of the cluster observed. To disentangle these effects will be extremely difficult.

5 THE EVOLUTION OF GROUPS OF GALAXIES IN THE PRESS-SCHECHTER FORMALISM

5.1 Introduction

5.1.1 Motivation

In Chapter 1, we have described the physical processes at work in dense environments that can be expected to modify the appearance and star formation properties of a galaxy. We have also discussed attempts that have been made to model these effects in order to account for the correlation between a galaxy's environment and its morphology. It is clear, however, that these models are unlikely to be entirely appropriate as they do not take into account the fact that the environment of a galaxy is evolving and that dense regions are continually fed with an infall of relatively isolated galaxies. It is the aim of the current chapter to develop an analytic theory that will allow these effects to be better understood. We make only a rudimentary attempt to interpret our results, that are derived in terms of the distribution of mass (and therefore galaxies) amongst groups of various total masses, in terms of possible evolutionary effects on the galaxies themselves.

The evolution of a system of self-gravitating particles is best studied using a full N-body computer code. This method, however, has two disadvantages. Firstly, the simulation is limited both by the resolution of the smallest particle size, and by the statistical variations in the properties and histories of the small numbers of massive groups. Secondly, while we would be able to obtain a solution to a particular well-defined problem, without an analytic frame-work, we would gain neither an understanding of the physical processes involved, nor

the ability to adapt our solution to a change in the cosmological parameters. Fortunately, N-body simulations started from scale-free initial conditions by Efstathiou et al. (1988, EFWD) showed that the analytic theory developed by Press & Schechter (1974, PS) provides a (surprisingly) good quantitative statistical description of the evolution of the distribution of mass amongst groups and clusters of various sizes (this distribution is referred to as the *multiplicity function*). However, their work is only able to predict the mass distribution in the universe as a whole. In the present chapter, we will extend the theory to follow the multiplicity function of the sub-components of a present-epoch group of given size.

5.1.2 The basic principles of the PS theory

For a detailed mathematical description of the PS theory, we refer the reader to the original paper and EFWD as the workings are a special case of those presented in Section 5.2. Here we briefly outline the basic principles involved.

At some early epoch, the universe is imagined to be well-described by an isotropic random Gaussian field of small density perturbations. The phases of the fluctuations are random so that the field is entirely defined by its *power spectrum* (ie., by the amplitudes of its Fourier components). The initial density variations are small (ie., $\delta \equiv \Delta\rho/\bar{\rho} \ll 1$) and their evolution, in this regime, is described by the*linear* form of Vlasov's equation. The density perturbations grow with time until they become non-linear (ie., $\delta \sim 1$), at which point their evolution can no longer be followed by simple analytic techniques. PS circumvent this difficulty by assuming that:

(1) The evolution of the density perturbations can be traced using linear theory until the clump 'turns around' and breaks away from the universal expansion. For a spherical top-hat perturbation this occurs at a density contrast $\delta_c \sim 1.68$ (Gunn & Gott, 1972).

(2) At this density contrast, the region collapses rapidly and independently of its surroundings. The internal structure of the clump is lost by *violent relaxation* (Lynden-Bell,

1967). To the rest of the universe, the region behaves as if it were a single body of large mass.

At the expense of our knowledge of the internal structure of the collapsing clumps, we can therefore continue to apply the linear equation to the 'gas' of particles to calculate their evolving mass distribution. Although this results in a considerable simplification of the equations describing the evolution of the density field, we must still solve the problem of counting the non-linear objects of a given mass. This requires that we are able to relate the probability distribution of the density fluctuations (averaged over a volume, V) to the probability that a given region is sufficiently overdense to collapse on the scale V but is not absorbed in the collapse of a larger volume. This probability can then be used to determine the fraction of the mass of the universe that will be contained in clumps of mass $\bar{\rho}V$. PS suggest a plausible transformation between the probability distribution function of the Gaussian field (smoothed on scale V), $P(\delta_V)$ and the *multiplicity function* of the condensed groups:

$$\rho(M,z) = -2\rho_0 \frac{\partial \mathcal{P}(\delta_V > \delta_c(z))}{\partial M} dM. \tag{5.1}$$

where ρ_0 is the mean density of the universe, and $\delta_c(z)$ is the overdensity threshold for collapse at the epoch corresponding to the redshift z. The derivation of this relation is, however, flawed by the fact that the factor of 2 must be inserted 'by hand' in order that the total mass of the universe remains constant. This weak point of the theory is given justification by the comparison with the N-body simulations of EFWD, and by the analytic investigations of Bond et al. (1990) (but see the alternative formulations suggested by Peacock & Heavens, 1990). We will adopt the transformation on an empirical basis in the work presented here.

In addition, to the approximations made in setting up the PS formalism, two further assumptions are usually made in order the that the problem is analytically tractable:

(1) The universe is taken to be flat (ie., $\Omega = 1$). This ensures that the density fluctuations grow linearly with the expansion factor.

(2) The initial power spectrum is taken to be a power-law (ie., $|\delta_k|^2 \propto k^n$). Mathematically, this results in considerable simplification as the variance of the density field can be written as a simple function of the smoothing scale. Although detailed models of the early universe (eg., Bond & Efstathiou, 1984) suggest that this approximation is not strictly correct, the curvature of the spectrum that they predict is very shallow. The power-law is still, therefore, a useful approximation (Kaiser, 1986).

These two assumptions ensure that there is only one characteristic scale in the universe (the expansion factor). The evolution of the mass distribution is therefore self-similar, having the same functional form at each epoch and only altering by a magnification factor, M_*, that determines the 'typical' size of the condensed groups. The actual form that is derived for the *universal multiplicity function* is:

$$\rho(M,z)dM = \frac{1}{\sqrt{2\pi}}\left(\frac{n+3}{3}\right)\left(\frac{M}{M_*(z)}\right)^{(n+3)/6} \exp\left[-\frac{1}{2}\left(\frac{M}{M_*(z)}\right)^{(n+3)/3}\right]\frac{dM}{M} \qquad (5.2)$$

where $M_*(z) \propto (1+z)^{-6/(n+3)}$.

The original PS theory deals only with the evolution of the multiplicity function of the universe as a whole. No attempt is made to determine how these masses are distributed in space. EFWD started to extend the basic theory in order to examine how the multiplicity function was altered in regions of large-scale density enhancement. The solution to this problem allows the evolution in a region that condenses to become a rich cluster at the present epoch to be compared with the evolution elsewhere in the universe. The analytical work of EFWD showed that the most massive groups at early times were incorporated into the most massive groups at the present — a result in qualitative agreement with their N-body simulations. Their analysis did not, however, take into account the correlations between the fluctuations on different scales and was therefore only applicable when the sub-components were very much less massive than the final cluster.

In the present work, we show that these cross-correlations have a simple dependance, and develop a more sophisticated treatment of the problem that is applicable over the full

range of sub-component masses. We are able to derive a *conditional multiplicity function* for the sub-components (at an epoch corresponding to redshift z) of a present-epoch group of given mass. This function is demonstrated to have the required property that it recovers the universal multiplicity function (at epoch z) when combined appropriately with the universal multiplicity distribution of the groups at the final epoch. We also demonstrate that it gives an extremely good *quantitative* fit to the numerical results obtained by EFWD from N-body simulations.

5.2 The Evolution of Groups — Mathematical Results

5.2.1 Conditional probabilities in random Gaussian fields

In the universe at an early time, we represent the probability distribution of the small variations in the otherwise smooth distribution of matter as a 3-dimensional Gaussian random field. In other words, the probability distribution of the density, measured as an average over a randomly selected volume V, is:

$$P(\delta_V) = \frac{1}{\sqrt{2\pi}.\sigma_V} \exp\left(-\frac{\delta_V^2}{2\sigma_V^2}\right)$$

where, δ_V is the *overdensity* of the volume $= (\rho_V - \bar{\rho})/\bar{\rho}$, and σ_V is the rms variation of δ_V. Even if the random field is not truly Gaussian, the Central Limit Theorem usually justifies the use of this approximation. The reader should note that the volume V contains a mass $M \approx \rho_0.V$.

In this section, our aim is to determine the probability distribution of the density fluctuations in a volume V that is contained within a larger volume V' in which the average overdensity has a predetermined value. Aside from the requirement that it is entirely contained within V', V is chosen at random. Bayes' formula allows us to express this *conditional* probability distribution in terms of the *joint* probability distribution of δ_V and $\delta_{V'}$:

$$P(\delta_V|\delta_{V'}) = \frac{P(\delta_V, \delta_{V'})}{P(\delta_{V'})}. \tag{5.3}$$

Where, $P(\delta_V)$ is the probability that we measure the density inside the volume V (chosen without reference to V') to be δ_V[†]; $P(\delta_V, \delta_{V'})$ is the probability that we measure the overdensities of V' (chosen at random) *and* V (chosen at random from within V') to be $\delta_{V'}$ and δ_V respectively; $P(\delta_V|\delta_{V'})$ is the probability that we measure the overdensity inside V to be δ_V *given* that we already know the overdensity of the large volume V' (that contains V) to be $\delta_{V'}$.

Abstracting from this problem, we consider a pair of Gaussian distributed random variables (x, y) that have a joint probability distribution that is also Gaussian. This is equivalent to stating that the joint probability distribution may be written as:

$$P(x,y) = \frac{1}{2\pi}\frac{1}{|\sigma_{ij}|^2}\exp\left(-\frac{1}{2}(\Delta x, \Delta y)\sigma_{ij}^{-1}(\Delta x, \Delta y)^T\right), \tag{5.4}$$

where $\Delta x = x - \overline{x}$, $\Delta y = y - \overline{y}$ and σ_{ij} is the covariance matrix $\begin{pmatrix} \sigma_x & \sigma_{xy} \\ \sigma_{xy} & \sigma_y \end{pmatrix}$. By expanding the matrix notation of Equation 5.4 and using Bayes' formula (Equation 5.3), the conditional probability $P(x|y)$ can be rewritten as the product of a normalisation factor and the exponential term

$$\exp\left(-\frac{1}{2}\frac{\sigma_x^2\sigma_y^2}{\sigma_x^2\sigma_y^2 - \sigma_{xy}^4}\left(\frac{\Delta x^2}{\sigma_x^2} - 2\frac{\Delta x \Delta y}{\sigma_x\sigma_y}\frac{\sigma_{xy}^2}{\sigma_x\sigma_y} + \frac{\Delta y^2}{\sigma_y^2}\right)\right) \Big/ \exp\left(-\frac{1}{2}\frac{\Delta y^2}{\sigma_y^2}\right)$$

$$= \exp\left(-\frac{1}{2}\frac{\sigma_x^2\sigma_y^2}{\sigma_x^2\sigma_y^2 - \sigma_{xy}^4}\left(\frac{\Delta x}{\sigma_x} - \frac{\Delta y}{\sigma_y}\frac{\sigma_{xy}^2}{\sigma_x\sigma_y}\right)^2\right). \tag{5.5}$$

This is a Gaussian distribution with mean

$$\mu_{x|y} = \left(\frac{\sigma_{xy}^2}{\sigma_x\sigma_y}\right)\left(\frac{\sigma_x}{\sigma_y}\right)\Delta y$$

and variance

$$\sigma_{x|y}^2 = \sigma_x^2 - \left(\frac{\sigma_{xy}^4}{\sigma_x^2\sigma_y^2}\right)\left(\frac{\sigma_x^2}{\sigma_y^2}\right)\sigma_y^2.$$

[†] For strict mathematical correctness, we should require the overdensity to lie between δ_V and $\delta_V + \epsilon$, where ϵ is an arbitrarily small number. We use the looser terminology for the sake of clarity.

If the joint probability distribution of δ_V and $\delta_{V'}$ is Gaussian, the above theorem (Adler, 1981) can be applied to calculate the conditional probability $P(\delta_V|\delta_{V'})$. As a consequence of the Central Limit Theorem, the precondition that δ_V and $\delta_{V'}$ have a bivariate Gaussian distribution will be met if the Fourier components of the random density field have independent phases (Bardeen et al., 1986). The density fluctuations that arise from quantum effects in an inflationary universe have just this property. Therefore, once we have established the variance and co-variance terms

$$\sigma_V^2 = \langle \delta_V^2 \rangle, \quad \sigma_{V'}^2 = \langle \delta_{V'}^2 \rangle$$

$$\text{and} \quad \sigma_{VV'}^2 = \langle \delta_V . \delta_{V'} \rangle$$

the conditional probability distribution of δ_V, given $\delta_{V'}$, is determined. The variances of δ_V and $\delta_{V'}$ are defined by the power spectrum that we *assume* for the density fluctuations. In the following section, we show that the power spectrum also determines the co-variance, $\sigma_{VV'}^2$.

5.2.2 Computation of the cross-correlation between scales

To establish the method by which we will determine the co-variance of the density within V and V' ($\sigma_{VV'}^2$), we review the technique (Peebles, 1980) by which the variance of the fluctuations on scale V can be determined. Initially, we adopt the notion that the universe is periodic on some scale much larger than V. This allows us to decompose the density field into discrete Fourier components. The overdensity at some *point*, $\mathbf{x}$, may then be written as[†]:

$$\delta(\mathbf{x}) = \sum_{\mathbf{k}} \delta_k e^{-i\mathbf{k}.\mathbf{x}}.$$

[†] Following Peebles (1980), we will not explicitly distinguish between the *real* and *complex* parts of the density field. This assists the clarity of our argument considerably. If care is taken to allow for the fact that only the *real* part of the field has physical significance, the numerical factor of $\frac{1}{2}$ and the moduli shown in the following formulae will be correctly obtained. If trying to reproduce these results, the reader should note that the summation over $\mathbf{k}$ should be confined to values in the positive octant.

The average density inside a volume V ('centered' at $\mathbf{x}_0$) is

$$\delta_V = \frac{1}{V}\int_V \sum_{\mathbf{k}} \delta_k e^{-i\mathbf{k}.(\mathbf{x}_0+\mathbf{x}')} \mathrm{d}^3\mathbf{x}'.$$

The variance of the density inside V is the mean *square* value of δ_V; the average of δ_V itself being zero by definition. Writing this explicitly we have:

$$\sigma_V^2 = \frac{1}{2V^2}\left\langle \left| \int_V \sum_{\mathbf{k}} \delta_k e^{-i\mathbf{k}.(\mathbf{x}_0+\mathbf{x}')} \mathrm{d}^3\mathbf{x}' \right|^2 \right\rangle$$

where the average, denoted by the angle brackets, is taken over all possible positions, $\mathbf{x}_0$, of the volume, V (ie., the entire universe). Swapping the order of integration and summation,

$$\sigma_V^2 = \frac{1}{2V^2}\left\langle \left| \sum_{\mathbf{k}} \delta_k e^{-i\mathbf{k}.\mathbf{x}_0} \int_V e^{-i\mathbf{k}.\mathbf{x}'} \mathrm{d}^3\mathbf{x}' \right|^2 \right\rangle.$$

Expansion of the square produces terms of the form $e^{-i(\mathbf{k}_1-\mathbf{k}_2).\mathbf{x}_0}$. Only if $\mathbf{k}_1 = \mathbf{k}_2$ will the term make a net contribution to σ_V^2 when the average is taken over $\mathbf{x}_0$ (the integral factor being independent of $\mathbf{x}_0$). We can therefore simplify the expression to

$$\sigma_V^2 = \frac{1}{2V^2} \sum_{\mathbf{k}} |\delta_{\mathbf{k}}|^2 \left| \int_V e^{-i\mathbf{k}.\mathbf{x}'} \mathrm{d}^3\mathbf{x}' \right|^2$$

Allowing the periodic volume in which we defined the discrete Fourier modes of the density field to become arbitrarily large, we may replace the summation with an integration in continuous k-space. Therefore,

$$\sigma_V^2 = \frac{1}{2}\int_{\mathbf{k}} |\delta_k|^2 |W_{\mathbf{k}}|^2 \mathrm{d}^3\mathbf{k} \tag{5.6}$$

where the *window function*, $W_{\mathbf{k}} = \int_V e^{-i\mathbf{k}.\mathbf{x}'} \mathrm{d}^3\mathbf{x}' \Big/ \int_V \mathrm{d}^3\mathbf{x}'$, is the Fourier transform of the top-hat† function that defines the volume V.

The cross-correlation between the overdensities in two volumes, one contained inside the other, is calculated in a similar manner. Starting from the definition of the co-variance as

† The term 'top-hat function' is used loosely here — we do not mean to imply that the volume V needs to be spherical.

$\sigma^2_{VV'} = \langle \delta_V . \delta_{V'} \rangle$ (the average being taken over all admissible pairs of volumes V and V') we have:

$$\sigma^2_{V\cdot V'} = \frac{1}{2VV'} \left\langle \left\langle \left(\int_V \sum_{\mathbf{k}} \delta_k e^{-i\mathbf{k}.(\mathbf{x}_0+\mathbf{x}')} \mathrm{d}^3\mathbf{x}' \right) . \left(\int_{V'} \sum_{\mathbf{k}} \delta_k e^{-i\mathbf{k}.(\mathbf{y}_0+\mathbf{y}')} \mathrm{d}^3\mathbf{y}' \right)^* \right\rangle_{\mathbf{x}_0} \right\rangle_{\mathbf{y}_0}$$

where the average over $\mathbf{y}_0$ is taken over all space, and the average over $\mathbf{x}_0$ is taken over values of $\mathbf{x}_0$ for which the volume V is contained in V' (as we discuss later, there is also an independence criterion that limits the choice of $\mathbf{x}_0$). We continue by separating $\mathbf{x}_0$ into two components ($\mathbf{x}_0 = \mathbf{y}_0 + \mathbf{u}_0$):

$$\sigma^2_{VV'} = \frac{1}{2} \left\langle \left\langle \left(\sum_{\mathbf{k}} \delta_k e^{-i\mathbf{k}.\mathbf{y}_0} e^{-i\mathbf{k}.\mathbf{u}_0} \mathrm{d}^3\mathbf{x}' W_{\mathbf{k}}(V) \right) . \left(\sum_{\mathbf{k}} \delta_k e^{-i\mathbf{k}.\mathbf{y}_0} \mathrm{d}^3\mathbf{x}' W_{\mathbf{k}}(V') \right)^* \right\rangle_{\mathbf{u}_0 : V \in V'} \right\rangle_{\mathbf{y}_0} .$$

We are now free to swap the order in which the averages are taken. As previously, when we expand the product of the two summations, we will obtain cross-products containing factors of the form $e^{-i(\mathbf{k}_1 - \mathbf{k}_2).\mathbf{y}_0}$. Few of these survive when we average over $\mathbf{y}_0$, and we are left with:

$$\sigma^2_{VV'} = \frac{1}{2} \left\langle \sum_{\mathbf{k}} |\delta_k|^2 e^{-i\mathbf{k}.\mathbf{u}_0} W_{\mathbf{k}}(V) W^*_{\mathbf{k}}(V') \right\rangle_{\mathbf{u}_0 : V \in V'} .$$

Changing to a continuous Fourier space, we may write:

$$\sigma^2_{VV'} = \frac{1}{2} \int_{\mathbf{k}} |\delta_k|^2 W_{\mathbf{k}}(V) W^*_{\mathbf{k}}(V') \langle e^{-i\mathbf{k}.\mathbf{u}_0} \rangle_{\mathbf{u}_0} \mathrm{d}^3\mathbf{k}. \tag{5.7}$$

Care is required at this point to define the meaning of the 'average' over $\mathbf{u}_0$ more exactly. $\mathbf{u}_0$ is a randomly chosen point for which the volume V that surrounds it is entirely enclosed in the volume V'. However, it is not clear whether we should: (1) choose a point at random, test to see if V is contained in V', then reselect another random point if this is not the case; or (2) select a random *set* of points $\mathbf{u}_0$ for which all the volumes V are *independent* and enclosed in V', then chose a point at random from this set. The practical difference is that if method (1) is adopted, the overdensity at a *point* near the outer edge of V' is less likely to contribute to the mean overdensity of V than a point that is close to the centre; with method (2) all points in V' have an equal chance to contribute to the mean overdensity of V. Later, when we come to extend the Press-Schechter theory, we will wish to apply the

present calculation to determine the probability of collapse of a region (eg., the volume V). On collapse, the matter in this region is not available to be included in an adjacent region (unless both regions collapse to form a single object on a larger scale, this circumstance being taken into account explicitly in the theory). We therefore argue that the volumes V in the averaging process must also be given this property of independence, and use method (2) to define the process by which we average over $\mathbf{u}_0$. The important consequence of this decision is that close to the edge of $\widetilde{V}$ (the volume covered by the points $\mathbf{u}_0$ for which V lies inside V') there are more *independent* choices for V *per volume element*, $\mathrm{d}^3\mathbf{u}_0$, as part of V lies outside $\widetilde{V}$ and therefore does not exclude other possible values of $\mathbf{u}_0$.

The averaged term, $\langle e^{-i\mathbf{k}.\mathbf{u}_0}\rangle_{\mathbf{u}_0}$, can be written to appear like another *window function*:

$$\widetilde{W}_{\mathbf{k}}(\widetilde{V}) = \int_{\widetilde{V}} w(\mathbf{u}_0) e^{-i\mathbf{k}.\mathbf{u}_0} \mathrm{d}^3\mathbf{u}_0 \Big/ \int_{\widetilde{V}} w(\mathbf{u}_0) \mathrm{d}^3\mathbf{u}_0$$

where, $\widetilde{V}$ is the volume covered by the points $\mathbf{u}_0$ for which V lies inside V'; $w(\mathbf{u}_0)$ is a weight function that gives increased weight to outer values of u_0 to account for the fact that the selection has been made as described in method (2) above.

It is possible for us to express $\widetilde{W}_{\mathbf{k}}(\widetilde{V})$ in terms of the window functions of V and V'. We introduce the functions $\Theta(\mathbf{x}; V, \mathbf{x}_0)$, that we define as:

$$\Theta(\mathbf{x}; V, \mathbf{x}_0) = \begin{cases} 1/V & \text{if } \mathbf{x} \text{ is contained in the volume } V \text{ 'centred' on } \mathbf{x}_0; \\ 0 & \text{otherwise.} \end{cases}$$

The k-space window functions $W_{\mathbf{k}}$ are the Fourier transforms of these real-space window functions:

$$W_{\mathbf{k}}(V) = \int_V e^{-i\mathbf{k}.\mathbf{x}'} \mathrm{d}^3\mathbf{x}' = \int_\infty \Theta(\mathbf{x}'; V, 0) e^{-i\mathbf{k}.\mathbf{x}'} \mathrm{d}^3\mathbf{x}'$$

where we have arbitrarily chosen to 'center' the volume V at the origin. By analogy, we also introduce the function $\widetilde{\Theta}(\mathbf{x}; \widetilde{V}, \mathbf{x}_0)$, which we define as:

$$\widetilde{\Theta}(\mathbf{x}; \widetilde{V}, \mathbf{x}_0) = \begin{cases} w(\mathbf{x}) \Big/ \int_{\widetilde{V}} w(\mathbf{x}) \mathrm{d}^3\mathbf{x} & \text{if } \mathbf{x} \text{ is contained in the volume } \widetilde{V} \text{ 'centred' on } \mathbf{x}_0; \\ 0 & \text{otherwise.} \end{cases}$$

Note that the normalisation of these functions is such that $\int_\infty \Theta(\mathbf{x}'; V, \mathbf{x}_0) \mathrm{d}^3\mathbf{x}' = 1$, and similarly for $\widetilde{\Theta}(\mathbf{x}; \widetilde{V}, \mathbf{x}_0)$.

We have defined the weighting function, $w(\mathbf{x})$, of $\widetilde{V}$ so that every *point* in the large volume V' has an equal chance of contributing to the average density measured in V. This is equivalent to stating that we can write the function $\Theta(\mathbf{x}; V', \mathbf{x}_0)$ as the convolution of $\Theta(\mathbf{x}; V, \mathbf{x}')$ and $\widetilde{\Theta}(\mathbf{x}'; \widetilde{V}, \mathbf{x}_0)$:

$$\Theta(\mathbf{x}; V', 0) = \int_\infty \widetilde{\Theta}(\mathbf{x}'; \widetilde{V}, 0)\Theta(\mathbf{x}; V, \mathbf{x}')\mathrm{d}^3\mathbf{x}'$$

By integrating the two sides of this relation over $\mathbf{x}$, we verify that the normalisation of the RHS is correct. We may rewrite this equation to make the convolution more explicit:

$$\Theta(\mathbf{x}; V', 0) = \int_\infty \widetilde{\Theta}(\mathbf{x}'; \widetilde{V}, 0)\Theta(\mathbf{x} - \mathbf{x}'; V, 0)\mathrm{d}^3\mathbf{x}'.$$

We then draw from the theory of Fourier transforms to note that in Fourier space:

$$W_{\mathbf{k}}(V') = \widetilde{W}_{\mathbf{k}}(\widetilde{V}).W_{\mathbf{k}}(V) \tag{5.8}$$

Returning to our expression for the co-variance of the volumes V and V', Equation 5.7, and using the relation between the window functions that we have derived above (Equation 5.8), we obtain:

$$\sigma^2_{VV'} = \frac{1}{2}\int_{\mathbf{k}} |\delta_k|^2 |W_{\mathbf{k}}(V')|^2 \mathrm{d}^3\mathbf{k} = \sigma^2_{V'}. \tag{5.9}$$

As we will see below, this strikingly simple result is not surprising since it must hold if the mean overdensity of the small volumes V contained in V' is to equal the overdensity of region V' as a whole.

5.2.3 The conditional probability distribution of density fluctuations

We now apply the conditional probability derived in Section 5.2.1 to the study of the modulation of density fluctuations on scale V by a field on scale V'. Rewriting Equation 5.5, and including the correct normalisation factor, we have:

$$P(\delta_V|\delta_{V'})d\delta_V = \frac{1}{[2\pi(1-\epsilon^2)]^{1/2}\sigma_V} \exp\left(-\frac{(\delta_V/\sigma_V - \epsilon\delta_{V'}/\sigma_{V'})^2}{2(1-\epsilon^2)}\right) d\delta_V$$

where, $\epsilon = \sigma^2_{VV'}/\sigma_V\sigma_{V'}$. This result was previously obtained by Bardeen et al. (1986). It can be considerably simplified using Equation 5.9 to obtain $\epsilon = \sigma_{V'}/\sigma_V$, giving:

$$P(\delta_V|\delta_{V'})d\delta_V = \frac{1}{[2\pi(\sigma_V^2 - \sigma_{V'}^2)]^{1/2}} \exp\left(-\frac{(\delta_V - \delta_{V'})^2}{2(\sigma_V^2 - \sigma_{V'}^2)}\right) d\delta_V . \tag{5.10}$$

It can be seen that this probability distribution has the anticipated mean (ie., $\langle\delta_V\rangle = \delta_{V'}$), and that in the case that $V' \gg V$ (ie., $\sigma_{V'} \ll \sigma_V$), it reproduces the 'k-split' approximation used by EFWD (ie., the distribution of δ_V has the same dispersion everywhere, but the mean level is shifted up or down by the 'background' overdensity, $\delta_{V'}$).

5.2.4 The conditional multiplicity function

Following EFWD, we proceed to determine $\tilde{F}(M, \delta_c; M', \delta')$, the fraction of regions of mass M, contained within a larger scale region of mass M' and overdensity δ', that are more overdense than the critical density, δ_c (at which non-linear gravitational effects become dominant). Note that we are now working in terms of mass, but that this is directly proportional to the volume of the region, $M \approx \rho_0.V$ since the overdensities are small. We have:

$$\begin{aligned}\tilde{F}(M, \delta_c|M', \delta') &= \int_{\delta_c}^{\infty} P(\delta_V = \delta|\delta_{V'} = \delta')\, d\delta \\ &= \int_{\delta_c}^{\infty} \frac{1}{\sqrt{2\pi(\sigma_M^2 - \sigma_{M'}^2)}} \exp\left[\frac{-(\delta - \delta')^2}{2(\sigma_M^2 - \sigma_{M'}^2)}\right] d\delta \\ &= \frac{1}{\sqrt{\pi}} \int_{\frac{(\delta_c - \delta')}{\sqrt{2(\sigma_M^2 - \sigma_{M'}^2)}}}^{\infty} e^{-y^2} dy\end{aligned} \tag{5.11}$$

These regions rapidly collapse (if they have not already done so) to form small dense objects. A large proportion of them will, however, be consumed in the collapse of a larger region that surrounds them. In Section 5.3, we will associate these objects with individual isolated galaxies, groups of galaxies or clusters of galaxies depending on their mass. For convenience, we refer to them collectively as *groups*. The spherical collapse models of Gunn and Gott (1972) suggest that the appropriate numerical value for δ_c is 1.68.

As it stands, Equation 5.11 gives the fraction of mass in collapsed groups of size greater than M only at the epoch, z_i, at which the power spectrum has been defined. However, as

the fluctuations are small, they evolve linearly (ie., the evolution of δ_k does not on depend its amplitude). The power spectrum therefore retains its initial shape, and changes only in its normalisation. In a flat universe (ie., $\Omega = 1$), the amplitude grows as $1/(1+z)$. Therefore we may apply Equation 5.11 to calculate $\widetilde{F}$ at any arbitrary epoch z by determining the fraction of regions which have overdensity greater than $\delta_c(z) = \delta_c.(1+z)/(1+z_i)$ at epoch z_i.

Continuing to follow the derivation of the original Press-Schechter theory, we relate $\widetilde{F}$ to the distribution of the total mass, M', among collapsed groups of given size by the ansatz (cf., Equation 5.1):

$$\widetilde{f}(M, \delta_c(z)|M', \delta')dM = -2\frac{\partial \widetilde{F}(M, \delta_c(z)|M', \delta')}{\partial M}dM. \tag{5.12}$$

where the *multiplicity fraction*, $\widetilde{f}$ is defined as the fraction of the total mass of M' that is contained in collapsed groups with masses between M and $M + dM$. As the integral in Equation 5.11 has been expressed in terms of the dummy variable y, the partial differentiation may be performed explicitly:

$$\widetilde{f}(M, \delta_c(z)|M', \delta')dM = -\frac{2}{\sqrt{2\pi}}\frac{\sigma_M}{(\sigma_M^2 - \sigma_{M'}^2)^{3/2}}(\delta_c - \delta')\exp\left[\frac{-(\delta_c - \delta')^2}{2(\sigma_M^2 - \sigma_{M'}^2)}\right]\frac{d\sigma_M}{dM}dM. \tag{5.13}$$

As described in Section 5.1.2, we assume that the initial spectrum of the density fluctuations is a power law with spectral index n (ie., $|\delta_k|^2 \propto k^n$). Equation 5.6 gives the variance of the fluctuations as:

$$\sigma_M = A.M^{-(n+3)/6}$$

where the normalisation constant A is determined by the amplitude of the density fluctuations at some initial epoch z_i, by the spectral index and by the form of the window function. Differentiating:

$$\frac{d\sigma_M}{dM} = -\left(\frac{n+3}{6}\right)\frac{\sigma_M}{M}.$$

Inserting this into Equation 5.13 we obtain:

$$\begin{aligned}\widetilde{f}(M, \delta_c(z)|M', \delta')dM = \frac{1}{\sqrt{2\pi}}\frac{(n+3)}{3}&\frac{\sigma^2(M)}{(\sigma^2(M) - \sigma^2(M'))^{3/2}} \\ &\times(\delta_c - \delta')\exp\left[\frac{-(\delta_c - \delta')^2}{2\left(\sigma^2(M) - \sigma^2(M')\right)}\right]\frac{dM}{M}\end{aligned} \tag{5.14}$$

where we have changed the notation used for the variances in order to emphasise that most of the functional dependence of $\tilde{f}$ on the scale M is contained in the variance $\sigma^2(M)$.

Equation 5.14 can be simplified and re-written to make the scaling of the masses with the amplitude of the initial power spectrum more explicit. We define:

$$\Delta = \left(\frac{\sigma^2(M) - \sigma^2(M')}{\sigma^2(M)}\right)^{1/2} = \left(1 - \left(\frac{M}{M'}\right)^{(n+3)/3}\right)^{1/2}$$

and write δ_0 for the critical overdensity that a structure must have at the initial epoch, z_i, in order to have just collapsed at the present-day (ie., $\delta_0 = \delta_c(z_i)/(1+z_i) = 1.68/(1+z_i)$). A region which just collapses at epoch z must have an overdensity at z_i of $\delta_c(z_i) = (1+z)\delta_0$. (We are here making the assumption that the universe is flat.) In this notation,

$$\tilde{f}(M, \delta_c|M', \delta')dM = \frac{1}{\sqrt{2\pi}}\frac{(n+3)}{3}\frac{1}{\Delta^3\sigma(M)}(\delta_c - \delta')\exp\left[\frac{-(\delta_c - \delta')^2}{2\Delta^2\sigma^2(M)}\right]\frac{dM}{M}$$

$$= \frac{1}{\sqrt{2\pi}}\frac{(n+3)}{3}\frac{1}{\Delta^3}\frac{M^{(n+3)/6}(1+z-\delta'/\delta_0)\delta_0}{A}\exp\left[-\frac{M^{(n+3)/3}{\delta_0}^2(1+z-\delta'/\delta_0)^2}{2\Delta^2A^2}\right]\frac{dM}{M}.$$

Note that $M_*(0) \equiv \left(\delta_0/A\right)^{-6/(n+3)}$ determines the typical mass (averaging over the whole universe) that has just collapsed at the present epoch, and that $M_*(z-\delta'/\delta_0) = \left((1+z-\delta'/\delta_0).\delta_0/A\right)^{-6/(n+3)}$ determines the typical size scale that collapses *in this region* at the epoch z. There is an obvious restriction that $1+z-\delta'/\delta_0 > 0$, or else the larger region M' would have collapsed *before* the epoch z, so that its division into sub-units at this epoch is impossible. The conditional multiplicity fraction can be simplified by using these variables to scale the solution:

$$\tilde{f}(M, \delta_c|M', \delta')dM = \frac{1}{\sqrt{2\pi}}\frac{(n+3)}{3}\frac{1}{\Delta^3} \times \left(\frac{M}{M_*(z-\delta'/\delta_0)}\right)^{(n+3)/6}\exp\left[-\frac{1}{2\Delta^2}\left(\frac{M}{M_*(z-\delta'/\delta_0)}\right)^{(n+3)/3}\right]\frac{dM}{M} \quad (5.15)$$

In the case that $M' \gg M$, $\Delta \approx 1$ (ie., the correlation between the scales is negligible) and we recover the 'k-split' approximation used by EFWD. In the limit $M' \to \infty$ (ie., the large scale region grows to include the entire universe), by definition $\delta' \to 0$, and the conditional

multiplicity fraction reduces to the universal multiplicity fraction, Equation 5.2 (divided by ρ_0).

As is explained in the following section, we will only apply this formula to present day regions are just sufficiently overdense to collapse on the scale M', but are not dense enough to collapse on a slightly larger scale. This requires that $\delta' = \delta_0$. Adopting this value, we have plotted, in Figures 5.1–5.3, $\tilde{f}$(M) for a selection of parameters covering the range of interest. In each diagram, we show 4 curves corresponding to the spectral indices 1, 0, -1 and -2. Three of the set of four diagrams at each epoch show the effect of altering the mass of the present-day group, M', between 32, 1.0 and 0.13 $M_*(0)$. In the remaining figure, we show the Press-Schechter *universal* multiplicity function at this epoch. In order to compare the evolution of the groups, the diagrams are repeated at redshifts of 0.5, 1.0 and 2.0. In order to be consistent with EFWD, we have plotted the multiplicity fraction as a function of *multiplicity* scaled to the present-day peak in the universal multiplicity function, ie., as a function of $m = \log_2 (M/M_*(0))$.

Careful study of these diagrams allows us to qualitatively understand the behaviour of $\tilde{f}$. Firstly, the fact that the region M' is overdense has the effect of accelerating the evolution of the groups inside its boundary. Thus the peak in the multiplicity function (ie., the typical size of a group) for the $M' = 32$ case is always shifted to higher masses than the peak in the universal distribution. The degree of 'acceleration' is greater for flatter (ie., more negative) power spectra. The factor M_* in the exponential of Equation 5.15 is always advanced above the M_* of the universal distribution (Equation 5.2) in any region which is collapsing at the present-day irrespective of its mass; however, there is clearly an upper limit to the masses of the groups that can be contained within M' (ie., M' itself). This cut-off is introduced by the factor Δ in the exponent that has arisen from the cross-correlation between the mass scales. The sharpness of the truncation changes with the spectral index, and the epoch at which the groups are 'observed'. It is this factor that distinguishes our formula from the k-split approximation derived by EFWD; for steep power spectra, eg., $n = +1$, the cut-off is very sudden, and the k-split is a good approximation over almost the full range of masses below

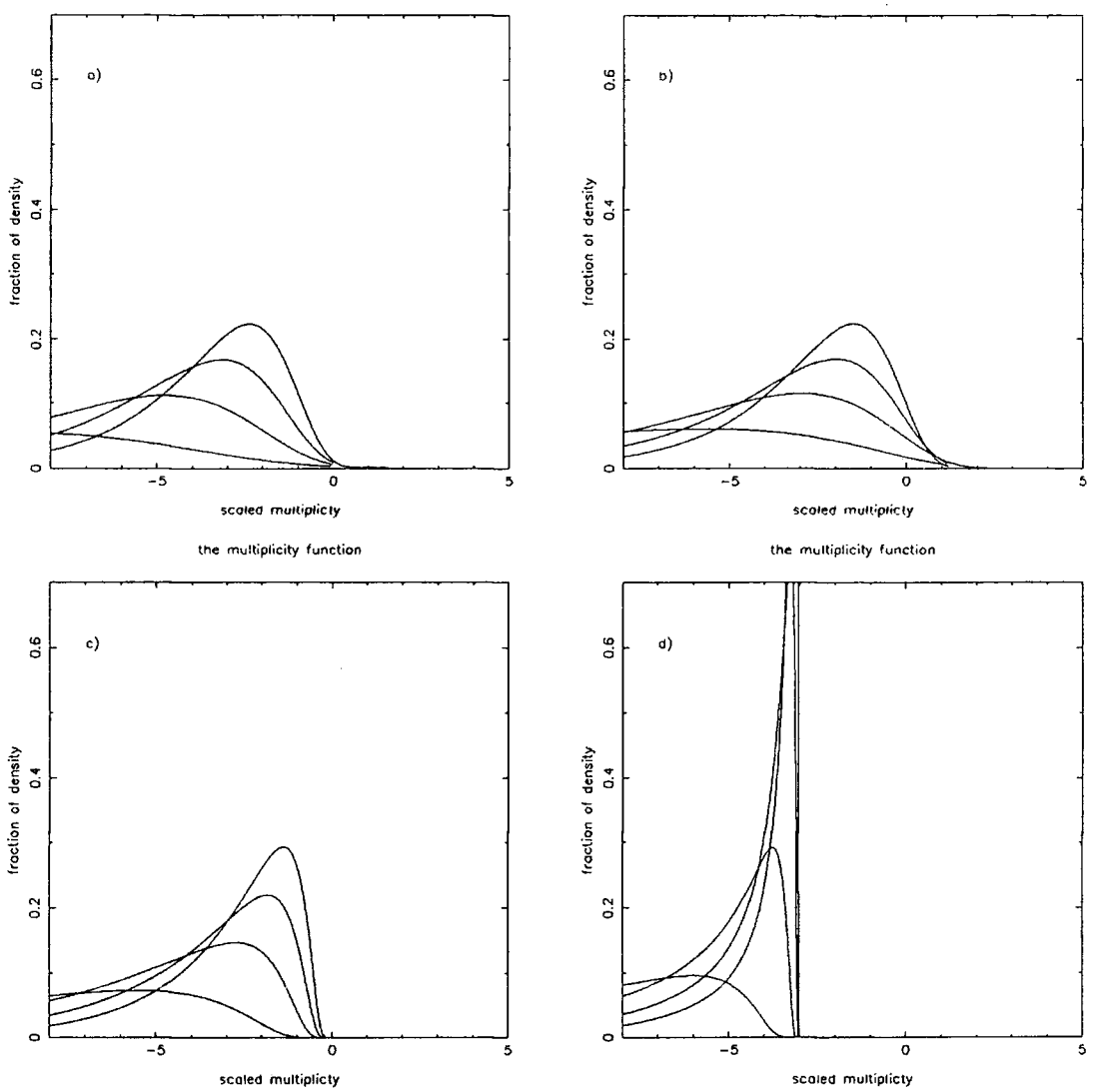

Figure 5.1. The *conditional multiplicity fraction* (the fraction of the present-day group mass, M', bound into groups of mass M at redshift z) plotted for $z = 2.0$. The group mass M is presented as *multiplicity* scaled to the typical mass of a present-day group, ie., $m = \log_2 \left(M/M_*(0) \right)$. The four curves in each plot correspond to spectral indices, n, of 1, 0, -1 and -2 (most to least peaked respectively). Plot (a) shows the universal multiplicity function (Equation 5.2) scaled to $\rho_0 = 1$. (b) shows the conditional multiplicity fraction, $\tilde{f}$, in a region which collapses to form a single group of scaled multiplicity $m' = 5.0$ at the present epoch. (c) and (d) show $\tilde{f}$ for $m' = 0.0$ and -3.0 respectively.

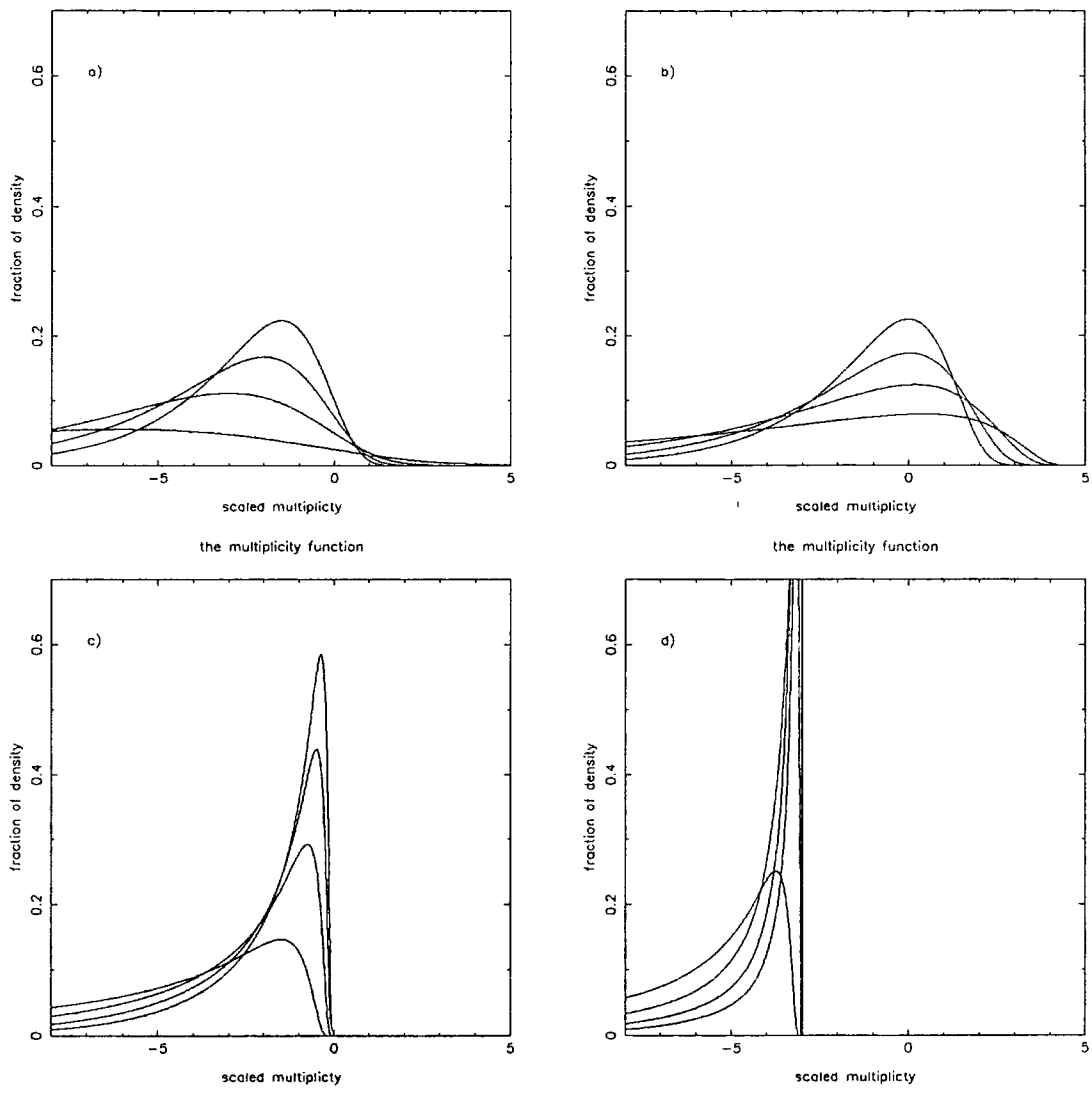

Figure 5.2. The multiplicity functions shown in Figure 5.1 reproduced at $z = 1.0$.

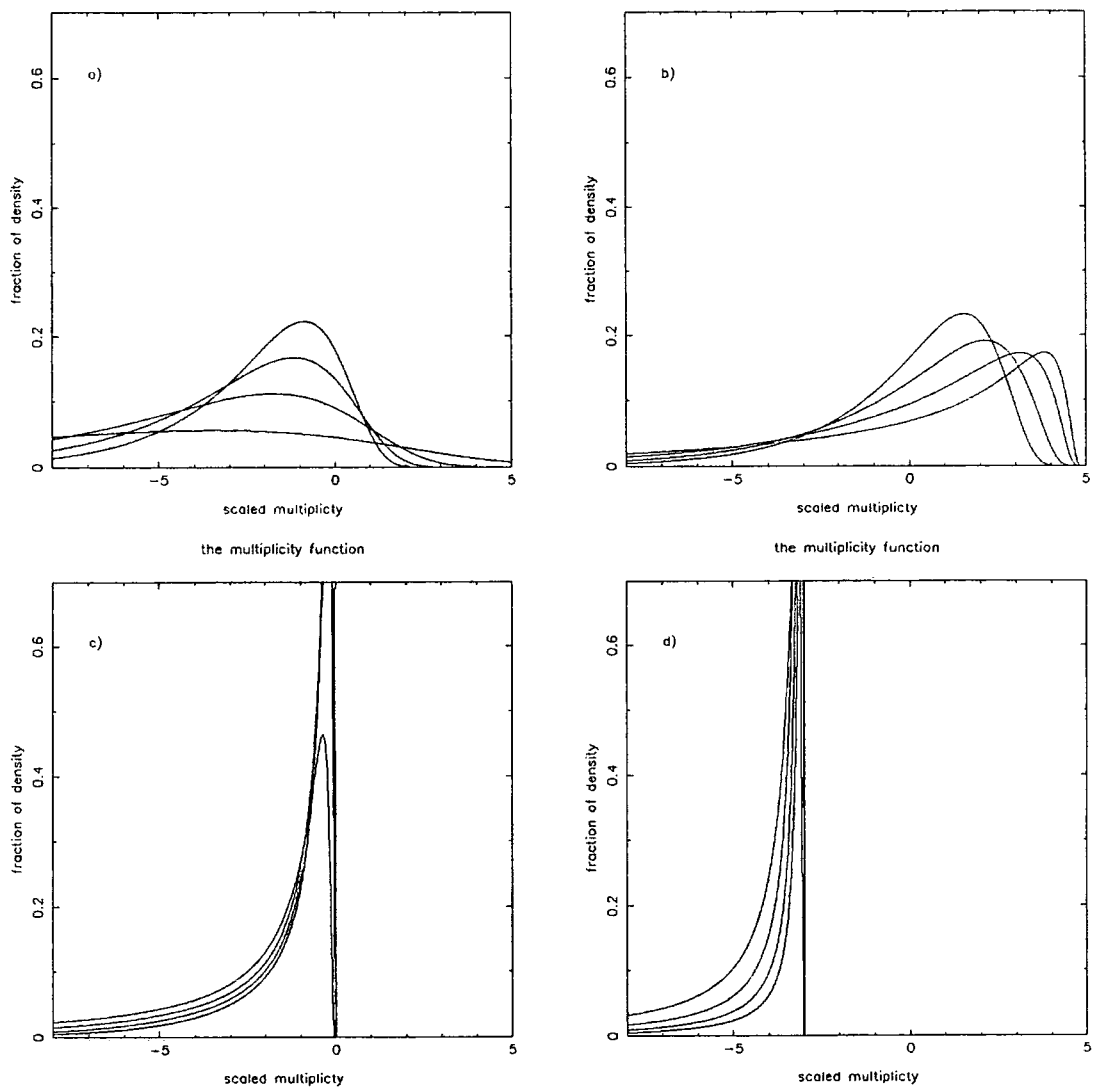

Figure 5.3. The multiplicity functions shown in Figure 5.1 reproduced at $z = 0.5$.

M' provided no attempt is made to renormalise the distribution. In the formula presented here (we will show later that it appears to be the exact solution), the normalisation of the multiplicity fraction (ie., the requirement that $\int_0^\infty \tilde{f}\,dM = 1$) is maintained by the $1/\Delta^3$ factor. It has the effect of piling up the 'extra' groups, which would have masses larger than M' in the absence of the cut-off, just below M'. If the power spectrum is steep, and the peak of the distribution in larger regions has advanced beyond M', a very sharp spike is produced. For flat initial power spectra (eg., $n = -2$), the distributions are always very broad, a wide range of group sizes contributing significantly to the final mass. The effect of the cut-off at M' is felt in the multiplicity fraction of group masses significantly smaller than M'.

We may now understand the time evolution of the multiplicity fraction displayed in Figures 5.1–5.3. At large redshifts, there is little tendency for groups inside M' to have masses that approach M'. The distribution is therefore very similar to the universal distribution at this epoch, but advanced to a somewhat larger mean mass (cf., Figure 5.1b). At later times, groups in the high-mass tail of the multiplicity function show some tendency to grow to masses approaching M'. This causes a distortion in the shape of the multiplicity fraction (cf., Figures 5.2b and 5.1c) which grows as the fraction of mass that would otherwise be bound into groups larger than M' increases (eg., Figure 5.2c). At late times, almost all the mass is bound into groups that are only slightly less massive than M' (eg., Figure 5.3c). Note that while the qualitative explanation of the evolution of $\tilde{f}$ is the same for all spectral indices and present-day masses (M'), the timescale is strongly dependent on n and M'.

5.2.5 The joint multiplicity function

The conditional multiplicity fraction derived in the previous section is not the ultimate goal of this chapter. In order to study the evolutionary history of groups and clusters of galaxies, we also require the *joint multiplicity function*, ie., the mass density of groups with masses in the range M to $M+dM$ at epoch z that are incorporated into groups with masses M' to $M'+dM'$ at the present epoch.

Before proceeding, it is helpful to review the reasoning behind the PS ansatz (Equation 5.1) in greater detail. We consider a volume V chosen at random. The probability that this volume has overdensity greater than the threshold for collapse, δ_c, is:

$$\mathcal{P}(\delta_V > \delta_c) = \int_{\delta_c}^{\infty} \frac{1}{\sqrt{2\pi}.\sigma_V} \exp\left(-\delta'^2/2\sigma_V^2\right) d\delta'$$

However, we wish only to count objects which collapse on the scale of V but do *not* collapse on a slightly larger scale, $V + dV$. The probability that this is true of region V is:

$$p(V)dV = \mathcal{P}(\delta_V > \delta_c).\mathcal{P}(\delta_{V+dV} < \delta_c | \delta_V > \delta_c)$$

or, if we introduce the short-hand notation $\mathcal{P}(V) = \mathcal{P}(\delta_V > \delta_c)$ and $\mathcal{P}(\overline{V + dV}|V)$ for the conditional probability that $V + dV$ has *not* collapsed, $\mathcal{P}(\delta_{V+dV} < \delta_c | \delta_V > \delta_c)$,

$$p(V)dV = \mathcal{P}(V).\mathcal{P}(\overline{V + dV}|V) = \mathcal{P}(V)\left(1 - \mathcal{P}(V + dV|V)\right) \tag{5.16}$$

with the obvious extension to the notation. Applying Bayes' formula to write the conditional probability, $\mathcal{P}(V + dV|V)$, in terms of the joint probability that both V and $V + dV$ are above the critical density, we have:

$$p(V)dV = \mathcal{P}(V)\left(1 - \frac{\mathcal{P}(V + dV, V)}{\mathcal{P}(V)}\right) = \mathcal{P}(V) - \mathcal{P}(V + dV, V)$$

The next step is to note that if $V + dV$ collapses, then so must V. We can therefore set $\mathcal{P}(V + dV, V) = \mathcal{P}(V + dV)$, giving:

$$p(V)dV = \mathcal{P}(V) - \mathcal{P}(V + dV) = -\frac{\partial \mathcal{P}(V)}{\partial V}$$

The number density of *independent* volumes of size V in the universe is proportional to $1/V$, but the mass of each group is proportional to V. The mass density (or multiplicity function) of groups of mass M ($\propto \rho_0.V$) is therefore proportional to:

$$\rho_0 \frac{\partial \mathcal{P}(M)}{\partial M} dM$$

In order that all the mass of the universe is bound into collapsed objects (even if their size is very small), the constant of proportionality must be 2.0 ($= 1/\mathcal{P}(0)$). This brings us to Equation 5.1.

Following the same technique, we can write the *joint multiplicity function* as the product of probabilities:

$$\rho(M, z, M')dMdM' =$$

$$\alpha\rho_0.\mathcal{P}(M').\mathcal{P}(\overline{M'+dM'}|M').\mathcal{P}(M|\delta_{M'}=\delta_0).\mathcal{P}(\overline{M+dM}|M, \delta_{M'}=\delta_0)$$

where we make use the short-hand notation adopted in Equation 5.16. α is a numerical constant of order unity. In addition, we have made use of the differentiability of the fluctuations in the density field (when smoothed on scale M) to note that the requirement that the region M' have mean overdensity greater than δ_0, but that the immediately surrounding region $M'+dM'$ have $\delta_{M'+dM'} < \delta_0$, forces $\delta_{M'} = \delta_0$. Expanding the probabilities as previously, and using the definition of the conditional multiplicity fraction, $\widetilde{f}$ (Equation 5.12), gives:

$$\rho(M, z, M')dMdM' = -2\rho_0\widetilde{f}(M, \delta_c|M', \delta')dM\frac{\partial P(\delta'_M > \delta_0)}{\partial M'}dM'$$

where the numerical factor of 2 (corresponding to $\alpha = 4$) has been chosen in accordance with the original hypothesis of PS. The expression is then simplified following the original derivation of PS to give:

$$\begin{aligned}\rho(M, z, M')dMdM' &= 2\rho_0\widetilde{f}(M, \delta_c|M', \delta_0)dM\frac{1}{\sqrt{2\pi}}\frac{(n+3)}{6}\frac{\delta_0}{\sigma(M')}\exp\left[\frac{-{\delta_0}^2}{2\sigma^2(M')}\right]\frac{dM'}{M'} \\ &= \frac{\rho_0}{2\pi}\left(\frac{n+3}{3}\right)^2\frac{1}{\Delta^3}\left(\frac{M}{M_*(z-1)}\right)^{(n+3)/6}\exp\left[-\frac{1}{2\Delta^2}\left(\frac{M}{M_*(z-1)}\right)^{(n+3)/3}\right] \\ &\quad\times\left(\frac{M'}{M_*(0)}\right)^{(n+3)/6}\exp\left[-\frac{1}{2}\left(\frac{M'}{M_*(0)}\right)^{(n+3)/3}\right]\frac{dM}{M}\frac{dM'}{M'}\end{aligned} \tag{5.17}$$

5.2.6 Recovering the universal Press-Schechter distribution

Since we have made no assumptions regarding the relative sizes of M and M', we should expect to be able to recover the universal (PS) multiplicity functions of M and M' from their joint distribution function. To recover the distribution of M' from $\rho(M, z, M')dMdM'$ is trivial (given the PS factor of 2). The integral of $\rho(M, z, M')dMdM'$ over M may be split into the integral of $\widetilde{f}(M, \delta_c(z)|M', \delta_0)dM$ over M, and the function

$\frac{\rho_0}{\sqrt{2\pi}}\left(\frac{n+3}{3}\right)\left(\frac{M'}{M_*(0)}\right)^{(n+3)/6}\exp\left[-\frac{1}{2}\left(\frac{M'}{M_*(0)}\right)^{(n+3)/3}\right]\frac{dM'}{M'}$ (which is exactly the universal multiplicity function at the present-day, Equation 5.2). From the way in which we have defined $\tilde{f}$ as a fraction (Equation 5.12), its integral over M must be unity.

It is *not*, however, obvious that we can recover the universal distribution of M, as we require a seemingly unlikely conspiracy that allows the suppression factor Δ to exactly compensate for the acceleration of the clustering hierarchy caused by the overdensity of the final region. The dependance of the joint multiplicity function on M' is of such a form that the integration cannot be performed analytically by *standard* techniques. However, numerical integration shows that the integral:

$$\begin{aligned} I &= \int_{M'=M}^{\infty} \rho(M,z,M')dMdM' \\ &= \frac{\rho_0}{2\pi}\left(\frac{(n+3)}{3}\right)^2 \cdot \frac{dM}{M} \\ &\quad \times \int_{M'=M}^{\infty} \frac{1}{\Delta^3}\left(\frac{M}{M_*(z-1)}\right)^{(n+3)/6} \exp\left[-\frac{1}{2\Delta^2}\left(\frac{M}{M_*(z-1)}\right)^{(n+3)/3}\right] \\ &\qquad \times \left(\frac{M'}{M_*(0)}\right)^{(n+3)/6} \exp\left[-\frac{1}{2}\left(\frac{M'}{M_*(0)}\right)^{(n+3)/3}\right]\frac{dM'}{M'} \end{aligned} \tag{5.18}$$

is at least a very close approximation to the universal multiplicity function $\rho(M,z)$. Below, we are able to demonstrate, by unusual analytic reasoning, that the inversion is indeed exact.

As a first step, we simplify the expression for the joint multiplicity function by making the transformations

$$u' = (M'/M_*(0))^{(n+3)/6}$$

and

$$\begin{aligned} u &= (M/M_*(0))^{(n+3)/6} \\ &= z^{-1}(M/M_*(z-1))^{(n+3)/6} \\ &= (1+z)^{-1}(M/M_*(z))^{(n+3)/6}. \end{aligned} \tag{5.19}$$

In these variables,

$$\rho(u,z,u')dudu' = \frac{4\rho_0}{2\pi}.\frac{1}{\Delta^3}.z.\exp\left(-\frac{z^2u^2}{2\Delta^2}\right)\exp\left(-\frac{u'^2}{2}\right)dudu'$$

with $\Delta = \sqrt{1-u^2/u'^2}$. Our aim is to integrate this expression over $u' = u$ to ∞. Progress can be made by noting that in these variables the universal multiplicity function (Equation 5.2) becomes

$$\rho(u,z)du = \frac{2}{\sqrt{2\pi}}(1+z)\exp\left(-\frac{(1+z)^2u^2}{2}\right)du. \tag{5.20}$$

This suggests that we attempt to simplify the exponent of the integrand by the substitution

$$x^2 = \frac{z^2u^2}{(1-u^2/u'^2)} - (1+z)^2u^2 + u'^2.$$

This expression reduces to

$$x = \frac{u'^2 - (1+z)u^2}{\sqrt{u'^2-u^2}}. \tag{5.21}$$

Differentiating, we obtain

$$\frac{dx}{du'} = \frac{u'^3}{(u'^2-u^2)^{3/2}}\left(1+\frac{u^2}{u'^2}(z-1)\right) = \frac{1}{\Delta^3}\left(1+\frac{u^2}{u'^2}(z-1)\right)$$

This is close to the Δ^{-3} factor in the integrand. For the special case $z = 1$ the agreement is exact and the integral, re-written in terms x, is of standard form.

We have not yet considered the limits to the integral in x-space. As $u' \to u$, $x \to -\infty$; at the other limit $x \to +\infty$. Also, $x = 0$ at $u' = (1+z)^{1/2}u$, but note that u'^2 is not a single valued function of x^2, so that it is best to proceed by splitting the integral into two parts corresponding to the two branches of u':

$$\begin{aligned} I =& \frac{4}{2\pi}\, z\, e^{-(1+z)^2u^2/2} \\ & \times \left(\int_{0,u'^2>(1+z)u^2}^{\infty} \frac{e^{-x^2/2}}{\left(1+\frac{u^2}{u'^2}(z-1)\right)}dx + \int_{0,u'^2<(1+z)u^2}^{\infty} \frac{e^{-x^2/2}}{\left(1+\frac{u^2}{u'^2}(z-1)\right)}dx\right) \end{aligned} \tag{5.22}$$

For z=1, both parts integrate to $\sqrt{2\pi}/2$, and since, in this case, $2z \equiv z+1$, we recover the universal distribution of M exactly. For other values of z, we note that the major contribution to the integral comes from $x \sim 0$. If we approximate the divisor in the integrand by $1 + \frac{z-1}{z+1} = \frac{2z}{1+z}$. The integrals are then soluble, the approximation to the divisor being exactly the factor required to recover the correct redshift dependance of $\rho(u,z)$.

This approximation is considerably better than our simple argument suggests as the overestimation of the divisor in the first integral is compensated for by its underestimation

is the second. Therefore, we continue by combining the two integrals, using the notation u'^2_+ and u'^2_- to distinguish the two values of u'^2 (one greater than $(1+z)u$, the other less) corresponding to each value of x. Squaring and expanding Equation 5.21 we obtain the quadratic equation for which u'^2_+ and u'^2_- are the *roots*:

$$u'^4 - \left(2(1+z)u^2 + x^2\right) u'^2 + \left((1+z)^2u^2 + x^2\right) u^2 = 0$$

The roots of this equation (ie., u'^2_+ and u'^2_-) satisfy the relations

$$u'^2_+ u'^2_- = \left((1+z)^2u^2 + x^2\right) u^2$$

and,

$$u'^2_+ + u'^2_- = \left(2(1+z)u^2 + x^2\right)$$

Combining the separate integrals in Equation 5.22 we have:

$$I = \frac{4}{2\pi} z e^{-(1+z)^2u^2/2} \times \int_{x=0}^{\infty} e^{-x^2/2} \left(\frac{1}{\left(1 + \frac{u^2}{u'^2_+}(z-1)\right)} + \frac{1}{\left(1 + \frac{u^2}{u'^2_-}(z-1)\right)} dx \right) dx \tag{5.23}$$

The bracketed part of the integrand may be rewritten by expressing the fractions in terms of a common denominator and using the expressions for the sums and products of u'^2_+ and u'^2_- to eliminate u':

$$\frac{2 + (z-1).\frac{x^2+2(1+z)u^2}{x^2+(1+z)^2u^2}}{1 + (z-1).\frac{x^2+2(1+z)u^2}{x^2+(1+z)^2u^2} + \frac{u^2(z-1)^2}{x^2+(1+z)^2u^2}}.$$

After considerable manipulation, this expression can be reduced to:

$$\frac{(1+z)x^2 + 4z(1+z)u^2}{zx^2 + 4z^2u^2} = \frac{1+z}{z}$$

ie., this term is in fact independent of x.

Replacing the bracketed term in Equation 5.23, we obtain:

$$I = \frac{4}{2\pi} z e^{-(1+z)^2u^2/2} \int_{x=0}^{\infty} \frac{1+z}{z} . e^{-x^2/2} dx$$
$$= \frac{2}{\sqrt{2\pi}} (1+z) \exp\left(-\frac{(1+z)^2u^2}{2}\right)$$

Comparison with Equation 5.20 shows that we have *exactly* recovered the universal multiplicity function for the masses M. We emphasise that this is an extremely striking result. It assures us of the mathematical self-consistency of the Press-Schechter formalism that we have applied in the derivation of the joint multiplicity function (Equation 5.17).

5.2.7 Comparison with N-body simulations

Comparison with the N-body simulations of EFWD provides a second test of the validity of the joint multiplicity function. These authors plot the fraction of groups of mass M (at 5 different epochs) which are incorporated into massive groups at the end of the simulation (massive groups are defined so as to contain 18% of the total mass at the final output time). This fraction is readily calculated from the joint multiplicity function:

$$F_{mg} = \frac{\int_{M'_{mg}}^{\infty} \rho(M, z, M')dMdM'}{\rho(M, z)dM}.$$

The parameters z and $M_*(0)$ are defined by the output times and initial perturbation amplitudes of the simulations. Table 5.1 lists the relevant values. The epoch is calculated from the expansion factors given by EFWD ($1+z = a_f/a$). A formula is also given for M_* at the final epoch time, but note that (1) the definition of M_* used by EFWD differs from ours by a factor of $2^{3/(n+3)}$; (2) the initial amplitude of the $n = -2$ simulations is defined at an expansion factor $a = 2$. There are no free parameters in our calculation of F_{mg}.

The PS predictions are superposed on the plots of EFWD in Figures 5.4–5.7. The fits can be seen not only to match the qualitative behaviour of the N-body result, but also, with a few exceptions, to give good numerical agreement. Where the fit is poor, it is not clear whether it is the PS theory or the N-body approach that is inaccurate — eg., in the $n = -2$ case, the discrepancy can be understood in terms of saturation and transient effects in the simulations. We conclude that the joint multiplicity function, that we have derived using the principles of PS, *provides an accurate description for the evolution of gravitational structure in the expanding universe.*

Table 5.1

Parameters Used to Form Comparison with the N-body Simulations of EFWD

n	$M_*(0)$	z_{f-1}	z_{f-2}	z_{f-3}	z_{f-4}	z_{f-5}
+1	260	0.848	2.415	5.311	10.66	20.55
0	194	0.585	1.512	2.982	5.311	9.00
−1	103	0.359	0.847	1.510	2.411	3.636
−2	82.4	0.166	0.360	0.585	0.848	1.155

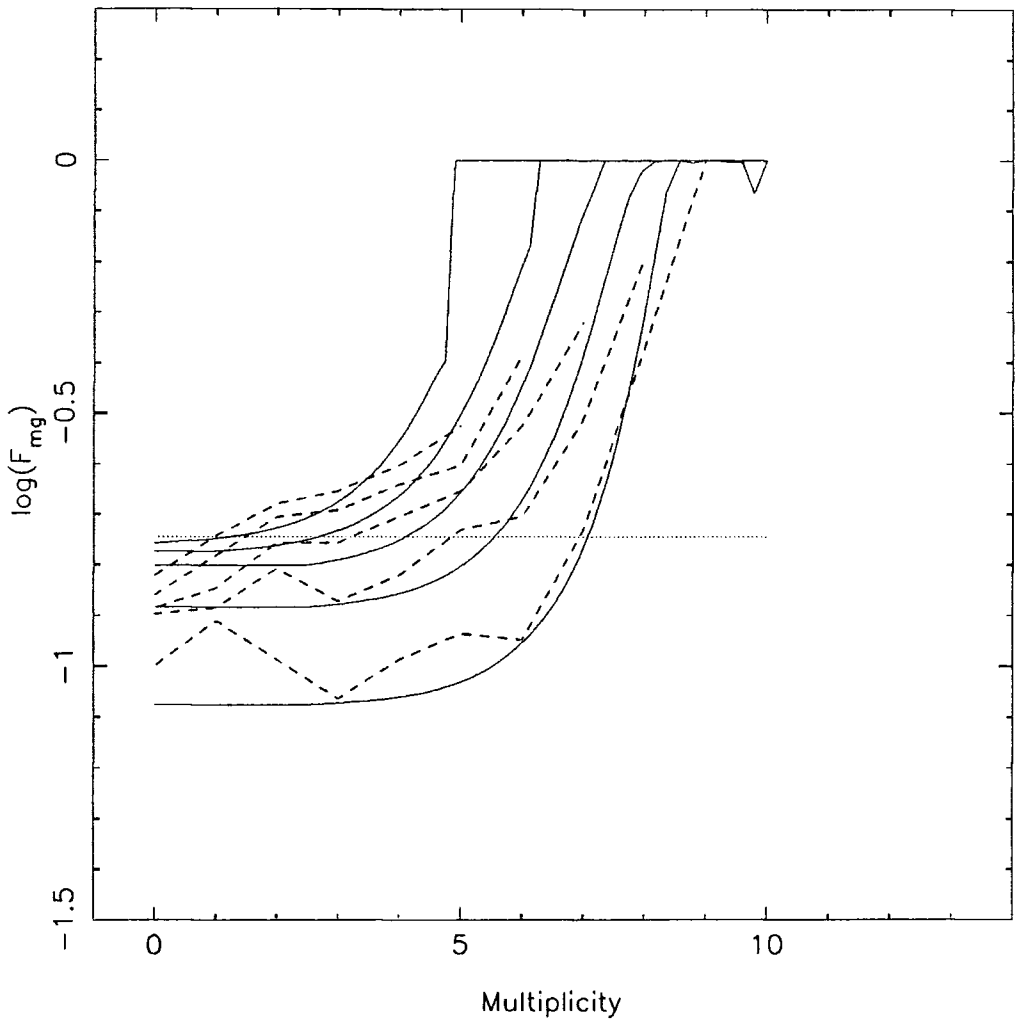

Figure 5.4. Comparison of the *mass fraction* (ie., the fraction of the mass contained today in the most massive groups that is bound into groups more massive than M at a previous epoch) calculated from the *joint multiplicity function* (smooth solid lines) with that measured in the simulations of EFWD. The last five output times from the simulations are shown as dashed lines. This plot shows the case of $n = 1$. The parameters used to define the theoretical curves are given in Table 5.1.

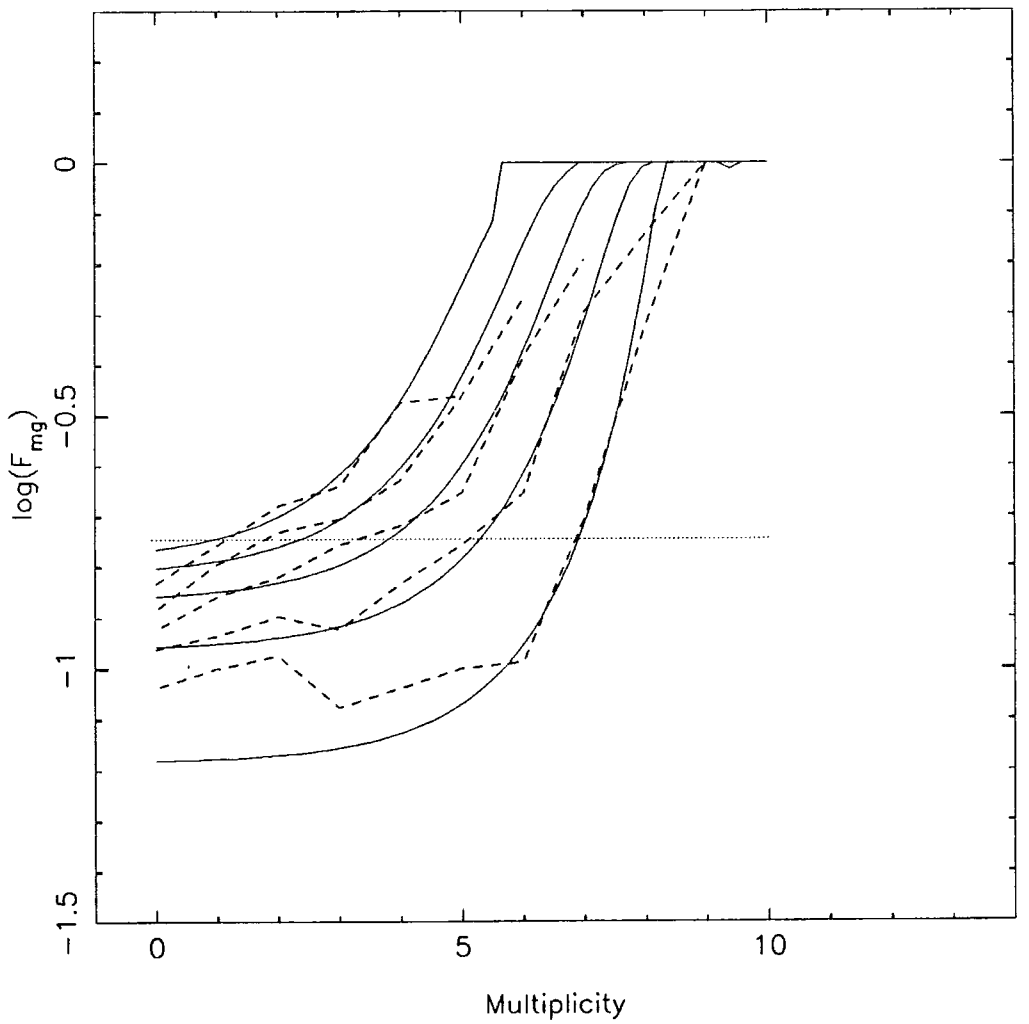

Figure 5.5. As for Figure 5.4, but for the case of $n = 0$.

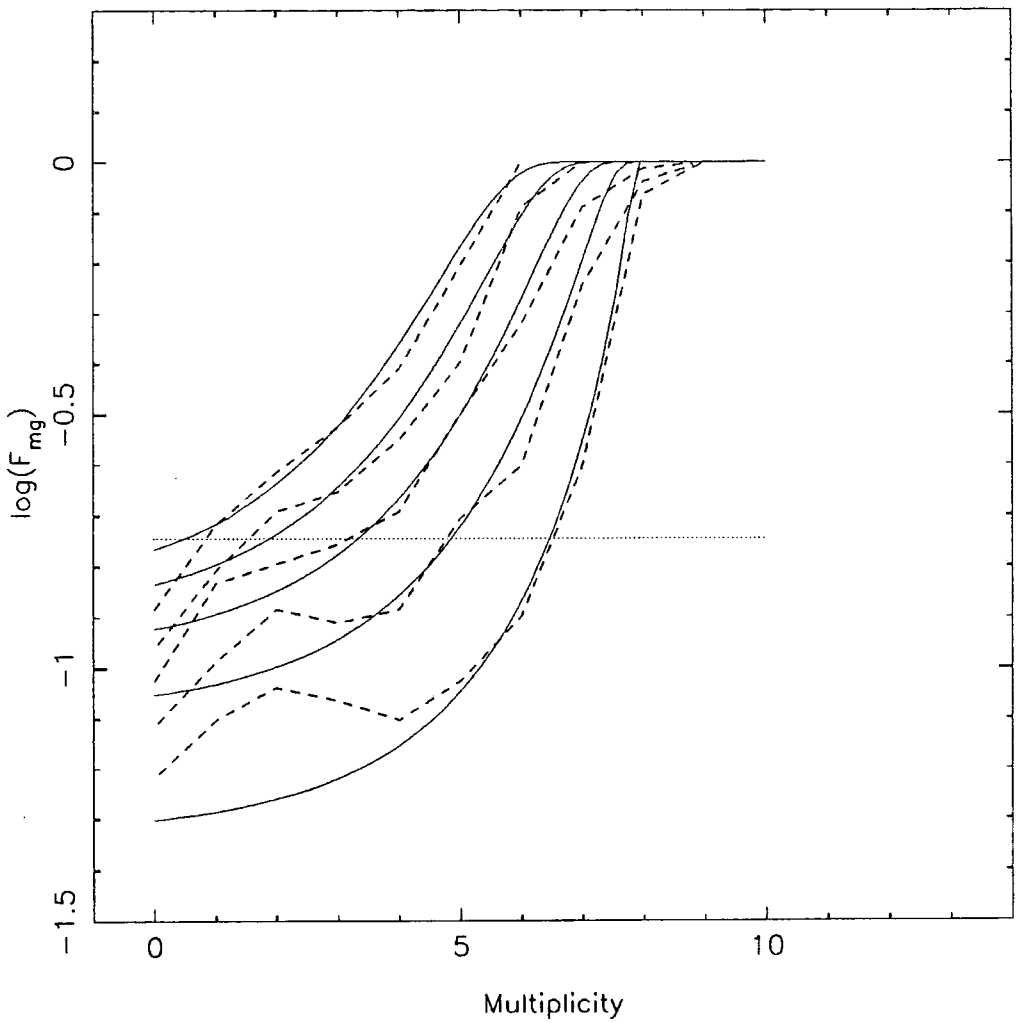

Figure 5.6. As for Figure 5.4, but for the case of $n = -1$.

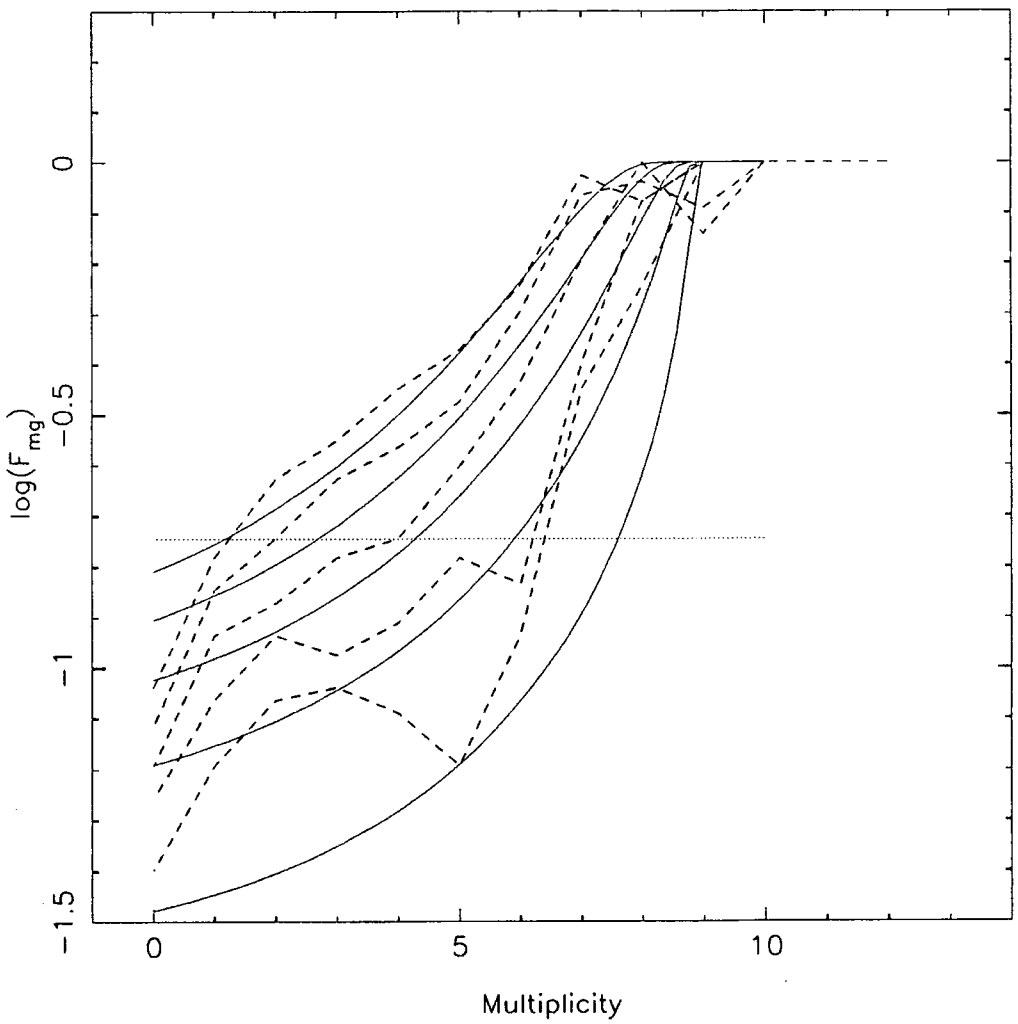

Figure 5.7. As for Figure 5.4, but for the case of $n = -2$.

5.3 Application to the Evolution of Groups of Galaxies

In order to illustrate the manner in which a cluster of galaxies builds up from the infall of smaller groups, it is convenient to divide groups into two types above and below a mass scale M_s. We apply the multiplicity fractions derived previously (Equations 5.15 and 5.17) to address problems relating to the mass flux of groups through the mass scale M_s.

At epoch z, the fraction of the final mass of a cluster that is contained in low mass groups (ie., $M < M_s$) is related to the conditional multiplicity fraction (Equation 5.15) by:

$$F_s(z, M') = \int_{M_s}^{\infty} \tilde{f}(M, z|M')dM \tag{5.24}$$

where $\tilde{f}(M, z|M') = \tilde{f}(M, \delta_c(z)|M', \delta_c(0))$ in the notation of Equation 5.15.

$$= \int_{u_s}^{\infty} \frac{2}{\sqrt{2\pi}} \frac{z}{\Delta^3} \exp\left(-\frac{z^2u^2}{2\Delta^2}\right) du$$

in the notation of Equations 5.19. After some working this can be rewritten in terms of the complementary error function:

$$F_s(z, M') = \text{erfc}\left[\frac{z}{\sqrt{2}.\Delta_s}\left(\frac{M_s}{M_*(0)}\right)^{(n+3)/6}\right]$$

where the final cluster mass enters through $\Delta_s = \left(1 - \left(\frac{M_s}{M'}\right)^{(n+3)/3}\right)^{1/2}$.

We apply this formula directly to calculate the epoch at which half of the present-day mass of a cluster is bound into higher mass groups (ie., $M > M_s$). Setting $F_s(z_s, M') = 1/2$ gives:

$$z_s = \frac{0.97}{\left(M_s/M_*(0)\right)^{(n+3)/6}}\left(1 - \left(\frac{M_s}{M'}\right)^{(n+3)/3}\right)^{1/2} \tag{5.25}$$

For the case $M_s = M_*(0)$, z_s is plotted for each of the spectral indices in Figure 5.8. Its behaviour may be readily understood as follows. In the limit $M' \to M_s$, $z_s \to 0$, and as $M' \to \infty$, $z_s \to z_\infty = 0.97\left(M_s/M_*(0)\right)^{-(n+3)/6}$; however the transition between the two extremes is sensitive to the spectral index. For $n = +1$, z_s reaches 90% of its final value at $5.6M_s$, ie., other than the small range of groups that have only recently grown through M_s, all large present-day groups assembled half their mass into groups more massive than

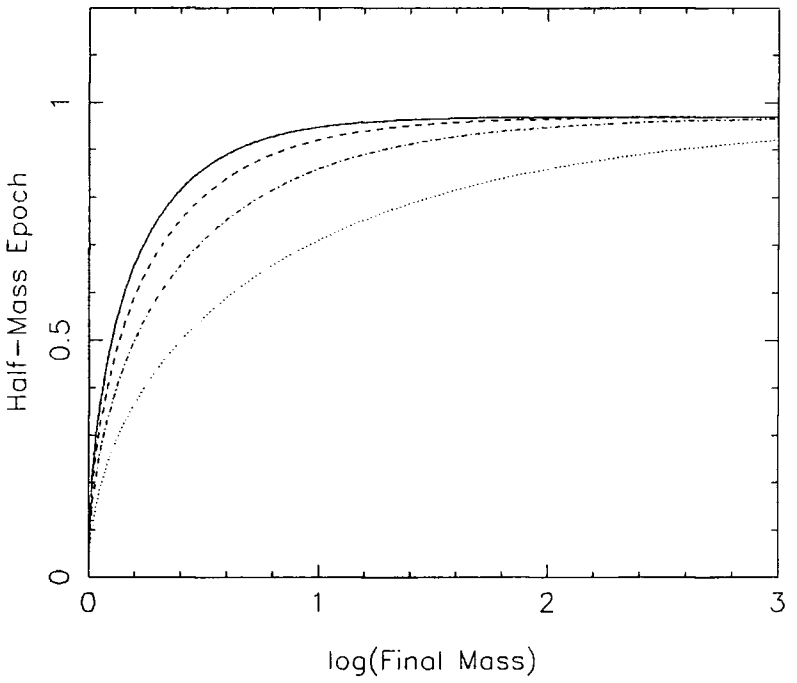

Figure 5.8. This figure shows the redshift at which half the present-day mass of a group is bound into groups more massive than the 'scale mass', M_s. It is plotted as a function of the Log (to base 10) of the present-day mass (in units of $M_*(0)$) for the case $M_s = M_*(0)$. The four curves show the effect of altering the spectral index of the initial perturbations. The solid line corresponds to $n = +1$; the dashed line to $n = 0$; the dot-dashed line to $n = -1$; and the dotted line to $n = -2$. All the curves tend to an asymptotic redshift of 0.97.

M_s at very similar epochs. On the other hand, z_s varies more slowly with M' for a flat initial power spectrum ($n \leq -2$). This leads to a somewhat stronger correlation between the present-day mass of a cluster and the history of its evolution.

We have not yet exploited the full information contained in the function F_s. The growth of F_s with time gives us information on the rate at which the mass contained in groups smaller than M_s is being accumulated into groups more massive than M_s. It is helpful to distinguish the two ways in which this growth may occur: (1) small groups ($M < M_s$) are accreted onto (a few) much larger condensations ($M > M_s$); (2) a few small groups, all having mass less than M_s, coalesce to produce a new massive condensation, this condensation later merging with other proto-cluster cores of similar size. Which of these mechanisms is dominant depends on the scale mass (M_s), the typical group mass (M_*), the present-day cluster mass (M') and the spectral index (n), and cannot readily be determined without recourse to numerical simulations. We will refer to $\partial F_s/\partial t$ as the *infall rate* — visualising it as the rate at which matter is infalling into the proto-cluster, either directly by accretion onto pre-existing proto-cluster cores, or by the creation of new proto-cluster core which subsequently coalesce with their longer established counter-parts. Note that we do not mean to imply that the proto-cluster is dominated by a single very massive condensation.

Up until this point it has not been necessary to distinguish between redshift (or the expansion of the universe) and time. However, as we will wish to apply the present results to systems in which the natural time scale is set by the clock of stellar evolution, it is necessary to derive the growth rate of F_s per unit proper time:

$$R_{\rm infall} = \frac{\partial F_s}{\partial t} = \frac{\partial F_s}{\partial z}\cdot\frac{dz}{dt}$$

$$= \frac{2}{\sqrt{2\pi}}\frac{\left(M_s/M_*(0)\right)^{(n+3)/6}}{\Delta_s}\cdot\frac{2}{3}(1+z)^{5/2}.\exp\left[-\frac{z^2}{2\Delta_s^2}\left(\frac{M_s}{M_*(0)}\right)^{(n+3)/3}\right] \qquad (5.26)$$

The infall rate is plotted in Figures 5.9 and 5.10 for initial power spectra with $n = 0$ and -2 respectively. We have set $M_s = M_*(0)$; the different line styles show final masses $M'/M_*(0) = 1.5, 3.0, 10$ and 1000. Firstly, we note that 'infall' for a given final mass peaks

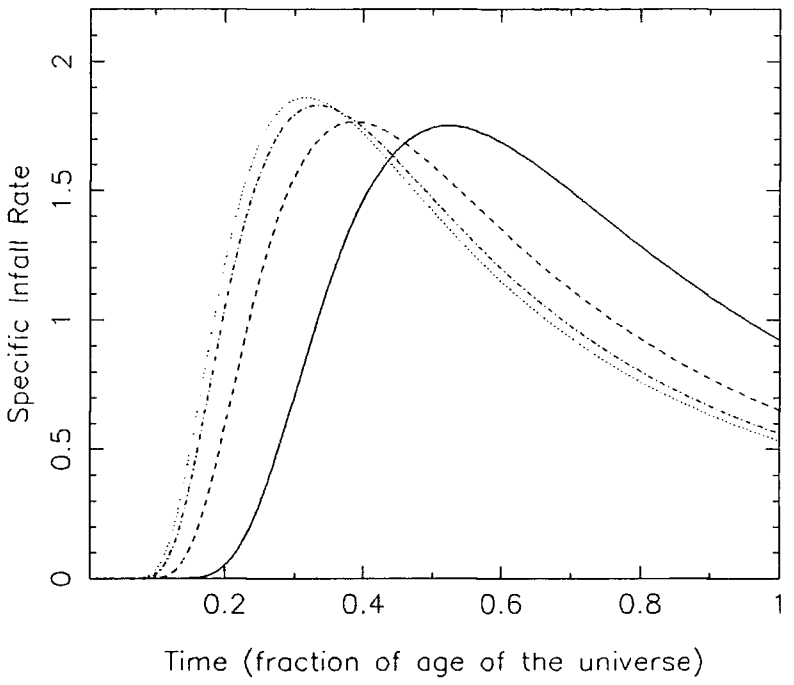

Figure 5.9. This figure shows the time dependence of the *infall rate* of small groups in to larger ones for a steep ($n = 0$) initial power spectrum. Time, expressed as a fraction of the total age of the universe, advances form left to right, ie., the present is at 1.0. The rate of infall is expressed as the fraction of the present-day mass of the group infalling per unit time. The four curves show the infall in regions which collapse to form present-day groups of masses 1.5 (solid line), 3.0 (dashed), 10.0 (dot-dashed) and 1000.0 (dotted). All masses have been expressed in terms of the typical present-day mass, $M_*(0)$, and we have divided small and large groups at $M_s = M_*(0)$.

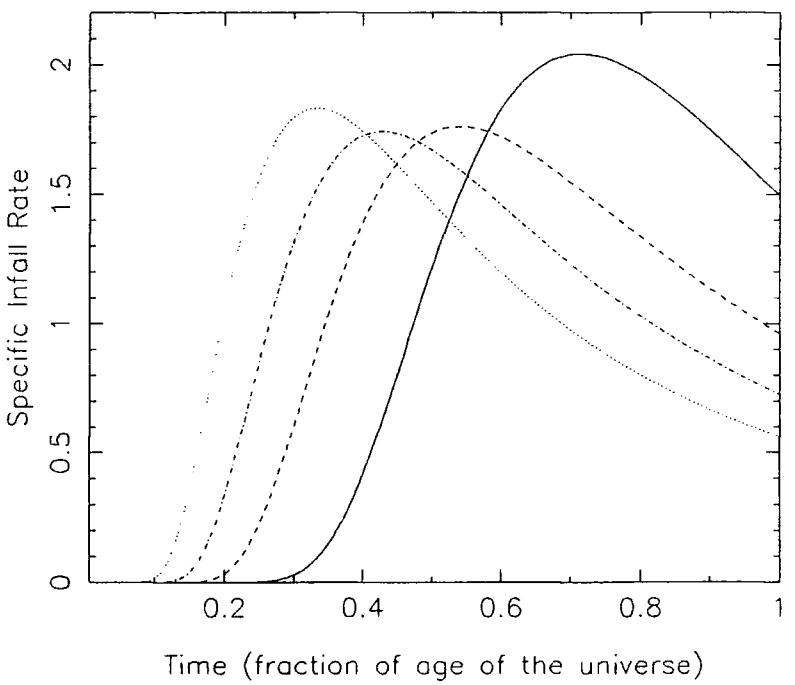

Figure 5.10. The time dependence of the infall rate for a flat ($n = -2$) power spectrum. The different curves show the effect of varying the present-day mass as described in Figure 5.9.

at a well defined time. The occurrence of this peak is purely a result of the compression of the relationship between redshift and time — the infall rate *per unit redshift* increases monotonically to the present-day. The epoch at which the peak infall rate occurs depends on final mass in the same manner as z_s. Secondly, we note that although there is a well defined peak to the infall rate, the fall-off is very slow so that the peak rate is enhanced over that at the present-day by a factor of only ~ 3, ie., in this model the infall of small groups into rich clusters is very much an on-going process.

It is interesting to apply this equation to compare the present-day infall rates of clusters of various masses.

$$R_{\rm infall}(0) = \frac{4}{3\sqrt{2\pi}} \frac{\left(M_s/M_*(0)\right)^{(n+3)/6}}{\Delta_s} \tag{5.27}$$

Comparison with Equation 5.25 shows that the present infall rate is intimately connected with the epoch at which half the mass of the present-day cluster became bound into groups more massive than M_s. (ie., z_s):

$$R_{\rm infall}(0) \propto \frac{1}{z_s}. \tag{5.28}$$

Yet further information on the evolution of groups may be extracted from the joint multiplicity function, Equation 5.17. We address the question of the destiny of the groups that are more massive than M_s (an arbitrary mass scale) at an early epoch. The fraction of these groups that become bound into groups of mass M' at the present epoch is:

$$f(M'|>M_s,z)dM' = \frac{\int_{M_s}^{\infty} \rho(M,z,M')dMdM'}{\int_{M_s}^{\infty} \rho(M,z)dM}$$

$$= \frac{\int_{u_s}^{\infty} \frac{4}{2\pi}\frac{1}{\Delta^3} z \exp\left(-\frac{z^2u^2}{2\Delta^2}\right) \exp\left(-\frac{u'^2}{2}\right) dudu'}{\int_{u_s}^{\infty} \frac{2}{\sqrt{2\pi}}(1+z)\exp\left(-\frac{(1+z)^2u^2}{2}\right) du}$$

in the notation of Equations of 5.19. The integrals in this equation can be written as complimentary error functions:

$$f(M'|>M_s,z)dM' = \frac{2}{\sqrt{2\pi}} \exp\left(-\frac{u'^2}{2}\right) \frac{\mathrm{erfc}\left(\frac{z}{\sqrt{2}.\Delta_s}u_s\right)}{\mathrm{erfc}\left(\frac{(1+z)}{\sqrt{2}}u_s\right)} du'$$

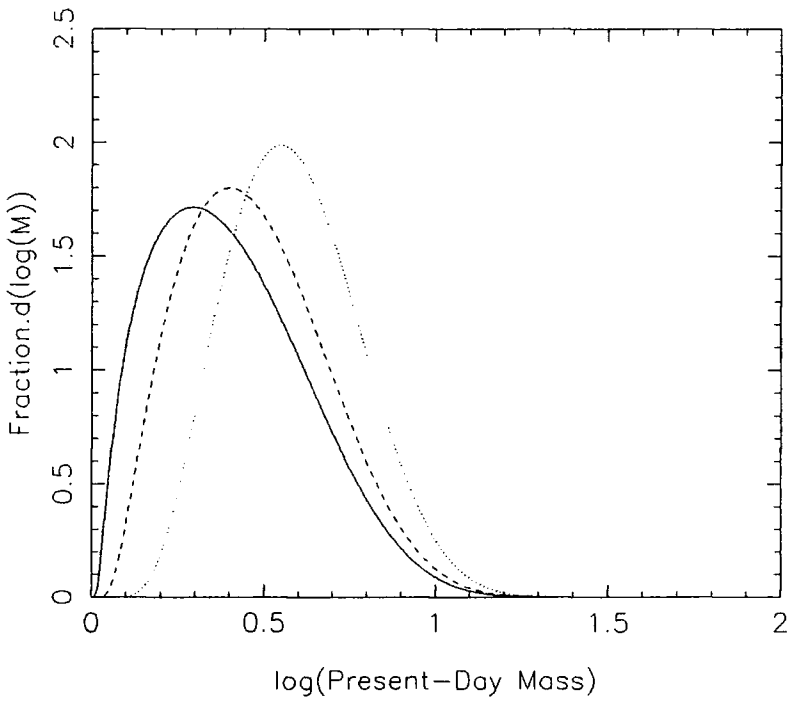

Figure 5.11. A group which is more massive than M_s at epoch z will evolve to become bound into a group of mass M' at the present epoch. This figure shows the distribution of M' for groups that become more massive than $M_s = M_*(0)$ at redshifts $z = 0.5$ (solid line), 1.0 (dashed line) and 2.0 (dotted line). These groups contain respectively 13%, 5% and 0.3% of the total mass of the universe. In this figure we illustrate the case $n = 0$.

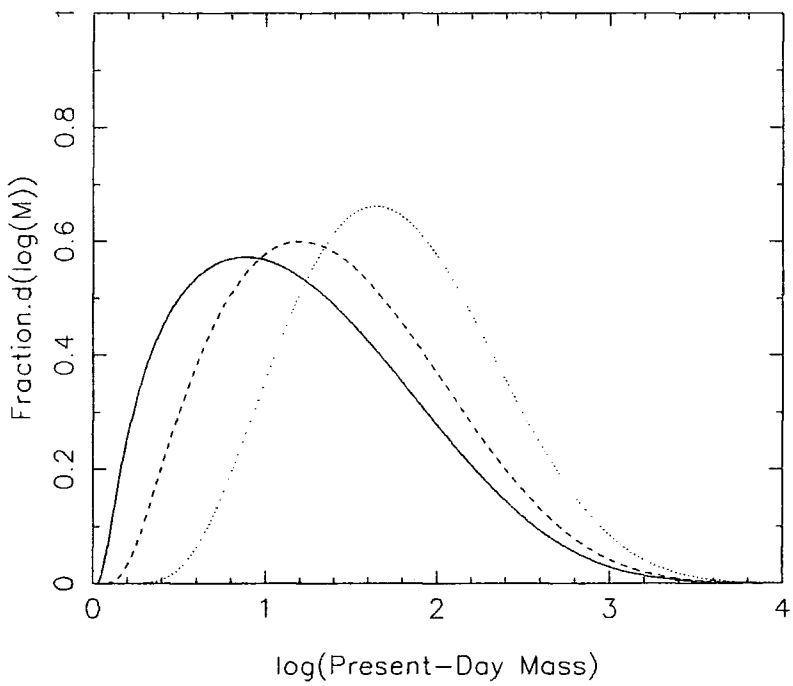

Figure 5.12. This figure presents the same information as Figure 5.11, but for the case of a flat ($n = -2$) power spectrum. Because we have chosen the special case of $M_s = M_*(0)$, the groups we distinguish in each of the curves contain the same fraction of the total mass of the universe.

$$= \frac{1}{\sqrt{2\pi}} \left(\frac{n+3}{3}\right) \left(\frac{M'}{M_*(0)}\right)^{(n+3)/6}$$

$$\times \exp\left(-\frac{1}{2}\left(\frac{M'}{M_*(0)}\right)^{(n+3)/3}\right) \frac{\mathrm{erfc}\left[\frac{1}{\sqrt{2}.\Delta_s}\left(\frac{M_s}{M_*(z-1)}\right)^{(n+3)/6}\right]}{\mathrm{erfc}\left[\frac{1}{\sqrt{2}}\left(\frac{M_s}{M_*(z)}\right)^{(n+3)/6}\right]} \frac{dM'}{M'} \qquad (5.29)$$

This equation is plotted for $n = 0$ and $n = -2$ spectral indices in figures 5.11 and 5.12 respectively. Its form can be qualitatively understood as follows. Apart from the factor formed by the ratio of the two error functions, the distribution follows that of the universal multiplicity function at the present epoch. However, the relationship between the mass scale, M_s and the present-day mass enters through the factor Δ_s in the argument of the upper error function. At values of M' close to M_s, Δ_s is small, forcing the value of the complementary error function towards zero. The effect is to cut-off the distribution from zero to slightly above M_s. For values of M' considerably larger than M_s, $\Delta \rightarrow 1$ and the ratio of the error functions reaches a constant value. This factor renormalises the distribution so that the total area under each of the curves remains at unity. From the study of the figures, it can be seen that the cut-off imposed by Δ_s becomes less sharp as the redshift at which the high mass groups are selected increases. Therefore, the groups that become massive at early times tend to evolve to become the most massive groups later on. Very few of the massive groups that we identify at epoch z will fail to grow significantly in their subsequent evolution. This effect is closely related to the ***natural biasing*** mechanism discussed by White et al., 1987.

5.4 Application to Galaxy Evolution and the Stellar Populations of Early-Type Galaxies

In this section we illustrate the intended application of our calculations. We wish to consider the effect that the evolution of the environment will have on the star formation properties of the galaxies that are contained within it. Obviously, this is an extremely complicated problem involving many poorly understood phenomena. These phenomena are often highly stochastic (eg., the collision between galaxies), and may be sensitive to the details

of the internal structure of the groups and clusters (eg., their density profile, or the degree to which the subclumping survives violent relaxation). Feed back effects may also be of importance (eg., ram-pressure stripping of gas from galaxies is only effective if the density of intra-cluster gas is raised to a sufficient level by other processes). To treat these effects correctly is far beyond the scope present work, but we will introduce an extremely simplistic (and unrealistic) model for their net effect in order both to demonstrate the power of the analytic techniques that we have developed in this work, and to set the stage for more comprehensive models of galaxy evolution.

The 'toy-model' we adopt for galaxy evolution is as follows. We treat galaxies that are isolated or in low mass groups as being in a steady-state. We imagine that the gas ejected from high-mass stars in the final stages of their stellar evolution is continually recycled to form new generations of stars. We ignore the fraction of gas that is locked up into low-mass stars, and the possible infall of fresh primordial gas from the halo. In regions of higher density, the environment plays a more active role in determining the star formation rate by stripping the galaxy of its available gas supply. We make the following simplifying assumptions.

(1) There is a one-to-one correspondence between the importance of the environmental processes in a group (that act to truncate star formation) and the *total mass* of the group.

(2) The environment acts abruptly to truncate star formation in all galaxies that are contained in groups with masses greater than M_{ev}; in groups of lower mass the galaxies are unaffected. We ignore any variation in the effectiveness, or speed of this truncation — it is solely a threshold effect.

(3) The orbits of galaxies that infall into a group or cluster are rapidly mixed into the same phase-space as the original galaxies. It is therefore impossible to distinguish the different 'populations' of galaxies, ie., to separate those that have recently arrived in the cluster, from those that were present in the most massive clumps at early times.

(4) We ignore the growth of masses on scales below that of a typical galaxy. Physically, this corresponds to disregarding dwarf galaxies and extra-galactic HII regions.

We do not attempt to rigorously justify these assumptions — indeed, it can readily be argued that they are incorrect. Rather, we outline our reasons (beyond mathematical convenience) for their choice. Assumptions (1) and (3) are in accord with underlying philosophy of the Press-Schechter theory, ie., we are assuming that the condensed point-like objects formed in the non-linear collapse phase form a single parameter family whose properties depend solely on total mass. Note that in applying assumption (1) to objects formed over a range of epochs, we have disregarded the changing mean *density* of the universe in which the objects form. The effect that this can be expected to have on the structure of these condensations is discussed in Kaiser (1986). An extension to the model presented here is clearly possible. Assumption (3) is equivalent to arguing that the evolving group/cluster potential is undergoing large fluctuations that are very effective at scattering galaxies into new random orbits (ie., violent relaxation is assumed to be highly efficient at phase-space mixing). Assumption (2) is obviously incorrect — large numbers of early-type galaxies *are* found in the field. We argue that as we are only interested in comparing the effects arising from the *evolution* of the gravitational structure (as opposed to the effects arising from the physics of the truncation process itself), it is helpful to replace the true probability of the truncation of star formation, $P_{\rm trunc}(M,...)$, with a step function (ie., threshold) so that our attention is focused on only one part of this inordinately complicated problem. To summarise, the model for the evolution of galaxies that we have proposed has limited relevance to the real universe, but we justify its adoption on the basis that it is a simple starting point incorporating the absolute minimum of *ad hoc* parameters. As we will show, the questions we wish to formulate have analytically tractable solutions that illustrate the important role played by the evolution of the environment in determining the evolution of individual galaxies. There is clearly, however, a need for more sophisticated models for the evolution of a galaxy in a steady-state environment. Great progress is to be made in the near future by uniting these two approaches.

What are the questions we wish to ask? As the PS theory only gives statistical information about ensembles of clusters, we must only ask questions about the properties of a typical galaxy in a typical cluster (though we may choose its total mass). We may extract the following four pieces of information from the conditional and joint multiplicity functions (Equations 5.15 and 5.17):

(1) How does the infall of *unevolved*† galaxies vary with time?

(2) How does the present-day infall rate of *unevolved* galaxies depend on the cluster mass?

(3) We define z_{ev} as the epoch at which half of the final mass of the cluster is contained in groups with masses greater than M_{ev}. This defines the mean 'age' (ie., epoch of last star formation) for galaxies in the cluster. How does z_{ev} vary with the cluster mass?

(4) What is the present-day environment of the galaxies in which star formation was truncated at relatively early times?

Before attempting to answer the questions above, it is useful to review the likely values of the parameters n, $M_*(0)$ and M_{ev}. Previous studies (Bachall, 1979, Moore et al., 1990) have used the CfA redshift survey to determine the combined luminosity function of galaxies, groups and clusters (we refer to this as the All Galaxy Systems, AGS, luminosity function). If the mass-to-light ratio of galaxies is universal, then $L.\Phi_{AGS}(L)$ may be directly compared with the universal (Press-Schechter) multiplicity function in order to determine values for the parameters $M_*(0)$ (given a value for M/L) and the density field spectral index, n. Moore et al. (1990) find that the best fit is given with $n = -1.5$ and $L_{*,AGS} = 3.9 \times 10^{10} L_\odot \approx 5L_{*,galaxy}$. A large cluster today, for example Coma, has total luminosity (Moore et al., 1990) $9.5 \times 10^{12} L_\odot$, ie., about $240 L_{*,AGS}$. The smaller Virgo cluster has a luminosity of $\approx 80 L_{*,AGS}$. M_{ev} is much more difficult to determine directly, as it is no more than a

† We refer to galaxies that are isolated or in small groups of mass less than M_{ev} as *unevolved*. Galaxies in more massive groups are referred to as *evolved*. The nomenclature indicates whether the galaxy continues to actively form stars.

convenient theoretical concept. However, as a typical group at the present epoch contains 5 average galaxies, it seems reasonable to set $M_{ev} = M_*(0)$. With these parameters, 32% of galaxies will be of *evolved* type at the present epoch. Considering the simplicity of our model, this fraction is in satisfactory agreement with the proportion of galaxies having early-type morphology in the real universe ($\sim 20\%$).

5.4.1 The evolution of the infall rate

The infall rate of *unevolved* galaxies (per Gyr, per unit present-day mass) in to clusters a various present-day masses can be directly obtained from Equation 5.26 by setting $M_s = M_{ev}$. It is plotted in Figure 5.13, with solid lines showing the curves defined by the parameters described above. It is seen that there is a well defined epoch at which the infall reaches a maximum; subsequently, the rate at which *unevolved* galaxies are accreted falls off, and the merging of small (proto-) clusters, rich in *evolved* galaxies, becomes the more dominant mechanism by which cluster grows to its present-day mass. However, the decay of the infall rate is relatively slow — even for an extremely rich cluster (eg., $M' = 1000M_*(0)$, $\approx 4L_{Coma}$ if the mass-to-light ratio is independent of mass), it is reduced by a factor of only 3 by the present day. In this model, therefore, the transition of infalling galaxies between *unevolved* and *evolved* states *is very much an on-going process at the present time.*

Before advancing to consider other aspects of the problem, we take advantage of the analytical nature of our model to investigate its sensitivity to the values chosen for the parameters. $M_*(0)$ is solely a normalisation factor. The effect of setting the spectral index to $n = 0$ can be seen in Figure 5.9. Principally, the effect is to make the histories of the clusters of different masses more similar (this is discussed below) but the qualitative evolution of the infall is not much affected. More dramatic effect is made by altering the parameter M_{ev}. Within our loose definition, it might be more reasonable to associate the strong environmentally driven evolution of galaxies with groups *more* massive than $M_*(0)$. In Figure 5.13, dashed lines show the infall rate when the distinction between *evolved* and *unevolved* galaxies is made at a group mass of $5M_*(0)$ (ie., containing ~ 25 typical galaxies). It can be seen

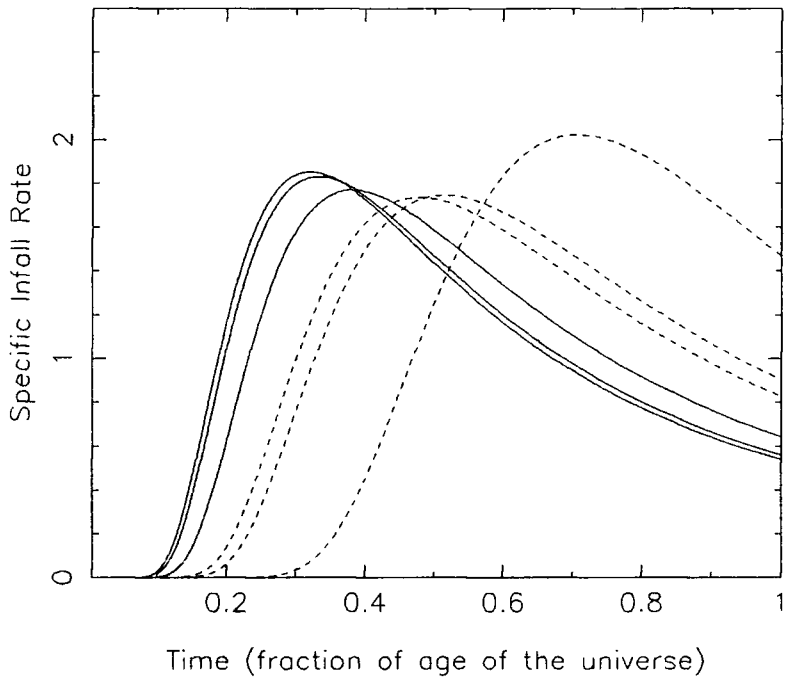

Figure 5.13. The time dependence of the infall rate of *unevolved* galaxies into the proto-cluster centres that will combine to form a single cluster of mass M' at the present epoch. Solid curves show the infall rate for present-day clusters of $M' = 1000$, 100 and 10 (peaking at successively later times) when the distinction between *evolved* and *unevolved* galaxies is made at $M_{ev} = 1$. Dashed curves present the same information for $M_{ev} = 5$. The units used in this figure are described in Figure 5.9. The spectral index has been set to -1.5, as is estimated from observation.

that the peak infall rate is shifted much more towards the present, amplifying the conclusion that we reached with our original selection of parameters. Only if we substantially *reduce* M_{ev} (so that we are, perhaps, drawing a distinction between the infall of isolated dwarf and giant galaxies) does the infall rate decay significantly by the present day.

5.4.2 The dependence of the infall rate on cluster mass

Focusing our attention on the present epoch, we consider how the infall of *unevolved* galaxies varies as a function of the cluster mass. Inspection of the solid line in Figure 5.14 shows that the dependance is strong only for groups with masses close to M_{ev}. As the notion of a sharp onset of processes acting to truncate star formation at a group mass of M_{ev} is clearly artificial, the simple model cannot be expected to bear much relation to reality. For example, we might hope to be able to pick-out *transition* galaxies that are between the *unevolved* and *evolved* states. Our simple model predicts that the fraction of these galaxies is zero in groups with masses less than M_{ev}, but rises rapidly to become constant in larger groups and clusters. If, however, a more sophisticated model was taken for the processes leading to the termination of star formation (eg., if we modelled it as a stochastic process with the probability of truncation smoothly increasing with group mass), then the rate of growth of the fraction of *transition* galaxies would reflect only the *detailed form* of this probability function. Therefore, we restrict ourselves to commenting that the model predicts that the number of transition galaxies is roughly constant in clusters that are much more massive than M_{ev}.

5.4.3 The half-mass epoch

We define z_{ev} as the epoch at which at which half of the galaxies in the present-day cluster have become *evolved*. In our simple model, the present-day infall rate and z_{ev} are intimately connected as shown in Equation 5.28. The comments we made above regarding the present-day infall rate apply equally here — the rudimentary model predicts a very sharp rise in z_{ev} from zero at M_{ev} to reach within a small fraction of its asymptotic value in groups of

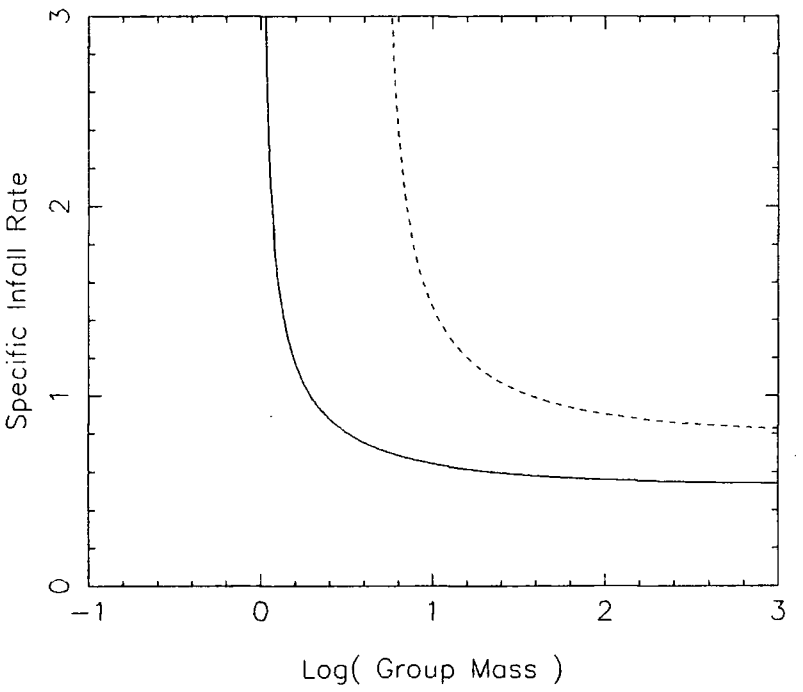

Figure 5.14. The dependence on the present-day infall rate of *unevolved* galaxies on the cluster mass, M'. The solid line shows the infall when the distinction between *evolved* and *unevolved* galaxies is made at $M_{ev} = 1.0$; the dashed line shows the effect setting M_{ev} to 5.0. As in all the figures, masses are quoted in units of $M_*(0)$. The unit of time is the present age of the universe.

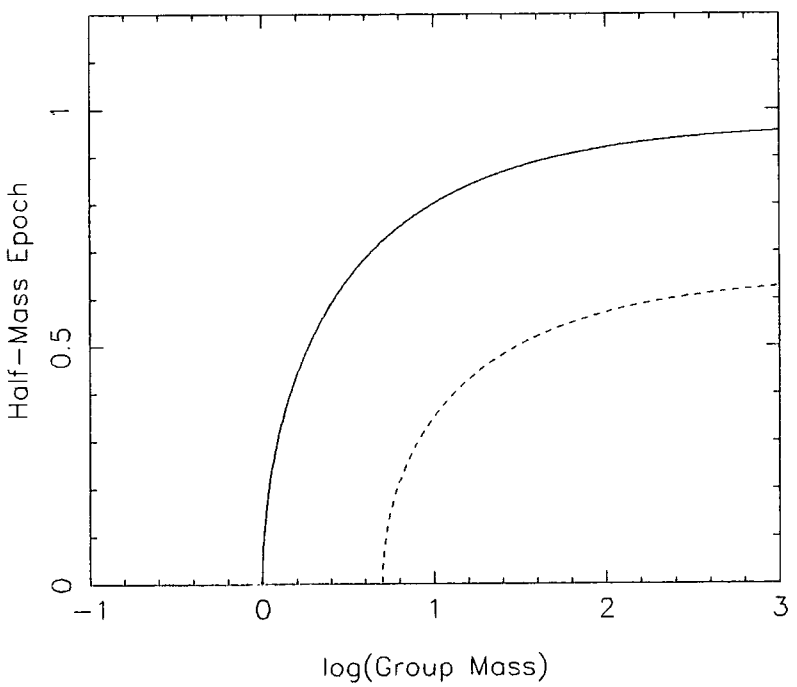

Figure 5.15. The redshift by which half of the galaxies in the present-day cluster, M', had become *evolved*. The solid and dashed lines distinguish $M_{ev} = 1.0$ and 5.0 respectively.

mass $3M_{ev}$ (Figure 5.15). The extreme abruptness of this transition is, however, an artifact of the model, a more realistic prescription for the galaxian evolution would smooth out the step. The degree of smoothing is, at present, difficult to determine.

There is a further difficulty that prevents us making a comparison between the model presented here and the 'Age'–Environment correlation that we have investigated in the previous chapters — we question the validity of our assumption that the galaxies infalling into the cluster at later times become completely mixed in with the original galaxies. In a very different context, studies of the mergers of spiral galaxies (eg., White, 1980) have shown that violent relaxation does not cause complete mixing of the systems, ie., the particles that are most tightly bound in the intial system are also the most tightly bound in the final system. We suggest that this incomplete relaxation will also occur in the evolving proto-cluster potential. The final structure of a *massive* cluster will then have an onion-shell structure (in phase space), the core being dominated by the original galaxies, the newly infallen galaxies being predominant in the outer parts. In less massive groups, the shell structure may be eroded by two-body relaxation. Clearly, this additional dynamical phenomenon complicates any comparison between the elementary theory and the observed properties of galaxies in the central parts of rich clusters.

5.4.4 The present-day environment of 'old' galaxies

Replacing M_s by M_{ev} in Equation 5.29 gives the distribution of galaxies that had become *evolved* before the epoch z amongst the present-day groups. The distribution is plotted in Figure 5.16 for several redshifts. The figure shows that the 'old' galaxies tend to be incorporated into more massive groups at the present time. However, the effect is rather to suppress the incorporation of 'old' galaxies into lower mass clusters than to enhance their inclusion in the high mass ones. As a result, the major fraction of the mass in even the most massive clusters comes from galaxies that have average age, despite the fact that the cluster has been seeded at an earlier time. This produces the weak dependence of the cluster formation history on cluster mass that we see in, eg., Figures 5.14 and 5.15. We

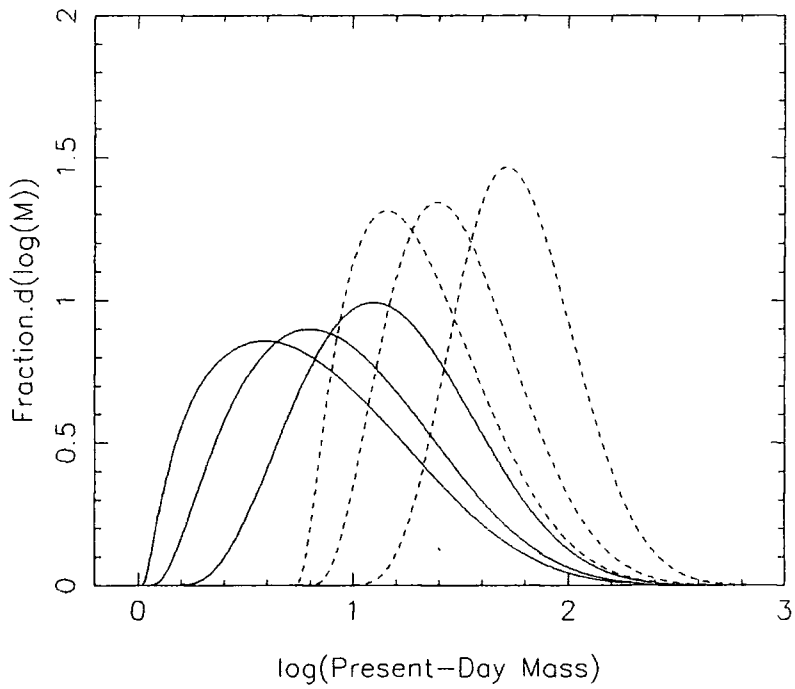

Figure 5.16. The distribution (multiplicity fraction) of the present-day clusters that contain galaxies that had become *evolved* at redshifts of 0.5, 1.0 and 2.0 (peaking from left to right respectively). Solid lines show the case $M_{ev} = 1.0$; dashed lines the case $M_{ev} = 5.0$.

devote further time to understanding how Figures 5.15 and 5.16 are to be reconciled at the end of Section 5.5.

5.5 Summary and Discussion

In the previous sections, we have presented the mathematical results that provide a frame work for the interpretation of the 'fosil record' of a galaxy's evolution that is contained in its present-day stellar populations. As the results have been interspersed with complex mathematical derivations, it is convenient to collect them together here.

We start by parameterising the initial conditions in the universe in terms of a power-law of density fluctuations with spectral index n. The first of these parameters is directly related to the typical mass of collapsed objects at the present time ($M_*(0)$), and it is convenient to make this substitution in all subsequent formulae. In terms of the parameters $M_*(0)$ and n, the Press-Schechter theory predicts the form of the *Universal Multiplicity Function* of groups at epoch z to be:

$$\rho(M,z)dM = \rho_0 \frac{1}{\sqrt{2\pi}} \left(\frac{n+3}{3}\right) \left(\frac{M}{M_*(z)}\right)^{(n+3)/6} \exp\left[-\frac{1}{2}\left(\frac{M}{M_*(z)}\right)^{(n+3)/3}\right] \frac{dM}{M} \qquad (5.2)$$

where $M_*(z) = (1+z)^{-6/(n+3)} M_*(0)$. The evolution of this distribution is self-similar; ie., its shape remains unchanged, the distribution only altering in its scale (defined by $M_*(z)$). The evolution is more rapid for smaller, or more negative, values of n.

In Section 5.2.4, we have extended the PS formalism to calculate the multiplicity fraction of groups given the added constraint that they must merge to form a cluster of size M' at the present epoch. We refer to this as the *Conditional Multiplicity Fraction.*

$$\tilde{f}(M,z|M')dM = \frac{1}{\sqrt{2\pi}} \left(\frac{n+3}{3}\right) \frac{1}{\Delta^3} \left(\frac{M}{M_*(z-1)}\right)^{(n+3)/6} \exp\left[-\frac{1}{2\Delta^2}\left(\frac{M}{M_*(z-1)}\right)^{(n+3)/3}\right] \frac{dM}{M} \qquad (5.15)$$

where $\Delta = \left(1-(M/M')^{(n+3)/3}\right)^{1/2}$. This differs from the previous function in two respects: (1) the evolution in a region of large final mass ($M' \gg M$) is 'accelerated' over that in

the universe as a whole; (2) the correlation between density fluctuations on different scales suppresses the formation of subclumps close to M' before the final epoch. The interplay between these two effects is sensitive to the spectral index n.

Combining the Conditional Multiplicity Fraction (Equation 5.15) with the distribution of the masses of present-day clusters (M') specified by the Universal Multiplicity Function (Equation 5.2) as is described in Section 5.2.5, we obtain the multiplicity function of masses M at epoch z that combine to form a group of mass M' at the present epoch. We refer to this as the *Joint Multiplicity Function.*

$$\rho(M,z,M')dMdM' = \frac{\rho_0}{2\pi}\left(\frac{n+3}{3}\right)^2\frac{1}{\Delta^3} \times\left(\frac{M}{M_*(z-1)}\right)^{(n+3)/6}\exp\left[-\frac{1}{2\Delta^2}\left(\frac{M}{M_*(z-1)}\right)^{(n+3)/3}\right] \times\left(\frac{M'}{M_*(0)}\right)^{(n+3)/6}\exp\left[-\frac{1}{2}\left(\frac{M'}{M_*(0)}\right)^{(n+3)/3}\right]\frac{dM}{M}\frac{dM'}{M'} \tag{5.17}$$

It is important to note that this multiplicity function is consistent with the universal distributions of M and M' — in Section 5.2.6 we demonstrate that integration of Equation 5.17 over M' gives the Universal Multiplicity Function of M at epoch z, and vice versa.

There is an important and fundamental difference between Equation 5.17 and the equivalent equation that would have been deduced by EFWD using the k-split approximation. In the formulae presented here, the enhancement in the hierarchy of group masses (caused by the presence of the long wavelength perturbation that will eventually collapse to form M') is independent of M'; M' enters only through the cross-correlation between the mass scales of M and M' (ie., through the factor denoted Δ in the formulae). In contrast EFWD attempt to allow for the total mass of the larger scale region by varying the overdensity of the long wavelength perturbation as a function of M'. This is incorrect — if the overdensity is averaged over the *whole* of M', it must be found to be $\delta_c(0)$ (ie., the critical overdensity for collapse at the present epoch), if it were found to be larger then the region would be absorbed into the collapse of an even larger object. As a result of the manner in which M' enters our formulae, the distribution of M is largely independent of M' if the scales are

sufficiently widely separated that cross-correlation effects are unimportant (ie., in the region where the k-split is a good approximation). This has important consequences when we come to compare the evolutionary histories of groups of differing M'.

In order to illustrate the evolution of groups by a simple example, we divide groups into two mass regimes at M_s. In doing this we have in mind a simple model for the environmentally driven evolution of galaxies. We calculate:

(1) The average epoch, z_s, at which galaxies make the transition between groups above and below M_s (given that at $z = 0$ they become bound into a group of mass M'):

$$z_s = \frac{0.97}{\left(M_s/M_*(0)\right)^{(n+3)/6}}\Delta_s \tag{5.25}$$

where the dependence of z_s on the mass M' enters through $\Delta_s = \left(1 - \left(\frac{M_s}{M'}\right)^{(n+3)/3}\right)^{1/2}$.

(2) The rate (in units of the age of the universe, and scaled to the mass of the present-day cluster) at which galaxies from low mass groups infall into the growing proto-cluster:

$$R_{\rm infall} = \frac{2}{\sqrt{2\pi}}\frac{\left(M_s/M_*(0)\right)^{(n+3)/6}}{\Delta_s}\cdot\frac{2}{3}(1+z)^{5/2}.\exp\left[-\frac{z^2}{2\Delta_s^2}\left(\frac{M_s}{M_*(0)}\right)^{(n+3)/3}\right] \tag{5.26}$$

(3) The rate at which galaxies from low mass groups infall into a cluster at the present time (this is a special case of (2) above):

$$R_{\rm infall}(0) = \frac{4}{3\sqrt{2\pi}}\frac{\left(M_s/M_*(0)\right)^{(n+3)/6}}{\Delta_s} \tag{5.27}$$

(4) The present-day distribution (in group mass M') of the mass contained in groups that exceed the mass scale M_s at, or before, redshift z:

$$f(M'|>M_s,z)dM' = \frac{1}{\sqrt{2\pi}}\left(\frac{n+3}{3}\right)\left(\frac{M'}{M_*(0)}\right)^{(n+3)/6} \times \exp\left(-\frac{1}{2}\left(\frac{M'}{M_*(0)}\right)^{(n+3)/3}\right)\frac{\mathrm{erfc}\left[\frac{1}{\sqrt{2.\Delta_s}}\left(\frac{M_s}{M_*(z-1)}\right)^{(n+3)/6}\right]}{\mathrm{erfc}\left[\frac{1}{\sqrt{2}}\left(\frac{M_s}{M_*(z)}\right)^{(n+3)/6}\right]}\frac{dM'}{M'} \tag{5.29}$$

Inspection of results (1)–(3) above shows that the history of a group of present-day mass M' (on the scale set by M_s) is strongly dependent on M' only if M' is close to M_s. As we have discussed above, this effect arises because the *mass* of the large-scale overdense region only modulates the smaller scale fluctuations through the cross-correlation of the density fluctuations (when averaged throughout the entire region). If M' is significantly larger than M_s, the effect is very weak. Study of the equations also shows that the modulation is stronger for flatter power spectra (ie., more negative n). However, it should be remembered that the rate of universal evolution is also more rapid in this case.

While our study shows that the more massive present-day clusters *do not* have significantly different average evolutionary histories (on group and galaxy mass scales) from their less massive counter parts, there *is* a strong tendency for the most massive groups at early times to be incorporated into the most massive clusters at the present-day. These two results may appear contradictory, but they are not. Confusion has arisen because we have not been careful to distinguish between masses that have been specified as a fraction of the present-day cluster mass (eg., in our calculation of z_s, Equation 5.25), and those that have been specified in absolute value (eg., in Equation 5.29).

For example, following the derivation of 5.25, we may calculate the epoch at which 1% of the present-day cluster mass is bound into massive groups:

$$z_{1\%} = \frac{3.65}{\left(M_s/M_*(0)\right)^{(n+3)/6}}\Delta_s$$

This function defines a series of curves similar to those displayed in Figure 5.8, but with the redshift axis rescaled. $z_{1\%}$ grows rapidly above M_s, but turns over so that there is little variation for $M' >\sim 10M_s$. It should, however, be noted that in a present-day group of mass $10M_s$ the mass in large ($> M_s$) groups at $z_{1\%}$ is implied to be $0.1M_s$. Clearly, this must be interpreted in a statistical sense, ie., approximately 1 in 10 of these present-day groups contained one group more massive than M_s at $z_{1\%}$. We may now ask a subtilely different question: "At what epoch does the region that collapsed to form a typical present-day cluster of mass M' contain a single group of mass $> M_s$?" From Equation 5.24, by

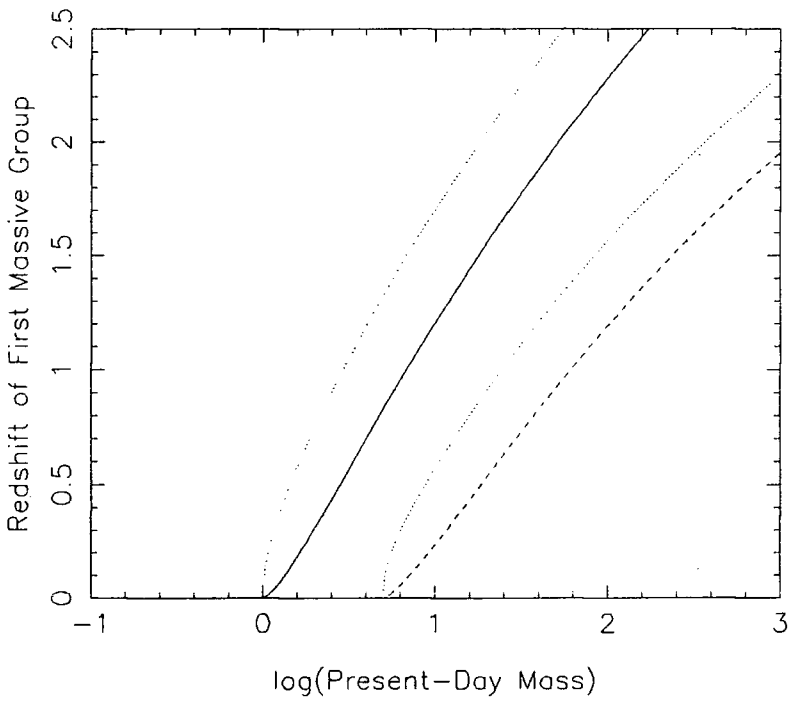

Figure 5.17. The redshift at which the first massive group (ie., $M > M_s$) is formed in a region that collapses to become a present-day cluster of mass M'. The curves shown illustrate the dependence on cluster mass for a flat power spectrum ($n = -2$), the distinction between high and low mass groups being made at masses of $M_s = 1.0$ (solid line) and 5.0 (dashed line). Dotted lines show, for each value of M_s, the epoch at which a group larger than M_s forms in 20% of regions destined to collapse to become a cluster of mass M'.

setting $F_s = M_s/M'$ (ie., we require a mass of $1M_s$ to be bound into a group of mass $> M_s$) we obtain:

$$z_{1M_s} = \frac{\sqrt{2}.\Delta_s}{\left(M_s/M_*(0)\right)^{(n+3)/6}} \mathrm{erfc}^{-1}\left[M_s/M'\right]$$

where erfc^{-1} denotes the inverse of the complementary error function. This function is plotted for $n = -2$ and $M_s = 1.0$ and 5.0 in Figure 5.17. It can be seen that this epoch is strongly correlated with M' — the same effect as that seen in Figures 5.11 and 5.12. We emphasise again that this is not in contradiction to the effect seen in $z_{1\%}$ (and z_s) as the contribution to the final mass of the cluster made by this early group becomes progressively smaller with increasing M'†. The dominant component of the final mass is made up from groups with average properties.

In order to illustrate the potential of the theoretical frame work that we have established in this chapter, we have suggested a simple illustrative model that incorporates the evolution of galaxies. We assume that galaxies make a transition between an active starforming (*unevolved*) phase and a passive evolution (*evolved*) phase when the group in which they are bound reaches a total mass of M_{ev}. Although this is clearly a gross oversimplification, it provides a pointer to the effects we would see if a more realistic model for the impact of the environment on the evolution of a galaxy were available to us. For this reason, it is illuminating to investigate its consequences. These are readily available from the study of Section 5.3. Firstly, we find that the properties of galaxies in large groups and clusters depend little on the actual group mass, M', so long as M' is somewhat larger than M_{ev}. This predicts that we should find neither an Age–Environment nor a Morphology–Environment

† Before the behaviour of z_{1M_s} can be compared with that of $f(M'| > M_s, z)$ (ie., with the distribution in present-day group masses of groups that were more massive than M_s at epoch z, Equation 5.29 and Figures 5.11 and 5.12), the relative abundances (ie., *number* densities as distinct from multiplicities) of present-day clusters of mass M' must be taken into account. Dotted lines in Figure 5.17 show the epoch at which 20% of regions destined to collapse to become clusters of mass M' at the present-day contain a groups more massive than M_s. It can be see that this epoch is not much different from z_{1M_s}. The different abundances of high- and low-mass groups is therefore unable to remove the strong correlation seen in Figure 5.17 from $f(M'| > M_s, z)$.

correlation. These relations only arise in our model if mixing by violent relaxation is not efficient in the mergers by which the cluster grows (ie., if the infalling *unevolved* galaxies are not mixed with the oldest galaxies in the core(s) of the growing proto-cluster). In this case, we should expect a correlation between both *density* and *morphology*, and, because the most massive groups at early times are incorporated into the most massive clusters of the present epoch, *density* and *age*. Secondly, our model shows that the infall rate of *unevolved* galaxies into rich clusters increases only slowly with look-back time. Therefore, observations of an increasing fraction of blue star-bursting galaxies in rich clusters at moderate redshifts (the Butcher-Oemler effect that we have described in Chapter 1) must be explained by an evolutionary effect that is *intrinsic* to the galaxies themselves, and cannot be explained as 'the epoch of cluster formation'.

6 CONCLUSIONS AND FURTHER WORK

6.1 Conclusions

In this thesis, we set out to study the stellar populations of early-type galaxies in a variety of environments. In particular, we wished to compare the galaxies found in dense rich clusters with those in the field and in lower density groups. The intention was that the difference, or similarity, between the galaxies' star formation histories would indicate whether their early-type morphology was predefined at their formation, or whether it was acquired at a later epoch due to the action of some process driven by their changing surroundings. In Chapters 3 & 4, we have presented two lines of observational investigation. Firstly, we used the spectral index technique of Rose (1985) to directly compare the average stellar surface gravities of representative samples of early-type galaxies in high- and low-density environments. We found evidence to suggest that the galaxies in the lower density regions were more dominated by dwarf star light at 4000Å. From this, we inferred that these galaxies were substantially younger than their counterparts in the rich clusters. Secondly, we compared the UVK colours of early-type galaxies in the dense Coma cluster with those of similar galaxies in the relatively weak Virgo cluster. In contrast to the previous result, we found that the average colours of galaxies (of the same absolute brightness) were *identical* (to within $0.^m02$) in both environments, and that even the variation between individual galaxies was remarkably small.

These two chapters therefore present a puzzling picture. On the one hand, E and S0 galaxies in rich clusters are more dominated by giant stars than similar galaxies in lower density regions; on the other hand, the broad-band colours of these systems are indistinguishable. In a simple single generation stellar population of solar metallicity, these two observations are not compatible — the surface gravity analysis requires that the high- and low-density systems differ in age by ~ 5 Gyr (cf., Rose & Tripicco, 1986); such stellar populations will differ in U-V (or V-K) colour by $\sim 0.^{m}2$ (Arimoto & Yoshii, 1987, and Arimoto, priv. comm.), a value that is an order of magnitude too large to be compatible with our observations. We suggest two factors that may help to resolve this paradox:

(1) In our spectral index analysis (Chapter 3), we were able to compare early-type galaxies in very rich clusters with similar galaxies occurring in very isolated environments. (Although three of the galaxies, NGC 4168, NGC 4564 and NGC 4660, in our low-density environment samples were drawn from the Virgo cluster region, these galaxies are located well away from the dense core.) In contrast, the method of colour comparison, presented in Chapter 4, can only be applied to a well-defined association of galaxies. It would therefore be difficult to apply this method in environments as sparse as those tested with the line index analysis. Previously, we argued that the environments (as deduced from the velocity dispersions of the galaxies) in the central parts of the Coma and Virgo clusters were markedly different. However, the velocity dispersion in the Virgo cluster is still much greater than that appropriate to loose groups in the field. Perhaps, therefore, we should not be too surprised if the early-type galaxies in the Virgo cluster share more in common with those of the Coma cluster than with the isolated E and S0 galaxies found in the 'true' field.

While this consideration may account for the absence of a detectable difference in the average properties of galaxies in the two clusters, the small scatter seen in the Virgo colour–magnitude relation remains uncomfortably small. A large scatter is to be expected since our photometry is not limited to galaxies in the dense core, but also includes many relatively isolated galaxies found in the outer parts of the cluster. We have looked for

an offset between the galaxies in the dense parts of the cluster (identified by Binggeli et al., 1987) and those further out. None is apparent. It would therefore seem that the relatively high average density of the Virgo cluster is unable to account, by itself, for the discrepancy between the observational results of Chapters 3 & 4.

(2) Our spectral index analysis suggests that the ages† of early-type galaxies in high- and low-density regions differ by $\sim$ 5 Gyr. Above, we translated this age difference into an offset in colour by assuming that early-type galaxies can be represented by single generation, solar metallicity stellar populations. This is a gross oversimplification. Firstly, although star formation has ceased at different times in these systems, we should still expect all these galaxies to contain significant populations of older stars. The presence of these stars will tend to dilute the changes seen, both in colours and line indices, in the single-age models. However, since the young stars must still be able to dominate the light of the system at 4000Å (in order to be consistent with the range of surface gravity measurements), this dilution cannot reduce the expected colour change by much more than a factor of 2. A second effect may, however, be of more consequence: if we assume that all galaxies commenced star formation at similar epochs, then the galaxies that continued active star formation until more recent times will have attained higher metal abundances. Metallicity and age affect the colours of galaxies in opposite senses — while younger stars tend to be bluer, higher metallicity stars are redder. Therefore, the colour differences that we infer from our naive models are likely to significantly overestimate the offset. The sensitivity of the colour–magnitude comparison presented in Chapter 4 is therefore likely to be considerably reduced. The same effect may also account for the small scatter seen in the colour–magnitude relationships of both clusters.

For a combination of the reasons outlined in (1) and (2) above, we believe that the differences (that we have inferred from our spectral index analysis) between the stellar populations of early-type galaxies in field and rich cluster environments may not be incompatible with the marked similarity of the colours of the early-type galaxies in the Virgo and Coma clusters.

† We identify the age of a galaxy with the time since the last major episode of star formation.

Clearly, the controversy can be settled with a few further observations. In particular, a series of high quality spectroscopic measurements of galaxies in the central parts of the Virgo cluster would allow the effects that we have outlined above to be quantified. In addition, these spectra would also allow the strengths of radial age gradients in these galaxies to be directly assessed. Further details of the project are outlined in Section 6.2.1.

In Chapter 5, we presented a theoretical study of the evolution of the galaxy clustering hierarchy. We now consider how this study relates to the variation of stellar populations with environment found in Chapter 3. The initial model suggested that: (a) *On average*, galaxies in both groups and large clusters have similar histories of environmentally driven evolution; but (b) despite this similarity in average properties, the groups that form unusually early in the history of the universe have a strong tendency to be incorporated into the richest clusters at the present epoch. As a result of conclusion (a), the rudimentary model does not predict a strong relationship between galaxy morphology and environment. An additional ingredient is clearly required. We suggest that the galaxies infalling into a cluster at late times do not become well-mixed with those present in the proto-cluster at early times. Under this hypothesis, the cluster will grow in a series of 'onion-shells'. The model then anticipates the existence of well-defined correlations both between morphology and density, and between age and density. This is qualitatively in accord with the observations presented in Chapter 3. In addition, we note that the largest differences in stellar populations are to be expected between early-type field galaxies and those in environments that are only *slightly* more dense. This lends substance to the comments made in (1) above.

It is important, however, to realise that it is equally possible to interpret this study within the frame work of the 'nature' scenario. If we accept the hypothesis that the morphology of a proto-galaxy can be substantially altered by the background density fluctuation, then the galaxies predetermined to be E/S0 types at the 'formation epoch' will tend to be incorporated into the cores of the rich clusters at the present-day. A density–morphology correlation will result. However, since galaxy morphology is sharply defined at the epoch of

formation, this scenario leaves us free to hypothesise that there will be no variation in the star formation histories of the galaxies (within the boundary of their morphological type).

The inability of our model to make a clear distinction between the 'nature' and 'nurture' scenarios suggests that these theories are not entirely disparate. Perhaps, instead of asking the question: "Is the morphology of galaxies determined by *nature* or by *nurture*?", we should ask: "Do the processes that define the morphology of galaxies continue to act at the present-day?". In this regard, it is interesting to note a further conclusion that arises from our theoretical work: namely, that the Butcher-Oemler effect (ie., the increased fraction of blue starburst galaxies seen in rich clusters of moderate redshift) cannot be explained without recourse to to an additional process, intrinsic to the galaxies themselves, that is not observed (in giant galaxies) at the present epoch. Other authors (eg., Broadhurst et al., 1988) have arrived at this same conclusion from the analysis of the redshift evolution of the number density of galaxies. There is, then, some evidence to suggest that the response of galaxy to its environment changes with look-back time. This effect may result from the higher disk gas densities of the galaxies of the past. Struck-Marcell & Scalo (1987) suggest that, at high gas densities, the star formation process becomes unstable and prone to chaotic behaviour. Small perturbations to a galaxy may thereby result in a strong, uncontrolled burst of star formation — as may indeed be observed in galaxies at redshifts ~ 0.5 (cf., Couch & Sharples, 1987, Broadhurst et al., 1988). There are thus two 'clocks' (or timescales) at work in the universe — the first clock is the state of the evolution of the gravitational clustering, the second is related to the density of the star forming gas. The first of these timescales is set by the macroscopic properties of the cosmos, the second by microscopic (even atomic) physics of the star formation process. As we outlined in the previous paragraph, these clocks interfere through galaxy–environment interactions, an effect that is cable of introducing great diversity, and at the same time homogeneity, into the properties of galaxies. It may be possible for such a scheme to produce both the density–morphology relation and the age differences between early-type galaxies in field and clusters environments, while maintaining

a tightness in the properties of early-type galaxies *within* the clusters. Further modeling of this competition is clearly required.

Having digressed into somewhat speculative discussion, it is now pertinent to gather together the main conclusions of this thesis. In Chapter 3, we have been able, using an analysis technique based on surface gravity sensitive spectral lines, to demonstrate that the ages of early-type galaxies vary with the density of the galaxies' environments. This trend is parallel to that between galaxy morphology and environment. Unfortunately, the above result is not independently confirmed through the analysis of the colours of galaxies in the Virgo and Coma clusters. We suggest that this discrepancy may be accounted for as follows. (1) As the density of the Virgo is significantly greater than that of the field, the low-density samples used in the two tests are not comparable. (2) Age and metallicity effects on the broad-band colours of galaxies conspire to conceal intrinsic differences in stellar populations. Together, these considerations may combine to allow the stellar populations of early-type galaxies to exhibit variations that are detectable in our spectral line analysis, but are not apparent in our comparison of broad-band colours. In addition to this observational work, we have made a theoretical study of the relation between the growth of gravitational structure in an expanding universe and its effects on the evolution of galaxies. We find that, if galaxy morphology is defined by processes driven by the galaxies' surroundings, both the abundances of the various morphological types and the ages of early-type galaxies should be closely linked with the density of the environment. However, our model demonstrates that the distinction between the 'nature' and 'nurture' scenarios for the origin of galaxy morphology is somewhat artificial. If the processes responsible for defining early-type morphology were more prevalent in the past, then this is an additional factor that could account for the small spread seen in the colour properties of the early-type galaxies in the Coma and Virgo clusters.

6.2 Directions for Future Work

In the discussion below, we outline several ways in which future studies may help to confirm (or refute) the interpretation we have placed upon our work. We divide our comments following the three projects of this thesis.

6.2.1 Line index analysis

The analysis of surface gravity sensitive spectral indices provides a simple and direct method by which to compare the ages of stellar populations. The most pressing needs in this work are to both enlarge upon the samples of early-type galaxies in high- and low-density environments (thus testing both the statistical significance and the universality of the effect found in Chapter 3), and to obtain direct measurements of the age-gradients within giant E and S0 galaxies. The first of these aims can be met (in part) by the analysis of further archival spectra.

A major advantage of this method is that it is readily possible to compare data-sets obtained with different instrumentation and having different characteristic redshifts. However, it is worrying that our present results might be susceptible to an unexpected systematic effect. Therefore, the security of our method could be greatly enhanced if we were able to obtain spectra of galaxies situated in a wide variety of environments (but having similar redshifts) using the same observational equipment. In particular, we have proposed to make extended observations of galaxies in the Virgo cluster with the aim of comparing the stellar populations of early-type galaxies in the core with those of similar galaxies in the outer parts. The spectra obtained in this project would also be used to determine the strengths of radial age gradients within individual galaxies.

6.2.2 The colours of early-type galaxies

The analysis of galaxy colours does not lend itself well to a cluster-by-cluster comparison as, in addition to possible systematic effects in the data itself, the comparison requires us to

accurately determine the relative distances of the clusters, their relative galactic extinctions and the K-corrections that must be applied to account for their differing redshifts. It is therefore extremely difficult to improve upon the analysis of the Virgo and Coma clusters presented in Chapter 4 of this work. The method is, however, particularly adept for the analysis of the variations in the properties of individual galaxies with a single cluster. The small intrinsic scatter in the colours of early-type galaxies in both of the clusters studied requires further investigation: is the variation caused by differences in the dynamical properties of the galaxies (eg., their surface brightness), or by genuine variations in their stellar populations? Resolution to this dilemma may be found if the correlations between the various galaxian parameters (both dynamical and stellar) are examined in a multi-dimensional parameter space. We are currently considering how best to perform this analysis in order to extract the maximum possible information in the face of contamination by random noise.

Additional work is required in order to relate these studies to models for the photometric and chemical evolution of composite stellar systems (eg., Arimoto and Yoshii, 1986). In particular, we are interested to determine whether a tight conspiracy is likely to occur between the photometric effects of metallicity and age. A study of this problem will allow us to determine how the variation in the star formation histories of early-type galaxies is constrained by the uniformity that we have found in the colours of these systems.

6.2.3 Cosmological models of galaxy evolution

The Press-Schechter formalism, described in Chapter 5, equips us with a simple analytic prescription for the evolution of gravitational structure. At the end of that chapter, we presented a rudimentary model for the effect that the evolving environment may have on the galaxies contained within it. This model was intended only as an example in order to illustrate some of the effects are to be expected in a more faithful representation of the universe. Several important features, that were omitted from this model, may be included in a more sophisticated treatment. Firstly, an improved description of the internal structure of the non-linear mass concentrations is required — the improved model should account for the

incomplete mixing of galaxies in group/cluster mergers, and for the different density structures of the groups formed at different epochs. These issues can be addressed with purposely designed N-body experiments. Secondly, we must reconsider our crude approximation for the interrelationship between the environment and the star formation rate of a galaxy. Progress can be made by replacing the threshold effect that terminates star formation, used in the present work, with a stochastic process. The parameterisation of the probability function describing this process must be established from the studies of specific galaxy-environment interactions published in the literature (cf. references given in Chapter 1).

The ultimate aim of this work is to compile a grandiose model for the combined evolution of both galaxies and their environment. Such a model is urgently required if we are to reach a unified understanding of the stellar populations of early-type galaxies, the changing galaxy populations of rich clusters at moderate redshifts, deep galaxy number counts and faint galaxy redshift surveys. As this study probes further into the past, the distinction between the evolution of galaxies and their formation becomes blurred. Eventually we must confront the condensation of galaxies from the primordial gas. This is a formidable hurdle, but, once crossed, we may finally have arrived at an **understanding** of *the realm of the nebulae.*

ACKNOWLEDGMENTS

Firstly, I would like to thank the people under whose guidance this work has been carried out: John Lucey, for sharing his observer's experience, scepticism and software; Jim Rose, for his unbounded enthusiasm; Carlos Frenk, for those many hours of obscure discussion; and my supervisor, Richard Ellis, for maintaining a healthy pressure during the course of this work. I am also very much indebted to Ray Sharples and Peter Teague for providing the data that made Chapter 3 possible. Without all of these people, this thesis would never have been written. Warm thanks are extended to my many astronomer-friends, both in this department and in more far-flung corners of the world, whose enthusiasm, questions, answers and general comradeship has been very much appreciated.

Let me not forget the various institutions that have made this work possible: *Starlink*, and in particular our node manager, Alan Lotts, is thanked for the provision of computing power (John Lucey must be mentioned once again for his excellent CCD reduction software); the RGO staff at the Roque de los Muchachos Observatory on La Palma, especially Dave Carter, are thanked for the essential facilities and support that they have provided; Matt Mountain, and the staff of UKIRT, are thanked for obtaining the excellent near-infrared photometry used in Chapter 4; the University of Durham is thanked for the provision of various other facilities. We thank PATT for having sufficient faith in these projects to allocate significant quantities of telescope time. The receipt of an SERC studentship is gratefully acknowledged.

Finally, let me thank all those — in particular, my parents — who have given me their love, support and friendship; this is, at last, a chance to say how much I have needed it.

BIBLIOGRAPHY

Aaronson, M., Cohen J., Mould J. & Malkan, M., 1978. *Astrophys. J.*, **223**, 824.

Aaronson, M., Persson, S. E. & Frogel, J. A., 1981. *Astrophys. J.*, **245**, 18 (APF).

Abell, G. O., 1958. *Astrophys. J. Suppl.*, **3**, 211.

Adler, R. J., 1981. *The Geometry of Random Fields* (Chichester: Wiley).

Arimoto, N. & Yoshii, Y., 1986. *Astron. Astrophys.*, **164**, 260.

Arimoto, N. & Yoshii, Y., 1987. *Astron. Astrophys.*, **173**, 23.

Bachall, N. A., 1979. *Astrophys. J.*, **232**, 689.

Bardeen, J. M., Bond, J. R., Kaiser, N. & Szalay, A. S., 1986. *Astrophys. J.*, **304**, 15.

Barnes, J. E., 1988. *Astrophys. J.*, **331**, 699.

Barrow, J. D., Bhavsar, S. P. & Sonoda, D. H., 1984. *MNRAS*, **210**, 19p.

Bautz, L. P. & Morgan, W. W., 1970. *Astrophys. J. Lett.*, **162**, L142.

Bica, E., 1988. *Astron. Astrophys.*, **195**, 76.

Bica, E. & Alloin, D., 1986. *Astron. Astrophys.*, **162**, 21.

Bica, E. & Alloin, D., 1986. *Astron. Astrophys. Suppl. Ser.*, **70**, 281.

Binggeli, B., Sandage, A. & Tammann, G. A., 1985. *Astron. J.*, **90**, 1681.

Binggeli, B., Tammann, G. A. & Sandage, A., 1987. *Astron. J.*, **94**, 251.

Bond, J. R., Cole, S., Efstathiou, G., & Kaiser, N., 1990. *in press.*

Bond, J. R. & Efstathiou, G., 1984. *Astrophys. J.*, **285**, L45.

Broadhurst, T. J., Ellis, R. S. & Shanks, T., 1988. *Mon. Not. R. astr. Soc.*, **235**, 827.

Bruzual, G., 1984. in *Spectral Evolution of Galaxies* (Oxford: Rutherford Appleton Laboratory publication RAL–84–008).

Burstein, D., 1979. *Astrophys. J.*, **234**, 435.

Burstein, D. & Heiles, C., 1984. *Astrophys. J. Suppl.*, **54**, 33, (BH).

Butcher, H. & Oemler, A., 1978. *Astrophys. J.*, **219**, 18.

Carlberg, R. G., 1984. *Astrophys. J.*, **286**, 403.

Carlberg, R. G., 1986. *Astrophys. J.*, **310**, 699.

Couch, W. J. & Sharples R. M., 1987. *Mon. Not. R. astr. Soc.*, **229**, 423.

Couture, J. & Hardy E., 1990. *Astron. J.*, **99**, 540.

Cowie, L. L. & Songalia, A., 1977. *Nature*, **226**, 501.

Davies, R.L., Efstathiou, G., Fall, S. M., Illingworth, G., & Schecter, P. L., 1983. *Astrophys. J.*, **266**, 41.

Davis, M., Efstathiou, G., Frenk, C. S. & White, S. D. M., 1985. *Astrophys. J.*, **292**, 371.

Davis, M., Huchra, J., Latham, D. W. & Tonry, J., 1982. *Astrophys. J.*, **253**, 423.

Doroshkevich, A. G., Sunyaev, R. A. & Zel'dovich, Ya. B., 1974. in *IAU Symposium No. 63*, ed. Longair, M. S. (Dortrecht: Reidel).

Dressler, A., 1980a. *Ap. J. Suppl.*, **42**, 565.

Dressler, A., 1980b. *Astrophys. J.*, **236**, 351.

Dressler, A., 1984. *Astrophys. J.*, **281**, 512, (D84).

Dressler, A., 1987. *Astrophys. J.*, **317**, 1.

Dressler, A. & Gunn, J. E., 1983. *Astrophys. J.*, **220**, 7.

Dressler, A. & Shectman, S. A., 1987. *Astron. J.*, **94**, 899.

Dreyer, J. L. E., 1888. *New General Catalogue, Memoires R. Astr. Soc*, XLIX, Part I.

Efstathiou, G., Davis, M., Frenk, C. S. & White, S. D. M., 1985. *Astrophys. J. Suppl.*, **57**, 241.

Efstathiou, G., Frenk, C. S., White, S. D. M. & Davis, M., 1988. *Mon. Not. R. astr. Soc.*, **235**, 715 (EFWD).

Elias, J. H., Frogel, J. A., Matthews, K., Neugebauer, G., 1982. *Astron. J.*, **87**, 1029.

Faber, S. M., 1972. *Astron. Astrophys.*, **20**, 361.

Faber, S. M. & Jackson, R., 1976. *Astrophys. J.*, **204**, 668.

Frogel, J. A., Persson, S. E., Aaronson, M. & Matthews K., 1978. *Astrophys. J.*, **220**, 75, (FPAM).

Giovanelli, R. & Haynes, M. P., 1983. *Astron. J.*, **88**, 435.

Giovanelli, R. & Haynes, M. P., 1985. *Astrophys. J.*, **292**, 404.

Gisler, G. R., 1979. *Astrophys. J.*, **228**, 385.

Godwin, J. G. & Peach, J. V., 1977. *MNRAS*, **181**, 323, (GP).

Gott, J. R. III, Miler, J., Thuan, T. X., Schneider, S. E., Weinberg, D. H., Gammie, C., Polk, K., Vogeley, M., Jeffrey, S., Bhavsar, S. P., Melott, A. L., Giovanelli, R., Haynes, M. P., Tully, R. B., Hamilton, A. J. S., 1989. *Astrophys. J.*, **340**, 625.

Gott, J. R. III & Thuan, T. X., 1976. *Astrophys. J.*, **204**, 649.

Gunn, J. E. & Gott, J. R. III, 1972. *Astrophys. J.*, **176**, 1.

Gunn, J. E., Stryker, L. L. & Tinsley, B. M., 1981. *Astrophys. J.*, **249**, 48.

Hamilton, D., 1985. *Astrophys. J.*, **297**, 371.

Harris, W. & Racine, R., 1979. *Ann. Rev. Astron. Astrophys.*, **17**, 241.

Hernquist, L. & Quinn, J. P., 1988. *Astrophys. J.*, **331**, 682.

Hubble, E., 1925a. *Astrophys. J.*, **62**, 409.

Hubble, E., 1925b. *Astrophys. J.*, **64**, 321.

Hubble, E., 1936. *The Realm of the Nebulae* (Yale: Yale University Press).

Hubble, E. & Humason, M. L., 1931. *Astrophys. J.*, **74**, 43.

Huchra, J. R., Davis, R. J., Latham, D. W., 1983. in *Clusters and Groups of Galaxies*, ed. Mardirossian F., Giuricin, G. & Mezzetti, M. (Dortrecht: Reidel).

Icke, V., 1985. *Astron. Astrophys.*, **144**, 115.

Illingworth, G., 1977. *Astrophys. J. Lett.*, **218**, L43.

Johnson, H. L. & Morgan, W. W., 1953. *Astrophys. J.*, **117**, 313.

Kaiser, N., 1986. *Mon. Not. R. astr. Soc.*, **222**, 323.

Kent, S. M. & Gunn, J. E., 1982. *Astron. J.*, **87**, 945.

Lake, G. & Dressler, A., 1986. *Astrophys. J.*, **310**, 605.

Larson, R. B., 1975. *Mon. Not. R. astr. Soc.*, **173**, 671.

Larson, R. B., Tinsley, B. M. & Caldwell, C. N., 1980. *Astrophys. J.*, **237**, 692.

Lynden-Bell, D., 1967. *Mon. Not. R. astr. Soc.*, **136**, 101.

Matthews, W. G. & Baker, J. C., 1971. *Astrophys. J.*, **170**, 241.

McClure, R. D. & van den Berg, S., 1968. *Astrophys. J.*, **73**, 313.

Metcalfe, N., 1983. *PhD. Thesis*, Oxford University.

Michard, R., 1982. *Astron. Astrophys. Suppl. Ser.*, **49**, 591.

Moore, B. E., Frenk C. S. & White, S. D. M., 1990. *in press.*

O'Connell, R. W., 1976. *Astrophys. J.*, **206**, 370.

O'Connell, R., 1980. *Astrophys. J.*, **236**, 430.

Oemler, A., 1974. *Astrophys. J.*, **194**, 1.

Ostriker, J. P. & Cowie, L. L., 1981. *Astrophys. J. Lett.*, **243**, L127.

Peacock, J. A. & Heavens, A. F., 1990. *Mon. Not. R. astr. Soc.*, **243**, 133.

Peebles, J., 1980. *The Large Scale Structure of the Universe* (Princeton: Princeton University Press).

Peletier, R. F., Valentijn, E. A. & Jameson, R. F., 1990. *preprint.*

Persson, S. E., Frogel, J. A. & Aaronson M., 1979. *Astrophys. J. Suppl.*, **39**, 61, (PFA).

Pickles, A., 1985. *Astrophys. J.*, **296**, 340.

Pickles, A., 1987. in *Structure and Dynamics of Elliptical Galaxies*, ed. de Zeeuw, T. (Dortrecht: Reidel).

Press, W. H. & Schechter, P., 1974. *Astrophys. J.*, **187**, 425 (PS).

Rees, M. J. & Ostriker, J. P., 1977. *Mon. Not. R. astr. Soc.*, **179**, 541.

Renzini, A., 1987. in *Stellar Populations*, ed. Norman, C. A., Renzini, A. & Tosi, M. (Cambridge: Cambridge University Press).

Rey, W., 1980. *Introduction to Robust and Quasi-Robust Statistical Methods* (Berlin: Springer Verlag).

Rood, H. J. & Baum, W. A., 1967. *Astron. J.*, **72**, 398.

Rood, H. J. & Dickel, J. R., 1976. *Astrophys. J.*, **205**, 346.

Rood, H. J. & Sastry, G. N., 1971. *Publ. Astron. Soc. Pas.*, **83**, 313.

Rose, J. A., 1985. *Astron. J.*, **90**, 1927.

Rose, J. A. & Tripicco, M. J., 1986. *Astron. J.*, **92**, 610.

Schlesinger, B. M., Astrophys. J.. *1969*, **157**, 533.

Sandage, A., 1961. *The Hubble Atlas of Galaxies* (Washington D. C.: Carnegie Institution of Washington).

Sandage, A., 1972. *Astrophys. J.*, **176**, 21, (S72).

Sandage, A., 1973. *Astrophys. J.*, **183**, 711.

Sandage, A., Binggeli, B. & Tammann, G. A., Astron. J.. *1985*, **90**, 1759.

Sandage, A. & Visvanathan, N., 1977. *Astrophys. J.*, **216**, 214.

Sandage, A. & Visvanathan N., 1978. *Astrophys. J.*, **223**, 707, (SV).

Salvador-Sole, E., Sanroma, M. & Jordana, J. J. Rdz., 1989. *Astrophys. J.*, **337**, 636.

Sarazin, C. L., 1988. *X-ray Emission from Clusters of Galaxies* (Cambridge: Cambridge University Press).

Sharples, R. M., 1989. *in prep.*

Sharples, R. M., Ellis, R. S. & Gray, P. M., 1987. *MNRAS*, **231**, 479.

Spitzer, L. & Baade, W., 1951. *Astrophys. J.*, **113**, 413.

Struck-Marcell, C. & Scalo, J. M., 1987. *Astrophys. J. Suppl.*, **64**, 39.

Teague, P., 1988. *PhD. Thesis*, Australian Nat. Univ.

Tifft, W. A., 1969. *Astron. J.*, **74**, 354.

Tinsley, B. M., 1972. *Astron. Astrophys.*, **20**, 383.

Tinsley, B. M., 1980. *Fundamentals of Cosmic Physics*, **5**, 287.

Toomre, A. & Toomre, J., 1972. *Astrophys. J.*, **178**, 623.

U. K. Infrared Telescope Support Unit, 1988. *UKIRT Observer's Manual* (Edinburgh: ROE).

de Vaucouleurs, G., 1948. *Ann. d'Astrophys.*, **11**, 247.

de Vaucouleurs, G., de Vaucouleurs A. & Corwin, H. G., Jr., 1976. *Second Reference Catalogue of Bright Galaxies* (Austin: University of Texas Press).

Wall, J. V., Laing, R. A., Argyle, R. W. & Wallis, R. E., 1989. *A User Guide to the INT Prime Focus CCD* (RGO user manual no. 12).

White, S. D. M., 1980. *Mon. Not. R. astr. Soc.*, **191**, 1P.

White, S. D. M., Davis, M., Efstathiou, G. & Frenk, C. S., 1987. *Nature*, **330**, 451.

Whitford, A. E., 1971. *Astrophys. J.*, **169**, 215.

Wolf, 1865. *Aston. Nach.*, **65**, 1.

Wood, D. B., 1966. *Astrophys. J.*, **145**, 36.

Woolf, N. J., Schwarzschild, M. & Rose, W. K., 1964. *Astrophys. J.*, **140**, 833.